THE ANGULAR DISTRIBUTION OF PHOTONEUTRONS FROM O^{16}

D. BRIAN C. B. SYME.

Submitted to the University of Glasgow

as a Thesis for the Degree of Doctor of Philosophy

April 1972

ProQuest LLC.
789 East Eisenhower Parkway
P.O. Box 1346
Ann Arbor, MI 48106 – 1346

SUMMARY

of the Ph.D. Thesis

"The Angular Distribution of Photoneutrons from O^{16}"

by

D. BRIAN C.B. SYME

• • • • • • • • • • • •

SUMMARY

The relative importance of competing reaction channels in the photo-excitation of the giant resonance in O^{16} has been studied by measurement of the angular distribution of the emitted photo-neutrons through the corresponding energy range using a multi-angle neutron time of flight spectrometer installed at the Kelvin Laboratory of the University of Glasgow.

Design factors for the spectrometer are discussed with regard to optimisation of energy resolution and counting rates under the constraints of the source, and the obtainable accuracy of normalisation between neutron detectors at different angles has been measured. A reliable method of calibration of the neutron energy scale at each angle is described and corrections to the neutron spectra for absorption by materials in the flight path have been made. The energy dependent efficiency of the neutron detectors is calculated in an appendix by a Monte Carlo technique using a new measurement of the scintillation response curve for recoil protons.

Angular distributions of photoneutrons from the $D^2(\gamma,n)p$ reaction with 26.9 MeV bremsstrahlung have been measured and are found to agree with previously published results and theoretical predictions to within the expected accuracy. This is taken as confirmation of good angular normalisation in the system.

Measurements by the author of the angular distributions of photo-neutrons from 26.9 MeV bremsstrahlung on O^{16} are presented and absolute

cross sections have been obtained with respect to that known for deuterium. Photoproton data from other authors is analysed in a similar way for comparison with the photoneutron results.

In the E1 approximation, the relative intensity of s/d wave admixture is found to follow the resonance structure for both protons and neutrons and the corresponding phase difference is found to vary about the value expected from optical model predictions. The E2 cross section has been extracted from the data and is found to rest mainly in two broad states centred at about 23 MeV and 24.7 MeV, while a Barker-Mann analysis shows the isospin impurity in the O^{16} giant resonance to be small and to be mainly associated with the regions of E2 strength.

The pure 1p1h dipole approximation fails to describe these features and the observed splitting of the giant resonance in O^{16} but the presence of more complicated excitations is shown to be more consistent with experiment.

INDEX

PREFACE

The work described in this thesis was performed by the author at the Kelvin Laboratory, University of Glasgow, during the period October 1967 to March 1972.

An investigation was made of the relative importance of competing reaction channels in the photo-excitation of the giant resonance in O^{16} by measuring the angular distribution of the emitted photoneutrons over this energy range using a multi-angle Time-of-Flight spectrometer installed at the linear accelerator of the Kelvin Laboratory.

The development of such a spectrometer is described with optimisation of energy resolution and counting rate under the constraints of the source and the possible precision of angular normalisation of such a system has been found for the neutron detectors used. Correct alignment of the energy spectra is demonstrated. This is essential for a meaningful comparison of the spectra from different angles as are the corrections for neutron absorption effects and detector efficiency which vary with neutron energy in the LAB. frame and are therefore necessary to avoid distortion in the C.M. frame of reference. A precise measurement of the absorption has been made and an original calculation of the detector efficiency is described, with an accurate measurement of the response of the scintillator used. Analysis of the data is entirely original.

Angular distributions of photoneutrons from 26.9 MeV bremsstrahlung on O^{16} are presented and absolute cross sections have been obtained with respect to that known for deuterium. Photoproton data from other authors is analysed in a similar way for comparison with the photoneutron results.

In the E1 approximation, the relative intensity of s/d wave admixture is found to follow the resonant structure for both protons and neutrons and the corresponding phase difference is found to vary about the value expected from optical model predictions. The E2 cross section has been extracted from the data and is found to rest mainly in two broad states centred at about 23 MeV and 24.7 MeV, while a Barker-Mann analysis shows the isospin impurity in the O^{16} giant resonance to be small and to be mainly associated with the regions of E2 strength.

The pure 1p1h dipole approximation fails to describe these features and the observed splitting of the giant resonance in O^{16} but the presence of more complicated excitations is shown to be more consistent with experiment. The interpretation of the results is entirely due to the author.

ACKNOWLEDGMENTS

The author would like to thank Professor G.R. Bishop and Professor P.I. Dee for the interest in his work and for the use of the many facilities of the Natural Philosophy Department of Glasgow University during his research programme.

The author would like to express his appreciation to Dr. G.I. Crawford for supervising his research work and for guidance and encouragement during this period.

Thanks are also due to Dr. J.D. Kellie, Dr. S.J. Hall and Dr. J. McKeown for a valuable exchange of information, equipment and effort in the course of this work and to Mr. N. Islam and Mr. H.R. Siddique for their assistance in operating the accelerator during the experiment.

The technical staff of this Laboratory under Mr. R.W. Costford and Mr. A. Keddie are thanked for the help provided on numerous occasions, and thanks are due to Mrs. E. Taylor for her assistance with the illustrations in the thesis.

The receipt of financial assistance from the Science Research Council (October 1967 to October 1970) is gratefully acknowledged. Since October 1970 the author has been a Research Fellow in the Natural Philosophy Department of the University of Glasgow.

Finally, the author would like to thank his wife for typing the thesis and for her encouragement and forbearance during the period of study.

Chapter 1

1.1 Introduction

Photons provide a convenient probe for nuclear structure studies since the electromagnetic interaction is well understood and the interaction with nucleons is weak, so that perturbation of the system is minimised.[1] A review of the photon absorbtion spectrum for a typical nucleus in section 1 of this chapter will show that the giant dipole resonance is its dominant feature and the following treatment will concentrate on this phenomenon, with a bias towards the light nucleii and the spectroscopy of emitted photoparticles.

Examination is first made of the reaction characteristics which depend on the nature of the interaction operator (selection rules, sum rules) rather than the nuclear structure effects and a review of the experimental trends is presented from this point of view before introducing the nuclear structure models and enquiring how they satisfy the experimental data. Predictions of the independent particle shell model for light nucleii will then be compared with more detailed experiments involving the fine structure of the giant resonance states, and justification is made for the author's experiment on the angular distribution of photoneutrons from the giant resonance of O^{16}. Finally, a review is given of experimental techniques for the study of the nuclear photoeffect, with emphasis on photoparticle spectroscopy and, in particular, high resolution measurements of photoneutron spectra by nanosecond time of flight techniques, as used in this project.

Fig. 1

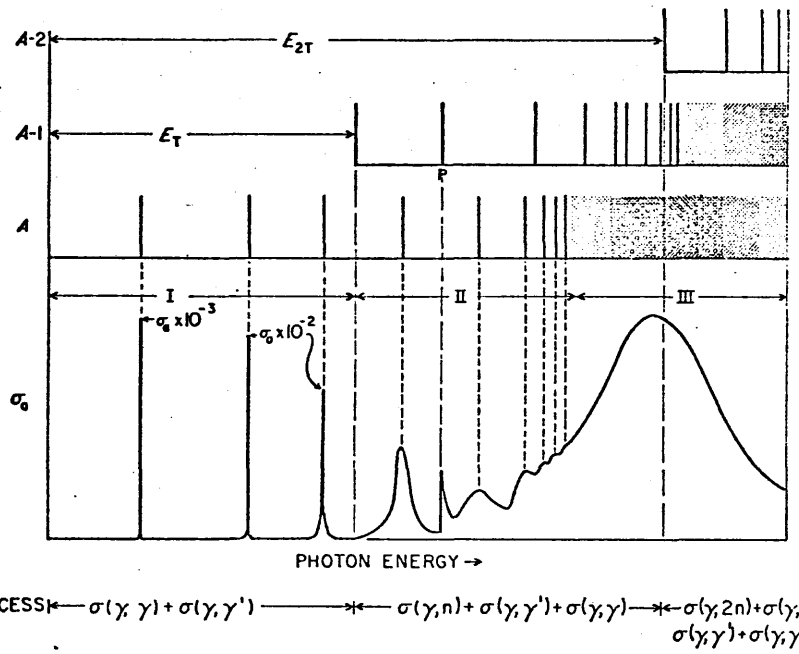

Fig. 1. The photon absorption cross section for an idealized nucleus. Region I is that part of the energy scale below the particle thresholds where the absorption is into discrete energy levels. Region II is the energy range above the binding energy where structure may still exist in the absorption cross section. In Region III the absorption cross section is smooth. The processes that can take place are indicated along the abscissa; $\sigma(\gamma, n)$ here stands for the cross section for nucleon emission. The energy levels in the nucleus A, $A-1$, and $A-2$ are illustrated at the top of the diagram. The binding energies for one and two particles are designated by E_T and E_{2T}. The level P_1 in $A-1$ represents a parent of the ground state of nucleus A.

1.2 Experimental Trends in the Nuclear Photoeffect.

The photon absorbtion spectrum for an idealised nucleus is reproduced in Figure 1 (from Reference 3). At the lowest photon energies, only Thomson scattering from the whole nuclear charge can occur (region 1 figurel) and since this does not disrupt the nuclear coordinates it will not be discussed further. Nuclear energy levels are excited at higher energies and absorbtion takes place into individual bound and continuum states, as in regions 2 and 3. Since successive states have a possibility of decay to all those preceding, the widths increase with excitation energy until the states overlap at some energy greater than the particle emission threshold.[3,4]

The dominant feature of the photon absorbtion spectrum for all nucleii is the Giant Resonance.[1,2,3,4,5] In 1947 this was discovered as a strong broad peak in the photofission cross sections [16] then found in the yield curves in (γ,n) reactions on C^{12} and Cu^{63} [17] and soon discovered to be a general effect in all photon induced reactions, appearing as a prominent peak some 5 M.e.V. wide at an energy between the photodisintegration threshold and 25 M.e.V.[2]. Many later experiments [20] have shown the Giant Resonance to correspond to a coherent collective motion of neutrons against protons following electric dipole absorbtion of the incident radiation, in agreement with the independent early suggestions of Goldhaber and Teller[18] and Migdal[19]. It will be shown in section 1.3 that the electric dipole operator separates neutrons and protons.

For energies above the Giant Dipole Resonance, photonuclear absorbtion takes place predominantly by the quasideuteron mechanism[21]

where the low momentum photon is able to eject high momentum particles by interacting with correlated nucleon pairs in the nucleus. The emitted particles show dynamic relations characteristic of the photodisintegration of the deuteron and the momentum distribution of nucleons in the nucleus.[21,2]

1.3 General Properties of Photonuclear Reactions.

Many of the characteristic features of photoreactions arise from the nature of the electromagnetic interaction which tends to limit the type of states reached in photon excitation to those closely connected to the ground state by simple single particle transitions. In particular, the giant dipole resonance is believed to be a coherent superposition of such one-particle one-hole (1p1h) states.[1] At low energy and linear momentum transfer, photon transitions are simplified by a preference for low angular momenta, so that only one or two multipoles make significant contribution, even if several are allowed by the well known angular momentum and parity rules which again follow from the nature of the operator. A brief indication of the sources and content of these rules will now be given. A more detailed account may be found in references (1,2,3,4,5).

The operator H', describing the perturbation of the nuclear Hamiltonian in the presence of the electromagnetic field for single photon transitions, is given by

$$H' = -\frac{1}{c}\int \underline{j}(\underline{r},t).\underline{A}(\underline{r},t).d\underline{r} \qquad (1.3.1)$$

where $\underline{j}$ and $\underline{A}$ are the nuclear current operator and the electromagnetic potential operator, respectively.[5] Since $\underline{j}$ transforms as a vector

operator under rotations, the selection rule for electric and magnetic transitions of order 2^{ℓ} arises from the form of the multipole expansion for A, as [5]

$$E(\ell) \qquad \Delta\pi = (-1)^{\ell}$$

$$M(\ell) \qquad \Delta\pi = (-1)^{\ell+1} \qquad (1.3.2)$$

Further properties depend upon the transition rate w between states $|i\rangle$ and $|f\rangle$, given in terms of the density of final states ρ_f as:

$$W = \frac{2\pi}{\hbar} \cdot |\langle f|H'|i\rangle|^2 \cdot \rho_f \qquad (1.3.3)$$

Evaluation of w requires some assumptions in order to bypass the problem of meson currents associated with $\underline{j}$, the nuclear current operator. In the long wavelength limit ($kR \ll 1$), H' simplifies to the product of an angular term and $\underline{\nabla}.\underline{j}$, which is substituted by the nuclear charge density $\rho(r,t)$ on the assumptions of continuity, and separable time dependence of the operators.[2-5] In this series of approximations, known as Siegert's theorem[6], the assumption of point proton charges is valid, and for electric dipole (E1) transitions, the transition operator simplifies to a multiple of the dipole operator:

$$\underline{D} = \sum_{i=1}^{A} e_i \underline{r}_i \qquad (1.3.4)$$

By introducing the centre of mass coordinate $\underline{R}$ and the relative nucleon coordinate $\underline{\rho}_j$,

$$\underline{R} = (1/A) \sum_{i=1}^{A} \underline{r}_i$$

$$\underline{\rho}_j = \underline{r}_j - \underline{R} \qquad (1.3.5)$$

the centre of mass dipole operator is obtained.

$$\underline{D}' = \sum_{i=1}^{A} e_i \underline{\rho}_i = e \frac{N}{A} \sum_{i=1}^{Z} \underline{r}_i - e \frac{Z}{A} \sum_{i=Z+1}^{A} \underline{r}_i \qquad (1.3.6)$$

so that neutrons and protons are separated by the dipole operator, and may be considered to have effective charges of $-Z/A$ and N/A,

respectively.[2,3,4,5] The difference between the operators D and D' is the Thomson scattering from the whole nuclear charge.

$$\underline{D} = \underline{D}' + e\mathcal{Z}\underline{R} \qquad (1.3.7)$$

Model independent effective charges cannot be derived for magnetic transitions, but general results may be derived for electric multipoles of order 2^l [2-5]

$$e_p = e \cdot \frac{1}{A^l} \cdot [(A-1)^l + (-1)^l (Z-1)]$$
$$e_n = e \cdot \mathcal{Z} \cdot \left(\frac{-1}{A}\right)^l \qquad (1.3.8)$$

and also for deuteron and alpha emission for El radiation.[2,3,4,5]

$$e_d = (N-\mathcal{Z})/A$$
$$e_\alpha = 2.(N-\mathcal{Z})/A \qquad (1.3.9)$$

In O^{16}, the proton and neutron effective charges are equal for El emission and are +29/32 and -1/32 for E2 direct emission respectively. This implies that proton emission should predominate after E2 absorbtion and El-E2 interference should produce forward peaked assymetry in the proton angular distributions and weaker backward peaking in the neutron distributions. Experimentally, both are forward peaked and this requires explanation eg., by postulating a nuclear structure model of the mechanism.[4] The El emission of deuterons and alphas from self-conjugate nucleii should be zero by these considerations but this is slightly violated in practice due to the effect of the coulomb interaction.[2,3,4]

More generally, the interaction between the electromagnetic field and the nucleus may be written, under the assumption of charge independence of nuclear forces, as [15]

$$H' = H_0' + H_1' = H_0' + \sum_i a(i)\,\tau_z(i) \qquad (1.3.10)$$

where Ho' is independent of isotopic spin but H ' transforms as the third component of a vector in isotopic spin space, so that for

H_o	TRANSITIONS	$\Delta T = 0$
H_1	"	$\Delta T = 0, \pm 1 \quad ; \; T_z \neq 0$
		$\Delta T = \pm 1 \quad ; \; T_z = 0$ (1.3.11)

By substituting the isospin projection operators for protons and neutrons

$$P_+ = \tfrac{1}{2}(1 + \tau_z) \qquad P_- = \tfrac{1}{2}(1 - \tau_z) \tag{1.3.12}$$

in equation (1,3,6), the dipole operator for a self-conjugate nucleus becomes

$$D' = (e/2)\sum_{i=1}^{A} (r\tau_z)_i \tag{1.3.13}$$

which is of the H ' type and therefore, we obtain the selection rules for self-conjugate nucleii

(1) El transitions obey; $\Delta T = \pm 1$

(2) Other transitions obey: $\Delta T = \pm 1, 0$ (1.3.14)

in agreement with the original work of Trainor[8] and Radicatti [9]. Isotopic spin impurities due to the coulomb force have been calculated [9,15] and agree with the measurements of Wilkinson [15'], so that, for the light elements, impurities vary between 0.2% and 5% and the forbidden transitions are inhibited by between 20 and 500.

The cross section integrated over the absorbtion line,

$$\int_{line} \sigma \, dE_\beta = \frac{L^3}{c} \int_{line} w \, dE_\beta \tag{1.3.15}$$

can be evaluated for El transitions under Seigert's theorem. Summing over the final states $|\beta\rangle$ and using the closure condition gives

$$S = \sum_{\beta\, line} \int \sigma \, dE_\beta = \frac{2\pi^2}{\hbar c} \cdot e^2_{eff} \cdot \langle \alpha | [z, [H, z]] | \alpha \rangle \tag{1.3.16}$$

which depends only on the wave functions in the ground state $|\alpha\rangle$.

H is the total nuclear Hamiltonian, written in the form

$$H = \sum_{i=1}^{A} (p_i^2/2m) + \sum_{i<j} (v_{ij}). \qquad (1.3.17)$$

The kinetic energy term contributes $\hbar^2/m$ to the double commutator so that, summing over the z protons and N neutrons and using the effective charges of equation (1.3.6), we obtain

$$S = (2\pi^2 e^2 \hbar/mc) \cdot (NZ/A) \cdot (1+V)$$

$$= 0.06 \ (NZ/A) \ (1+V) \ \text{M.e.V. Barns.} \qquad (1.3.18)$$

V is the contribution from the potential energy, which is non-zero and serves to increase the sum rule for exchange forces or velocity dependent forces which do not commute with H. The minimum value provided by the kinetic energy term is known as the Thomas Reiche Kuhn (T.R.K.) sum rule[11] for atomic systems or as the Classical Dipole Sum Rule, since the same result holds for a classical charged oscillator.[2,12] Typical attractive exchange force mixtures increase the dipole sum by about 40%.[13]

The sum rule is useful in that it provides a model - independent lower limit to the E1 strength in a nucleus and indicates the presence of exchange or velocity - dependent nuclear focus in nucleii with larger integrated cross sections. But the upper limit of integration is undefined and the cross section for pure E1 processes is seldom measured. A more useful sum rule was obtained in 1954 by Gell-Mann, Goldberger and Thirring (G.G.T.).[14] Assuming that photons of energy greater than the meson threshold contribute only to meson production and that the forward scattering amplitude for a nucleus approaches that of z free protons and N free neutrons as the photon energy tends to infinity, they obtained the integrated cross section for all

multipoles up to the meson threshold as

$$S' = \int_0^{\mu} \sigma(E)\, dE = 0.06\,(NZ/A)(1 + w) \qquad (1.3.19)$$

where w depends on the difference between measureable photonucleon cross sections at high energies, and is estimated to be about 0.6 ± 0.2.[14]

The two rules have equal values within the errors, showing the importance of E1 transitions. This is confirmed by the calculations of Levinger and Bethe,[13] who showed that quadrupole transitions can amount to only about 6% of dipole transitions. Under charge independence of nuclear forces and neglecting exchange forces, Gell-Mann and Telegdi[15] derived an E2 sum rule for $\Delta T=0$ (H_0) transitions in self-conjugate nucleii

$$\int \frac{\sigma(E2)}{E^2}\, dE = \frac{\pi^2}{137} \cdot \frac{A}{12} \cdot \frac{\langle r^2 \rangle_{00}}{mc^2} \qquad (1.3.20)$$

where $\langle r^2 \rangle_{00}$ is the mean square displacement of a nucleon of mass m from the nuclear centre. For O^{16} this sum rule has the value 5.5 uB./M.e.V.(26)

The above model - independent results have proved to be useful guides in the study of photonuclear reactions for they provide orders of magnitude by which to judge the importance of nuclear structure features in the measured phenomena. The values for O^{16} will be consulted later in this thesis.

1.4 The Giant Dipole Resonance and Nuclear Models.

For medium to heavy nucleii, the coalescence of individual levels in photoabsorbtion occurs about the energy of the Giant Resonance which tends to be a smooth curve whose properties depend only on the gross nuclear parameters of size and shape.[1,2,3,4] Because of the large

coulomb barrier, photoabsorbtion for these nucleii is followed overwhelmingly by neutron emission, and the absorbtion cross section is found from the neutron yields.[1,2] When integrated over just the Giant Resonance region, the absorbtion cross section is found to exceed the classical electric dipole sum rule.[1-5] This indicates the importance of the Giant Resonance in taking nearly all the El strength the nucleus may have, and further, the extra strength present at higher energies demands exchange or velocity - dependent terms in the nuclear Hamiltonian. (section 1.2.)

The variation in the Giant Resonance Peak energy, E_o, is well predicted by the hydrodynamic model of the dipole oscillations as:

$$E_o = 80\ A^{-1/3}\ \text{M.e.V.} \qquad (1.4.1)$$

This model [18,22,23] considers the nucleus as two interpenetrating fluids of neutrons and protons with collective vibrations of one fluid against the other excited by electric dipole absorbtion of photons. For nucleii with large intrinsic prolate deformations, the hydrodynamic model correctly predicts the observed splitting of the Giant Resonance into two components corresponding to charge oscillations along the nuclear symmetry axes, [25,24] and the derived values of intrinsic quadrupole moments of such nucleii are in good agreement with other measurements.[ ] The shape dependence leads naturally to the observed variation of the width of the Giant Resonance with A, and its minimum value for closed shell nucleii.[1-5] Although the neutron spectra and angular distributions from the decay of the Giant Resonance are found to be in accord with the predictions of statistical evaporation from the compound nucleus,[29,1-5], these

collective models offer no mechanism to explain the observed high yield of directly emitted fast photoparticles.

In complete contrast, the dipole resonance of light nuclei is always between 20 and 25 M.e.V, and is composed of a number of individual resonances. The density of this level structure is found to increase and the level widths found to decrease from C^{12} to Ca^{40}. Direct photonucleon emission is found to predominate, and the smaller coulomb barrier allows the yields of neutrons and protons to be comparable. The total cross section is essentially the sum of the (γ,n) and (γ,p) reactions and its value integrated to 25 M.e.V. is only ~60% of the T.R.K. sum rule, the missing El strength being assumed present in the higher energy quasideuteron cross section.

These features are incompatible with hydrodynamic model predictions and the observed individual level structure suggests an independent particle shell model description of the photoeffect, in which the giant dipole resonance is due to electric dipole absorbtion of photons by excitation of nucleons from the uppermost shell to the next shell of opposite parity, under the selection rule $\Delta l=\pm 1$. In the simple Harmonic oscillator shell model, the transitions are all at the energy of the oscillator spacing (neglecting the spin orbit splitting) and this is the energy of the giant dipole resonance, so that, in this model

$$E_o = 40\ A^{-1/3}\ M.e.V. \qquad (1,4,2)$$

which is wrong for both the light and heavy nucleii. Although the splitting of the giant resonance in deformed nucleii can be predicted successfully by this model, it has no mechanism to produce the

Transitions in O^{16}

TABLE 1

Transition	$3D^2/q^2$	F^2 (%)	E(MeV)	E'(MeV)	D'^2 (%)	F
$1p_{\frac{3}{2}} \rightarrow 2s_{\frac{1}{2}}$	4/3	11	18.53	19.6	2	.951
$1p_{\frac{3}{2}} \rightarrow 1d_{\frac{5}{2}}$	6	50	17.65	22.2	73	.898
$1p_{\frac{1}{2}} \rightarrow 1d_{\frac{3}{2}}$	10/3	28	16.58	18.1	1	.903
$1p_{\frac{1}{2}} \rightarrow 2s_{\frac{1}{2}}$	2/3	5.5	12.38	13.5	4	.996
$1p_{\frac{3}{2}} \rightarrow 1d_{\frac{3}{2}}$	2/3	5.5	22.73	25.2	20	.963

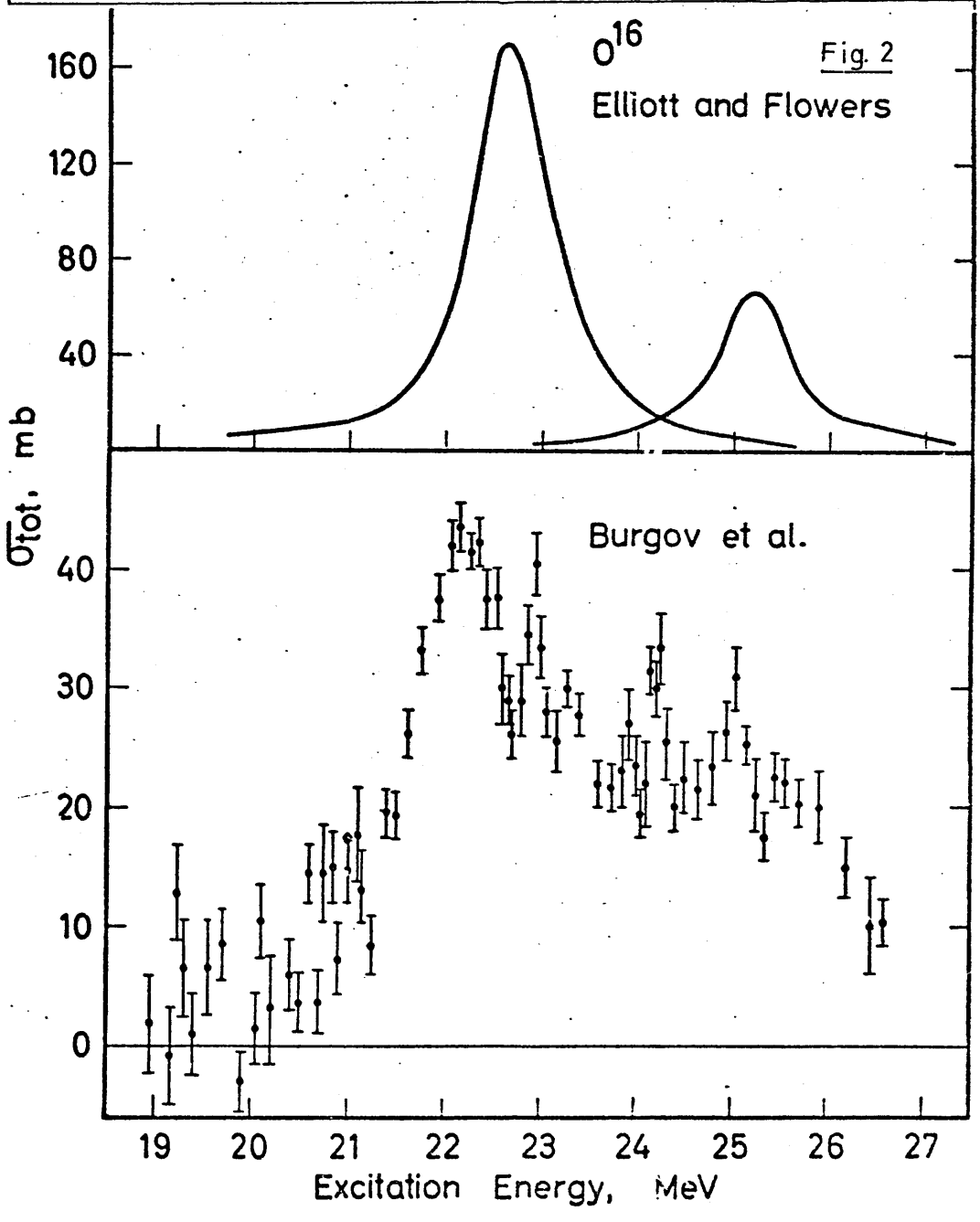

Fig. 2

observed absorption at higher energies.

1.5 The Independent Particle Shell Model and the detailed structure of the dipole resonance in Light Nucleii (0^{16})

The simple shell model was improved to give better agreement with observed transition energies in 0^{16} by Elliot and Flowers.[30] The basic shell model transition energies were defined as the sum of the energies of the excited particle and residual hole, assumed to be the known bound states of 0^{17} and 0^{15}(or N^{15}) respectively. Perturbation by the residual interaction between the particle and the hole mixed these states and changed the energies, so that most of the strength was taken by one or two high energy transitions. Brown et. al.[31] used the schematic model to explain that the success of this calculation lay in the effect of the residual interaction. Later one particle one hole (1p1h) calculations produced results entirely similar to those of Elliot and Flowers.[3]

The nucleus 0^{16} has become a testing ground for theoretical study because of its convenient closed - shell structure and the relative simplicity of its excited configurations. The five main 1p1h excitations in 0^{16} are noted in table 1 with the energies and strengths for unperturbed and perturbed transitions in the calculation of Gillet.[32] The fraction F of the initial transition in the final state is high and the two most intense are the nodeless transitions ($1p^{-1}_{3/2}$; $1d_{5/2,3/2}$,). The Elliot and Flowers result is compared with the total cross section of Burgov et. al.[33] in figure 2, where arbitrary widths have been assigned to the peaks.[3] The gross structure is reproduced reasonably well, but the calculated cross -

section ($\sum_k E'_k D'^2_k$) is necessarily too large due to the use of artificially increased E'_k values and unchanged values of D'^2_k with respect to the basic simple Harmonic oscillator case.[1-4] Emission of predominantly d - wave photoparticles in the 22-25 M.e.V. region is, however, correctly predicted.[34]

Explanation of the fine structure was sought by consideration of the effect of higher multipole absorbtion in the El giant resonance. Dodge and Barber[34] found a fairly constant finite value of the A1 coefficient in the angular distribution of protons, implying a broad region of quadrupole absorbtion, which was correctly predicted by the 1plh calculation of Spicer and Eisenberg[35] and the later 1plh and 2p2h calculation of Eisenberg, Spicer and Rose(36) for 1+ and 2+ levels in this region. More accurate angular distribution coefficients from the (p,γ) experiment of Earle and Tanner[92] showed a broad E2 resonance centred at 30 M.e.V., some 10 M.e.V. wide, with a peak cross section of about 1uB and due mainly to f - wave proton capture. The observed constancy of the odd (interference) coefficients with energy implied that the structure in the cross section was not due mainly to E2-El interference but was equally probably due to interference between the strong broad El resonance and weaker El resonances of different phase.[92]

In attempting to predict the experimental structure, the shell model did not estimate the widths of the resonances, in fact the use of the energies of bound states in the neighbouring nucleii neglected the finite widths of the real states, for protons in the 1d3/2 state or neutrons in the 1d3/2 or 2s states of O^{16} lie in the continuum and

can decay by penetration of a potential barrier.[1] Considerations of the width of the dipole state as proportional to the product of state intensity and barrier penetrability for particle emission lead to qualitative explanation of the observed narrowing of the dipole states through the 2s - 1d - 1f shells.[1]

In 1966, Buck and Hill[38] performed a continuum calculation of the giant resonance in O^{16}, using the optical model potential to describe the interaction between a nucleon and the corresponding mass 15 nucleus. Reaction channels with quantum numbers $J^{\pi} = 1^-$ were studied and the giant resonance capture states were taken as 1p1h only, neglecting matrix elements mixing in higher configurations. The scattering wave functions produced by the model were used to calculate reaction amplitudes and cross sections directly as a function of energy. Inclusion of quadrupole capture from the incident elastic channels allowed evaluation of the small E2 cross section and its effect on the angular distributions. The results were compared directly with the measurements of (p,γ) cross sections and angular distributions of Earle and Tanner[92] and the polarization data of Bertozzi et. al.[39]

The magnitude of the calculated cross section was adjusted to fit experiment by inclusion of a finite absorbtion term in the optical model potential, which the authors describe as a device approximating the effect of the competing reactions not explicitly treated in the calculation ((p,α) (p,p')) and as a substitute for the two - body correlations in the nuclear wave function which move some of the strength out of the giant resonance to higher energies. They

Fig. 3

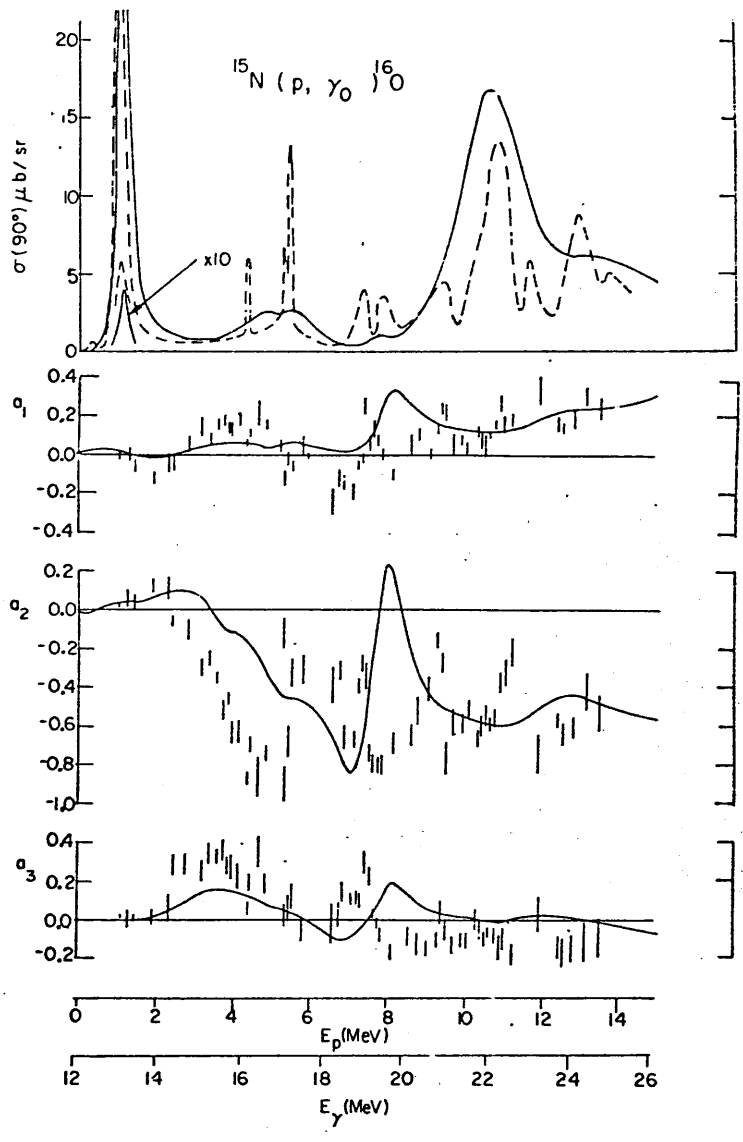

FROM EARLE & TANNER (92)

Fig. 4

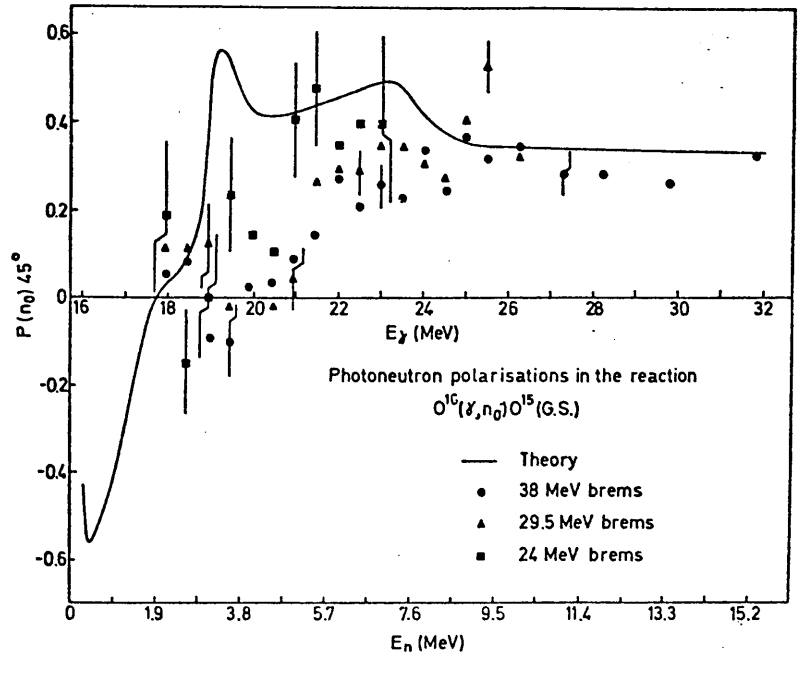

FROM BUCK & HILL (38)

therefore expected to predict the envelope of a more detailed structure, and this prediction is well borne out by the comparison with experiment reproduced in figure 3. The angular distribution and polarization results gave more approximate agreement. (figure 4). Buck and Hill concluded that the 1plh model reproduced the main features of the giant resonance but that prediction of the observed structure effects required a theory encompassing higher ph configurations or more scattering channels.

Some confirmation of this postulate came from the calculations of Gillet et. al.[40] who coupled 2p2h excitations into the 1plh basis for the giant resonance and correctly predicted the dip at 22.7 M.e.V. in the O^{16} spectrum. A peak in the $N^{14}(d,\gamma)$ spectrum of Suffert et. al.[41] at this energy, was related to the 2p2h state calculated to cause the dip in the O^{16} absorbtion. The emitted gamma ray was found to be dipolar in the $N^{14}(d,\gamma)$ reaction,[41] but the deuteron effective charge is zero for pure T=1 electric dipole transitions (equation 1.3.9) so that the reaction must proceed through a T=0 admixture in the T=1 giant dipole resonance. This corresponds to the construction $|0^+;T=0;1^-,T=1\rangle$ of the 2p2h state in reference 40.

This was the situation at the time of commencement of the author's researches (1967). The giant dipole resonance in O^{16} was approximately described by the 1plh shell model but the observed structure was not predicted and nature was somewhat more complicated. Further study of this nucleus required detailed knowledge of the cross sections of the reactions competing for strength from the giant resonance, in particular, a measurement of the neutron angular

distributions would be useful to provide multipole information and an accurate total cross section for comparison with the proton channel.

If isospin is a good quantum number, the (γ,n) and (γ,p) cross sections should be identical. Barker and Mann [42] have shown that the admixture of isotopic spins is sensitive to the cross section ratio. Their expression may be written

$$\frac{d\sigma_p(\theta)}{d\sigma_n(\theta)} = \frac{F_p(\theta)}{F_n(\theta)} \cdot \frac{P_p}{P_n} \cdot \frac{\gamma_p^2}{\gamma_n^2} \left| \frac{a_1 - a_0}{a_1 + a_0} \right|^2 \qquad (1.5.1)$$

where σ_p, F_p, P_p and γ_p are the proton cross section, angular distribution, penetrability and reduced width respectively, and similarly for the neutrons, and a_1 and a_0 are the amplitudes of T=1 and T=0 components in the wave function. Assuming equal reduced widths for neutrons and protons and using calculated values of the slowly varying penetrability ratio gives a direct measure of the isospin impurity of a state, if the angular distributions are identical. This assumption has been made in calculations of the T=0 admixture in the dominant T=1 giant resonance states of O^{16} [90] but an accurate measurement of the poorly known photoneutron angular distributions [78] was required to confirm its validity.

In addition, continuum calculations of the (γn) process in O^{16} were being made at this time [44] and a further detailed assessment of the lplh model would be possible by direct comparison of (γ,n) theory and experimental angular distributions. The author therefore feels that a measurement of the angular distribution of photoneutrons from the giant resonance of O^{16} was required for several reasons and that the selection of this experiment as his research project was

justified on theoretical grounds.

1.6 The Development of Experimental Techniques in Photodisintegration.

The following discussion will concentrate on the techniques applicable to the study of the modes of excitation of the Giant Resonance in light nucleii, especially the photoparticle spectroscopy, but a briefer review of the general development of photonuclear experiments will be presented. More comprehensive summaries of the early work are to be found in references 1 to 5, and the Bibliography of Photonuclear Disintegrations [20] provides many references.

The type of experiment performed at a particular time was naturally goverened by the source of gamma rays available. Although the relatively weak photon sources from natural radioactivity and nuclear reactions continue to be useful in restricted areas of study,[3] systematic trends through the periodic table and with energy could not be observed until the development of the Betatron (Kerst, 1941)[47] provided reasonably intense, variable energy bremsstrahlung. With the introduction of high current electron linear accelerators in the 1957 to 1960 period, more precise experiments, using electron scattering [48-54] and neutron time of flight spectroscopy[55-64] became possible, and monochromatic photon beams[79] (produced by position annihilation in flight) were provided, although with initially low fluxes. The present trend[83] is towards high current, high duty factor, linear accelerators in order to provide good fluxes of monochromatic photons or to enable coincidence experiments and the study of correlations between nuclear particles.

Early attempts[66] to measure the nuclear absorbtion cross section for photons directly (by target in and out measurements with a long

absorber) were hampered by the uncertain values of the dominant atomic absorbtion coefficients, but later developments[67] gave agreement with photon scattering data[68] and the more usual yield measurements. (2)

The classic Betatron experiment involved measurement of the yield Y(E) of a photonuclear reaction as a function of E, the end point energy of the continuous bremsstrahlung spectrum ($\Gamma(E)$), so that:

$$Y(E) = \int_0^E \Gamma(W)\ \sigma(W)\ d(W) \quad . \qquad (1.6.1)$$

Since the (γ,n) process frequently results in residual activity of reasonable half life, this activity has been often used as the measured yield in determining the (γ,n) cross section as a function of energy.[16,17,69] By coulomb barrier considerations, this is essentially the total cross section for the elements heavier than about tin. The data on the trends in cross section and width of the Giant Resonance in the heavier nucleii has in fact been gained mainly from the neutron yield measurements.[2,3] However, the analysis of the yield curve data has faced many problems, including uncertainties in the neutron detection efficiency, the monitor response function, the neutron multiplicity corrections and the shape of the bremsstrahlung spectrum near the end point.[3] The method used of inversion of the bremsstrahlung matrix[70] is sensitive to these uncertainties and especially to the statistical uncertainties on the yield curve, so that activation curve statistics of 0.1% were required to produce 5% to 10% accuracy in cross sections.[3] Comparison of results obtained by this method and by the later monoenergetic source measurements showed 10% to 30% discrepancies[1] until errors in the efficiency of the type

of neutron detector used in the older experiments were discovered. [1,p57] The two methods now give agreement.

Measurements of elastic photon scattering are sensitive to the magnitude and shape of the photon absorbtion spectrum.[68,2,34] Early results from these experiments[63] were useful mainly as a check on the yield measurements, but later, the existence of the tensor polarizability of the deformed nucleii was first confirmed in this way. [71] Discrepancies of up to 30% still existed between cross sections from different laboratories however, [1,p53] and quantitative estimates of the magnitude of the tensor term in the scattering amplitude were not possible. An estimate of the effect of this term, integrated over the whole energy spectrum, was made in 1965 from bremsstrahlung yield subtraction measurements on aligned nucleii[72] and then as a function of energy using monochromatic photons in 1969.[73] This may serve to illustrate the advancement of experimental methods in the field.

For the light elements, the (γ,n) contribution could be measured as above, but the important (γ,p) part of the total cross section usually produces stable or long lived isotopes, so that it could not be determined by activity measurements, and emulsions or cloud chambers were initially used to measure the proton tracks.[74,20] Although limited in statistical accuracy, the visual techniques made important contributions, for Gorbunov et. al.[76] showed the significant contribution of high energy spallation reactions to the integrated absorbtion cross section using a cloud chamber, and Milone et. al. [77,78] found evidence for structure in the photon absorbtion spectrum by the close similarity between their emulsion spectra for

(γ,p) and (γ,n) events in O^{16}. The existence of this structure had been a point of controversy for some time because of the inconsistent energies of "breaks" found in yield curves from different laboratories and the fragmentary nature of data on the photoparticle energy spectra.(2,p35)

High resolution experiments were required to resolve the possible structure and confirm the validity of either the collective model or shell model approaches to the giant resonance in light nucleii. In fact, techniques for high resolution spectroscopy on the neutron and proton spectra were evolving at about the same time, as the application of inelastic electron scattering to the giant resonance. (48-51)

In electron scattering, the excitation of both longitudinal and transverse modes may occur, and form factors for each are measured as a function of momentum transfer for each level, allowing assignments of spin and parity by comparison with theoretical predictions.(48-54) Although early experiments showed that detailed studies of level schemes and continuum transitions in light nucleii were possible by this method(50,51) it is only since about 1968 that results with high resolution in the giant resonance region have been attained(55) so that this technique will not be discussed further at present.

Measurements of proton yields using counters (20,85,86,87) showed the same gross features of the giant resonance found in the neutron results, but gave little detailed information on proton spectra, a notable exception being the O^{16} (e,e'p) experiment of Dodge and Barber (34) who used a magnetic spectrometer with about 2% resolution to

determine O^{16} proton energy spectra and preliminary angular distributions. The significant advance was made later by the Yale group (59,p219;93) who used solid state counters to determine the energies of protons extracted from the (γ,p) target via a magnetic lens. This avoided the severe background problems associated with the intense γ - flash in the target area, and permitted resolutions of 1% over the giant resonance region in the preliminary results of Morrison(93). However, other (γ,p_o) spectra obtained by this method were published after the start of the author's research and will be discussed in a later chapter. High resolution proton data was obtained mainly from precision (p,γ) measurements in the pre-1967 period, for the tandem accelerators provided proton beams of less than 10 k.e.V. spread.(88-92) The principle of detailed balance allowed the giant resonance of nucleus ${}_{Z}X^{A}$ to be studied by bombarding nucleus ${}_{Z-1}X^{A-1}$ with these protons and the limit of experimental resolution was set by the target thickness, so that later measurements gave excitation spectra for several light nucleii with 50 k.e.V. resolution in the giant resonance (90). A similar performance in neutron energy measurement was developed in about the same time by applying new technology to the old technique of neutron time of flight spectroscopy.(62)

The time of flight 't' of a neutron of energy E (M.e.V.) over a distance 'd' metres is given in nanoseconds (n.s.) by

$$t = 72.3 * d / \sqrt{E} \qquad (1.6.2)$$

so that the energy resolution is given in terms of Δt the time dispersion of the system by:

$$\Delta E = (1/56.15) * E^{3/2} * (\Delta t/d). \qquad (1.6.3)$$

In order to study giant resonance photoneutrons from the light elements (typically 6 M.e.V.) with a resolution of 200 k.e.V. or 60 k.e.V. requires a time of flight resolution of 0.5 n.s./m. or 0.15 n.s./m. respectively, so that time resolutions of less than 10 n.s. are required to use the 10-20 m flight paths imposed by typical accelerator shielding conditions. Therefore a fast timing detector of neutrons is needed, as is an accelerator with a pulsed electron beam of suitably short duration and high instantaneous current.

The M.I.T. group developed these techniques[55] and produced the first measurements of fast photoneutron spectra in 1958.[56] Unfortunately they were restricted, by their accelerator, to photon energies below the giant resonances of the interesting '4n' light nucleii and such information was obtained from a similar system installed on the Harwell Linac by Fink and collaborators.[57,58]

These nucleii are convenient experimentally in that the corresponding residual nucleii formed in photo disintegration have first excited states which are well separated from the ground state, by some 'G' M.e.V. Since the top 'G' M.e.V. of the photonucleon energy range can only be produced by ground state transitions, only a few runs at widely spaced bremsstrahlung energies are required to give ground state photonucleon spectra, which can be related to the spectra of the absorbed photons by kinematics. The first excited state of O^{15} is at 5.2 M.e.V. so that a run at just one bremsstralung end-point energy provides a good energy range of ground state transitions in the O^{16} (γ,n) O^{15} reaction.

Fink et. al. obtained a neutron energy resolution of about 200 - 300 k.e.V. in the giant resonance of O^{16} [57] which they subsequently improved to give spectra for this and other light nucleii with less than 100 k.e.V. resolution throughout the giant resonance.[59] This allowed detailed comparison with the (p,γ) data[90,60] and preliminary estimates of isotopic spin purity in the giant resonance states.[90] To make accurate measurements of this required knowledge of the photoneutron angular distributions (as previously discussed) but these did not exist in any quantitative form.

The emulsion measurements of Milone and Rubbino[78] had indicated assymmetry in the angular distributions of photoneutrons from the giant resonance region but with little energy resolution and few statistics, while the only modern measurement[63] (by time of flight) had covered but three angles and did little more than confirm the earlier results.

A measurement with good energy resolution was required to resolve the individual level structure and allow determination of the mixture of partial waves from resonance to resonance, so that only the time of flight method was useful. To obtain information on up to 5 Legendre coefficients (A0 to A4) required data from at least six angles which should span as much of the range 0 to π as possible, in order to be sensitive to the higher coefficients. The angular variation could be obtained simultaneously by six flight paths or by using one flight path and successively altering the angle between the incident photon beam and this direction. The former method has the advantage of simultaneous collection of data from all angles which

increases the total count rate and decreases the problems of angle to angle normalisation by essentially removing its dependence upon time. This requires six expensive detector systems instead of one however, and few laboratories have shielding geometry flexible enough to allow six 20 m. flight paths.

The geometrical conditions were satisfied at the linear accelerator of the Kelvin Laboratory, University of Glasgow, and the author's research project at this establishment has been the commissioning of a multi-angle nanosecond time of flight spectrometer and the measurement of the angular distribution of photoneutrons from the photodisintegration of O^{16}.

Chapter 2

2.1 Introduction.

This chapter describes the development of a multi - angle time of flight (T.O.F.) spectrometer for measurement of photoneutron angular distributions with good energy resolution. The linear accelerator of the Kelvin Laboratory, University of Glasgow is considered as a source for such experiments and its characteristics are shown to have determined the choice of basic experimental perameters.

Advantage was taken of the open geometry of shielding in this laboratory to provide six 20m. flight paths for simultaneous acquisition of angular distribution data and one 53m. evacuated flight path for higher resolution work. Flight path collimation was designed to allow the solid angle subtended by each detector to be determined by the detector size, so that by using identical detectors, angular normalisation depended simply on the bias level set on each detector. The choice of detector is made with respect to the required efficiency, count rate and resolution and the possible accuracy in normalisation between detectors is demonstrated.

2.2 Nanosecond T.O.F. spectroscopy at the Kelvin Laboratory.

It was shown in chapter 1 that the energy resolution in neutron T.O.F. experiments was

$$E = (1/36.15) \cdot E^{3/2} \cdot \Delta t/d \qquad (1.6.3.)$$

so that a system with good resolution must have a small time dispersion (Δt) and long flight paths (d). Both these requirements decrease the count rate, which can only be rectified by increasing the peak current available in the photon pulse produced by the

FIGURE 5. PLAN OF T.O.F. FACILITY AT THE KELVIN LABORATORY.

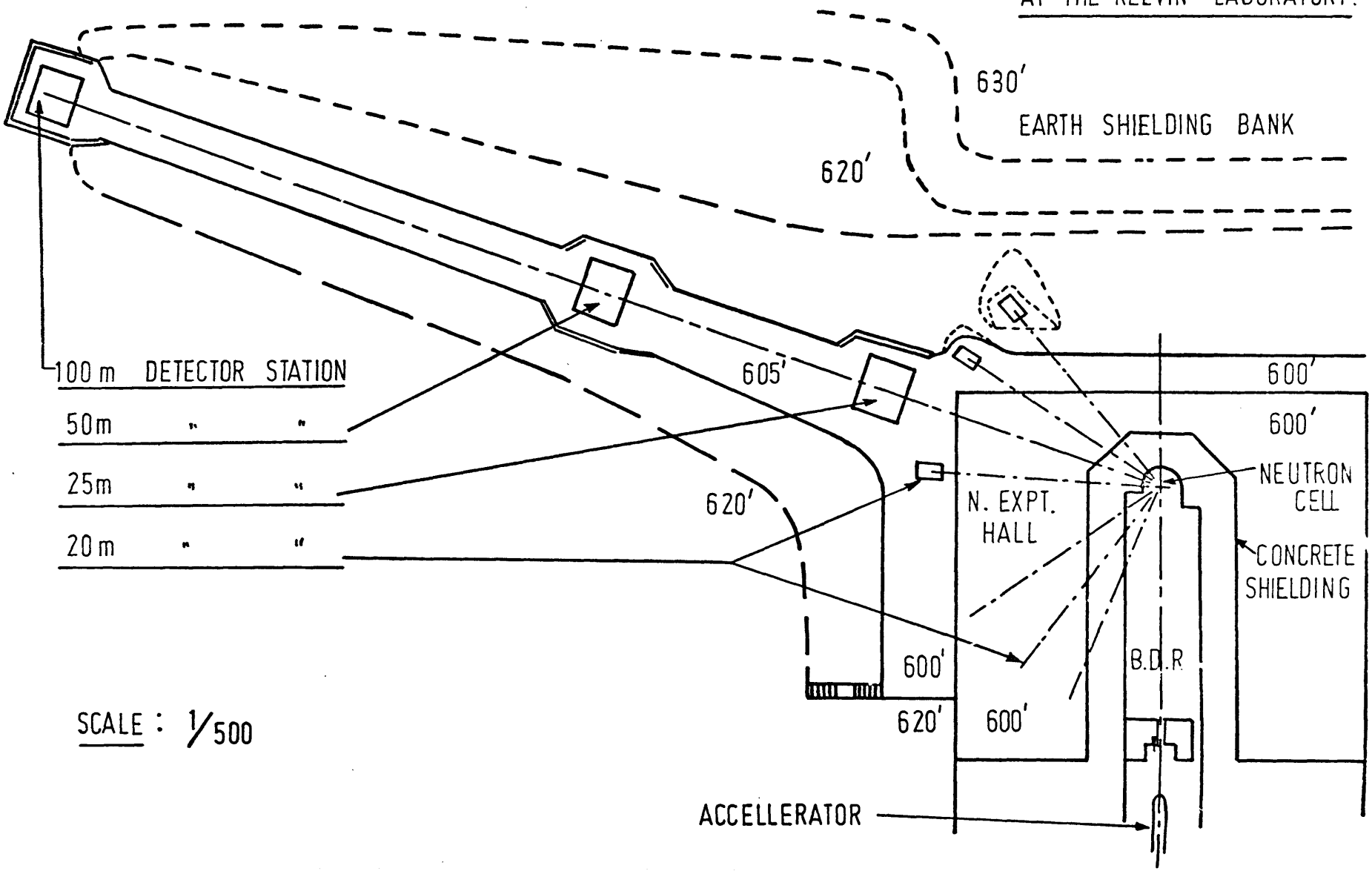

electron accelerator. The neutron T.O.F. is measured by a form of clock which is started by some time zero signal and stopped by the pulse from the neutron detector. Such systems normally count only one stop pulse per start pulse so that the absolute count rate is proportional to the pulse repetition frequency of the accelerator. A more obvious constraint on accelerator performance is that the electron energy range available must span the region of interest and the beams produced should be stable.

The electron linear accelerator at the Kelvin Laboratory of the University of Glasgow satisfies most of these requirements. Electrons at 30 k.e.V. are injected from a Pierce geometry cylindrical diode gun capable of 2A current. The beam is deflected in to the accelerator by a fast 10k.V. pulse from a thyratron driven spark gap applied to a pair of deflection plates giving 3.5ns. F.W.H.M. pulses of up to 200m.A. peak current in the first section of the accelerator. Peak currents of 50 to 150m.A. are available after acceleration depending upon the final energy (25 to 100 M.e.V.) used and repetition rates of up to 480 Hz. are possible. The energy is measured round the 90° magnetic analysis system in the beam deflection room (B.D.R.) (figure 5).

Nanosecond experiments are performed in the straight through position in the well shielded neutron cell where the electron beam strikes a thick tungsten bremsstrahlung converter placed some 4" before the photoneutron target which sits at the intersection of all the flight paths with the electron beam line (figure 5). Ferrite toroids placed at intervals down the accelerator and beam transport

FIGURE 6. ELECTRONIC SYSTEM FOR TIME MEASUREMENT AND DATA STORAGE

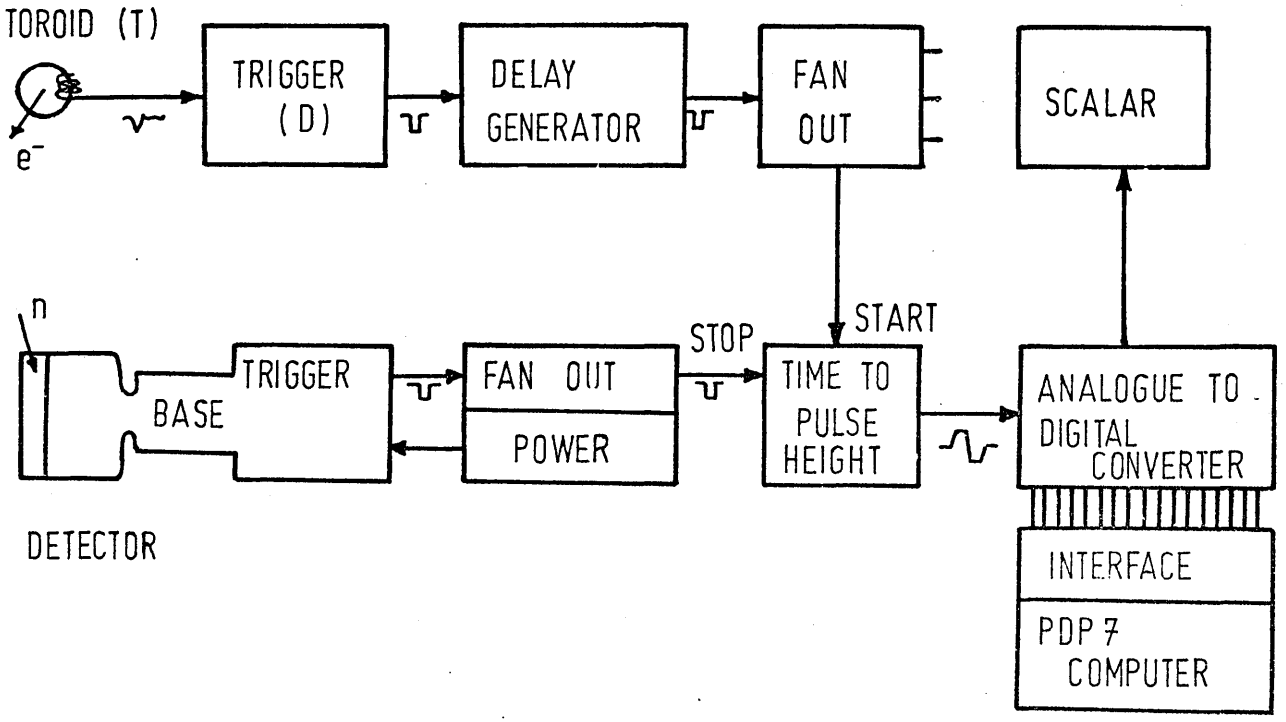

Count Rate Estimate

Table 2

(1)	N^0 electrons/pulse $= \frac{i*T}{q} = \frac{5*10^{-2}A*3.5*10^{-9}}{1.6*10^{-19}\ \text{coulomb}} = 1.1*10^{+9}$
(2)	Bremsstrahlung Conversion = γ's per electron * geometrical factor Efficiency * energy bite $= 0.15*0.66*0.035 = 3.5*10^{-3}$ (using bremsstrahlung spectrum, fraction between 22 and 27 M.e.V. $= .035^{(100)}$)
(3)	Photoneutrons/photon $= \frac{\text{No.p.t.}\sigma}{A} = \frac{6*10^{23}*1.0 * (1.5) * 16*10^{-27}}{.16}$ $= 6.7*10^{-4}$ (since $\int\sigma\, dE$ = 26 M.e.V. m.b. (Ref. 101))
(4)	Therefore, Photoneutrons/pulse = $2.6*10^{3}$
(5)	Solid Angle = $2.25*10^{-6}$
(6)	Detector Efficiency = 0.3
(7)	Counts/second (4,5,6) = 0.84/sec.
(8)	Channels for 5–10 M.e.V. = 360ns/1.4ns/channel = 250 channels. neutrons
(9)	Count Rate = 12/channel/hour = 290/channel/day.
(10)	3% statistical accuracy in 3 – 4 days.

NOTE THAT DEAD TIME EFFECTS ARE SMALL AT THESE RATES

system allow monitoring of the electron current, and the time zero pulse (START pulse) for the system is conveniently taken from one of these. 'STOP' pulses are obtained from suitable neutron detectors placed in the flight paths and the time interval is converted by the subsequent electronics to an analogue pulse to be stored by a multi-channel analyser. The timing system is shown in figure 6.

The resolution of the present spectrometer is determined mainly by the 3.5 n.s. width of the electron pulse. Flight path and detector perameters have been determined by the compromise between resolution and count rate.

2.3 Count Rate Estimate.

A calculation of the counting rate is performed in table 2 using typical values of electron current and some necessary limitations on target thickness which will be explained more fully later. Although the total experimental time required (1 week) is not unusual, the count rate is severely limited by these factors and the low solid angles involved to the point where general background radiation contributes 10% in the interesting time region (from 5 to 10 M.e.V. neutron energy). Experimental techniques involving loss of counting rate (such as fine analysis of the beam energy or the use of 'thin - target' bremsstrahlung) are then impossible without increase in accelerator peak current.

The following system has been designed to maximise counting efficiency inside useful limits of resolution and to reduce the total accelerator time required by simultaneous acquisition of data from all angles.

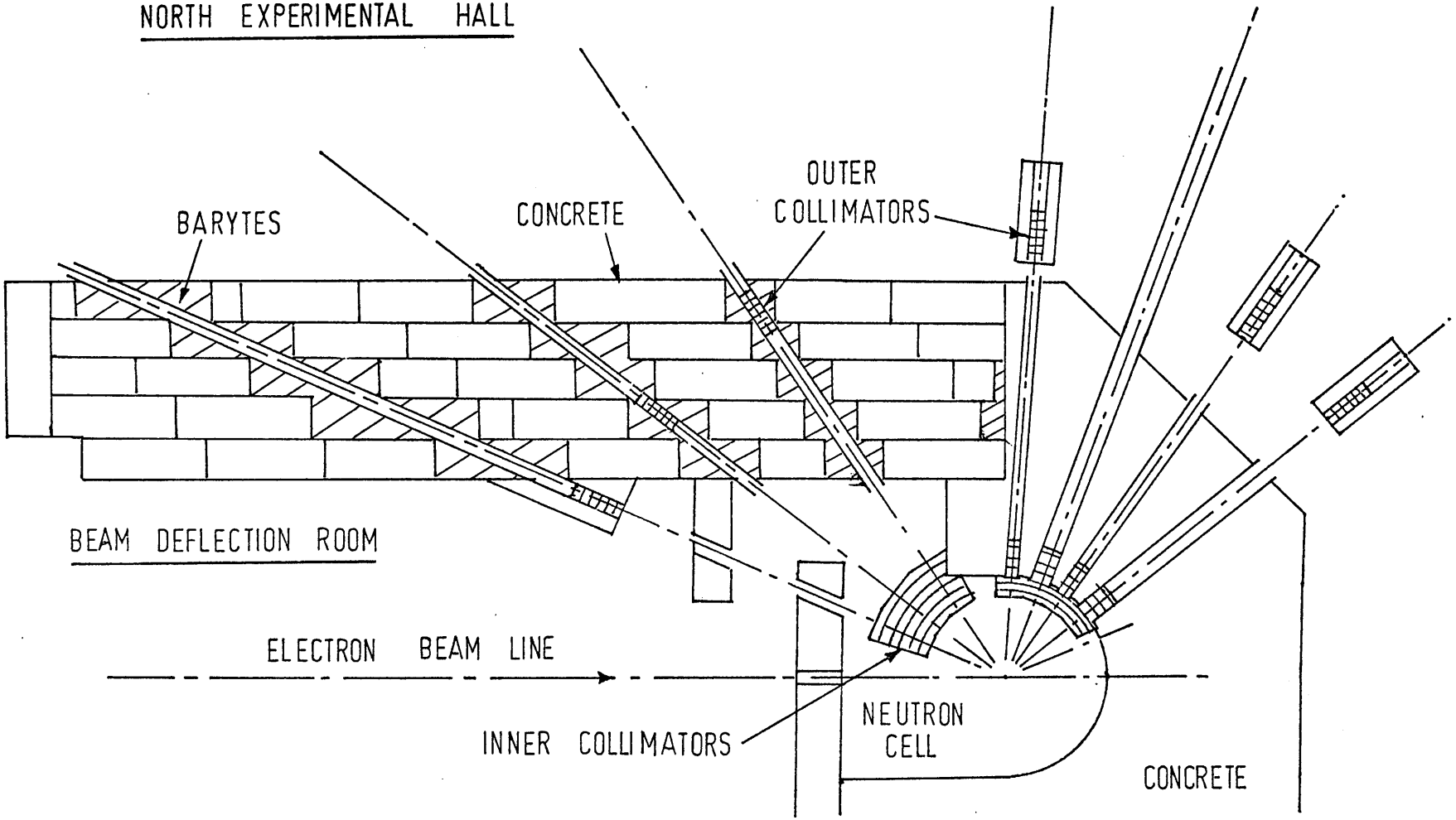

FIGURE 7. DETAILS OF FLIGHT PATH CONSTRUCTION

2.4 Geometrical Considerations.

The flight path system installed by the author is shown in figure 5 and details of the neutron cell and the engineering and collimation of the flight paths are shown in figure 7. The neutron cell was originally designed with five flight path apertures, all at forward angles. These terminated at the building wall after various path lengths from 8m to 17m. The earth banking round the experimental area was designed to allow erection of one long flight path, possibly to 100m. The author was not responsible for this preliminary work.

Energy resolutions of 100 k.e.V. for 6 M.e.V. neutrons could be obtained from the expected 4-5ns. time resolution only by using flight paths of about 20m. The $23\frac{1}{2}^{o}$ forward angle was discarded on these grounds and because of the enormous flux of Compton - scattered gamma rays expected at the forward angles. This 'gamma flash' causes background effects in the detector and can paralyse it in severe cases. Six angles covering a good angular range were required. The author installed 3 **backward** flight paths through the sectional shielding wall of the B.D.R. at well spaced angles which avoided the main structural supports of the building and gave useful values for Legendre polynomials. (figure 8) Measurements at these six angles should give good definition of the contribution of polynomials of different order. To obtain 20m., the forward flight paths were extended outside the building and each was equipped with a detector station in the form of a hut with a power supply, a cable link to the counting room and a temperature regulated heating system. This involved some excavation of the shielding bank at the two most forward

FIGURE 8. LEGENDRE POLYNOMIAL VALUES.

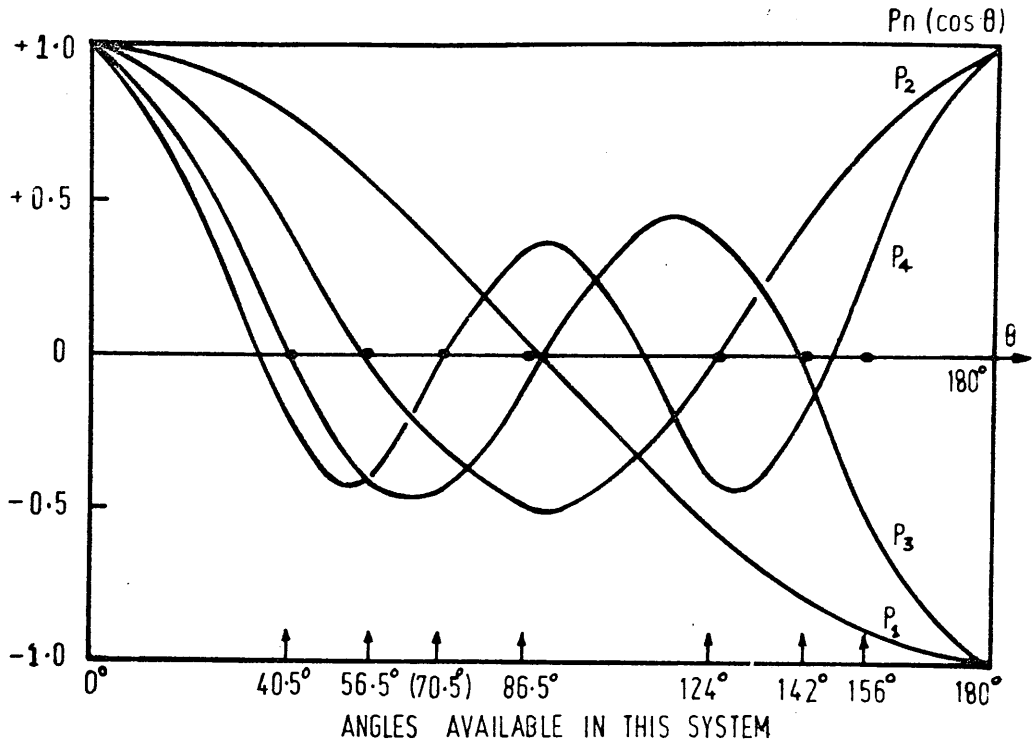

FIGURE 9. GEOMETRY OF T.O.F. EXPERIMENTS

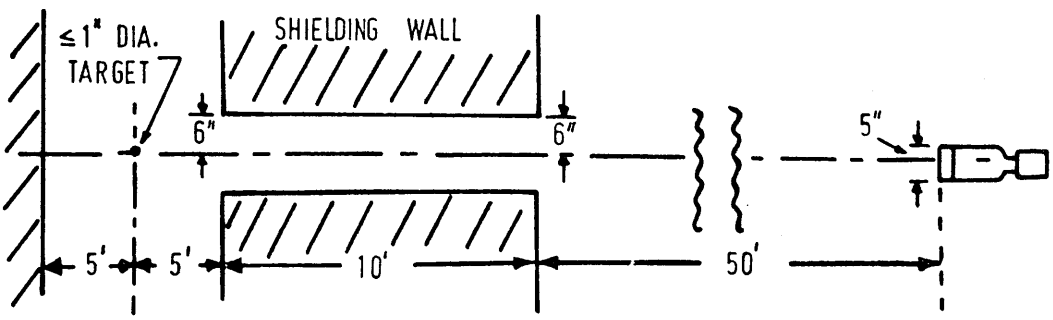

angles. The original $70\frac{1}{2}^{o}$ detector stations were retained and an evacuated flight path assembled for high resolution measurements at 25m and 50m. The vacuum pipe is 12 dia. to 25m. and 16" thereafter, and this large volume is evacuated by a rotary pump to pressures less than 1% atmospheric in ten minutes and to final pressures less than 100μ. The neutron cell flange is $\frac{1}{2}$" thick steel except for a 2" dia. central thin window of .01" 'Mylar', while the 16" window required at the detector end is of .05" aluminium for safety reasons.

The backward flight tubes are of 6" i.d. thick - walled plastic supported rigidly by steel formers and surrounded by a matrix of Barytes chips. (figure 7) This material is suitably dense and provides a convenient method of sealing the radiation weaknesses introduced in the sectional shielding wall.

The alignment of the flight path tubes was surveyed by **theodolite** against a small target, dead centre of the neutron cell and the known electron beam line. Small non - linearities in the pipe were unimportant since the target - detector cone was to be defined by collimators which could be adjusted for optimum alignment.

2.5 Collimation of the Neutron Beams.

The demands of radiation shielding impose a basic geometry on neutron time of flight experiments. The neutron source is always in a small enclosure surrounded by many feet of concrete and the particles emerge from flight tubes in this shield as shown in figure 9 where the dimensions are those found in the Kelvin Laboratory but are not unusual. The disadvantage of such a system is that the flight path pipe and its image on the back wall subtend a solid angle at the

source which is very much greater than that subtended directly by the detector, and rescattering into the detector from these areas is not negligible. From the solid angles in figure 9 the relative probability of scattered radiation being detected is about $\frac{1}{2}\%$, but the neutron scattering cross sections of fast neutrons are highly back and forward peaked so that the effect leads to highly contaminated spectra in some cases. This was observed in early experiments and cured by collimation at the inner aperture of the flight tube, for the contamination is proportional to the solid angle of this aperture.

Neutrons were then accepted only from a small volume round the photoneutron target, which allowed the bremsstrahlung converter to be placed close by, in order to maximise the useful photon flux. The collimator must discriminate sharply against neutrons from the bremsstrahlung converter and since the neutron yield from this was less than from the photoneutron target (target thicknesses are discussed later) an attenuation factor of 10^3 for the collimators was considered adequate. This factor had to be achieved as compactly as possible because of access problems in the neutron cell.

The neutron capture cross section is only appreciable at thermal energies, so that fast neutrons are best removed by scattering out of the beam. For neutrons below 3 M.e.V. kinetic energy, elastic collisions with light nucleii (preferably hydrogen) provide the fastest reduction in neutron energy, but neutrons of higher kinetic energy are better slowed by inelastic processes for which the materials with high mass number offer lower thresholds and high cross sections.[103] This is confirmed by the effective neutron absorbtion

FIGURE 10. EFFECTIVE ABSORBTION COEFFICIENT OF COLLIMATOR MATERIALS

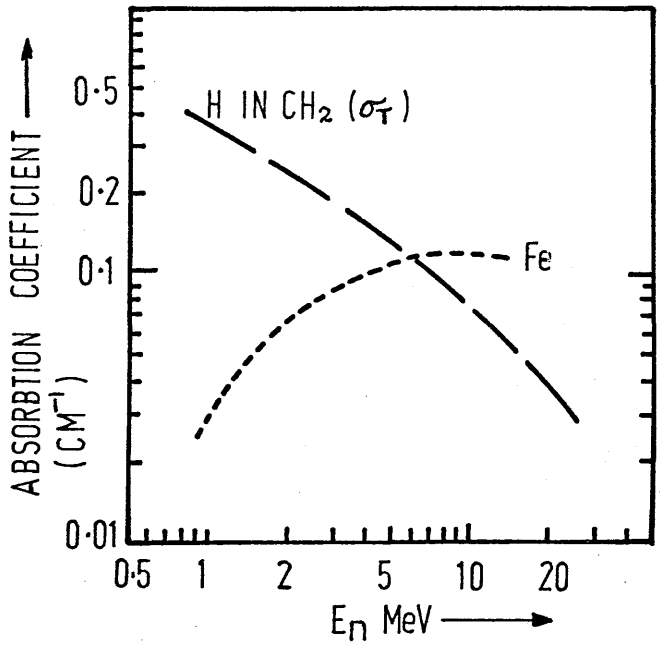

FIGURE 11. COLLIMATOR CONSTUCTION

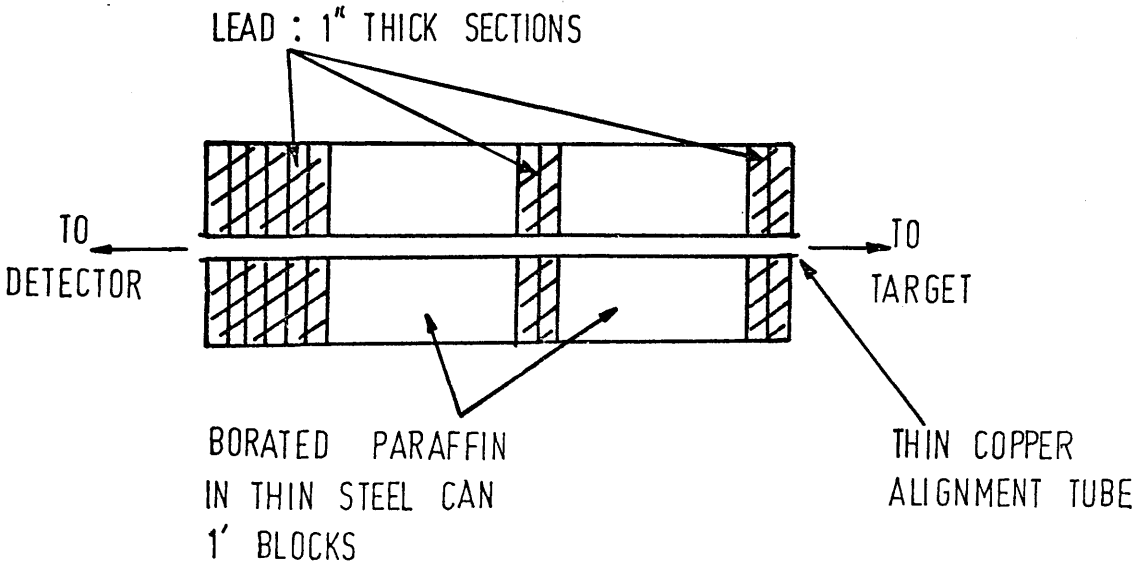

coefficients measured as a function of energy by Hopkins et. al.[102] (figure 10).

A composite collimator is therefore most effective and those designed by the author utilised 2' of borated paraffin and 10" of lead. The attenuation factors so gained for fast neutrons and gamma rays (of 1 M.e.V.) were 10^3 and 10^9 respectively using the data of Hopkins et. al.,[102] confirmed by the shielding data from references 103 and 104. The construction was sectional (figure 11) with about 6" of the lead at the detector end to absorb any capture gamma radiation produced. The collimators fitted in to the flight tubes in the concrete shielding wall or in to specially built concrete blockhouses, depending upon angle, so that the concrete completed the absorbtion of the scattered neutrons (figure 7).

Exactly the same type of construction and the same attenuation factors were used for outer collimators placed nearer the detector end of all flight paths, in order to define accurately the extent of the neutron beam at the detector and prevent scattering from the background shield. The diameter of this collimator and its distance from the source were chosen to define a beam of neutrons at the detector which would have a radius 2" larger than that of the detector ($2\frac{1}{2}$") and the lead background shield was built at least $1\frac{1}{2}$" outside this beam at all points.

The philosophy behind the collimation procedure is shown in figure 12. Target and detector are reciprocally entirely in view, well inside the conical limit set by the collimators on the escaping radiation. Note that the position of target or detector is non -

PHILOSOPY OF COLLIMATION

FIG. 12.

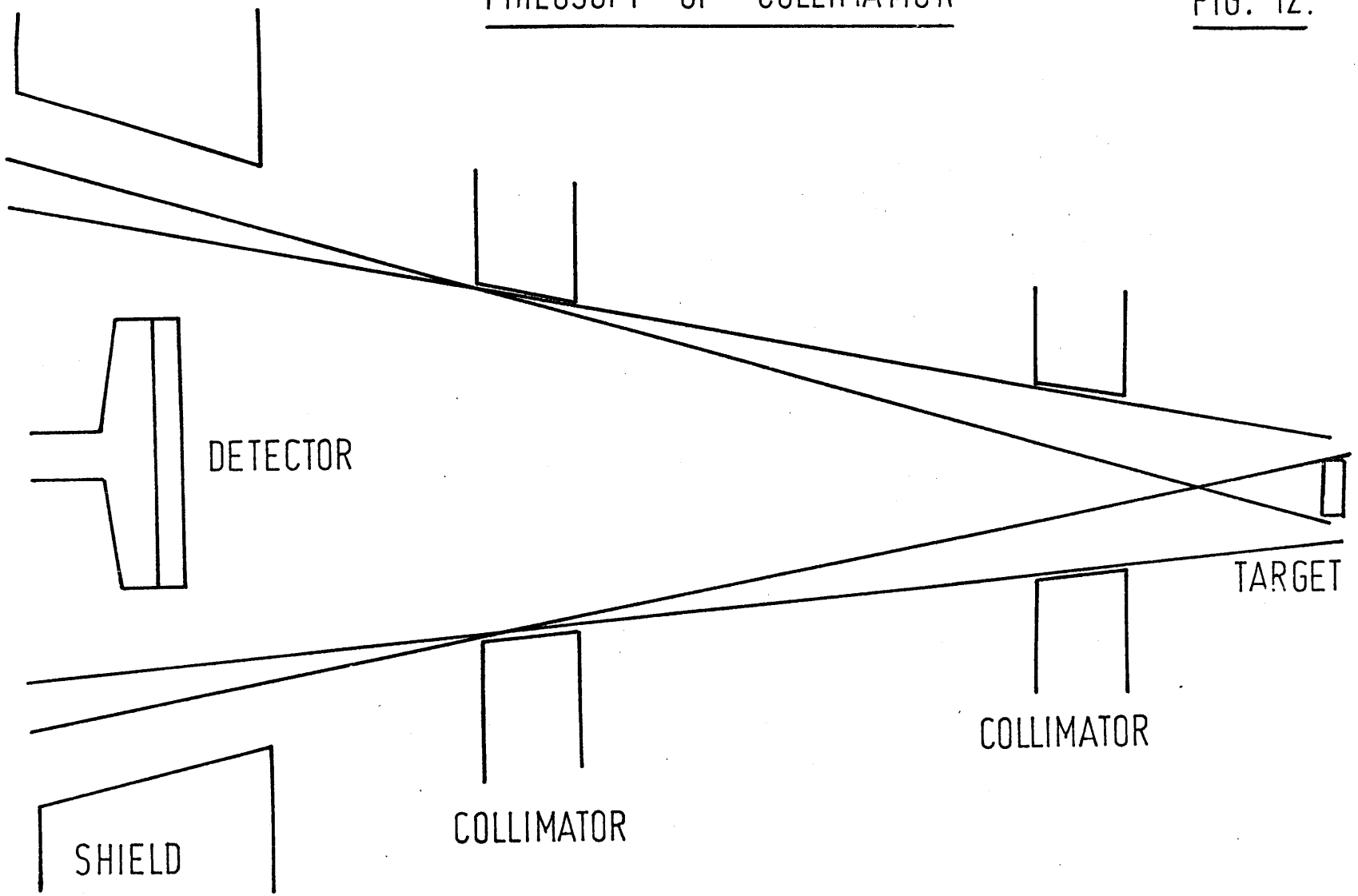

(b) NEUTRON BEAM MEASUREMENT

½" d. Pb. TARGET DETECTOR WAS ½" x 1" dia. Ne102 SCINTILLATOR

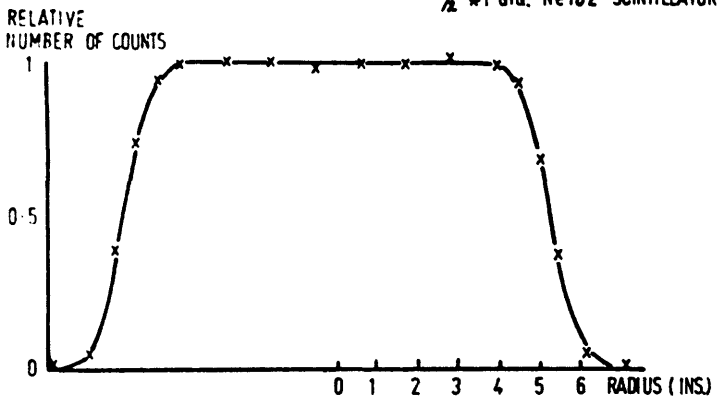

FIG 13. COLLIMATOR POSITIONS AND NEUTRON BEAM PROFILE

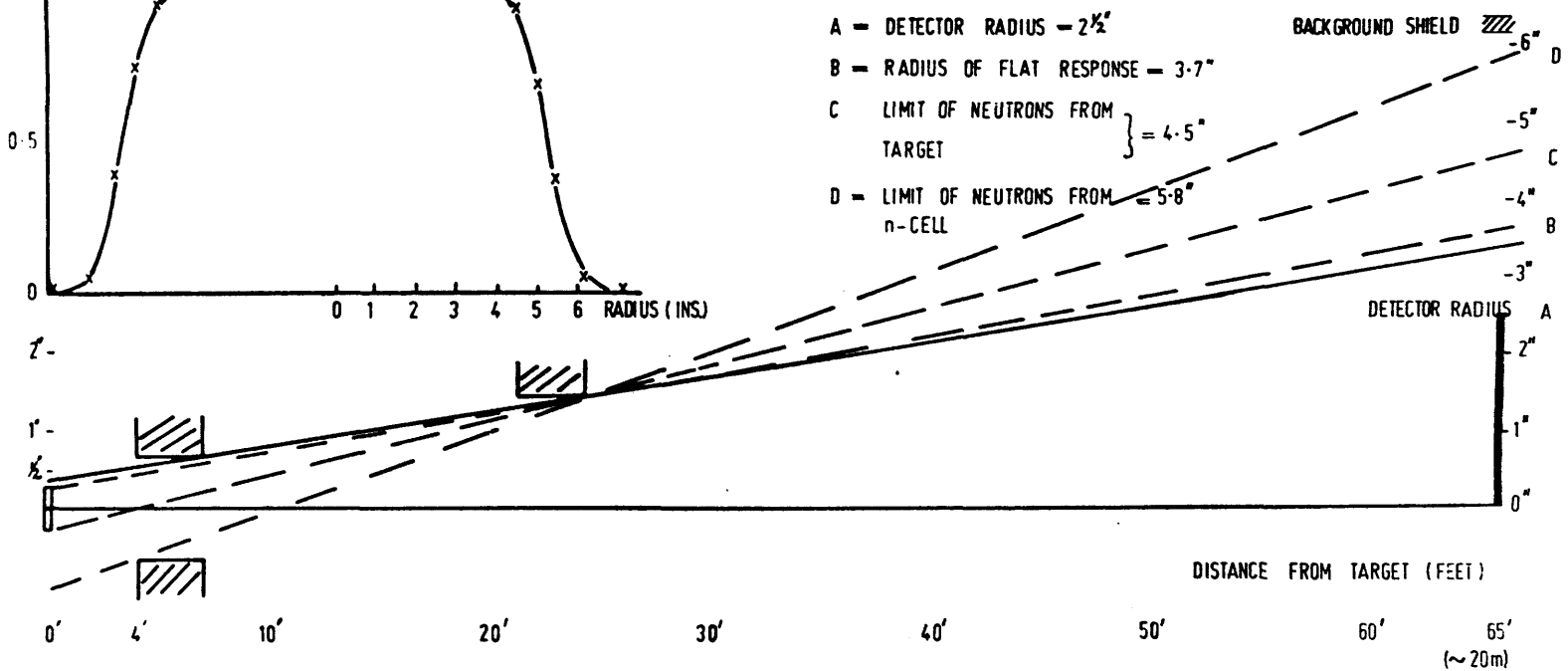

critical. This system allows the solid angles to be made the same for all flight paths by the simple process of using identical detectors at identical distances. Some trouble was taken to arrange all the corresponding (inner or outer) collimators to be identical and at the same distance from the source and geometrical constraints led to the present positions (figure 7) where concrete blockhouses enclose the collimators which lie outside the shielding wall.

Typical flight path dimensions are shown in figure 13 where the penumbra effects are shown to be acceptable. The measurement of neutron flux over a typical detector position is also shown in figure 13. A flat topped beam is found with cut-offs where expected.

2.6 T.O.F. detectors.

Organic scintillators have been found to be the most useful detector of fast neutrons in T.O.F. spectrometers[105] for large volume detectors are available with high efficiency and good timing resolution. Very large scintillators coupled to several photo-multipliers have been used in some T.O.F. systems[106] but the gain obtained in solid angle is at the expense of a worsened time resolution and a non - uniform light collection and the cost of reproducing such a device six times prohibits its use in the present arrangement.

The detector used was a 5" dia. 5" thick plastic scintillator directly coupled to an XP1040 photomultiplier which has the desirable properties of a large diameter photocathode and good timing resolution. High voltage from a stabilised supply was applied to a resistor 'base' chain to set the dynode voltages and fast signals from a 50Ω anode

load were taken to trigger a discriminator. The timing signal from the discriminator was transferred to the counting room and subsequent (N.I.M.) electronics. This arrangement gave a reasonably sized detector with good timing resolution and a relatively simple electronic arrangement.

2.7 Total Timing Resolution and Scintillator Thickness

Time uncertainties arise from the duration (B) of the electron pulse, the transit time variation of neutrons in target and detector (D) and the time resolution and 'jitter' of the detection process and subsequent electronics (O). In this system, O will later be shown to be smaller than B or D, so that the resolution (R) is related to B,D and the flight path length L for neutrons of velocity V, by the expression.[105]

$$R = \Delta t/t = \Delta V/V = V^{-1}L^{-1}*(B^2+ D^2)^{1/2} \qquad (2.7.1)$$

The counting rate (C) is proportional to B and to $\frac{1}{L^2}$ and also, for a given velocity, approximately proportional to D, so that

$$C \propto^{\ell} R^2* B*D* (B^2+ D^2)^{-1} \qquad (2.7.2)$$

and

$$(dC/dD)_{R,B} \propto^{\ell} (B^2-D^2)/(B^2+D^2) \qquad (2.7.3)$$

For a given B the count rate is maximised for a given resolution R, when D=B. Better resolution can be obtained by decreasing the scintillator thickness and hence D, but only by reducing the count rate. D has a useful upper limit, equal to the mean free path in scintillator material and since the (n,p) cross section is approximately proportional to 1/V up to 4 M.e.V.,[105] this upper limit is nearly constant (and equal to 3.5n.s.) over this range. It increases to about 4½n.s. at 10 M.e.V. Therefore the optimum

scintillator thickness (in this case, with a 3.5n.s. electron beam) is given by the mean free path for 4 M.e.V. neutrons - about 5" in typical scintillators. This size was finally used in the author's experiment although many of his preliminary measurements were made in higher count rate conditions (at a higher bremsstrahlung end point energy) with thinner (2") scintillators and somewhat better resolution. The thick and thin detectors finally gave resolutions of about 5n.s. and 4n.s. for 6 M.e.V. neutrons so that the factor of 2 gained in count rate is more than justified by the small decrease in resolution.

2.8 Detector Timing Resolution:

Time measurements with scintillator - photomultiplier combinations have been reviewed by several authors[108-113] and the causes of finite time resolution are well known. These are

(1) The variation of the time of interaction of the incident radiation with the scintillator.

(2) The variation in the energy deposited by radiation in the scintillator.

(3) The finite decay time of the light emitting states in the phosphor and the different times of arrival at the photocathode for photons.

(4) The statistical variation in the number of photoelectrons released per photon.

(5) Transit time variations in the tube because of (a) different path lengths for electrons starting from different areas of the photocathode and (b) the statistical variation in the energy and emission direction of secondary electrons.

(6) (a) Triggering uncertainty in the associated electronics ('jitter') (b) variation in triggering time with pulse amplitude ('walk').

The effect of (1) has already been considered for neutrons but will be much smaller for gamma rays which can therefore be used to measure the other effects. Because of the non-linear light response to recoil protons, the maximum pulse heights produced by neutrons of 1 to 10 M.e.V. vary by a factor of 50 (appendix 1), and since a white spectrum of recoil protons is produced up to the maximum possible energy, extremely large pulse height ranges must be covered. The effect (2) requires triggering circuits with small 'walk' 6(b) and such circuits will be discussed shortly. Statistical effect (4) is normally minimised by accepting pulses only if they are greater than a given 'bias' value which is set at a fairly large number of photoelectrons (~20).

Hydrocarbon scintillators are now available in both solid and liquid form with high light output and pulse decay times of 2-3n.s. so that effect (3) does not seriously contribute to the time spread. Fast liquid scintillators NE211 and NE213 were used successfully by the author in several preliminary measurements and the plastic NE102A* was used in the experiment to be described. This has a fast decay time of 2.6n.s.[114]

The timing resolution of an XP1040 photomultiplier with a large scintillator is limited by effect (5) to about 1n.s. - the transit time variation over the whole photocathode.[111] Effects (2) and (6) can be almost eliminated by modern timing circuits,[112,113] if these can be used, and measured resolutions approach the transit time variation.

* Supplied by Nuclear Enterprises Ltd., Edinburgh, Scotland.

FIGURE 14. DELAYED COINCIDENCE TIMING

(a) LEADING EDGE

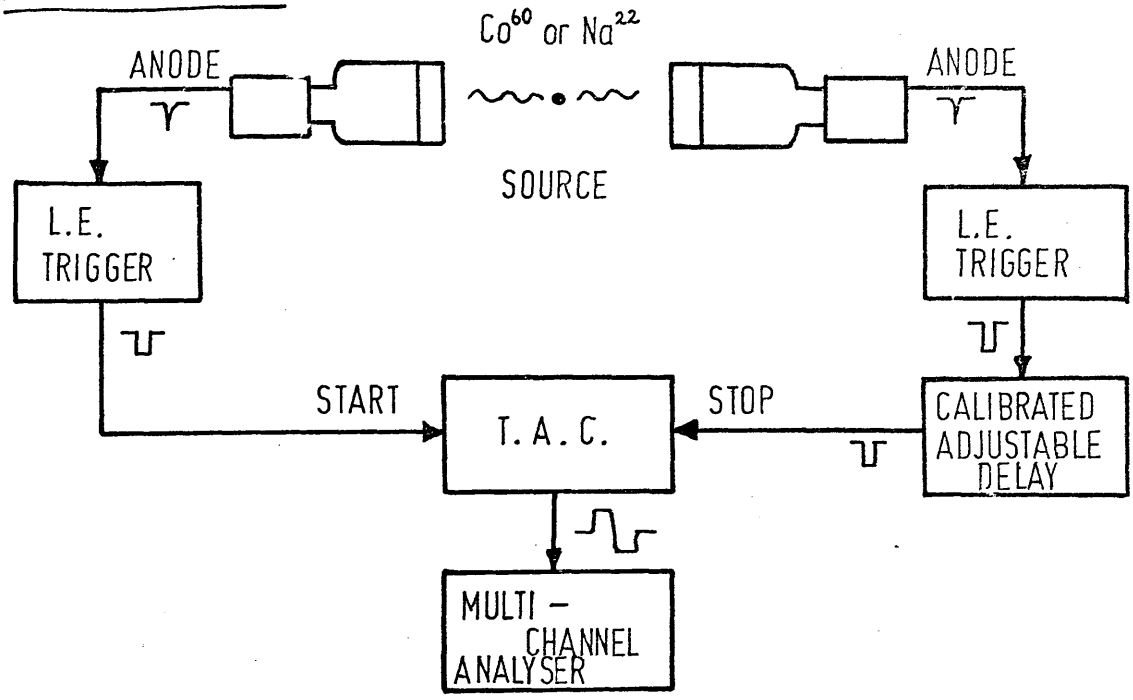

(b) SLOW CROSS-OVER

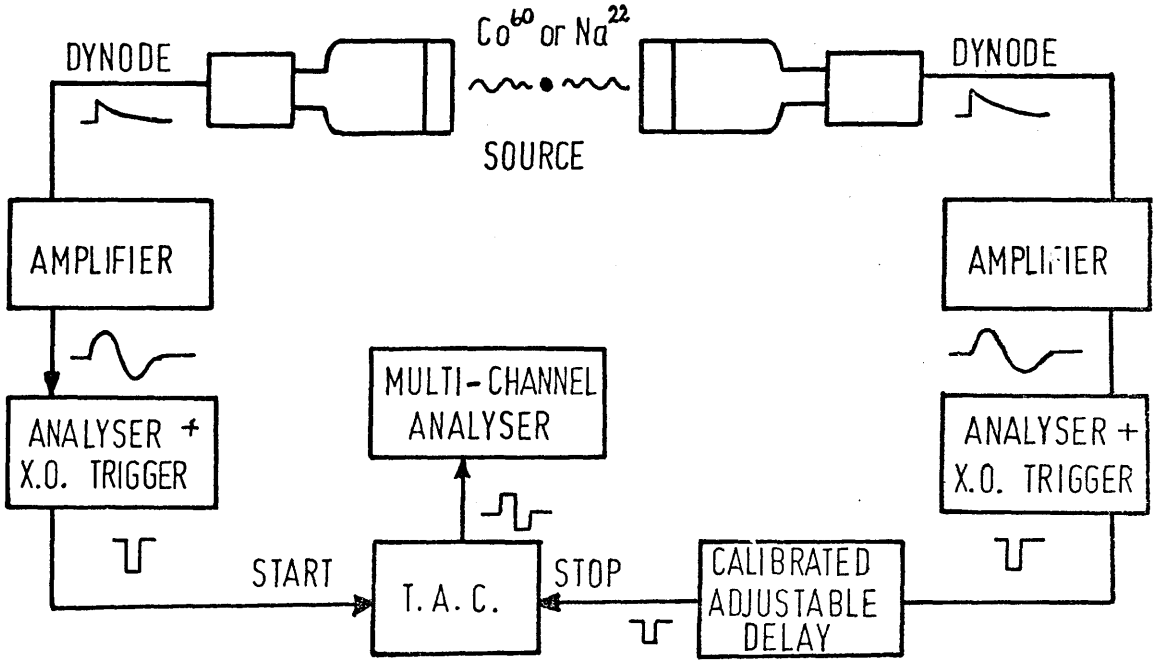

FIGURE 15. TIMING RESULTS (DELAYED COINCIDENCE METHOD ON Co^{60})

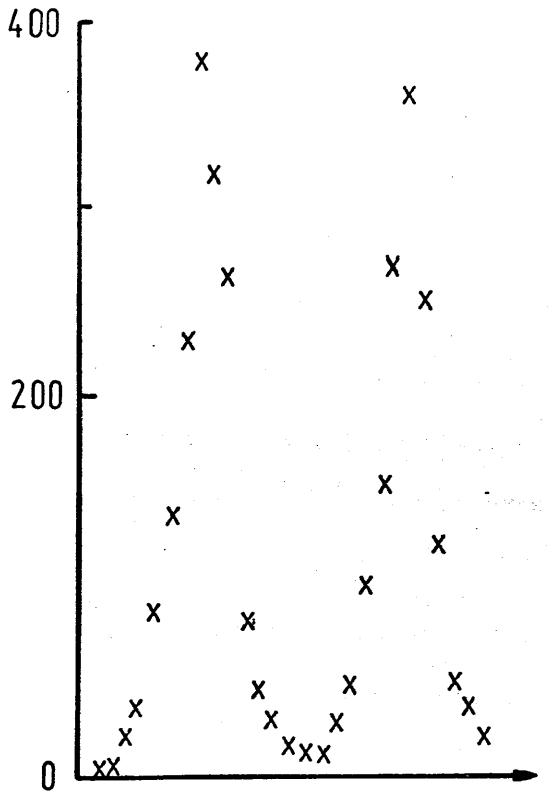

a) LEADING EDGE

DELAY = 10·0ns.

F.W.H.M. = 2·4ns.

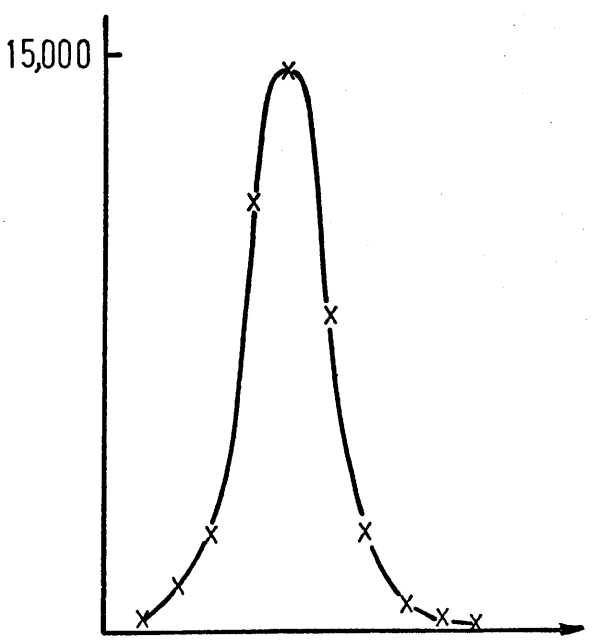

b) SLOW CROSS OVER

1 CHANNEL 2·6ns.

FWHM = 5·0ns.

2.9 Timing Circuits for Photomultipliers.

This subject has been reviewed theoretically and experimentally by several authors[108-113] and the reader is referred to these for a more general discussion. The traditional methods of triggering on the leading edge of the fast anode pulse (L.E.) and triggering on the cross over (X.O.) of the doubly - differentiated full energy dynode pulse were compared by the author for large photomultiplier - scintillator systems using the delayed coincidence technique. (figure 14) The delay between coincident events, produced in the two detectors by Na^{22} annihilation γ rays or Co^{60} cascade gamma rays, is measured by the time-to-amplitude-converter (T.A.C.) as an analogue pulse stored by the multichannel analyser. The width of the coincidence peak is the total time resolution of the system calibrated by means of a known adjustable delay in one channel. To duplicate experimental conditions, only a lower pulse height limit was used, the pulse height ratio being determined by the maximum size of pulse from the source. Typical results for a 20:1 pulse height range are shown in figure 15. The conventional 'slow' cross-over method did not give adequate resolution and the necessary integration of the dynode pulse gave a dead time (1μs.) which would have prevented neutron counts being accepted until long after the γ - flash pulse so that this technique was discarded. The L.E. method provides adequate (≈2n.s.) time resolution for the present purposes, despite its inherent 'walk' with pulse height.

This 'walk' is essentially eliminated by recently introduced timing methods[112,113] which use fast cross-over (F.X.O.) or constant fraction of pulse height (C.F.P.H.) triggering techniques on the fast

FIG. 16 CONSTANT FRACTION OF PULSE HEIGHT TIMING

(a) DELAYED COINCIDENCE ARRANGEMENT.

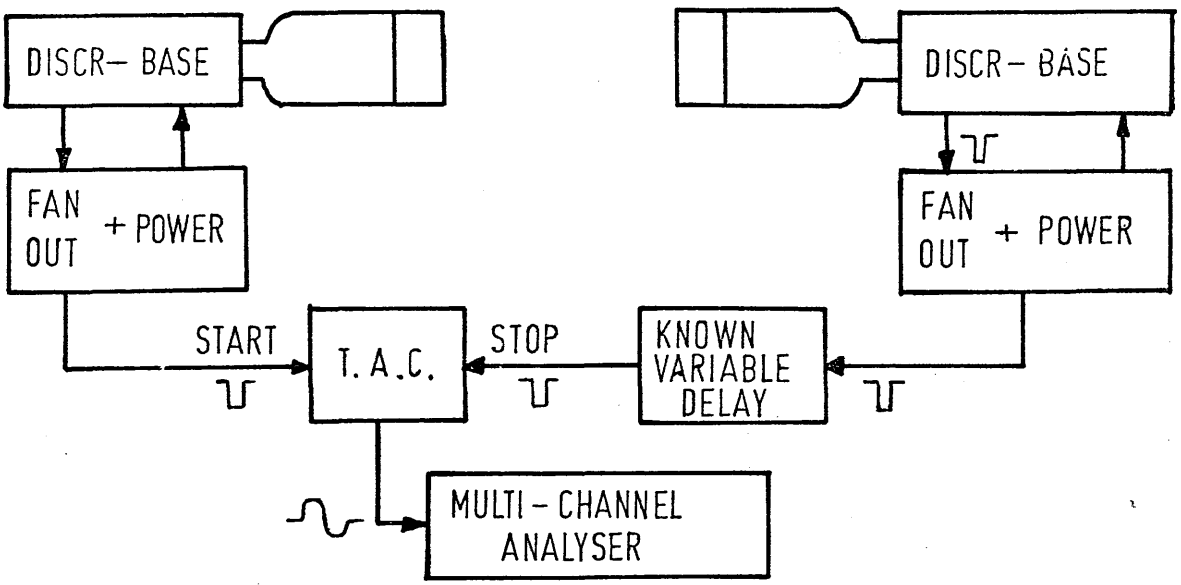

(b) C.F.P.H. TIME RESOLUTION : WITH 2 * 5" DIA. SCINTILLATORS. AND XP1040 PHOTOMULTIPLIERS.

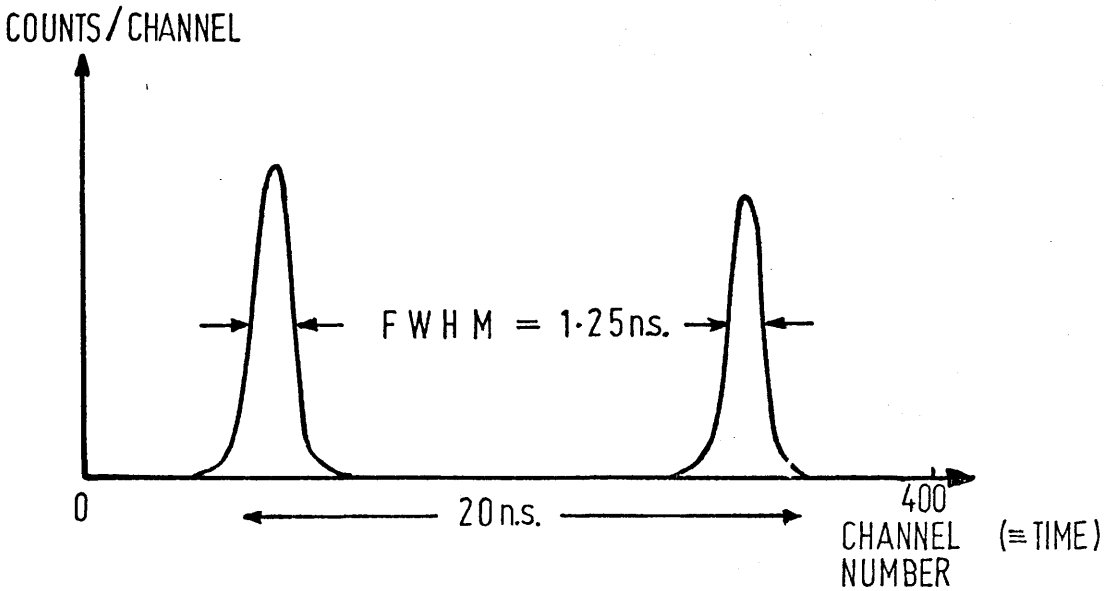

anode pulse. The discriminator - trigger systems are included in the photomultiplier base chain assembly in these compact commercial units* so that duplication is easy and these have been used where possible in the author's system. The corresponding delayed coincidence electronics and typical results are shown in figure 16. The 1n.s. photomultiplier transit time limitation is now the only significant timing contribution even for pulse height ranges greater than 30:1. However, the improvement in total neutron timing resolution was only from 5n.s. to 4.9n.s. because of the other factors previously considered.

Photomultiplier switching at forward angles was found to be essential to avoid satellite pulses caused by the large γ-flash pulse. This could not readily be implemented on the commercial base chain - discriminator units, so that L.E. timing was used here following specially adapted base chain structures[115]. Both techniques used fast discriminators with similar cut - off functions, so that the effective bias point and therefore the detector efficiency was still the same for all angles.

2.10 The final timing system and other contributions to the total time resolution.

The electronics used for the acquisition of neutron T.O.F. events was shown in figure 6. The electron beam generates a fast time - zero pulse in toroid 'T' which is coupled to trigger 'D' by a four - turn transformer winding and high quality double - screened 50Ω cable. Typical pulses - 0.5V by 4n.s. F.W.H.M. trigger the discriminator at

* Supplied by Ortec Ltd., Tenn., U.S.A.

FIGURE 17

T.A.C. — A.D.C. RESOLUTION

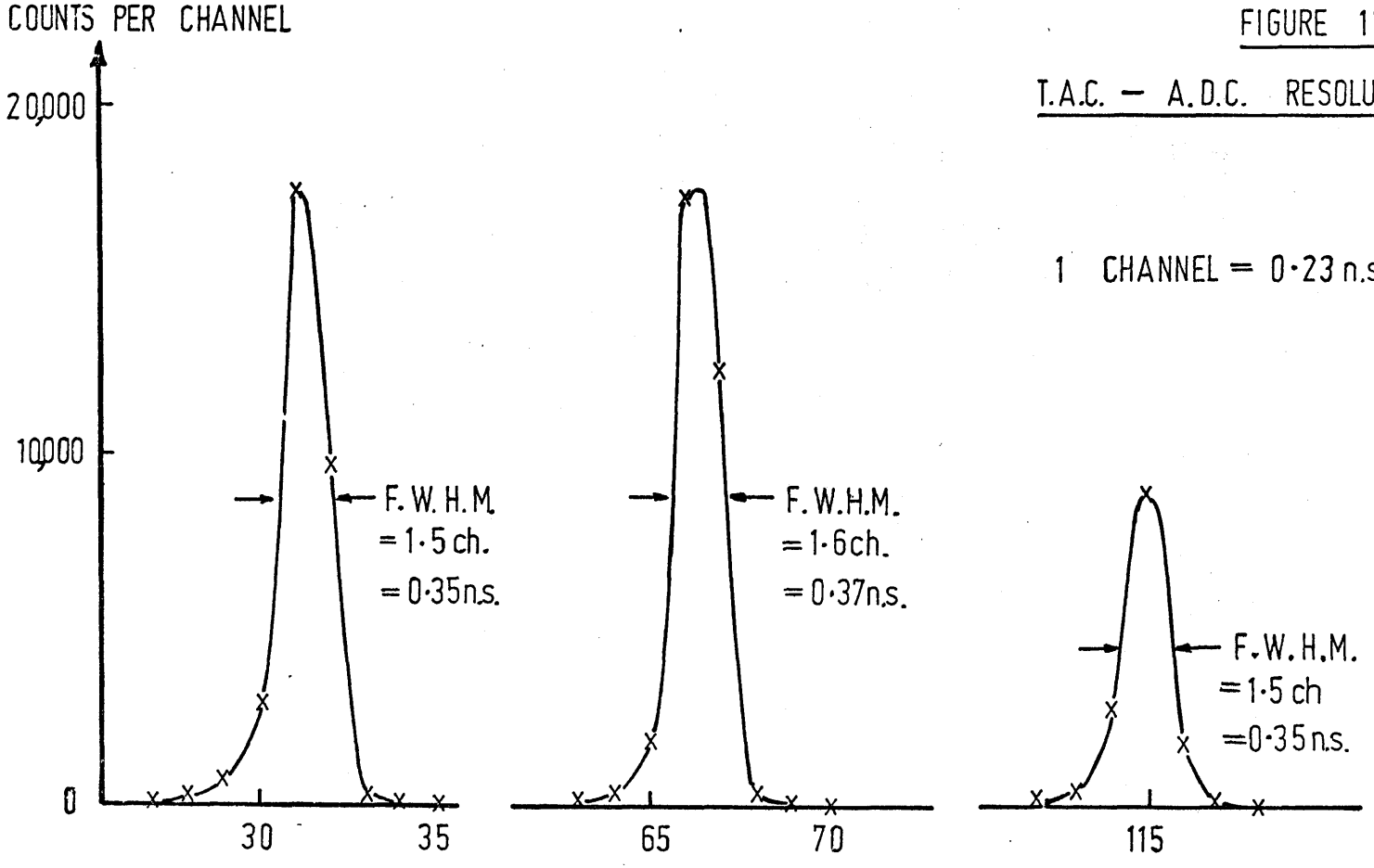

1 CHANNEL = 0·23 n.s.

Total T.O.F. Resolution for Neutrons. Table 3

(1) Basic Limiting factors.

(a) Electron Beam width = 3.5 n.s.

(b) Detector timing resolution = 2.5 n.s.
worst estimate (L.E.)

(c) Walk on start pulse = small

(d) Bin width in A.D.C.-T.A.C. = 1.4 n.s.

(e) Basic Total = 4.46 n.s.

(2) Walk due to neutron transit times in target and detector.

(a) ½-thickness of target = radius = 0.76 cm.

(b) ½-thickness of scintillator = 6.35 cm.

Note that this is an over-estimate because of the exponential decrease in the number of interactions throughout the scintillator.

(3) Result Table.

Energy (MeV.)	Speed (ns/cm.)	T (ns.) Target	T (ns.) Detector	Total T +(e) (ns.)	ΔE/E (%)	ΔE (k.e.V.)
12	.21	.16	1.33	4.66	2.22	266
9	.24	.18	1.52	4.72	1.95	176
6	.30	.23	1.90	4.85	1.62	97
4	.36	.27	2.29	5.04	1.51	60
2	.50	.38	3.18	5.50	1.10	22
1	.72	.55	4.57	6.40	0.89	9
		Neglect				

'D' (set at - 100mV.) which produces -.7V. by 30n.s. 'start' pulses with negligible walk, to be fanned out in the counting room and used to start the individual T.A.C. units used for each angle. The T.A.C. conversion is stopped by the neutron pulse from the detector at that angle. Delays are arranged so that the prompt gamma flash comes before the start pulse at the T.A.C. and is not counted. The analogue pulse proportional to the measured delay leaves the T.A.C. to be digitised by the Analogue to Digital Converter (A.D.C.) and strobed into the PDP7 computer for storage, through the interface (I).

Non - linearities in this process will be discussed in the next chapter but the resolution of the T.A.C. was easily demonstrated to be less than 0.4n.s. by starting and stopping on the same (delayed) pulse. Typical results are shown in figure 17. The time range required to cover neutrons from less than 1 M.e.V. to above 16 M.e.V. (plus some allowance for non - linearities at the ends of the scale) gave a suitable maximum conversion range as 1.4us. The storage capacity of the PDP7 computer was 16K, so that 6*1024 channels for the detectors (plus a few hundred more for monitors) were easily accomodated giving 1024 channels per spectrum or about 1.4n.s. per channel. This represented the optimum value in the compromise between count rate per channel (proportional to channel width) and resolution, for it provided $3\frac{1}{2}$ channels per resolution width (5n.s.) or an increase in the time dispersion of less than 10%.

Table 3 is a summary of the values of the different contributions to the total time resolution and the resulting energy resolution for neutrons of various energies.

2.11 Angular Normalisation.

The ideal neutron angular distribution experiment would present equal probability of neutron detection for all energies and angles in the centre of mass (C.M.) frame. Practically this is never the case and the problem is treated by ensuring good angular normalisation in the laboratory (LAB.) frame then considering the effect of changes to the C.M. These transformation effects will be considered in a later chapter.

2.12 Normalisation in the LAB. system.

Angular normalisation has been much simplified in the present system by the use of identical systems at all angles, so that only non - regularities in the equipment following the identical solid angle, identical scintillator arrangement can introduce possible systematic errors from angle to angle.

Variations in photomultiplier characteristics were minimised by using only XP1040 phototubes with sensitivities between 57 and 71 μA. per Lumen and possible differences in the distributions of photo-cathode sensitivity were minimised by a careful setting - up procedure, using similar dynode resistor chains for each tube. Base chain - photomultiplier tube pairs were chosen so that all the phototubes were operated at similar H.T. voltages. Phototube gains were optimised by focussing for maximum pulse height from a Co^{60} gamma ray source (1.33 M.e.V.), whose largest pulses are of the same height as those of a few M.e.V. neutron (**appendix 1**). This procedure also minimises the variation in gain over the photocathode,[111] minimises the transit time variations[111] and discriminates against

the amplification of the small satellite pulses which follow large depositions of light on the photocathode[115] so that it is to be much preferred to the common practice of maximising gain for the small pulses obtained from 60 k.e.V. Am^{241} X rays.

The detector efficiency is determined mainly by the value of the threshold set on the anode pulse by the fast timing discriminator. This 'bias' is necessary to discriminate against photomultiplier noise and low energy background events in the scintillator. Fast discriminators, do not gather a large fraction of the total pulse energy and cannot produce a sharp discrimination between different pulse heights so that a finite cut - off function is produced as in figure 18(a). The bias was set by the procedure of figure 18(b), where the discriminator simply gates the charge (linear) pulses into the analyser. A Co^{60} source was normally used and the required cut - off was expressed as a fraction of the known energy of the mid-point of the slope on the observed Compton 'edge' (see chapter 6). The linearity of the system was checked by observing the Na^{22} annihilation gamma ray Compton edge and the photopeak from Am^{241} 60 k.e.V. X rays. The separation of this peak from tube noise was a useful indication of the satisfactory coupling of the scintillator - photomultiplier assembly. The effective bias was taken as the mid-point of the slow cut-off curve measured conveniently on Co^{60} which is a fairly 'white' spectrum in the normal range of bias levels (from Am^{241} (~1/20 Co^{60}) to $\frac{1}{4}$ Co^{60}). This procedure was found to be unambiguous and reproducible and allowed satisfactory normalisation of detector efficiencies.

The detector responses can never be absolutely identical, for the steps taken do not entirely eliminate the possible variations in response already mentioned and small differences existing in the light collection efficiency or the discriminator cut - off shapes are difficult to find and to improve, so that a measurement was required of the degree of normalisation possible in this system. This was done for four identical detector electronics assemblies for which the above setting up procedures had been carefully followed. The detectors were placed 24.0" distant from a central point which held a cylindrically symmetrical AmBe neutron source enclosed in a $\frac{1}{4}$" thick lead pot to absorb the 60 k.e.V. X rays from $Am.^{241}$ (The source emitted 1 curie of gamma rays and about $2.5*10^{6}$ neutrons per second in to 4π).

Measurements were made of count rates with and without an extra 1" of lead around the source to give different neutron/gamma flux conditions and the common bias level was varied. The detector responses were found to have a R.M.S. deviation from the mean of 3.1 $\pm$ 1.0% which did not depend strongly upon the actual bias level. Later measurements obtained a R.M.S. deviation of 1.7$\pm$ 1.0% and a total spread of 3% under optimum conditions but it was felt that separating the counters to 20m. stations would only allow results of the previous quality, so that the practical limit of normalisation was taken as 3% R.M.S. This gave a guide to the statistical accuracy which would be usefully obtained in the experiment.

Chapter 3.

3.1 Introduction.

This chapter describes further preparations and calibration procedures leading to the taking of experimental data.

The thicknesses of bremsstrahlung and photoneutron targets have been chosen to maximise the counting rate within certain limitations of background and multiple scattering effects. Sorting and storage of data was by a computer controlled system and calibrations of this and the other units prior to data acquisition are discussed. A description is given of the procedure adopted in taking data, preceded by the necessary optimisation of current at the measured energy and of signal - to - background ratio in this condition.

Bremsstrahlung of 26.9 M.e.V. end point energy was used to induce the O^{16} (γ,n) O^{15} reaction in a water sample and good resolution photoneutron spectra have been taken by time of flight, simultaneously at six angles using identical flight path - detector systems.

3.2 O^{16} Photoneutron Target.

The photoneutron target must be large enough to give a reasonable probability of (γ,n) events while not so large as to cause severe attenuation of photon flux by atomic collisions or to cause much scattering of the outgoing nucleons.

In this case water is the most convenient target. Liquid or solid O^{16} could be provided by cryogenic methods but the target holder is necessarily complicated in this case especially for the cylindrically symmetrical configuration to be preferred in angular distribution measurements, and therefore it becomes a significant

source of background. Gas targets would have been too large and would have caused large variations in the transit time of neutrons which would have degraded the T.O.F. resolution.

Water targets suffer from the disadvantages of requiring a container and of having a large proportion of Hydrogen in their chemical composition. Although the Hydrogen cannot cause (γ,n) background it may distort the O^{16} photoneutron spectrum because of the large cross section for (n,p) scattering. This sets the upper limit on target size, for 6 M.e.V. neutrons have a (1/e) attenuation length of about $3\frac{1}{3}$" in water[103] while the absorbtion of photons of about 25 M.e.V. in water has been measured to have an attenuation length of about 24" [120] and is therefore less significant. In order to keep the probability of neutron scattering below 9% the cylindrical targets were made 0.6" dia., giving 0.3" average thickness. Since the container had to be much thinner, target rigidity became a problem.

The target holders used were 0.6" dia. cylinders of .001" 'Mylar' with a bottom of the same material, the seals being made with 'Araldite' adhesive. The height was determined by the amount of water used, for the cylinders were 5" long and fitted tightly over a cylindrical 'Tufnol' former along $2\frac{1}{2}$" of their length, so that the remaining holder length derived its rigidity from this fit. In fact the cylinders had been rolled on formers of this diameter and the good fit was enhanced by a thin layer of petroleum jelly to form a seal which prevented evaporation of the water. The Tufnol former was constructed to fit a slider on an optical bench which the author had fitted along the electron beam line some 6" above the bremsstrahlung and photoneutron

Fig. 19

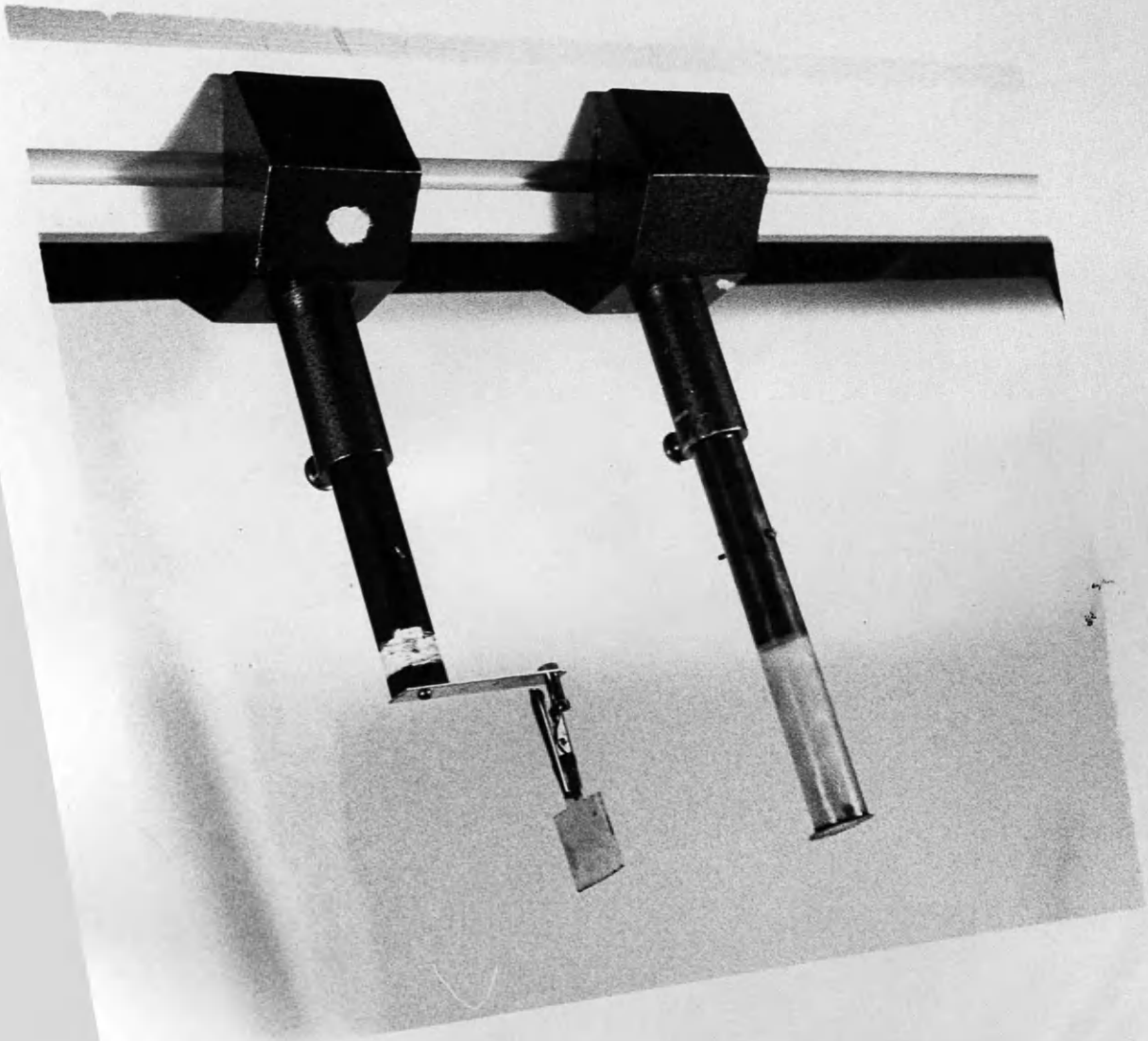

Elastic Scattering Formulae for neutrons — Table 4.

1. Notation: m,M = masses of neutron and other nucleus, resp.
C.M. quantities have a bar, eg., $\bar{\theta}$, $\bar{T}$
$\theta, \bar{\theta}$ = LAB, C.M. angle of scatter (for the neutron)
Ti, Ts = LAB. kinetic energy of incident, scattered neutron.

2. Equations:

$$T_S = (M^2/(m+M)^2).(1+(m/M) + 2.(m/M).\cos\bar{\theta}).\ Ti$$

$$\tan(\theta) = \sin(\bar{\theta})/(\cos\bar{\theta} + (m/M))$$

$$\frac{d\sigma}{d\Omega}\Big/\frac{d\sigma}{d\bar{\Omega}} = \frac{d\bar{\Omega}}{d\Omega} = \frac{(1+(m/M)^2+2.(m/M)\cos(\bar{\theta}))^{3/2}}{(1+(m/M)\cos(\bar{\theta}))}$$

3. (n,p) case: (M = m.)

$$\cos\theta = \sqrt{Ts/Ti} \quad ; \quad \theta = \bar{\theta}/2$$

$$\frac{d\sigma}{d\Omega}\Big/\frac{d\sigma}{d\bar{\Omega}} = 4.\cos\theta = 4.\sqrt{Ts/Ti}$$

4. (n,p) production of 5→10 M.e.V. scattered neutrons.

a. Incident 10 M.e.V. $\cos\theta_{max} = \sqrt{5/10} = 1/\sqrt{2}$: $\cos\theta_{min} = 1$

$\theta_{max} = 45^o$: $\theta_{min} = 0^o$

b. Incident 6 M.e.V: $\cos\theta_{max} = \sqrt{5/6} = .911$: $\cos\theta_{min} = 1$

$\theta_{max} = 24^o$: $\theta_{min} = 0^o$

c. Conclusions: Neutrons must make a (LAB) angle of $\leq 45^o$ with the detector to be inscattered. (Solid angle $\leq 4\pi/18$str.) This is 90^o in the C.M. and since $d\sigma/d\bar{\Omega}$ is isotropic, $(20\text{-}23)_{\frac{1}{2}}$ the total cross-section is available to these neutrons.

5. (n,O^{16}) case: (M = 16*m)
All angles are possible; little change in $\theta - \bar{\theta}$ or $d\sigma/d\Omega - d\sigma/d\bar{\Omega}$: loss in neutron energy = (.887*(1/8)*($\Delta\cos\theta$))*Ti ; maximum energy loss = 22%.

targets. This arrangement, shown in figure 19, allowed adjustment and exact replacement of the position of the targets. With a 0.6" high water sample, the mass of the target holder in the beam was less than 3% of the water.

3.3 Multiple Scattering.

The interaction of about 9% of the neutrons leaving the photo-neutron target leads to some distortion of the neutron spectra by outscattering (or attenuation) and inscattering. The first can be treated simply, for the total cross sections are well known, but the second requires a complete Monte Carlo simulation of the process and this was prohibited by the extremely small solid angles involved ($\sim 10^{-6}$) and the total amount of computer time required.

The contamination due to inscattering is reduced because of the restricted energy range of interest in the present experiment. Ground state transitions are observed only for the top 5.2 M.e.V. of the neutron spectrum or from 5 to 10 M.e.V. for 27 M.e.V. bremsstrahlung on O^{16}. Kinematic relationships are presented in table 4 for neutron elastic scattering (the dominant reaction at these energies). The kinematics and the restricted energy range limit the photoneutrons inscattered by (n,p) collisions to those originally travelling at less than 45° with respect to the detector direction and only half the total cross section is available to this restricted solid angle ($=4\pi/18$), so that the final inscattering from Hydrogen is negligible ($\leq 0.2\%$). This arguement does not hold for the inscattering from O^{16} collisions and the total possible spectrum distortion due to inscattering from

FIGURE 20.

TARGET GEOMETRY

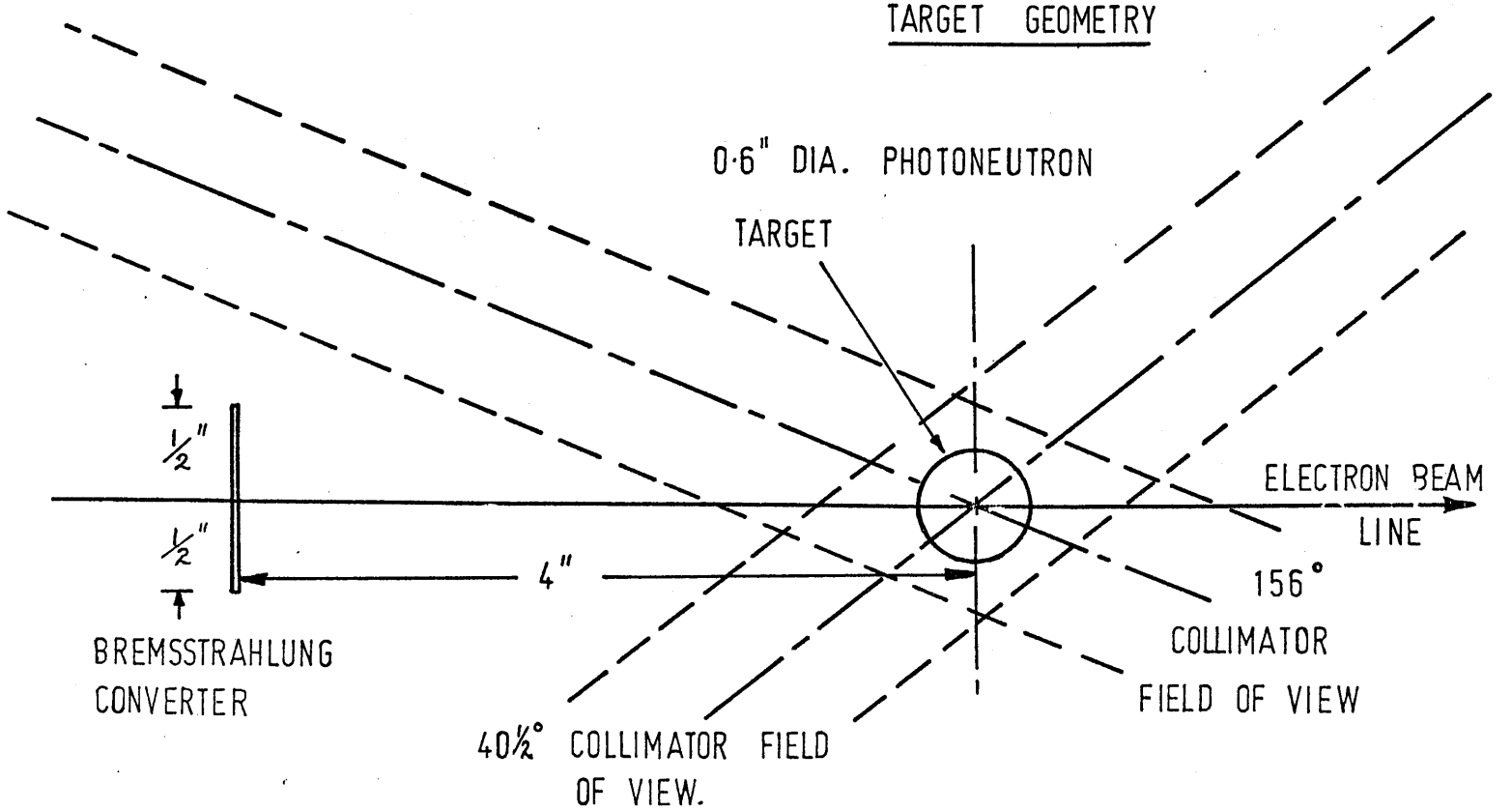

both nucleii is always below 3% in the 5 - 10 M.e.V. energy range.

To summarise, the spectra are corrected for neutron attenuation in the sample and the inscattering which is not corrected for, has been shown to be smaller than the normalisation and statistical errors expected.

3.4 Bremsstrahlung Converter.

In order to obtain the maximum yield of photons a high Z 'thick - target' converter was used close to the photoneutron target. The choice of target position and thickness was a compromise between many factors. A thicker target would produce more bremsstrahlung in the forward direction (but not very much more after 0.1r[121]) and would stop more of the electrons. Therefore the converter would be useful as a charge monitor and fewer electrons would hit the water target. Those electrons which did reach the water could cause bremsstrahlung and photoneutron production and could also cause direct electro-production of neutrons which would distort the observed angular distribution. But a thicker target would spread the photon beam and increase the background from neutrons produced in itself and the walls of the neutron cell, while the angular resolution of the system (and therefore the C.M. energy resolution) would be decreased if the thicker target was moved nearer the water.

The target used was 0.5 m.m. (0.15r) of Tungsten in the form of a square of 1" side placed perpendicular to the electron beam 4.0" from the water target. The position is chosen to avoid the forward and background detectors seeing the converter while being as near to the target as possible (figure 20). The target thickness is just that

THEORETICAL BREMSSTRAHLUNG ANGULAR DISTRIBUTION FROM THICK TUNGSTEN TARGETS FOR RELATIVISTIC ENERGIES.

FIGURE 21.

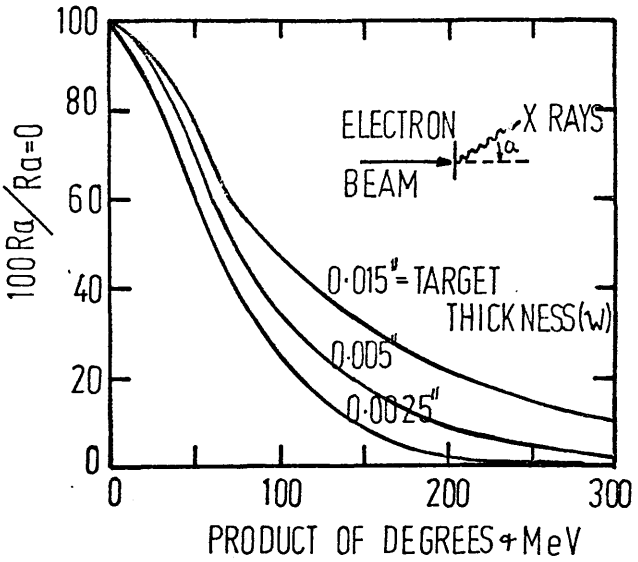

R_α = FRACTION OF K.E. OF INCIDENT ELECTRON RADIATED AT ANGLE α

ELECTRONICS OF CHARGE MONITOR

FIGURE 22

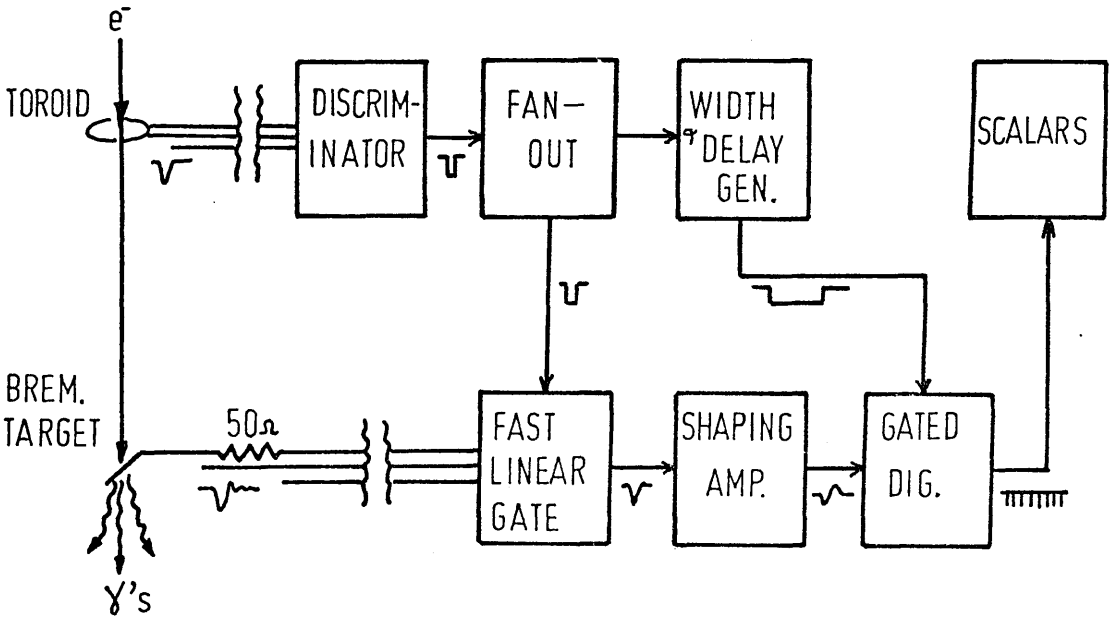

which produces a photon beam with gaussian distribution falling to half maximum at the solid angle subtended by the water target (assuming a point source). This was obtained by interpolation from figure 21 reproduced from National Bureau of Standards Handbook 55.[100]

3.5 Angular Spread of Bremsstrahlung and Energy Resolution.

The half angle subtended by the water target was about 5^{o} and since the electron beam had a finite extent on the bremsstrahlung converter (a gaussian distribution with F.W.H.M. about 0.7") the combination of angular spreads became 6^{o}. The variation in $\cos\theta$ corresponding to this $\pm 6^{o}$ causes an energy spread of upto $\pm$ 18 k.e.V. in O^{16} spectra (equation (4.6.1)) but this is unobservable with the present resolution for neutrons above 2 M.e.V. kinetic energy.

3.6 The effect of electrons in the photoneutron target.

An estimate of the number of electrons which traverse the water target in the present system can be used to calculate the effect on the neutron yield of bremsstrahlung produced in the photoneutron target and of electroproduction.

Since the electrons form a wider cone than the photons, the ratio of photon flux to electron flux on the water target is increased to about 0.2 (from the 0.15 expected purely on converter interaction probability). The direct electroproduction correction is performed more accurately later but electron events will be inhibited by about $\alpha = 1/137$ with respect to photon ones and the nett effect of the electrons will be of order $3\frac{1}{2}\%$.

The 0.6" dia. water target presents an average thickness of about 0.45" to the electron beam, or 0.03 of radiation length.[121]

But the critical energy in water is 93 M.e.V.,[121] so that for 27 M.e.V. electrons ionisation predominates and the bremsstrahlung flux generated is about 5% of that from the tungsten. Since only half of the target thickness is available for photoneutron production from self - bremsstrahlung, the final contribution is $2\frac{1}{2}\%$, which is small enough to cause little distortion in comparisons with target empty background runs.

3.7 Bremsstrahlung Spectrum.

Thick target brehmsstrahlung spectra are difficult to calculate especially for configurations which use a large range of emission angles.[121] Measurements of such spectra were made by O'Dell et.al.[122] by using the brehmsstrahlung to induce the $D^2(\gamma,n)p$ reaction and observing the neutron spectra by T.O.F. Experiment[123] and theory[124] are in good agreement for the cross section and angular distribution of this reaction and the incident γ - spectrum was obtained from these spectra and the reaction kinematics.

This technique is convenient in the present experiment, for the water target may be replaced by an exactly similar heavy water target and the oxygen component subtracted to give D $(\gamma,n)p$ spectra. The O^{16} cross section may then be obtained at any photon energy by comparison with that of deuterium, and the angular distribution of the deuterium photoneutrons may be compared with theory and other experiments to check the angular normalisation.

3.8 Current Monitoring.

The bremsstrahlung converter was intentionally made just larger than the photoneutron target so that it would intercept all the

FIGURE 23

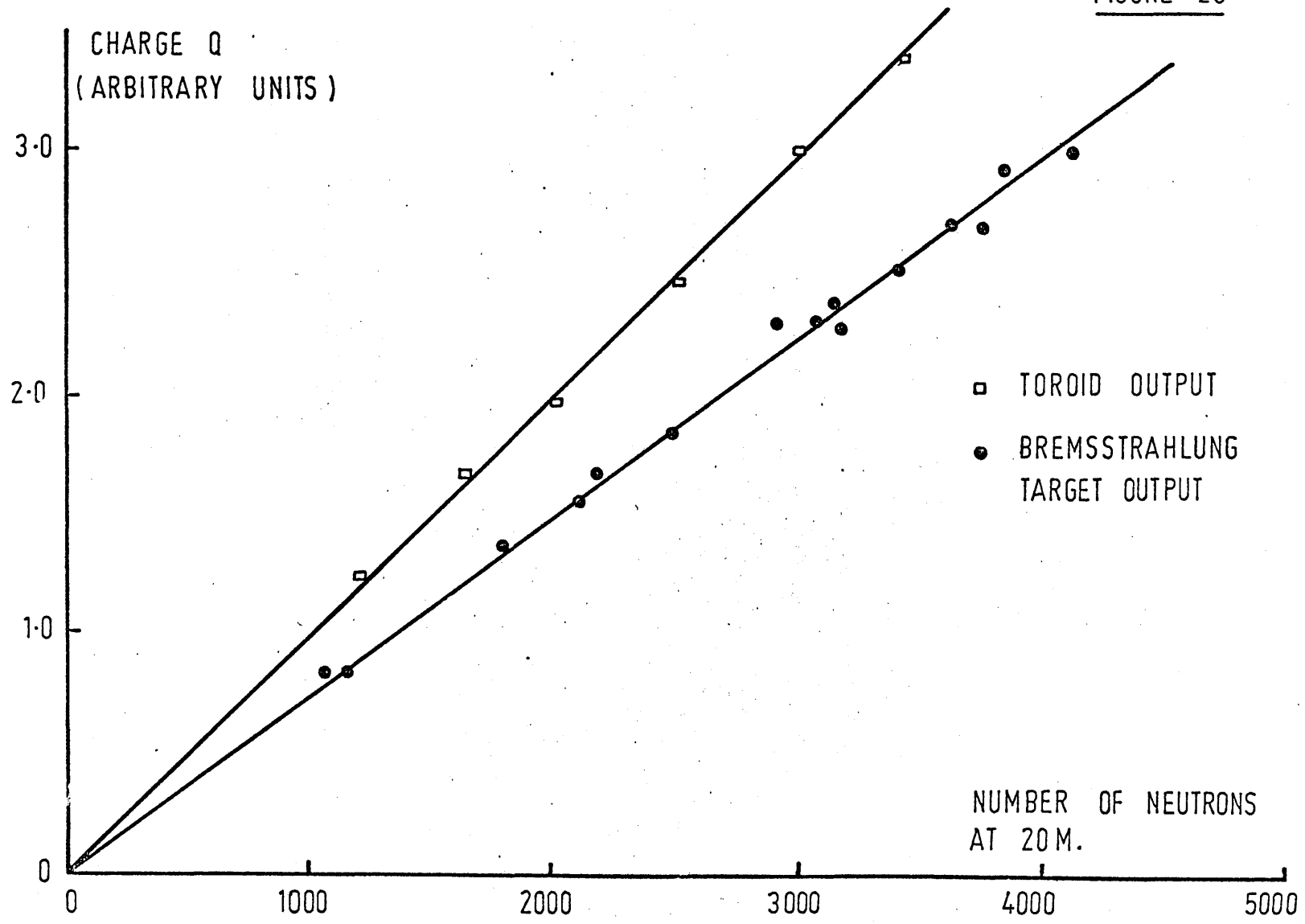
CHARGE Q
(ARBITRARY UNITS)
3·0
2·0
1·0
0
0
1000
2000
3000
4000
5000
TOROID OUTPUT
BREMSSTRAHLUNG TARGET OUTPUT
NUMBER OF NEUTRONS AT 20 M.

electrons which could hit the water while remaining a sensitive monitor of beam position and current. The charge was collected over a 50Ω resistor to the earth of a high quality cable which transferred the fast pulse to the counting room and the electronic arrangement of figure 22. The pulse from an early toroid pick - off was used to gate the charge pulse into the amplifier to eliminate the slower pick - up on the cable. The amplifier pulse was to be digitised by a 256 channel A.D.C. controlled by the PDP7 computer (which collected all of the data) but the A.D.C. unit unfortunately caused trouble and this system was replaced by the one shown just before the start of the experiment. The monitor response was checked against that of a toroid in the neutron cell and both were checked against the neutron counters for linearity. The results are shown in figure 23.

Because ionisation in the Tungsten target occurred for only 5% of the electron beam this monitor was slightly less sensitive to small changes than one with a larger signal. A system was investigated which used a beam dump block after the bremsstrahlung target.

3.9 Beam Dump Block.

This required a low Z material with high critical energy, for the electron beam had to be stopped with as little bremsstrahlung production as possible. The device also interested the author as a 'beam hardener' because the attenuation of the low energy bremsstrahlung photons (up to 1 M.e.V.) is much greater than that of high energy photons (25 M.e.V.) in the same material.

The energy dependences of the bremsstrahlung spectrum and the Compton effect ensure a predominance of low energy photons in the

'γ - flash' scattered from the photoneutron target. These low energy photons cause only background effects and any method of reducing their intensity while retaining that of the useful high energy photons would help the signal - to - background ratio.

Insertion of a dump block requires the bremsstrahlung converter to be further from the photoneutron target so that the photon 'spot' will be too large and many quanta will miss the water target unless the converter thickness is reduced. Therefore the count rate must be smaller. Tests with a 4" Aluminium block showed a reduction in γ-flash, but also in real - to - background rate and the device was discarded. Charge normalisation was performed using the converter system already discussed.

3.10 Monitoring of Relative Detector Response.

Angle to angle normalisation has been planned on the basis of identical detectors and the stability of these is all-important. The relative count rates should be constant for fixed experimental conditions, and these were monitored by observation of the integrated T.O.F. counts every 5 minutes from each detector, conveniently typed out by the PDP7 computer which controlled the data collection.

3.11 Data Collection and Storage.

The information generated in the angular distribution experiment must be sorted and stored during data acquisition. Each of the six angles requires 1024 channels for T.O.F. storage and extra monitors need similar facilities. To satisfy the requirements the author has extended the data acquisition system on the PDP7 computer* which

* Supplied by Digital Equipment Corporation, Maynard, Mass., U.S.A.

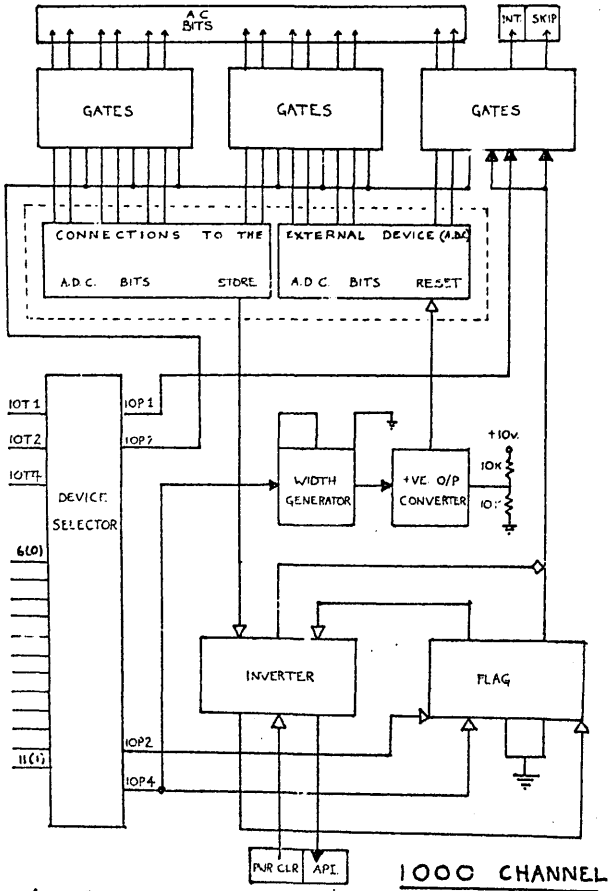

Fig. 24

1000 CHANNEL PDP7 INTERFACE

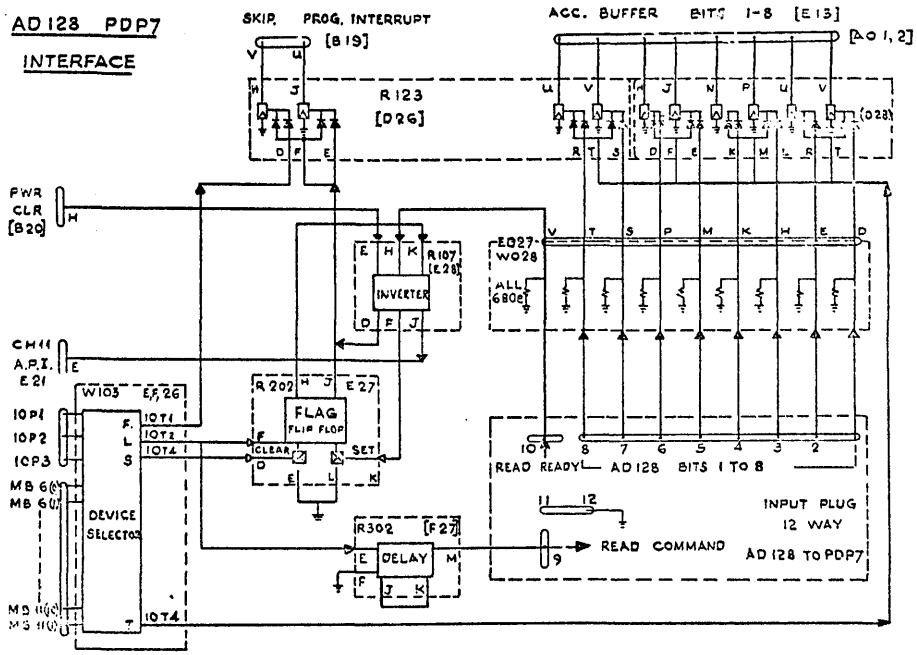

FIG. 25

originally serviced four 1024 channel A.D.C.'s. A typical data collection line has already been shown (chapter 2 figure 6).

By extending the computer memory to 16K (of 18 - Bit words) 12,288 channels of storage were made available (plus that of the 'kick-sorting programme) and the system now has 9 A.D.C.'s. The original four provide up to 1024 channels each, four more allow up to 8000 channels each and one provides up to 256 channels. The programme normally spends its time displaying the data but responds to interrupt signals from the A.D.C. units to read in T.O.F. pulses in digital form and update the storage locations. Data output is to magnetic tape or 'hard copy' (paper tape or typeout).

The programme was written by Dr. J.D. Kellie of this laboratory who kindly extended it to service the extra A.D.C.'s installed by the author, and to include, at the author's suggestion, the periodic typeout routine for relative detector monitoring. The system has worked reliably in taking the author's data and in other (neutron scattering) experiments.

3.12 Interfacing of A.D.C.'s.

The PDP7 computer features an interrupt system which allows many external devices to be controlled. In this case, each new A.D.C. was serviced through an interface designed by the author (figure 24). The purpose of the interface is to convert the digital information from the A.D.C. to standard voltage levels and to gate these into the computer accumulator buffer (A.C.B.) in synchronism with the input output timing (I.O.T.) cycle of the PDP7.

When the A.D.C. has finished converting a data pulse it signals

Fig. 26

(a) CIRCUIT TO TEST DIFFERENTIAL LINEARITY

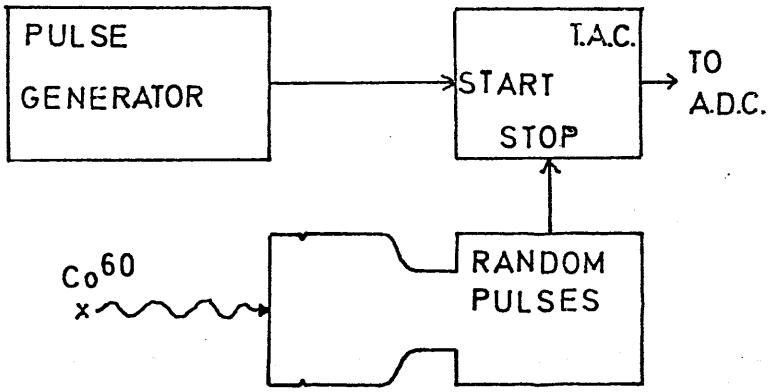

(b) TYPICAL RESULTS (1μs. SCALE)

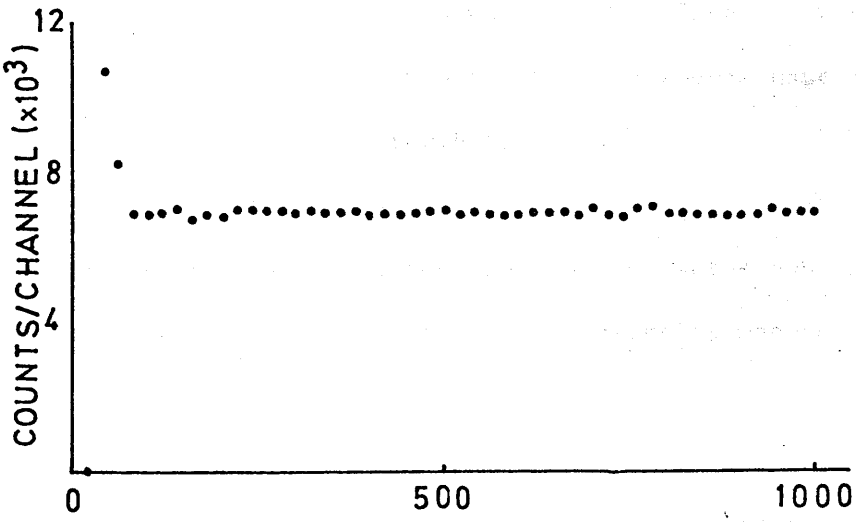

the fact by sending a 'STORE' pulse to the interface, where a 'FLAG' pulse is generated to trigger the assigned channel of the automatic priority interrupt (A.P.I.) on the computer. The programme is therefore interrupted in its background job (displaying the data in this case) and jumps to a subroutine to service the device identified by the A.P.I. This it does by emitting memory buffer voltage levels, in the correct code to gate synchronising input-output transfer (I.O.T.) pulses through a 'device selector' into only the correct interface. The resultant (I.O.P.) pulses gate into the accumulator buffer the digital information from the A.D.C. (which is already present as voltage levels on the connecting lines) then reset the A.D.C. and the interface triggering mechanism. By this means, data from only the correct device is transferred to the computer in synchronism with the I.O.T. timing cycle.

The voltage levels and mode of use of the 256 channel A.D.C. were somewhat different and therefore so was the interface (figure 25), but since this device was not finally used in the author's experiment its features will not be discussed further.

3.13 Calibration of Electronics.

The electronic arrangement used for running was shown in figure 6 and the time resolution of detector and electronics was considered in section 2·10. The T.A.C. – A.D.C. combinations were checked for differential and integral linearity before experimental runs.

Figure 26 shows the circuit used to test for differential linearity and typical results. By using a detector and radioactive source to provide pulses with a random distribution in time, the pulse

(a) CIRCUIT TO TEST INTEGRAL LINEARITY Fig.27

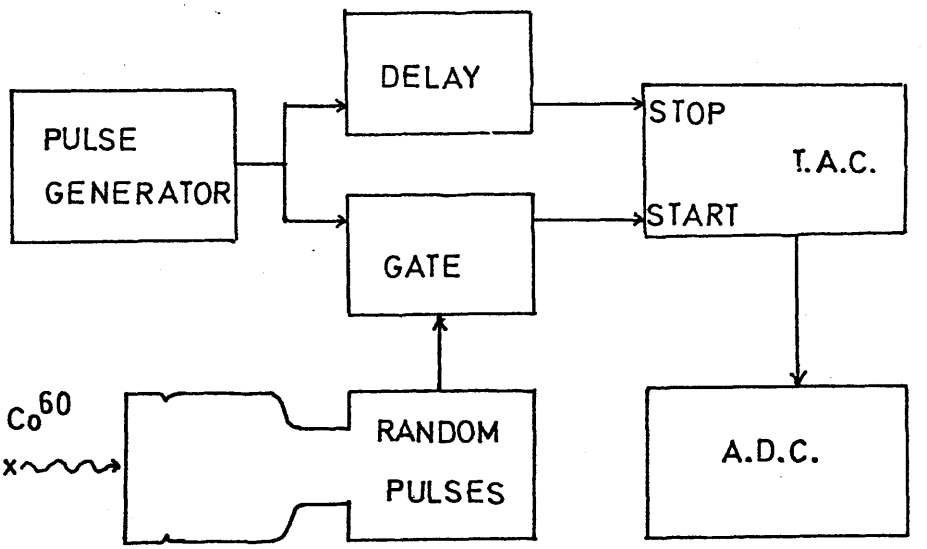

(b) TYPICAL RESULTS

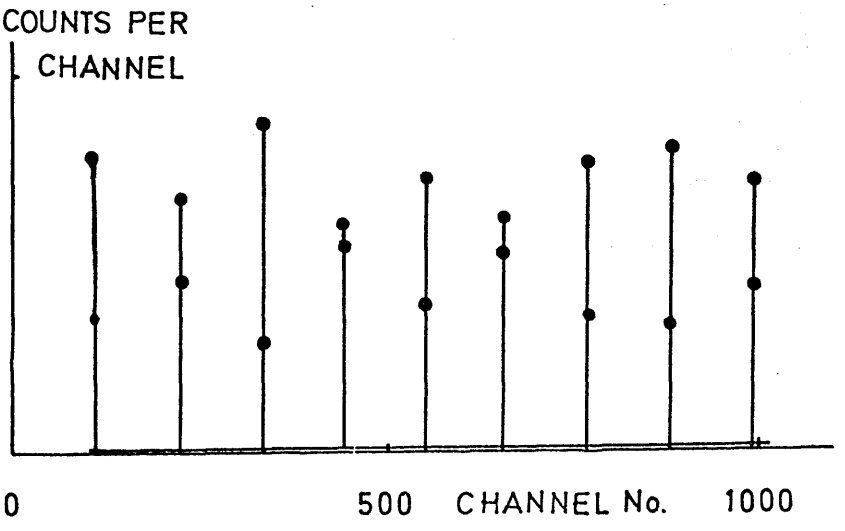

height spectrum from the T.A.C. should be truly 'white' and each A.D.C. channel should acquire an equal number of counts. Significant variations would lead to distorted spectra in normal measurements. The T.A.C. - A.D.C. combinations showed total differential linearities of $\leq 2\%$, within specification for the fraction of the range (10% to 100%) normally used (figure 26).

Integral linearity was measured by the gated oscillator method shown in figure 27(a). A pulse from an oscillator of known (high) frequency is used to start the T.A.C. which is stopped by some later pulse from the same oscillator selected by coincidence with a random source so that the time interval is a multiple of the oscillator frequency and the spectrum obtained is a series of peaks equidistant in time. The A.D.C. - T.A.C. combination is then calibrated (in n.s./channel) in terms of the known time interval and the integral linearity is found by comparing the number of channels between peaks (which should be constant). Results are shown in figure 27(b) where the linearity is seen to be very good ($<.1\%$) over the usual 10% to 100% range. A commercial (N.I.M.) unit* using a crystal oscillator was later used to perform the same calibrations.

The stability of the system was measured by applying the same pulse to start and stop all the T.A.C.'s and noting the time channel of the peak over a period of several days. No significant drifts were observed.

* Supplied by Tennelec, Inc., Oak Ridge, Tenn., U.S.A.

3.14 Gamma Flash, After-Pulsing and Photomultiplier switching

Satellite pulses are produced in photomultipliers following intense illumination of the photocathode because of ionisation in the residual gas of the tube. These pulses arrive 500 -- 600 n.s. after the initial pulse in the XP1040 photomultiplier, and can cause contamination of neutron T.O.F. spectra from electron linear accelerators because of the large flux of Compton-scattered gamma rays which precedes the photoneutrons.

The Compton scattering cross section is highly forward-peaked so that this problem is most severe for forward angles and it was found by experiment that the $40\frac{1}{2}^{o}$ angle exhibited characteristic after-pulsing contamination in initial tests but the effect was not discernible at $86\frac{1}{2}^{o}$ and the more backward angles.

After-pulsing effects can be minimised in several ways. Most previous neutron T.O.F. measurements have been made at 90^{o} to avoid the worst forward angles but obviously all angles had to be covered here. Beam hardening had already been discarded for other reasons although it would have helped. Inclusion of a thin filter of high Z material in the flight paths can stop most of the low energy photons but this cannot be carried very far for the neutrons are also attenuated, although more slowly, and the count rate will fall (1" of lead would stop about 90% of the gamma rays and about 50% of the neutrons). Up to $\frac{1}{4}$" may be useful to stop the large number of very low energy photons with little neutron attenuation and simple corrections to the neutron spectra. In this system, 1/8" of lead was placed in all flight paths at the neutron cell and next to the first

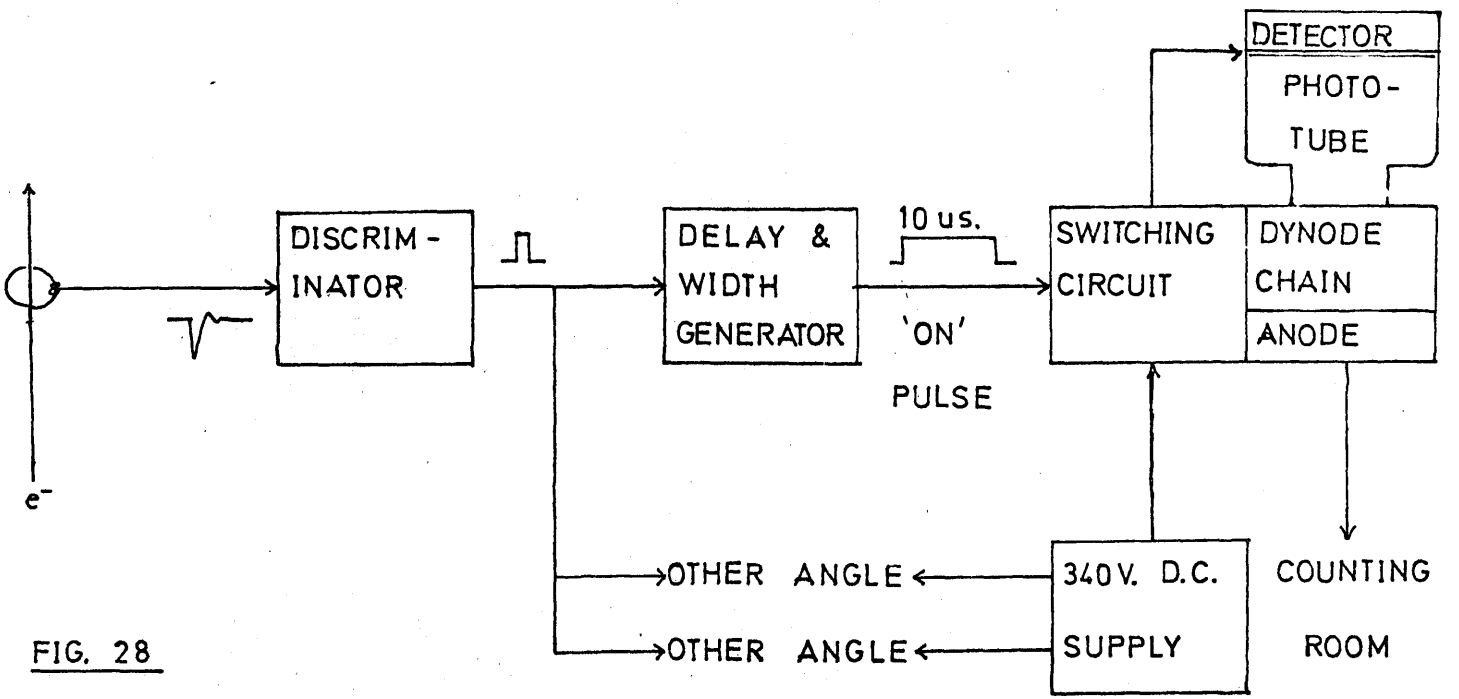

FIG. 28

SWITCHING OF PHOTOMULTIPLIERS

collimator.

In some systems the delay in the timing chain can be arranged to put the γ - flash on - scale of the T.A.C. - A.D.C. so that analysis of events following a gamma flash is prevented by the dead time of the T.A.C. (one count per start pulse). But for multiangle systems the gamma flash comes with very different frequencies for different angles so that the dead time corrections would vary and for forward angles, the γ - flash comes essentially every time, so that no neutrons would be recorded.

The best method of reducing the after - pulsing effect is by switching voltages in the photomultiplier dynode structure to prevent acceleration of the large electron pulse produced in the photocathode by the γ - flash.[115] Mr. J. M^{c}Keown of this laboratory has studied the satellite pulses from XP1040/58 A.V.P. photomultipliers for reasons similar to those of the author and has developed a method of inhibiting the formation of large pulses by reverse biasing the photocathode to dynode one voltage,[115] and he kindly provided suitably modified dynode chain assemblies for use in the author's experiment. These provide a reduction in gain of ~300 for the γ - flash and therefore the same reduction in after - pulsing.

The electronic circuit used by the author to initialise the switching is shown in figure 28. The photomultiplier is normally 'off' and is pulsed 'on' 150n.s. after the γ - flash by a signal derived from the pulse from a fast toroid pick off in the neutron cell, which arrives promptly enough to allow the photomultiplier to switch and reach a stable D.C. voltage level before the arrival of the fastest

FIGURE 29 (a)

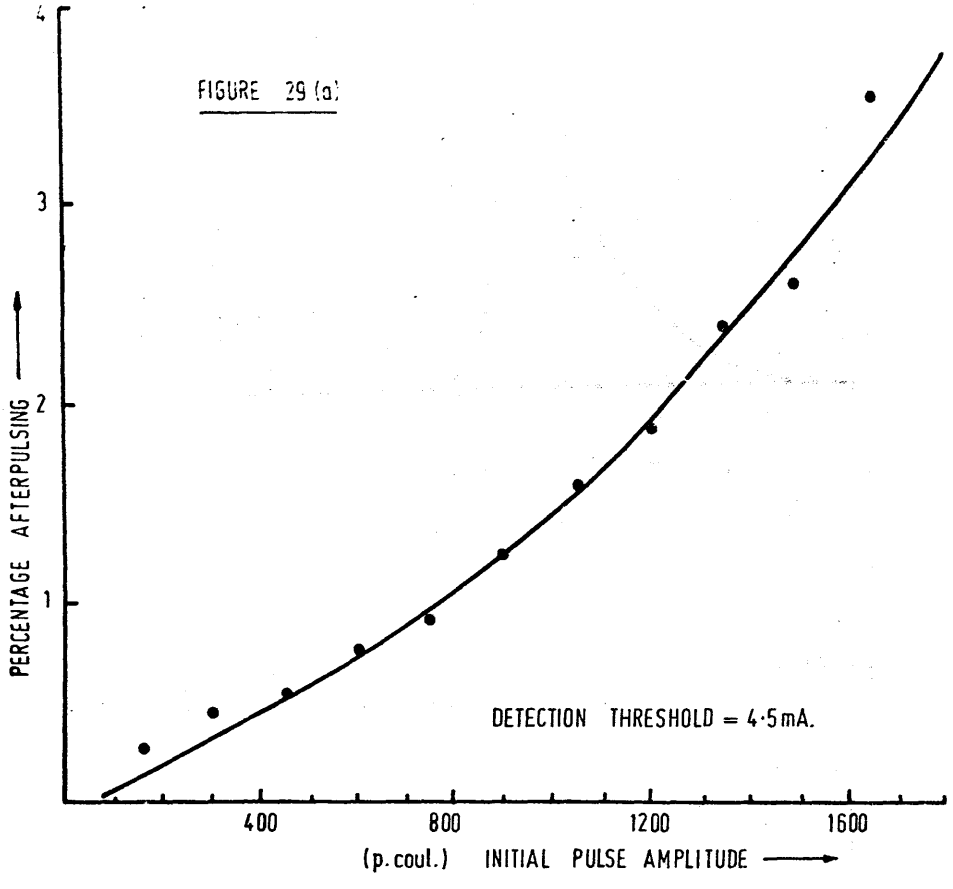

FIGURE 29(b)

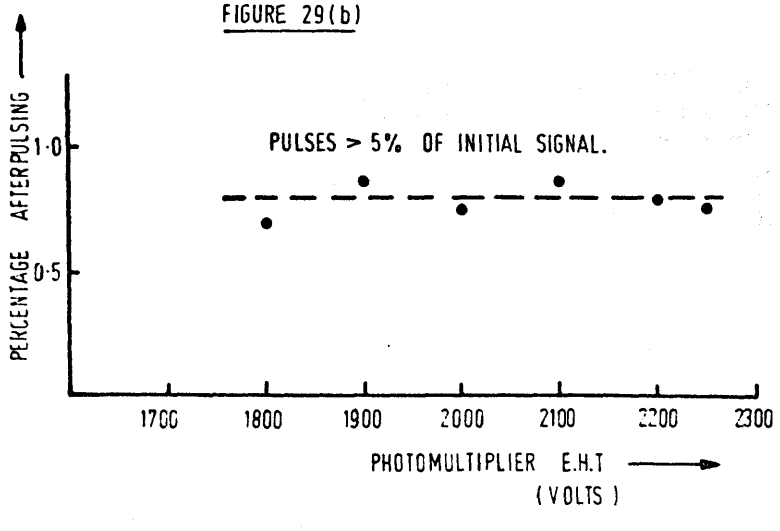

TIME DISTRIBUTION OF AFTER-PULSES FIGURE 29(c)

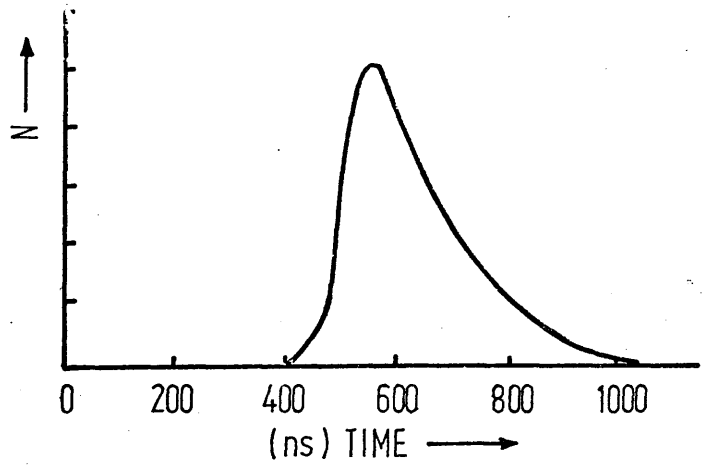

INVESTIGATION OF AFTER-PULSING FIGURE 30.

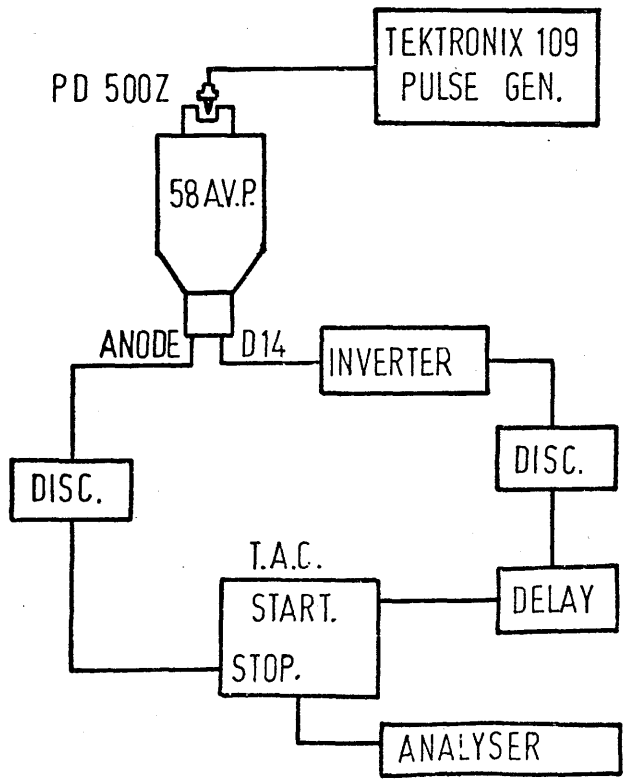

neutrons.

Switching was found necessary for the three forward flight paths, because of the angular distribution of the photons from Compton scattering. This assessment had been made during preliminary accelerator runs by measurement of the pulse height of the γ - flash. After - pulsing characteristics of the XP1040 are reproduced in figures (29,a-c) where the percentage after - pulsing is seen to increase exponentially with the ratio of the initialising pulse to the discriminator threshold with a value of about 1% for 20:1 ratios.(115) These results were confirmed by the author using the circuit of figure 30 to measure possible variations in the after - pulsing characteristics of his photomultipliers.

The light source was a gallium arsenide photodiode (Ferranti PD5002) optically coupled to the photocathode by a well of optical cement in a small perspex block and electrically triggered by a fast pulse generator. For various values of total charge in the anode pulse, an investigation was made of percentage after - pulsing versus fractional triggering level. This entirely confirmed McKeown's results and the author's photomultipliers were found to have a fairly small spread in after - pulsing characteristics as expected from their similar sensitivity and noise values.

These results showed that if the γ - flash pulse height in the experiment were less than 5* the detector threshold, the total after - pulsing would be 0.01%, which in the usual conditions (of 480 γ - flash pulses per second) would produce 1.8 counts per hour. These satellite counts have a definite time distribution with respect to the

γ - flash as shown in figure 30.[115] About 300 channels are so covered in this system and the peak channel can be shown to take ~1% of the total so that the count rate per channel due to this effect is insignificant compared to that due to real counts (about 18 per channel per hour).

In setting up the experiment with an O^{16} (water) target, linear pulse height spectra were taken for the γ - flash at all the backward angles. The γ - flash was 5 to 10 times the detector bias used and was reduced in intensity and average height by the 1/8" lead inserted on all flight paths, so that after - pulsing effects were negligible. Typical γ - flash ratios of up to 100* the discriminator threshold were found for the very forward angle but this was more than dealt with by the switching procedure.

3.15 Detector Bias Levels.

To avoid after - pulsing, the detector bias level should be high, but it must be low enough so that small variations in the level do not significantly effect the efficiency of detection of the high energy neutrons. The value used was $1/8^{th}$ of the Compton edge of a Co^{60} spectrum which corresponds to the maximum pulse height from a 0.9 M.e.V. neutron (Appendix 1). Since 5 M.e.V. neutrons produce an essentially white energy spectrum up to 15 times this height (Appendix 1) a 10% change in this bias level will only affect the detection efficiency of 5 M.e.V. neutrons by 0.7%. This makes normalisation errors due to differences in bias level very small.

3.16 Energy Calibration of Electron Beam.

The present 0^{o} system relies on the stability of the accelerator

focussing and steering to maintain the energy of the electrons which is initially measured by deflection round the 90^0 magnetic system. Since all the electrons were required for count rate purposes, a good resolution ($\leq 1\%$) beam was not possible using the typically $3\frac{1}{2}\%$ F.W.H.M. nanosecond beam at 27 M.e.V.

The author investigated the resolution and stability of the 27 M.e.V. nanosecond beam and found that the basic resolution (determined by the accelerating structure and the input focussing conditions) was 3% to $3\frac{1}{2}\%$ with small ($\sim\frac{1}{2}\%$) variations in peak energy due to the residual jitter of the accelerator pulsing networks. Investigation before and after accelerator trips showed the initial energy to be re-established each time after a few minutes warm - up. The input focussing and steering conditions essentially fix the value of the energy, apart from the control achieved by variation of the relative phase in successive sections of the accelerator. These settings were always stable and were untouched during runs. Periodic tests over several days showed the long term drifts to be less than half the resolution width.

The beam energy was measured before, after and during the 3 day O^{16} run, also before and after the background and D_2O normalisation measurements (of about 24 hours each) and the above statements were confirmed. The electron energy used was 26.9 M.e.V.

3.17 Accelerator Running Procedure.

The detectors and electronic arrangements were positioned and calibrated two days before the experiment began and left on to stabilise. Switching bases with L.E. timing were used on the 3

forward angles and C.F.P.H. timing - base assemblies on the 3 backward ones. Targets were positioned shortly before running, using the methods and criteria already described.

The accelerator was set up by the experimenter who adjusted (by experience) the input conditions (gun steering and focus and the sweep voltage on the deflection plates) to provide stable input conditions with a good current pulse 3.5n.s. wide and minimum 'dark current'. This is caused by stray electrons from the gun which are accelerated not in the 3.5n.s. fast pulse, but at other times during the 1µs. when both gun and R.F. accelerating field are on. The gun current is normally steered to miss the entrance iris to the accelerator and hit a metal beam stop and electrons are deflected in to the accelerator by the fast 15k.V. pulse applied to the deflection plates. If steering and focussing are not good, the perumbra of the spot may reach the iris and be accelerated to the neutron cell, causing γ - flash and photoneutrons with timing characteristics entirely unrelated to those from the 3.5n.s. start pulse. This is a source of background which is beam and target dependent and cannot be simply subtracted.

The dark current is simply measured by delaying an accelerator pre-pulse so that it coincides with the usual toroid derived start pulse (which requires a 3.5n.s. electron pulse). The new pulse was then used to start the T.A.C.'s and the count rate with beam on is confirmed to be the same as before. Then the 15k.V. deflection pulse was switched off and the count rate found with no 3.5n.s. pulse injected. Finally, the gun was switched off and allowed to cool and the new count rate found. If the last two rates are not identical

(and due to the background rate in the detector) then dark current is present.

By observing that the shape of the dark current spectrum followed the R.F. pulse envelope, the author realised that the effect must be mainly due to detection of the scattered gamma rays (not photoneutrons) and found that by injecting the electrons at the end of the R.F. pulse these gamma rays could be delayed out of the system along with the 3.5 n.s. gamma flash, so that the total effect was reduced by the probability of neutron emission or about 10^{-3}. Dark current effects are now easily avoided but the tests were made periodically throughout the experiment.

The energy required is obtained by adjusting the attenuation and the relative phase of the R.F. power in alternate sections of the accelerator and the energy value and resolution are obtained from measurements round the well - calibrated 90° magnetic analysis system, before steering and focussing the beam to a spot on the bremsstrahlung target in the neutron cell. The converter was covered with a thin layer of zinc sulphide and viewed by a television camera - mirror system to give visual indication of the beam position and intensity. The value of the current was optimised by examination of the pulse from the toroid pick-off in the neutron cell and the charge from the bremsstrahlung converter. The delay in the start channel was adjusted to put the γ - flash just on scale, when the dark current was measured and confirmed to be indistinguishable from the random background rate. A further adjustment of the delay then put the γ - flash some 200n.s. off - scale and count rates were measured for signal and

background conditions.

3.18 Sources of Background.

In the 5"*5" dia. scintillators used, the random background (from cosmic rays and K^{40} and other gamma rays from the surroundings) gives rise to a d.c. count rate of ~1k.Hz., even in the shields constructed by the author. These can only cover half the total solid angle and therefore cut the rate by about two. When multiplied by the duty factor of the part of the T.A.C. range of direct interest (480/s* 200 n.s.) the random background gives contributions of up to 10% of the real rate, but this can be subtracted easily.

The γ - flash causes several background effects, and the steps taken to avoid after - pulsing have already been considered. The bremsstrahlung pulse also injects a cloud of positrons in to the environment of the target sample and these form ortho-positronium in air which converts to para-positronium and decays by annihilation with a mean life of about 150n.s.(61) These gamma rays can cause contamination for about 300n.s. after the γ - flash, but because of the long flight paths used this is well before the arrival of the fastest neutrons of interest and is no problem. The effect is also reduced by the present use of small samples and good collimation which limits the volume of air visible.

The most serious background effects arise from the large angular spread of the bremsstrahlung - electron cone because this can directly intersect the $40\frac{1}{2}^{0}$ collimator, causing photoneutron production, and it also hits the shielding wall viewed by the backward flight paths. A small flux of neutrons, multiply scattered from the shielding walls

fig.31

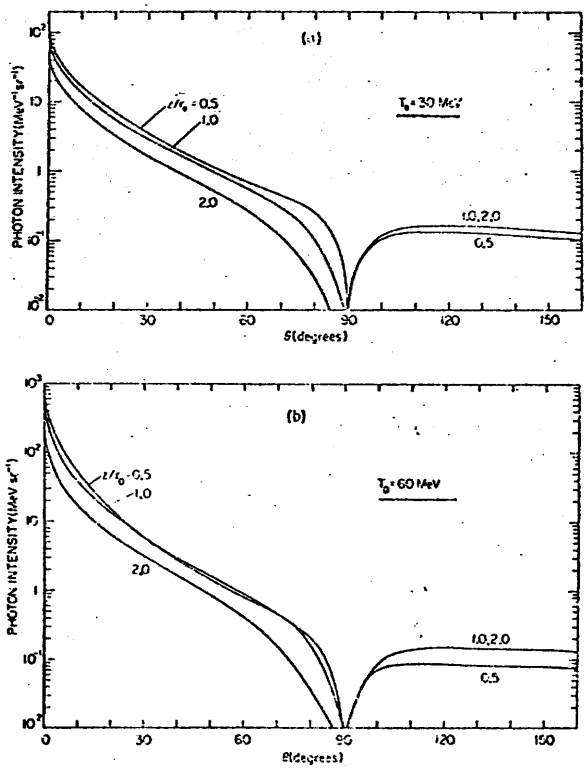

FIG. 5. Calculated bremsstrahlung intensity, per incident electron, as a function of the angle of emergence, for monoenergetic electron beams incident perpendicularly on thick tungsten targets. (a) $T_0 = 30$ MeV, and (b) $T_0 = 60$ MeV.

-FROM BERGER & SELTZER[125]

of the neutron cell is present for all angles but is much less than the random rate and is simply subtracted to good accuracy by target - out measurements.

The bremsstrahlung intensity as a function of angle of emission was calculated for thick (0.5r) tungsten targets by Berger and Seltzer, (125) and their results for an end point energy of 30 M.e.V. are shown in figure 31 where it is seen that the flux at 14^0 and 40^0 is respectively about 10% and $2\frac{1}{2}\%$ of that at 0^0. Although these targets are thicker than those used by the author the end point energy was slightly higher so that the fall off will be similar or slightly quicker in this case. The collimator or wall has a smaller solid angle than the water target by about 100 but the target thickness is increased by about this amount and the final contributions are determined roughly by the bremsstrahlung intensity and are therefore of some significance.

The number of photons reaching the $40\frac{1}{2}^0$ collimator was reduced by putting the lower Z paraffin material inside and by the insertion of 4" lead baffles between the bremsstrahlung target and the collimator entrance. The machine dependent background at this angle was then less than the general radioactive background.

Signal to background was worst at the 156^0 angle. Neutron production in the opposite shielding wall was limited and outscattering of these neutrons was encouraged by inserting one foot of low Z lithium hydride before the concrete but the improvement was slight. A re-entrant cavity in the shielding wall was considered but this would have had to be several feet deep to be useful and would have constituted a

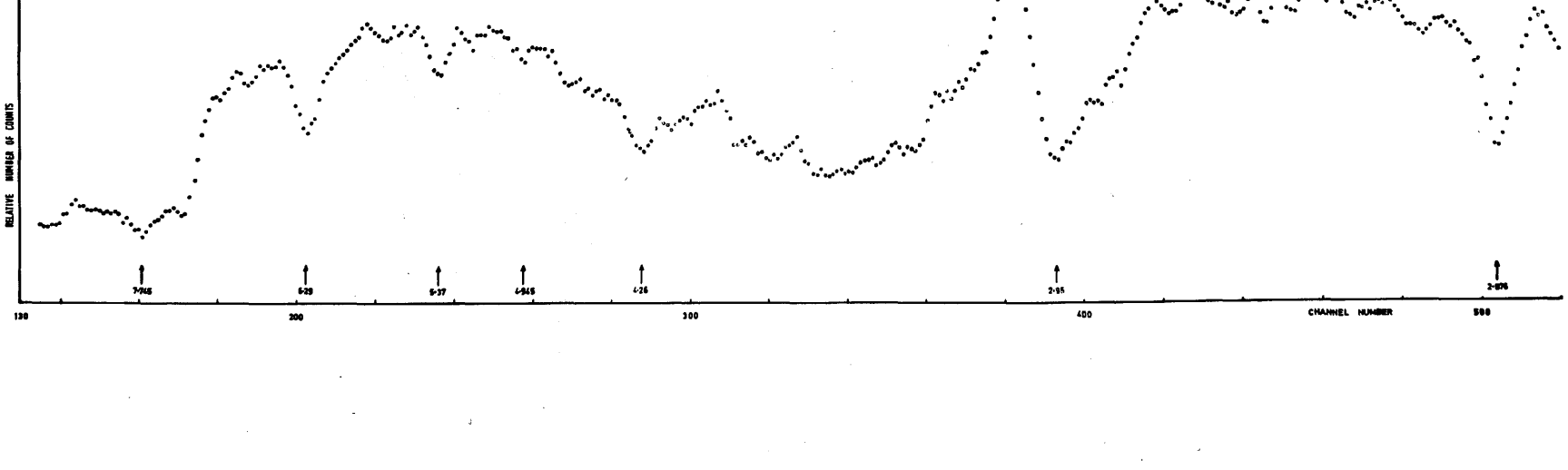
NEUTRON ABSORPTION IN CARBON
FIG. 32.
RELATIVE NUMBER OF COUNTS
7-945
6-29
9-37
4-945
4-26
2-95
2-876
100
200
300
400
CHANNEL NUMBER
500

radiation hazard. The detector at this angle was closest to the accelerator vault and was therefore in a slightly higher d.c. background field due to the residual activity in the energy defining slits in the vault. Since the angular distribution of El d-wave photo - nucleons is $(1+3/2*\mathrm{Sin}^2\theta)$, this angle had the lowest yield and therefore its signal to background in the 5 to 10 M.e.V. time range was worst at 20%. Other angles had much better ratios (5% to 10%).

Backgrounds were subtracted by target in - target out measurements, the relative times allocated to each being optimised for the back angle by the recipe of Browning.(126)

Once count rates with O^{16} were determined and signal to background ratios optimised, a small ($\frac{1}{4}$" x $\frac{1}{4}$") lead target was substituted and normalisation from angle to angle confirmed to first order by comparing (count - background) rates since the lead photoneutron cross section is known to be isotropic in the energy region 1.5 to 3.5 M.e.V. where the yield is maximum.(127)

3.19 Absolute Calibration of Neutron Energies.

Although the energies of the O^{16} peaks are well known, from measurements by several authors (59,60,63) (at one angle), an independent calibration of neutron energy for each angle was essential to make a detailed study of the change in angular distribution across the peaks. This calibration was obtained by observation of the well known levels in the neutron absorbtion spectrum of C^{12} (Al,21-23) A lead target provided a source of neutrons and spectra were taken at all angles simultaneously with 1.5" of graphite in each flight path. A typical spectrum is shown in figure 32. C^{12} has become a standard

for cross section measurement and the energies of the lines are well known. In particular, narrow lines are present at 6.29 M.e.V. and 5.37 M.e.V. just where they are required in this experiment and also at 2.076 M.e.V. The positions of the 4 broader peaks are still helpful however in fitting the absolute energy scale. The method used will be described later.

3.20 Normalisation.

A second set of lead spectra were taken with no C^{12} in the way and the number of counts was integrated between the positions of the 2.076 M.e.V. and 2.947 M.e.V. C^{12} peaks to confirm the normalisation of the six detectors. The beam energy was then re-measured before beginning the run with the water sample.

The counting time for the water target was 63.7 hours and the background was 23.3 hours. These were followed by energy calibrations and a run with a heavy water (D_2O) target closely matched to the original water target in volume (and number of O^{16} atoms). This 1 day run was performed as an extra normalisation for the angular distribution of deuterium photonucleons is well known[123,124] and also as a means of obtaining an absolute cross section value for the O^{16} (γ,n) O^{15} reaction since that of $D_2(\gamma,n)p$ is again known.[123,124] This is equivalent to measuring the absolute bremsstrahlung intensity as a function of energy.

These measurements were followed by another similar one at higher bremsstrahlung end point energy (30.9 M.e.V.) and a 50m. run at 27 M.e.V. but the results of these latter runs will be reported elsewhere.

Chapter 4.

4.1 Introduction.

This chapter describes the energy calibration of the raw T.O.F. spectra and their conversion to C.M. energy spectra and spectra of angular distribution coefficients.

Photons of one energy produce neutrons with different kinetic energies at different LAB. angles and this effect is shown to be observable with the present resolution so that corrections for distortions of the neutron spectrum which depend on the LAB. neutron kinetic energy must be made before conversion to the C.M. in order to avoid systematic errors in the angular distribution data. This requires good resolution information on the detector efficiency and the effect of absorbing materials in the flight paths and the acquisition of this data is described.

Kinematics are presented for conversion of the LAB. energy spectra to the C.M. frame and the interpolation procedure used to find the yield for each C.M. angle at given photon energies is described in some detail. The C.M. spectra are corrected for electroproduction effects before being fitted to a sum of Legendre Polynomials at each energy.

4.2 Background Subtraction.

During data acquisition, the spectra were periodically transferred to magnetic tape by the PDP7 computer and the final spectra were also punched out on paper tape in a format suitable for reading by the PDP-10 computer of this laboratory. Data analysis was performed on this computer by a series of 'FORTRAN' programmes written by the author.

The first such programme simply allowed each paper tape to be read

in to memory, and the spectrum could then be displayed on a C.R.T. monitor, printed out and transferred to PDP-10 magnetic tape for compact storage and easy access by other programmes. The data stored consisted of 3*1024 channel spectra for each of the six angles (a water run, a heavy water run and an empty target (background) run for each).

Normalisation factors between different runs were obtained from the monitor readings and the PDP7 typeout and this allowed the backgrounds to be removed in a second programme by direct subtraction of the T.O.F. spectra, since the time calibration was constant from run to run.

4.3 Energy Calibration of T.O.F. Spectra and Spectrum Alignment.

The time of flight (T) of a neutron group is obtained from its channel number (X) in the spectrum by the linear relationship

$$T = T_z + A*X \qquad 4.3.1$$

where T_z is the time corresponding to channel zero and A is the calibration of the T.A.C. - A.D.C. combination in n.s. per channel. T_z and A were unaltered throughout the series of 26.9 M.e.V. irradiations so that background subtraction was simplified.

The value of A was obtained firstly from the measurement of integral linearity by the gated oscillator method as discussed in section 3.13 and secondly by fitting the calculated T.O.F. values of the C^{12} absorbtion lines to the corresponding channel numbers observed in the lead-C^{12} spectra taken for each run. This also provided an absolute energy calibration (=T_z value) for each spectrum section. T_z could have been obtained by switching in a known delay in to the start channel and so putting the γ-flash on-scale but this required a

calibrated delay of 500ns to bring the γ-flash well on to the linear region of the T.A.C. range and it was not used.

Energies of C^{12} absorption lines have been obtained from references (A1.20-23) and these are reproduced in Table 5. The error assigned to each line is an estimate by the author of the maximum possible error in the assignment of the energy of the peak of the line, obtained by comparison of the two sets of data and by consideration of the sharpness of the line. Since the present energy resolution is between 50 and 100 k.e.V. in the 5-10 M.e.V. range of neutron energies the C^{12} absorption spectrum provides an excellent calibration, especially if several lines are used.

The calibration was performed by a computer programme written by the author which reads in the flight path length (measured to ∠2cm in 20m.) and then the energy of each C^{12} line and its possible error followed by its observed channel number (estimated to $\frac{1}{4}$ channel) and the estimated error in assignment of this channel number. A preliminary value of A (ns./channel) is calculated from two of the sharper lines and this is used to calculate all the errors associated with each point in terms of the time variable, before a least - squares fit is made to the straight line of equation (4.3.1) passing through the channel numbers and calculated T.O.F. values. Values of A and T are produced with errors and typical results are (40^{o})

$$A = 1.4180 \pm 0.0070 \text{ ns/channel.}$$

$$T_z = 264.85 \pm 2.852 \text{ ns}$$

The value of A obtained from the gated oscillator method was inside the error assigned to A from the C^{12} calibration eg., for this ($40\frac{1}{2}^{o}$)

Energies of neutron absorption resonances in C^{12} Table 5

E peak (M.e.V.)	2.076	2.950	4.260	4.945	5.370	6.290	7.745
± error k.e.V.)	2.	10.	30.	10.	7.	7.	35.

Deviations of resonance peaks from fitted line Table 6

E peak (M.e.V.)	2.076	5.370	6.290	7.745
Estimated error (n.s.)	0.7	1.1	1.0	2.0
R.M.S. deviation of measured points (n.s.)	0.57	1.26	0.55	2.0
equivalent R.M.S. energy deviation (keV)	2.48	21.5	11.7	60.4
Estimated R.M.S. energy deviation (keV)	2.80	18.7	21.5	60.4

line

$$A\ (\text{oscillator}) = 1.422\ \text{ns/channel.}$$

The error in T_z appears large but this is merely because the calibration points are all distant from T_z. The error in the absolute calibration in the interesting region is provided by programme output of the deviations of each calibration point from the fitted line.

Table 6 shows the R.M.S. deviations of several C^{12} lines from the six spectra in n.s. and in energy. The results show R.M.S. deviations inside the errors estimated from the accuracy of knowledge of the energies and the accuracy of assignment of the measured channel numbers. Consideration of the deviations of the sharper lines demonstrates that the energy calibration technique is acceptable and the spectra from different angles are aligned to better than 1 channel.

4.4 Conversion from T.O.F. to LAB. Energy.

Since a computer was used to analyse the data it was possible to use relativistic kinematics throughout the calculations. The spectra were converted to energy spectra in the LAB. using the calibrations of the last section and the known flight path lengths(D) which ranged from 19.93m. to 20.11m. The calculation proceeded in the following way:

channel number $\rightarrow$ T.O.F. $\rightarrow \beta = D/(T.O.F.*C) \longrightarrow \gamma = 1/\sqrt{1-\beta^2}$

kinetic energy = $Tn = m_n*(\gamma-1)$

The data was collected in equal time bins which do not convert to equal energy bins (equation 1.6.3) and the measured yield per channel (dN/dt) was converted to an energy spectrum (dN/dE) by the relation

$$\frac{dN}{dE} = \frac{dN}{dt}\ \frac{dt}{dE} \qquad (4.4.1)$$

where dt/dE was obtained from equation (1.6.3). The statistical error per channel was taken as that in the T.O.F. spectrum for that channel and stored as a percentage.

The above procedure was followed in early programmes for each of the 1024 data points and output data was produced in the form of 1024 channels each of energy, dN/dE and error. This data was then consulted by a following programme which converted to the C.M. frame. The intermediate output allowed checking of the programme by hand calculation.

It will be shown in the next section that a proper treatment of the (LAB-CM) conversion requires knowledge of several LAB quantities which need not be permanently stored if the process is performed in one continuous operation. Although the author's programme now converts directly to the C.M. frame the corrections and kinematics involved will be described more clearly as separate stages.

4.5 Laboratory to Centre of Mass Transformation

Consider a nucleus of mass number A, mass Ma which after absorbing a photon of energy k emits a neutron of kinetic energy Tn, rest mass Mn, in a direction making a laboratory angle θ with the photon beam. If Q is the binding energy of the neutron in nucleus A and the rest mass of the nuclear recoil is Mr then conservation of energy and momentum allow k to be calculated from the other known quantities:

$$k = \frac{Tn*(1+(Mn-Q)/Mr) \; + \; Q*(1-(Q/(2*Mr))}{1 - (Tn + Q)/Mr \; + \; (Tn(Tn+(2*Mn))^{1/2} * (\cos\theta/Mr)} \qquad 4.5.1$$

Following the relativistic kinematics of references 130 and 131 for the particular case of the zero mass photon as incident particle, the total

energy of the system in the C.M. may be expressed as

$$\bar{E}t = \sqrt{Ma((2*k) + Ma)} \qquad (4.5.2)$$

and the C.M. photon energy (excitation energy) becomes

$$\bar{k} = Ma * k/\bar{E}t \qquad (4.5.3)$$

The total energy of the neutron in the C.M. is

$$\bar{E}n = \frac{\bar{E}t^2 + Mn^2 - Mr^2}{2 * \bar{E}t} \qquad (4.5.4)$$

If the motion of the C.M. is described with respect to the LAB. by Γ and $B^{(=V_{CM}/c)}$ where $\Gamma = 1/\sqrt{1-B^2}$, and if KL = B/β where cβ is the neutron velocity in the LAB. then the C.M. angle of neutron emission ($\bar{\theta}$) is given in terms of the LAB. angle θ by:

$$\tan\bar{\theta} = \frac{1}{\Gamma} \cdot \frac{\sin\theta}{\cos\theta - KL} \qquad (4.5.5)$$

$\bar{\theta}$ will vary with neutron energy (unlike θ) and must be stored as a separate variable for each energy point. The solid angle subtended by a detector also varies with angle and energy in the C.M. reference frame and the data must be corrected for this effect. In an obvious notation:

$$\frac{d\sigma}{d\Omega}\Big/\frac{d\bar{\sigma}}{d\bar{\Omega}} = \frac{d\bar{\Omega}}{d\Omega} = \frac{\sin^3\bar{\theta}}{\sin^3\theta \cdot .(1+K*\cos\bar{\theta})} \qquad (4.5.6)$$

where K is B/$\bar{\beta}$ and c$\bar{\beta}$ is the velocity of the neutron in the C.M.

The order of the angular correction is greatest at $86\frac{1}{2}^{o}$ where the change is 5^{o} for Deuterium spectra and 1^{o} for O^{16}. The D^2 effect is a significant fraction of the angular resolution ($\pm 7^{o}$).

Solid angle changes are greatest at the more extreme angles and are of order 2% and 17% for O^{16} and D^2 spectra respectively.

A monoenergetic beam of photons of energy k will produce "n" neutrons into the detector cone with a fixed kinetic energy T_n determined by the kinematics of the reaction. If N_o is the number of scattering centres per cm^2 and $n\gamma(k)$ is the number of incident photons normalised to unit flux, then

$$n(T_n) = N_o n\gamma(k) \left(\frac{d\sigma}{d\Omega}\right)_{k,\theta} d\Omega \qquad (4.5.7)$$

In the present case, the number of counts is classified by T.O.F. or kinetic energy and the detector efficiency $\varepsilon(T_n)$ and the effect of absorbing materials in the flight path $\lambda(T_n)$ must be included, so that,

$$\frac{dn}{dT_n} = \frac{dn}{dt} * \frac{dt}{dT_n} = N_o \cdot \frac{dn\gamma}{dk}\frac{dk}{dT_n} \cdot \left(\frac{d\sigma}{d\Omega}\right) \cdot d\Omega\ \lambda(T_n)\ \varepsilon(T_n) \qquad (4.5.8)$$

and,

$$Y = \left(\frac{d\sigma}{d\bar{\Omega}}\right)_{k,\theta} * \frac{dn\gamma}{dk} = \frac{1}{N_o}\left(\frac{dn}{dt}\frac{dt}{dT_n}\right)/\left(\frac{d\bar{\Omega}}{d\Omega}\frac{dk}{dT_n}\lambda(T_n)\varepsilon(T_n)d\Omega\right) \qquad (4.5.9)$$

Since all the other quantities are known or calculable from the previous equations, values of differential cross section at each angle may be accumulated as a function of the LAB photon energy (or the excitation energy of the nucleus or the C.M. energy of photon or neutron since a one-to-one correspondence exists between these). This information plus the value of the C.M. angle at each energy point is that needed for angular distribution assignments. If the same photon energy is used for all angles the bremsstrahlung spectrum value $\frac{dn\gamma}{dk}$ is common and need not be known for determination of the relative angular distributions. It may be inserted to give the correct scale and energy dependence for the absolute cross section (i.e. the A_o coefficient in the expansion of equation (4.14.1)).

Table 7 Nuclear Masses.

(a) Mass excesses (from Ref. 19)

particle	M - A (M.e.V.)	error (M.e.V.)
n	8.07144	$1.0*10^{-4}$
p	7.28899	$8*10^{-5}$
d	13.135,91	$1.3*10^{-4}$
$^{16}_{0}$	-4.736,55	$2.6*10^{-4}$
$^{15}_{0}$	2.859,9	$1.2*10^{-3}$
$^{15}_{N}$	0.1004	$8*10^{-4}$

(b) Q values for photodisintegration (from (a))

Reaction	Q value (M.e.V.)	error (M.e.V.)
O^{16} (γ,n) O^{15}	-15.668	.0012
O^{16} (γ,p) N^{15}	-12.1259	.00085
D^{2} $(\gamma,n)p$	-2.2245	.0001

(c) 1 a.m.u. = 931.4812 M.e.V. from References 20,21.

The quantity $\frac{dn\gamma}{dk}$ may be found by a measurement under the same conditions of the T.O.F. spectrum from $D_2(\gamma,n)p$ as already described, using equation 4.5.9 with the known value of the differential cross section for Deuterium. In fact the angular distribution assignments were made for both nuclei in terms of 'Y' and the absolute values of differential cross section for Oxygen were obtained more accurately by comparison of the total cross-sections so derived.

Note that the correction factor $\lambda(T_n)\mathcal{E}(T_n)$ and its associated errors appear twice in this process (at different 'T' values for the same 'k'). This is the main motivation for extracting the angular distribution data before inserting the bremsstrahlung spectrum.

The values of nuclear mass constants used in the author's calculations are shown in Table (7).

4.6 Kinematic effects in the LAB. frame.

It can be seen from equation (4.5.1) that one excitation (γ) energy in the LAB. (or C.M.) is not represented by equal LAB. neutron energies at different angles. The order of the effect may be written as:

$$\frac{\Delta k(\theta)}{k} = (.046*(\sqrt{Tn}) / (A-1))*(\Delta\cos\theta) \qquad (4.6.1)$$

so that in the middle of the giant resonance in O^{16} (where 6 M.e.V. neutrons correspond to 22 M.e.V. photons) the change in photon energy Δk is about 300 k.e.V. for the present angular range ($\Delta\cos\theta = 1.73$). This is about 3 times the resolution of the present experiment and therefore the effect of phenomena with a strong dependence on the LAB. neutron kinetic energy ($\lambda(T),\mathcal{E}(T)$) must be removed before conversion to

the C.M. if systematic errors are not to result. In $D^2(\gamma,n)p$ spectra 22 M.e.V. photons produce ~10M.e.V. neutrons but the change in neutron energy from forward to back is 6 M.e.V. so that a good knowledge of all distortions of the LAB. spectra is essential for evaluation of the $D^2(\gamma,n)p$ angular distribution and for the derivation of the bremsstrahlung spectrum. We note again that the assignment of an absolute cross section to the $O^{16}(\gamma,n)O^{15}$ reaction using this spectrum involves two separate applications of the correction spectrum. $(\lambda(T_1)\varepsilon(T_1)\lambda(T_2)\varepsilon(T_2))$

The author decided to obtain this information at 100 k.e.V. intervals over all the range of neutron energies measured (1.0 to 16 M.e.V.) since this matched the resolution of the experiment in the useful 5-10 M.e.V. region and each T.O.F. channel would be well corrected by extrapolation between these stored values. This procedure was also adopted for neutrons of lower energy, for these did not represent ground state transitions in the $O^{16}(\gamma,n)O^{15}$ reaction and the main use of this data was for (D_2O-H_2O) subtraction and the calculation of D_2 (γ,n) spectra for which this resolution was adequate.

The two effects which depend strongly upon the kinetic energy of the neutron in the LAB. frame are the attenuation of neutrons by materials in the flight paths $(\lambda(Tn))$ and the detection efficiency of the neutron counter. $(\varepsilon(Tn))$

4.7 Efficiency of Neutron Detectors

High efficiencies are available for fast neutron detection by organic scintillators because of the high n-p cross section in this energy region and the good density of hydrogen atoms in these devices.

DETECTOR EFFICIENCY CURVE

Fig. 33

FROM O'DELL et al [122]

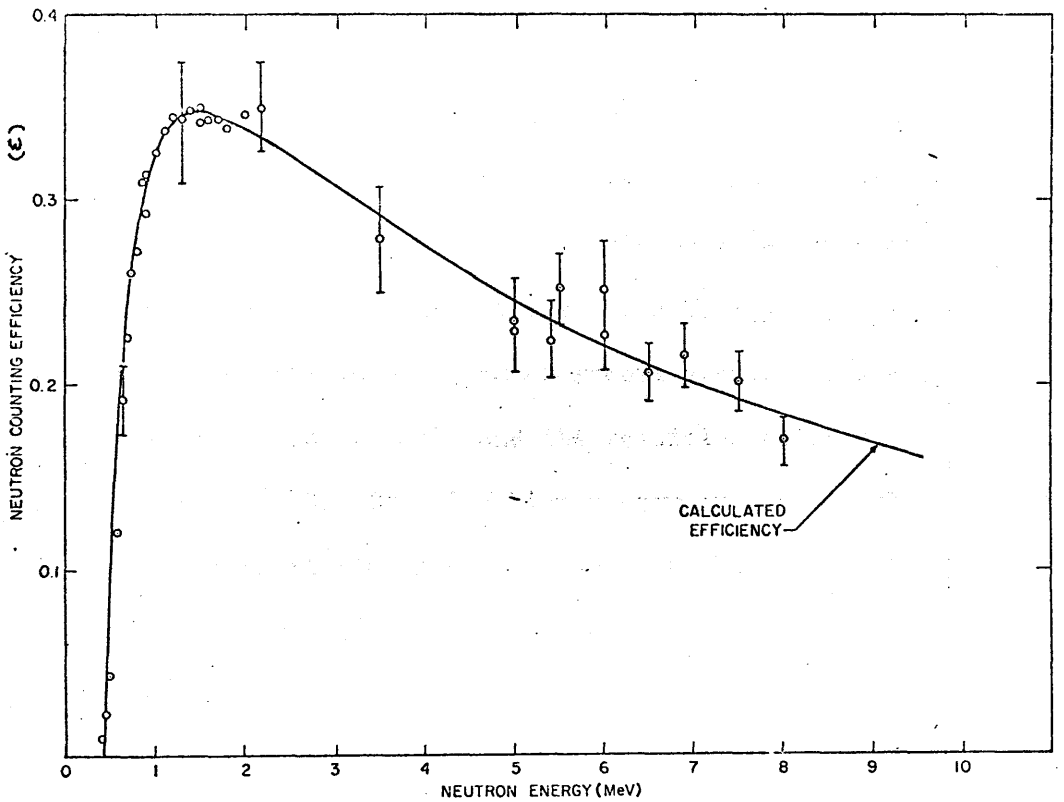

Comparison of measured and calculated efficiency for a 2" dia. by 2.5" thick NE 213 neutron detector biased at 425 keV.

$$\varepsilon = \{n_H\sigma_H/(n_H\sigma_H+n_C\sigma_C)\}\cdot \cdot\{1-\exp[-(n_H\sigma_H+n_C\sigma_C)t]\}\{1-(B/E)\},$$

where

n_H = hydrogen atoms per cm^3;
n_c = carbon atoms per cm^3;
σ_H = total n-p cross sections;
σ_c = total inelastic carbon cross section;
t = average scintillator thickness;
B = neutron energy bias;
E = neutron energy.

The n-p cross section varies smoothly with energy but the presence of Carbon in the material introduces a rapidly fluctuating cross section which prevents the efficiency curve being smooth. Detector efficiencies are often required just to enable the shape of the spectrum to be adjusted by the general trend in energy (dominated by the Hydrogen cross section) and approximate efficiency formulas suffice. In one of the more successful of these,(122) the efficiency is taken as the product of the stopping power, the probability of a Hydrogen collision and the probability of obtaining a proton recoil greater in energy than the detector bias. The formula and the resulting efficiency curve are shown in figure 33. By using fine energy increments this formula can take the Carbon fluctuations in to account but it does not consider multiple scattering in the scintillator nor any of the smearing processes involved in the detection of proton recoils so that the estimate is not quantitative.

More precise efficiency calculations require Monte Carlo simulation of the physical processes and usually do not provide good energy resolution or statistical accuracy because of their heavy demand on computer time. (A1,15-17) However, the author has used the Monte Carlo technique to obtain efficiency values at closely spaced energies from threshold ($\frac{3}{4}$ M.e.V.) to 16 M.e.V. with good statistical accuracy and with small estimated errors. (2% - 4%) This required a considerable amount of new work by the author, including an accurate measurement of the scintillation response to recoil protons in the scintillators Ne211, Ne213 and Ne 102A, and consideration of several features of the detector assembly which are normally neglected. This whole project is

FIGURE 34

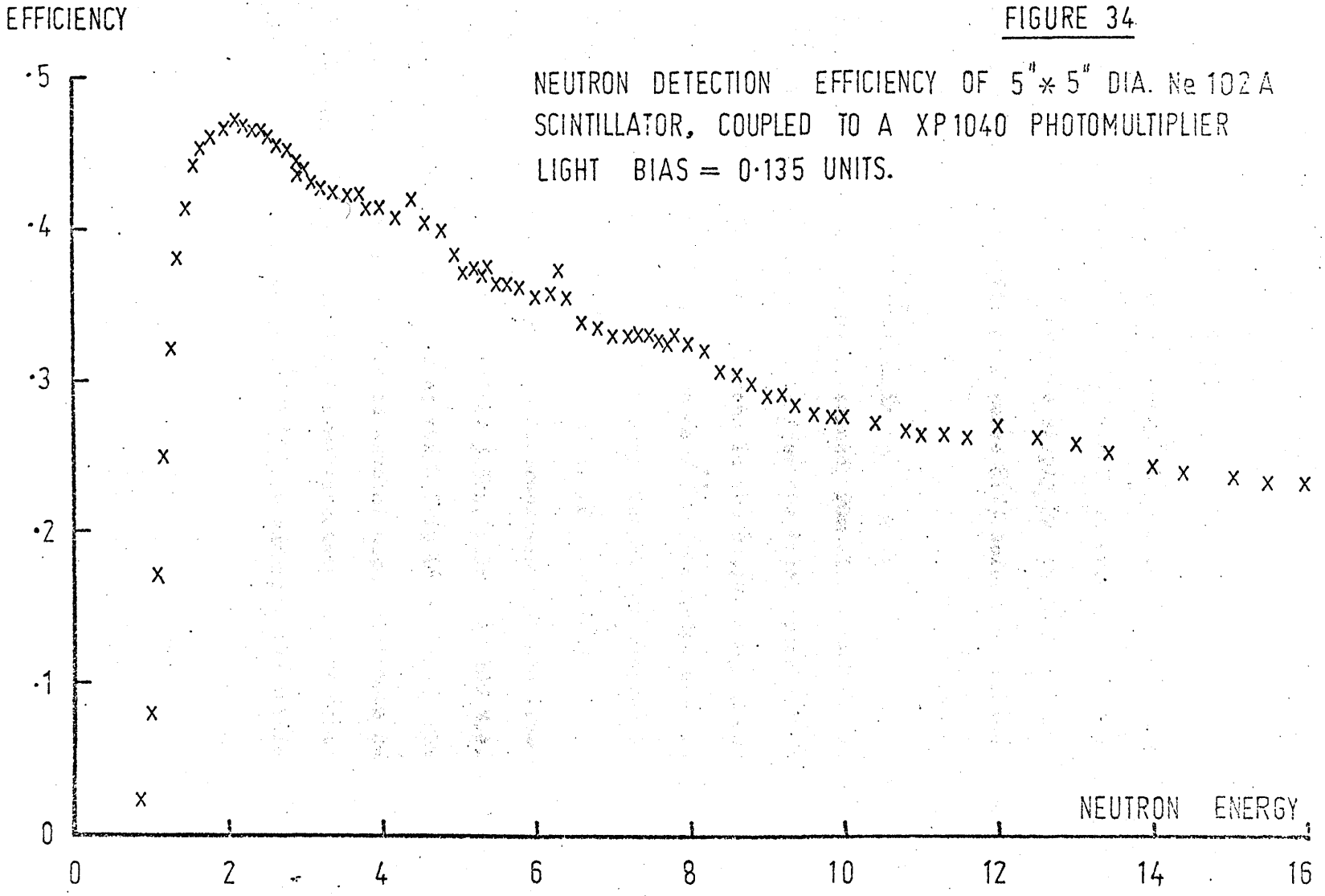
EFFICIENCY
NEUTRON DETECTION EFFICIENCY OF 5" * 5" DIA. Ne 102 A SCINTILLATOR, COUPLED TO A XP1040 PHOTOMULTIPLIER
LIGHT BIAS = 0·135 UNITS.
·5
·4
·3
·2
·1
0
NEUTRON ENERGY
0
2
4
6
8
10
12
14
16

presented as Appendix 1. (A1).

The results of the efficiency calculations for the 5" dia. by 5" thick Nel02A scintillators used in the author's photoneutron experiment, are presented in figure 34 where it is seen that significant changes in efficiency do occur inside 300 k.e.V. intervals and the correction is indeed required. This is made simply by dividing the spectrum at any LAB. angle by the efficiency curve $\varepsilon(T)$ before conversion to the C.M. frame.

4.8 Neutron Attenuation in Air.

All the flight paths contained 20m of air and the air attenuation factor was calculated directly from the total cross sections[129,A120-23] of O^{16} and N^{14} for fast neutrons in the energy range where both were known (up to 4 M.e.V.). Since no N^{14} data existed with the required energy resolution above this energy, the author has measured the neutron attenuation in air by the T.O.F. method.

An intense source of fast neutrons was obtained from a 3 radiation length lead target irradiated by 3.5ns. pulses of 100 M.e.V. electrons from the linear accelerator of the Kelvin Laboratory. The multiangle T.O.F. spectrometer has allowed several high resolution neutron physics experiments to be carried out simultaneously on different flight paths using such a pulsed source.[115,116] For example, the author measured the effect of having 22.8m of air in the (otherwise evacuated) 53m. flight path while the total cross section of P^{31} was measured on one of the backward flight paths.[128] Experimental monitors were common to both experiments. (These were neutron detectors on other lines).

The main detector at 53m was a 2" dia. x 1" thick Nel02A plastic

scintillator coupled to a 56 A.V.P. photomultiplier with C.F.P.H. electronics as already described, and a second similar detector was placed some 6' away (and just in the neutron beam) to confirm the stability of the first. Small detectors were used on $2\frac{1}{2}$" dia. 56 A.V.P. tubes to give good time resolution and decrease the effects of the intense γ-flash generated by the increased electron energy and the increased Z of the target. The author found that 56 A.V.P. photomultipliers were much superior to the larger (XP1040) ones in such conditions (for the same photon input to the photocathode) since they could withstand pulses some 20 times greater for the same production of after-pulsing. The after-pulses arrived well before the fastest neutrons of interest at this distance so that they did not contaminate the neutron spectra and the number of such pulses was made small by absorbing most of the low energy photons in $\frac{1}{2}$" of lead placed in the beam line 4' from the lead neutron target.

2048 channels were used to cover the 4μs. conversion time needed for neutrons down to 0.5 M.e.V. and this combined with the 3.5ns beam width to give a resolution of 0.075 ns./m at 53.4m and energy resolutions of 6,16,30 and 54 k.e.V. for 2,4,6 or 9 M.e.V. neutrons respectively. The count rate was limited by the need for pile-up corrections to one every ten beam bursts, or 48 per second, and more than 4000 counts per channel were obtained in two-day runs. The target-in and target-out runs had a difference of 22.8m of air which was calculated to give about 20% absorbtion and to duplicate the 20m. used in the angular distribution experiment as closely as was possible, in the evacuated line. About 10% statistical accuracy per channel was

EFFECT OF AIR IN FLIGHT PATHS ON NEUTRON SPECTRA

Fig. 35

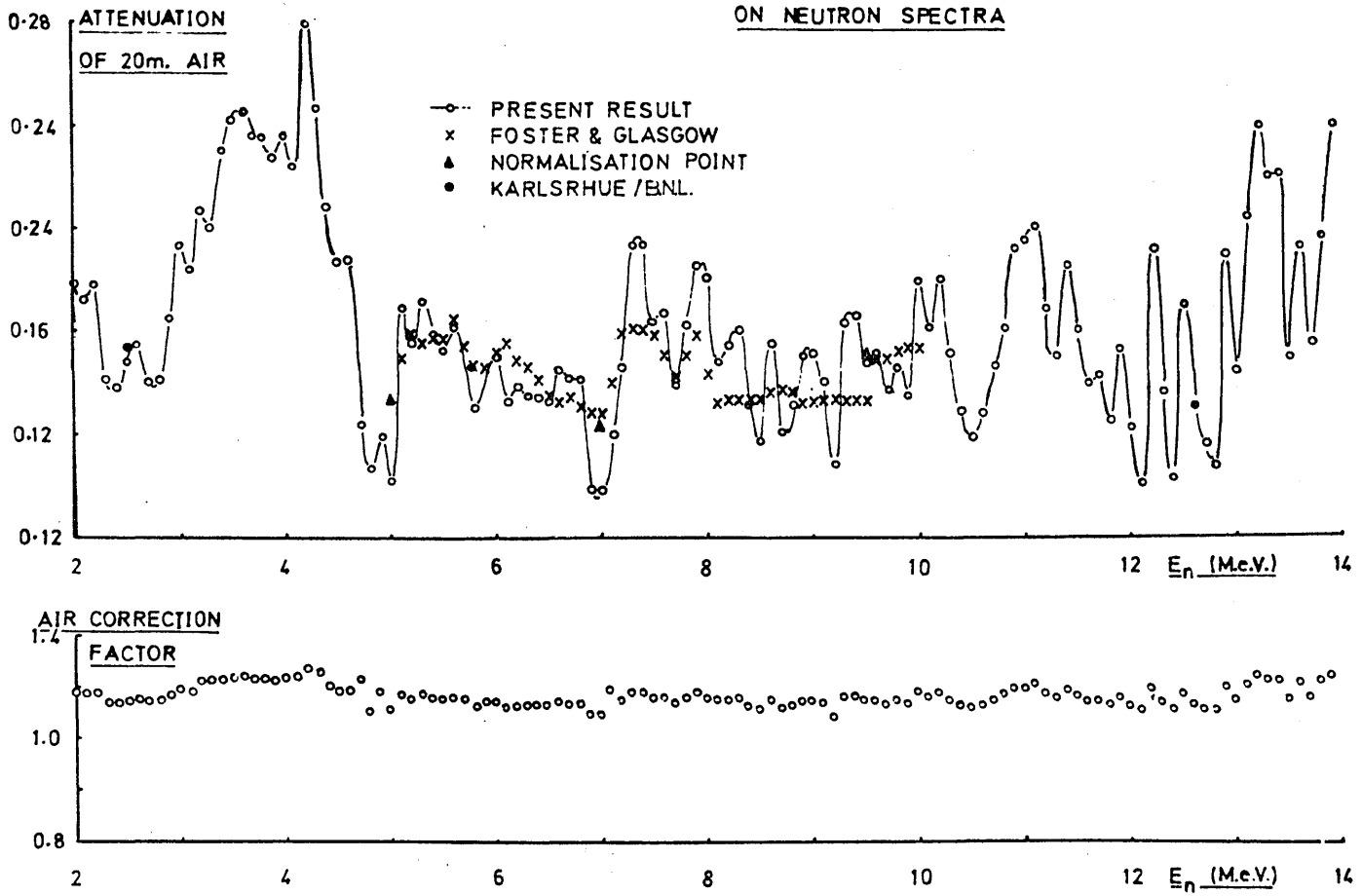

obtained and the results are shown in figure 35 where the correction factor has been normalised to the values obtained from references Al, 21-23 in the energy regions of overlap.

The attenuation factors for 20m. air at 100 k.e.V. intervals from 1.0 to 16.0 M.e.V. were extracted from this data by a programme written by the author to find the average attenuation in a bin extending 50 k.e.V. below and above each chosen energy. The integral number of channels was found between the upper and lower limits and the final attenuation was taken as the average of the contributions from each channel and the fractions of a channel at each end. In this way several channels were added for each output point and the statistical accuracy was improved to less than 5% (3.5%) for neutron energies below 10 M.e.V. (5 M.e.V.). Since the air effect is between 15% and 20% for 5-10 M.e.V. neutrons the residual errors should be less than 1%.

4.9 Neutron Attenuation in Lead and Water

The effect on the neutron spectra of the 1/8" lead filter in each flight path was removed by using the good resolution total cross section data of reference 132. Since the attenuation was less than 5% for the neutrons above 4 M.e.V. and the errors in the cross section are below 10%, the residual errors should be small.

The attenuation of neutrons in the water sample was calculated (assuming that all neutrons are produced in the centre of the target) using the total cross section data of references (Al,21-23). This data is accurate to <1% for Hydrogen and to <3% for Oxygen because the bins used here are wide compared to those in the original data and the average cross section in each bin was used. The original attenuation

FINAL CORRECTION TO NEUTRON SPECTRA

Fig. 36

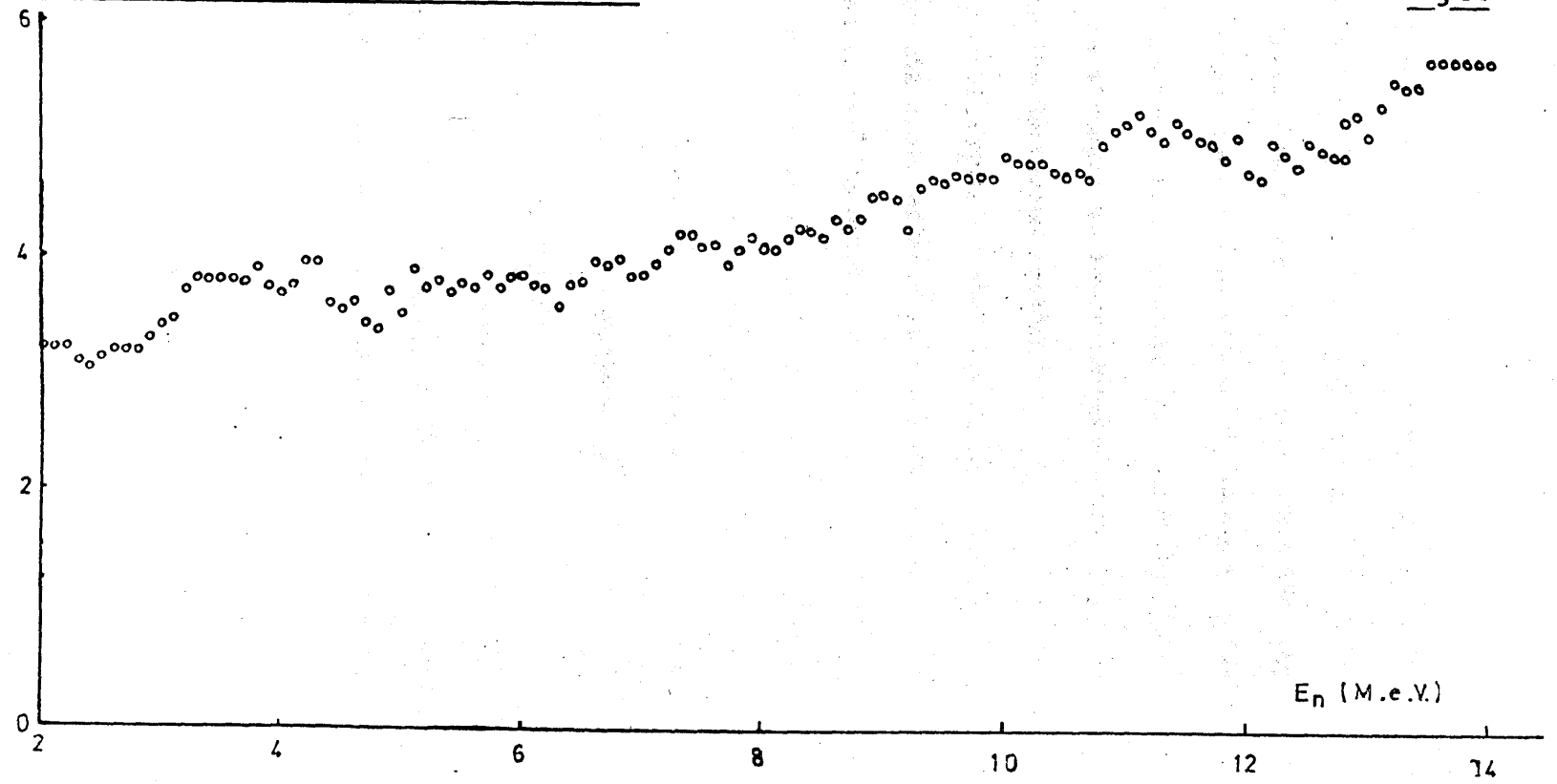

was = 10% so that the residual errors in treating this effect should be negligible (=3% of 10%).

4.10 Corrections to the LAB. spectra

The final value of correction factor $\lambda(T)\mathcal{E}(T)$ for each energy bin was computed by a small programme from the input of the combination of effects just given then stored in the main kinematics programme. The correction spectrum is shown in figure 36 where it is seen to be fairly smooth in the 5-10 M.e.V. region. Variations in neutron attenuation are stronger at lower energies, and the correction is more important for the Deuterium spectra.

The number of counts in each T.O.F. bin is corrected for the bin width and for the above effects as its LAB. energy is found. Linear interpolation is used to obtain the correction factor from the stored values and since the variations between adjacent values are fairly small the interpolation procedure does not introduce a significant error. Errors in $\lambda(T)\mathcal{E}(T)$ are dominated by those in $\mathcal{E}(T)$ and therefore have values between 2% and 4% (Appendix 1).

4.11 Conversion from LAB. to C.M.

The number of counts per unit energy in the LAB. (dN/dE) is corrected as above and stored temporarily while the kinematic parameters of section 4.5 are calculated. The LAB. neutron energy and angle of detection determine the LAB. γ energy which leads to the C.M. values of γ and neutron energy if required. The C.M. angle of detection and the solid angle correction require calculation of the quantities Γ, KL and K which follow from the energies already found. This allows the final value of 'Y' to be calculated (assuming $dn\gamma/dk = 1$ at this stage) and

Energy Interpolation Procedure. Table 8

(a) O^{16} Case: Final Spacing = 50 k.e.V. Field = 18 to 32 M.e.V.

Energy Bin (M.e.V.)	18.0 18.5	18.5 19.0	19.0 20.0	20.0 22.0	22.0 27.0	27.0 37.0
Fine Energy Interval (k.e.V.)	2.5	2.5	5.0	10.0	25.0	50.0
Number of points per energy bin	200	200	200	200	200	200
Number of points per 50 k.e.V.	20	20	10	5	2	1

(b) D^2 Case: Final Spacing = 100 k.e.V. Field = 4 to 27 M.e.V.

Energy Bin (M.e.V.)	4. 5.	5. 6.	6. 8.	8. 12.	12. 22.	22. 27.
Fine Energy Interval (k.e.V.)	5.0	5.0	10.0	20.0	50.0	100.0
Number of points per energy bin	200	200	200	200	200	200
Number of points per 100 k.e.V.	20	20	10	5	2	1

this is stored as a function of excitation energy along with the values of the statistical error, and the emission angle in the C.M., before repeating the whole process (from channel number to C.M. parameters) for the next channel. Including the input spectrum, 6*1024 storage locations are required for this stage of the processing.

4.12 Conversion to Common Energy values in the C.M.

The angular distribution at any photon energy is determined by knowledge of the C.M. differential cross section at the different C.M. angles. The data is not taken at a common set of photon energies at each angle and this information is obtained at 50 k.e.V. intervals by the following interpolation procedure.

Straightforward interpolation at the required energies would not use all the information in the spectrum at low energies where there are many channels between 50 k.e.V. points, so that the interpolation was done at smaller energy intervals in these regions with a spacing approximately equal to that in the original and these results were averaged to produce the final 'Y' value for each 50 k.e.V. point. The scheme used is shown in Table 8.

The value of Y for each energy was obtained by quadratic interpolation between the 3 nearest original channels and the error in this was taken to be that of the nearest original data point. The scattering angle is averaged in a similar way. The final error in Y at each 50 k.e.V. point is naturally smaller than that at each component energy.

The output of the computer programme written by the author to perform this procedure is in the form of values of Y, error and C.M.

Virtual Photon Spectra for a Point Nucleus. Table 9

(1) Definition: $N = \sigma_T(\gamma) / \sigma_T(e^-)$

(2) Sum of Transverse and Longitudinal terms. $N(p,w) = N^t(p,w) + N^l(p,w)$

(3) Notation: energy, momentum of incident e^- = e,p

energy, momentum of scattered e^- = e',p'

m = electron mass, α = fine structure constant.

$A = (e^2 + e'^2)/p^2$ $\quad B = \ln((ee' + pp' + m)/m(e-e'))$

$C = (e + e')^2/2p^2$ $\quad D = \ln((p+p')/(p-p'))$

(4) Results.

Transverse El: $N(p,w) = (\alpha/\pi)(AB - CD - (p'/p))$

Transverse Ml or E2: $N(p,w) = (\alpha/\pi) AB$

Longitudinal El: $N(p,w) = (\alpha/\pi)(CD - p'/p)$

Longitudinal E2: $N(p.w) = (\alpha/\pi)(8/3)\, p'^2/(e-e')^2$

Longitudinal Ml: $N(p,w) = 0$

angle at 50 k.e.V. intervals of LAB. photon energy up to the bremsstrahlung end point. Including the input spectrum, 6*1024 storage locations are required for this stage of the processing and the results are stored on magnetic tape, so that the data from all six angles may be read in by another programme which makes the angular distribution assignments.

4.13 Electroproduction Corrections.

The number of electrons incident on the photoneutron target was shown in section 3.6 to be about five times the number of incident photons. The relative number of electrons and photons emerging from the target is 7:1 and the geometry has been chosen to select most of the photons and less of the electrons which form a wider cone. (The average scattering angle is greater for electrons by $\sqrt{2}$.) The factor used in the following calculation of electroproduction effects for the present target geometry was:

$$\text{Relative flux on Photoneutron Target}\left[\frac{\text{electrons}}{\text{photons}}\right] = \frac{5.7(+.6)}{1} \qquad (4.13.1)$$

The ratio of the total cross-section for the electron process to that for the corresponding photon process can be calculated from the interaction between the scattering system and the field produced by the scattered electron.[51] This ratio is expressed as a function of energy by the longitudinal and transverse virtual photon spectra which depend on the matrix elements of the corresponding nuclear current operators. The virtual photon spectra for various multipoles up to E2 have been presented by Bishop[51] for the case of a point nucleus (or a real nucleus in the long wavelength limit $kR \ll 1$) and these expressions (reproduced in Table 9) were used to calculate the electroproduction effects in this

FIGURE 37 VIRTUAL PHOTON SPECTRA FOR 27·0 MeV ELECTRONS

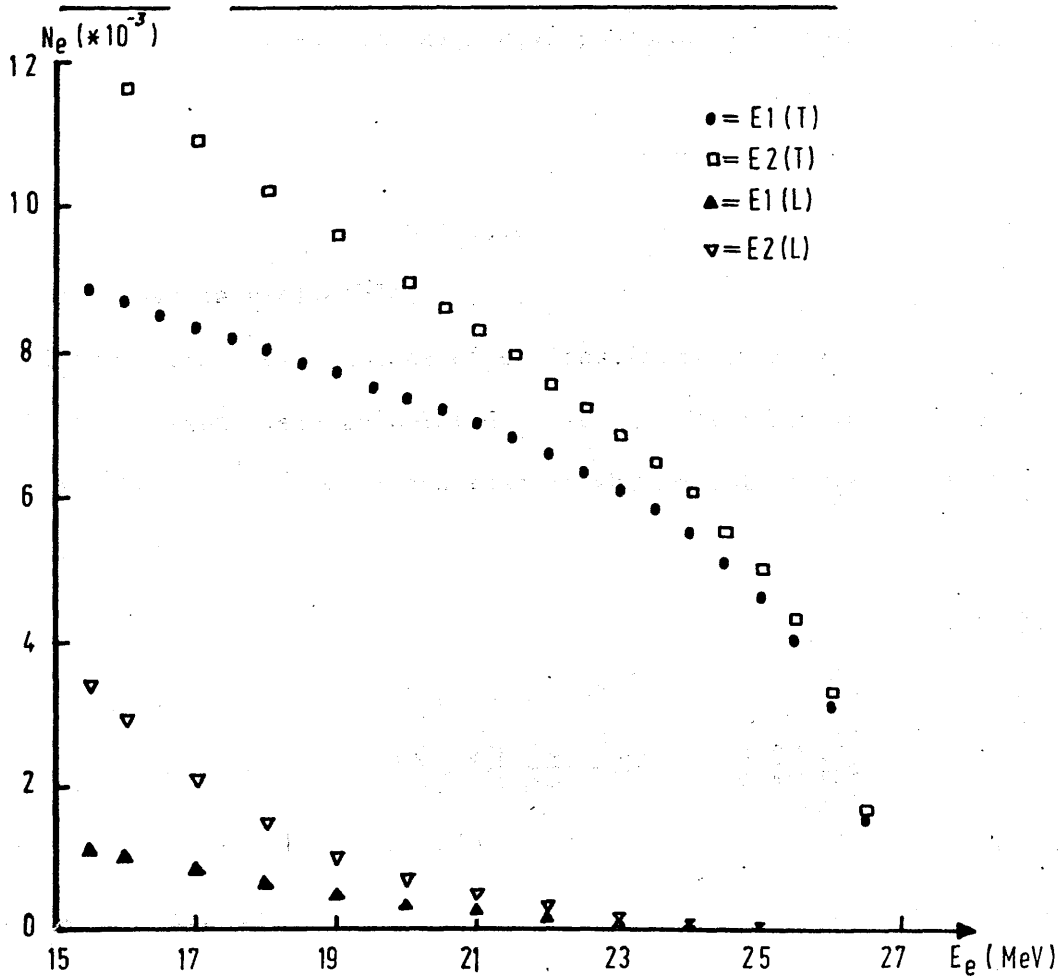

case.

For real nucleii, the currents must be multiplied by the form factor (51)

$$F(k) = 1 - 1/6\ k^2\langle r^2\rangle \qquad (4.13.2)$$

where $\langle r^2\rangle^{1/2}$ is the R.M.S. radius of the system and

$$\langle r^2\rangle^{\frac{1}{2}} = R = 1.2*A^{1/3}\ \text{fm.} \qquad (4.13.3)$$

For $0^{16}_{,}$ R is 3.0 fm. and for 27 M.e.V. photons, k is 0.018 fm.^{-2} so that

$$F(27) = 1-1/6\ (.018)^2*3^2$$

$$= 1-0.0006 \qquad (4.13.4)$$

and the change is negligible.

Theoretical distributions of photonucleons produced by El photon or electron events were calculated in the long wavelength limit by Bosco and Fubini[133] who found that if the angular distribution from photoproduction were:

$$\frac{d\sigma}{d\Omega} = \alpha+\beta\ \sin^2\theta \qquad (4.13.5)$$

then that from electroproduction would be

$$\frac{d\sigma}{d\Omega} = C\left[\left(\frac{e^2+e'^2}{ee'}\lambda - 2\right)\alpha + \frac{e}{e'}\beta + \left(\left(\frac{e^2+e'^2}{ee'}\lambda - 2\right) - \frac{3}{2}\frac{e}{e'}\right)\beta\cdot\sin^2\theta\right]$$

where $\lambda = \ln\ (2\,ee'/\ (mc^2\ (e-e')))$ (4.13.6)

and C is independent of θ.

The author has written a computer programme to calculate these expressions and results of virtual photon spectra are given for 27.0 M.e.V. incident electrons in figure 37 The longitudinal components are seen to be negligible in the energy region above 21 M.e.V. In this energy range, the El virtual photon spectrum is = 0.7% and the

corrections applied to the cross-section data are = 4.0 ($\pm$0.4)%. E2/M1 transitions are expected to be weaker than E1 transitions by an order of magnitude (Chapter 1) so that electroproduction effects from these higher multipoles are negligible and consideration of electric dipole processes provide adequate corrections to the data.

In order to calculate the correction to the yield at each angle the constant 'C' must be evaluated for equation 4.13.6. This is done for each energy by using the measured data (without the 4% electroproduction correction) to find the coefficient (β/α) of the $\sin^2\theta$ part of the angular dependence of the photoprocess. The two equations are then evaluated in terms of (β/α) and the unknown constant ($C^*\alpha$) for 20 bins of equal solid angle covering the entire angular range. By requiring the ratio of the integrated cross-sections so found to equal the corresponding value of the virtual photon spectrum, the electroproduction correction at each angle was expressed as a percentage of the photon yield at that angle.

If the dominant process is the E1 emission of d-wave photoneutrons from O^{16} the angular distribution takes the form:

$$W_{E1,d}(\theta)\ (\gamma) = 1 - \tfrac{1}{2}*P_2\ (\cos\theta) \qquad (4.13.7)$$
$$= \tfrac{1}{2}\ (1+\tfrac{3}{2}*\sin^2\theta)$$

With this definition of $\beta/\alpha = (3/2)$ the electroproduction spectrum was typically

$$W_{E1,d}(\theta)\ (e^-) = \text{CONSTANT} * (1+0.9*\sin^2\theta).$$

Corrections to the yield at any angle were $\leq$ 4.5% and the variation in this factor over the present angular range was $\leq$ 0.7%, so that the correction has a very small effect on the angular distribution

data for O^{16}.

For Deuterium, $\alpha = 0$ and 4.13.6 is simplified to

$$W(\theta) = \sin^2 \theta$$

corrections to the yield in this case were typically 5% with a variation from 4% to 8% over the range of angles used.

4.14 Derivation of Angular Distribution Data.

The six sets of 380-channel spectra are read in one at a time by a programme written by the author to fit the data to the Legendre series

$$W(\theta) = An.Pn(\cos\theta) \qquad (4.14.1)$$

This programme solves the normal equations for the least squares fit of each set of six data points by inverting the matrix involved. It takes into account the errors associated with each data point and outputs the coefficients An (n= 0,4 usually) and the ratios An/Ao; (n = 1,4) with errors and gives residuals to the fit for each data point and results of a goodness of fit (x^2) test on the data. The basis for the programme may be found in references 134 and 135. Tests were made of the programme accuracy by inputs of pre-calculated angular distributions and it was found to function satisfactorily.

The author has altered the programme mainly in its input - output stages but the storage has been extended to allow conversion of the whole energy spectrum in one process. The results are provided as line printer output and are also stored on magnetic tape for access by plotting programmes.

As an independent check of the above techniques the data was fitted to the Legendre series by another programme using a minimisation routine[136] to optimise the least squares criterion. The coefficients obtained by the two methods agreed to within a small fraction of the

T.O.F SPECTRA (present experiment) fig.38

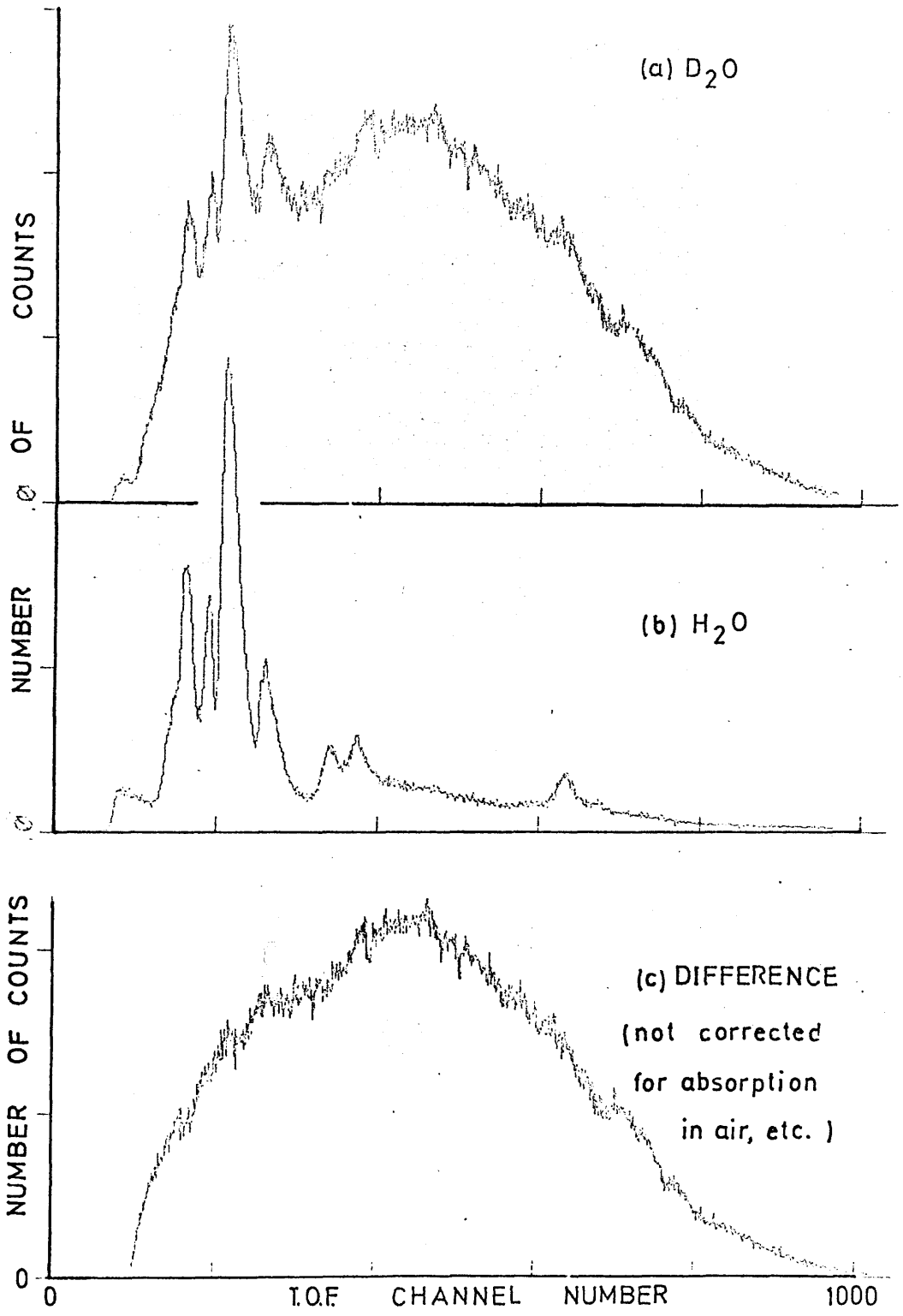

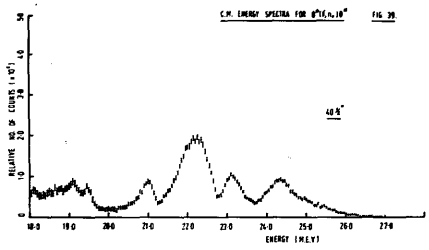
C.M. ENERGY SPECTRA FOR $^{6}Li(t,n_0)^{8}B$ FIG 39
40.5°
RELATIVE NO. OF COUNTS (x10³)
ENERGY (MEV)

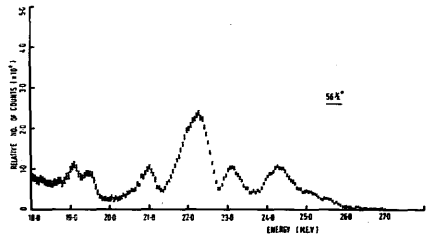
56.5°
RELATIVE NO. OF COUNTS (x10³)
ENERGY (MEV)

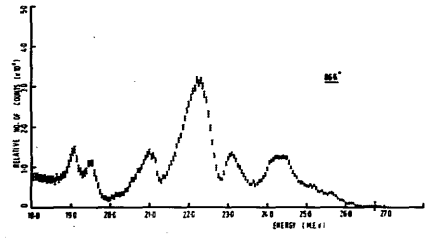
86.5°
RELATIVE NO. OF COUNTS (x10³)
ENERGY (MEV)

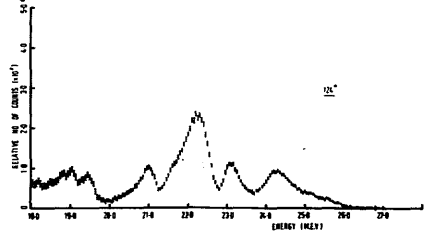
125°
RELATIVE NO. OF COUNTS (x10³)
ENERGY (MEV)

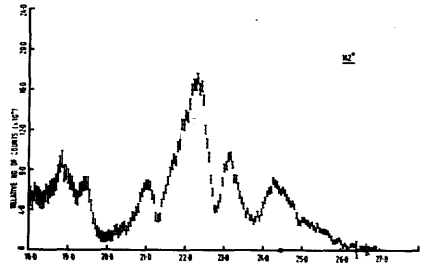
162°
RELATIVE NO. OF COUNTS (x10³)
ENERGY (MEV)

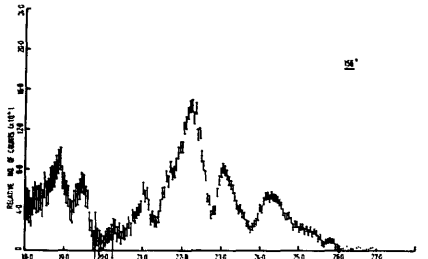
158°
RELATIVE NO. OF COUNTS (x10³)
ENERGY (MEV)

Fig 40

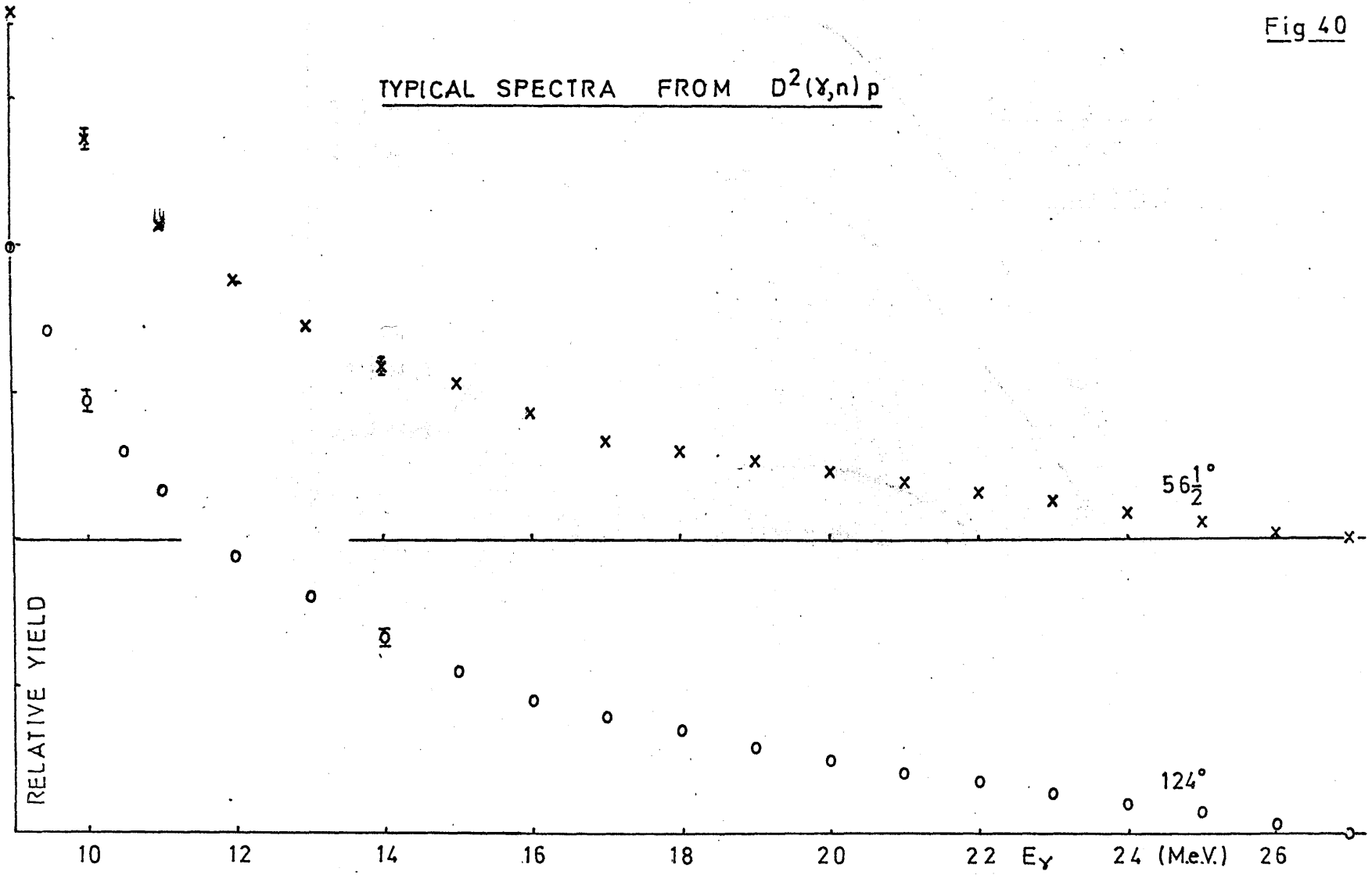
TYPICAL SPECTRA FROM $D^2(\gamma,n)p$
RELATIVE YIELD
$56\frac{1}{2}°$
124°
10
12
14
16
18
20
22
E_γ
24 (M.e.V.)
26

FIG. 1A

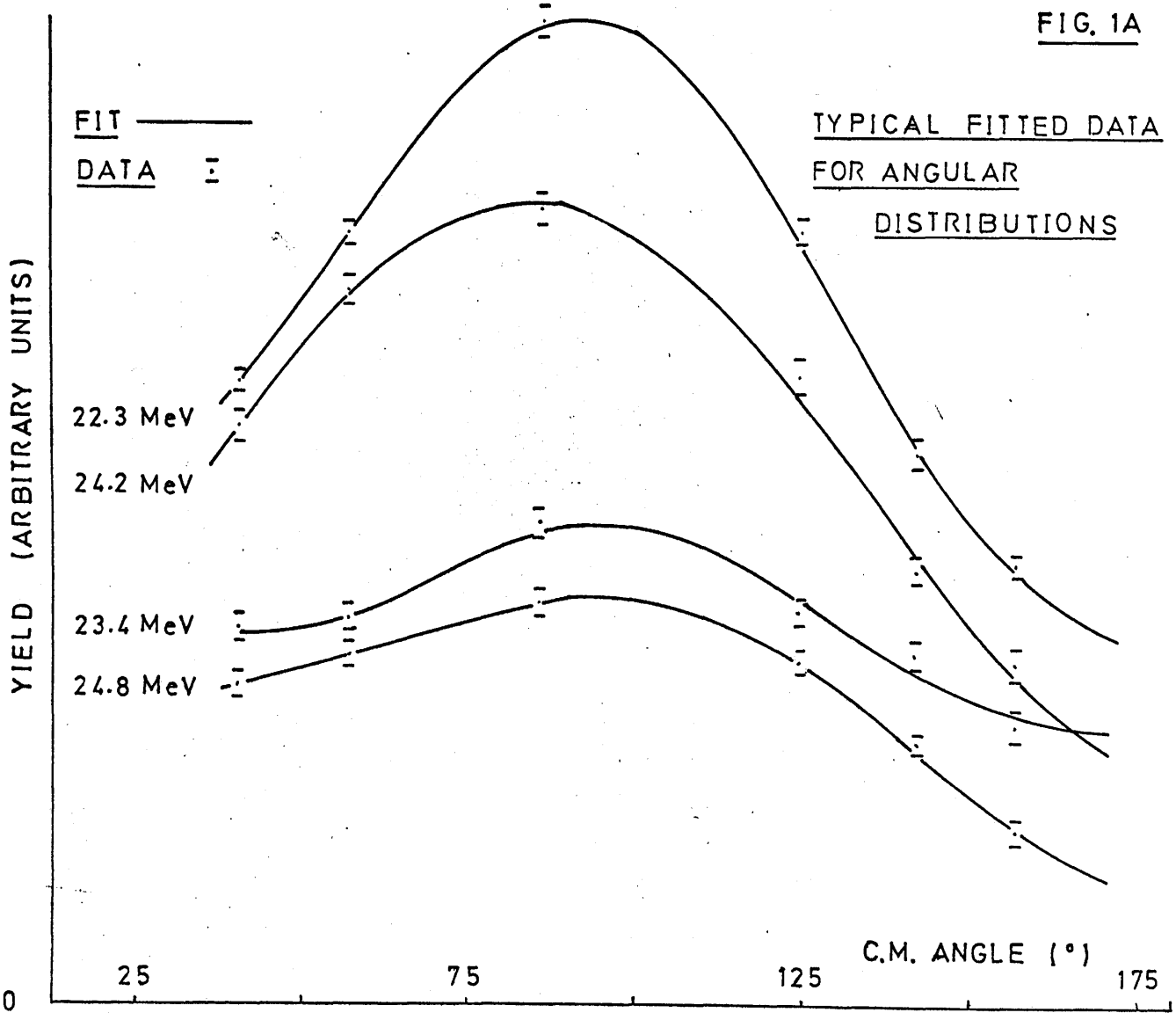
FIT
DATA
TYPICAL FITTED DATA FOR ANGULAR DISTRIBUTIONS
22.3 MeV
24.2 MeV
23.4 MeV
24.8 MeV
YIELD (ARBITRARY UNITS)
0
25
75
125
175
C.M. ANGLE (°)

estimated error in all cases.

4.15 Propagation of Errors.

The statistical errors on the original data are propagated in the standard way when the various T.O.F. spectra are subtracted and the effect of the estimated errors in the normalisation constants are included. The resultant percentage error is carried through the energy conversion processes and the final error on each datum point is obtained as previously described upon interpolation to equally spaced bins.

The errors on the yield values for each angle are combined with the goodness of fit results to obtain the error in the desired coefficients at a given energy.

4.16 Summary and Presentation of Spectra.

Typical T.O.F. spectra obtained by (γ,n) reactions on H_2^1O, D_2^2O and their difference are shown in figure 38 By the methods described in this chapter, this data was converted to spectra of C.M. yield versus LAB. photon energy at each C.M. angle.

Figure 39 shows the yield measured for the reaction $O^{16}(\gamma,n)\,O^{15}$ at the average C.M. angles shown. Note that the bremsstrahlung spectrum shape has not been divided out of this data and it may be seen that the end point is 26.9 M.e.V. in all the spectra, confirming the energy calibration. The familiar structure of the giant resonance of O^{16} is apparent, and the energies associated with this structure agree with previous determinations, confirming the present techniques of energy calibration and data processing. Typical Deuterium energy spectra are shown in figure 40.

The cross sections and angular distribution coefficients derived

from these spectra are presented in the following chapter where comparison is made with previous measurements and the detailed predictions of the nuclear models of the giant resonance.

Chapter 5

5.1 Introduction.

The total cross section, the differential cross section at 87^{o} and the angular distributions of ground state photoneutrons from O^{16} are presented in the energy range 21.5 M.e.V. to 26 M.e.V. Analysis of this data allows an estimate to be made of the relative intensity of the dominant partial waves of photoneutron emission and the variation of the phase difference with energy. The E2 cross section for ground state transitions is extracted from the data and is found to rest mainly in two broad states centred at about 23 M.e.V. and 24.7 M.e.V. Using similar data for photoproton emission, the isospin impurity in the O^{16} dipole resonance is found to be small and appears to be associated with the regions of E2 strength.

The failure of the basic 1plh dipole approximation in describing these features leads to the investigation of the effects of more complicated excitations and these are shown to be consistent with the observed structure in the giant resonance, and with the observed distribution of isospin impurity and E2 absorption.

5.2 The Angular Distribution of Photoneutrons from Deuterium.

The Legendre coefficients describing the angular distribution of Deuterium photoneutrons from 9 to 26 M.e.V. are presented in figure 41 where the data have been averaged over 1 M.e.V. intervals to reduce the statistical fluctuations inherent in the subtraction of large numbers in the T.O.F. spectra. Also shown are the (γ,p) results of Weissman [123] and the theoretical predictions of Partovi.[124] The $D^{2}(\gamma,n)p$ reaction has been fairly well understood for some time and the quoted

LEGENDRE COEFFICIENTS IN $D^2(\gamma,n)$ Fig.41.

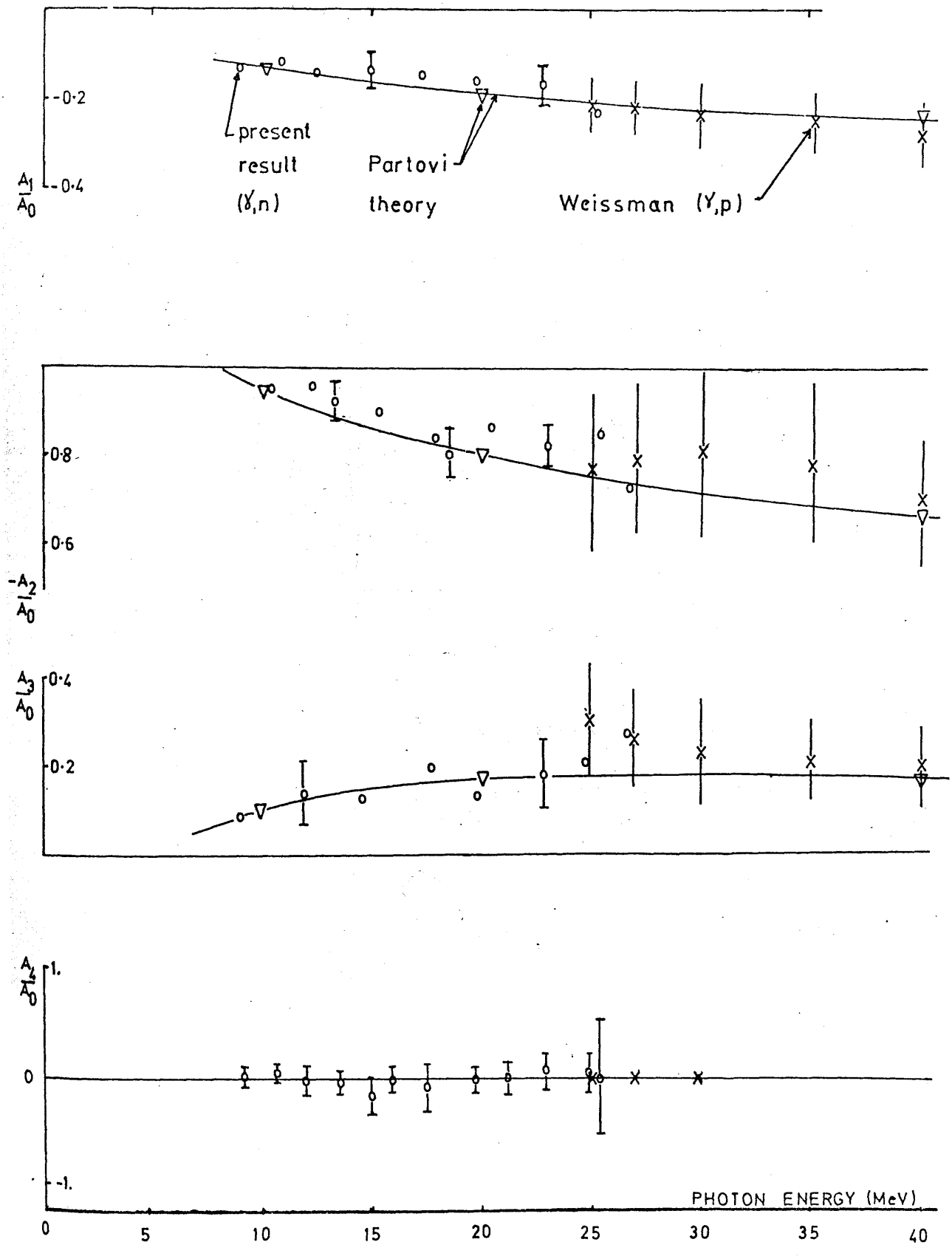

FIGURE 42 CUBIC FIT TO A_0 COEFFICIENT IN $D^2(\gamma,n)p$ SPECTRUM.

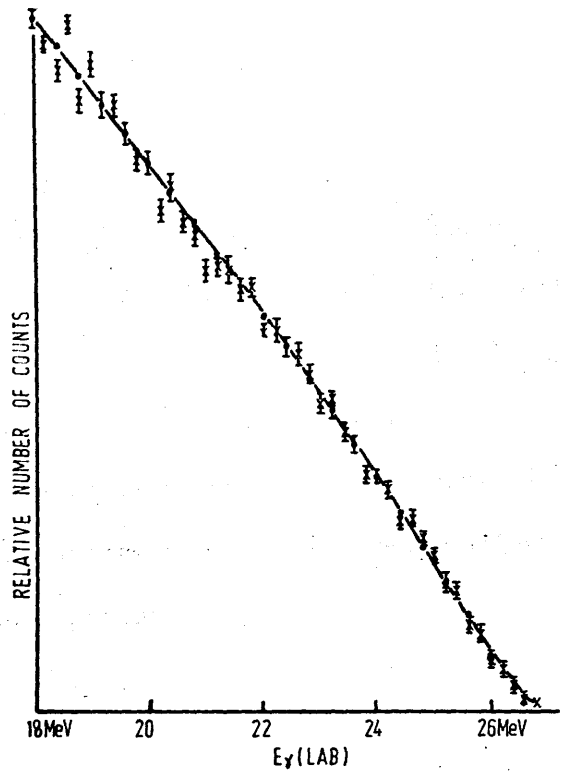

FIGURE 43 BREMSSTRAHLUNG SPECTRUM

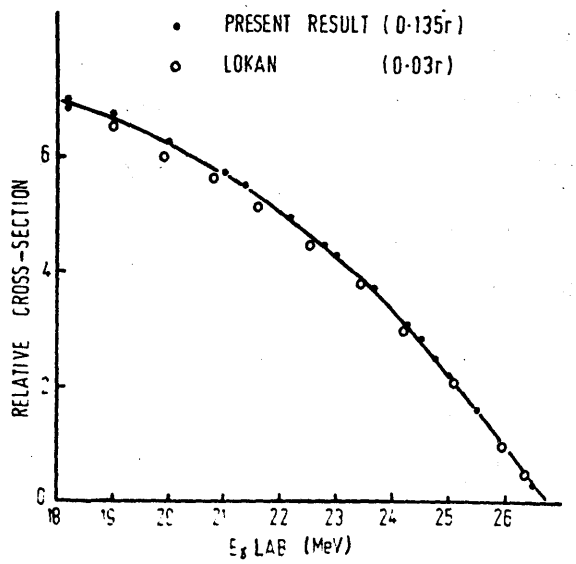

results represent some of the most precise confirmation of this general accord of experiment and theory.

The good agreement found between these and the present results is taken as illustration of good angular normalisation, for no correction factors were necessary to obtain the coefficients A_1/A_0 to A_3/A_0 shown. The original value of A_4/A_0 so obtained was, however, found to be ~0.1 and the data has been renormalised to remove the small systematic angular dependence responsible. This involved renormalisation factors of less than the expected accuracy of normalisation (3%) at any angle and it had a negligible effect on the other coefficients.

The same small factors were used to renormalise the $O^{16}(\gamma,n)O^{15}$ angular distribution spectra.

5.3 The $D^2(\gamma,n)p$ A_0 Coefficient and Derivation of the Bremsstrahlung Spectrum.

The constant coefficient in the Legendre expansion of the $D^2(\gamma,n)p$ reaction is presented as a function of photon energy (k) in the laboratory frame (LAB) in figure 42. This spectrum is the yield 'Y' defined (4.5.9) as the product $4\pi(dn\gamma/dk)*A_0(k)$, where $A_0(k) = \sigma_T(k)/4\pi$ and $\sigma_T(k)$ is taken as the Partovi cross section of figure 41. In figure 43, the Partovi cross section has been divided out of figure 42 to show the shape of the bremsstrahlung spectrum for the present experiment, and comparison is made with the 'thick-target' calculation of Lokan[57] (for a 0.03r Tantalum target). The spectrum shapes are quite similar although that of the present experiment is slightly softer as expected from the use of a thicker (0.13r) target. This agreement is taken as confirmation of the reliability of the technique used to obtain the O^{16} cross sections.

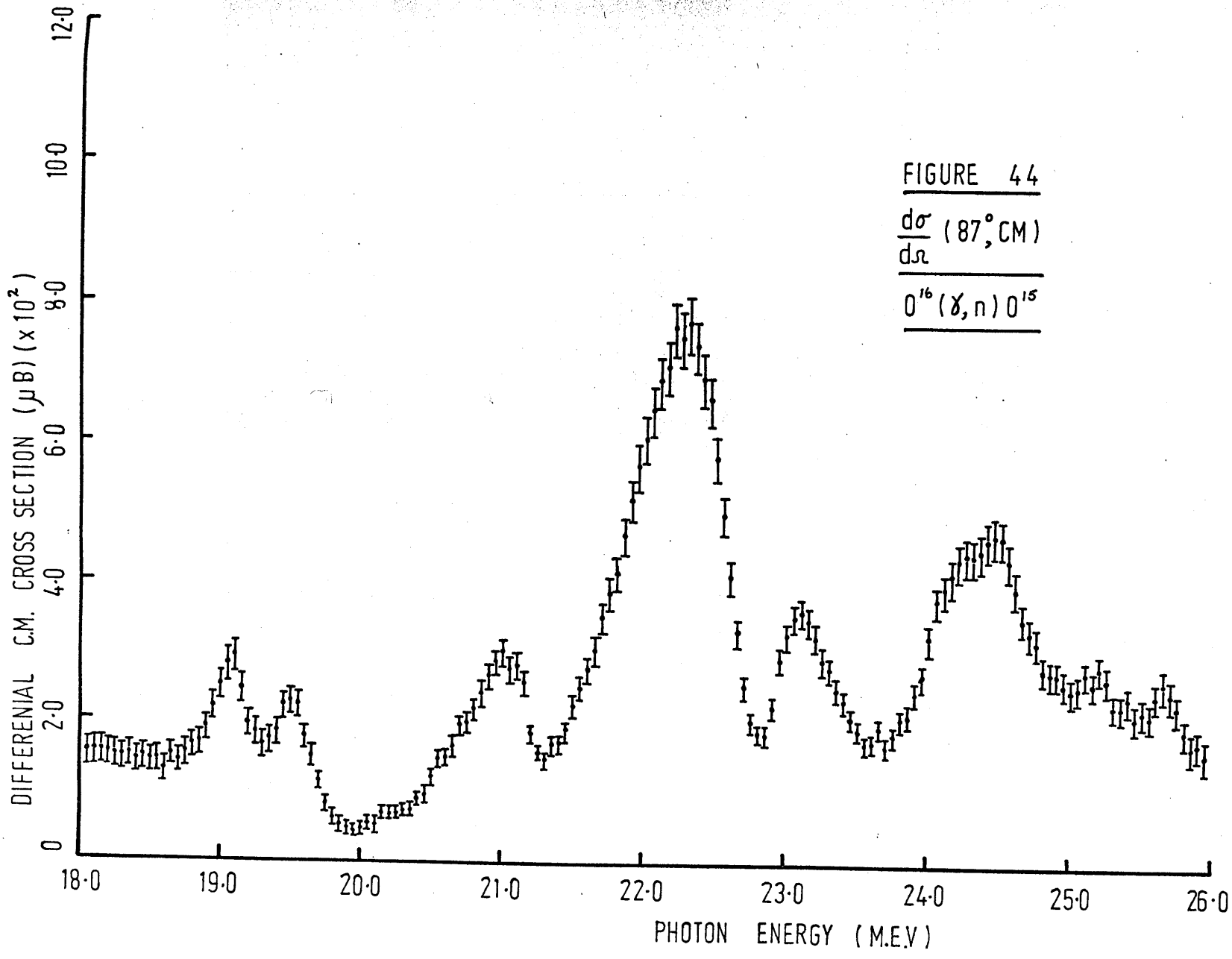
FIGURE 44
dσ/dΩ (87°, CM)
O16 (γ, n) O15
DIFFERENIAL C.M. CROSS SECTION (μB) (x 10²)
0
2·0
4·0
6·0
8·0
10·0
12·0
18·0
19·0
20·0
21·0
22·0
23·0
24·0
25·0
26·0
PHOTON ENERGY (M.E.V)

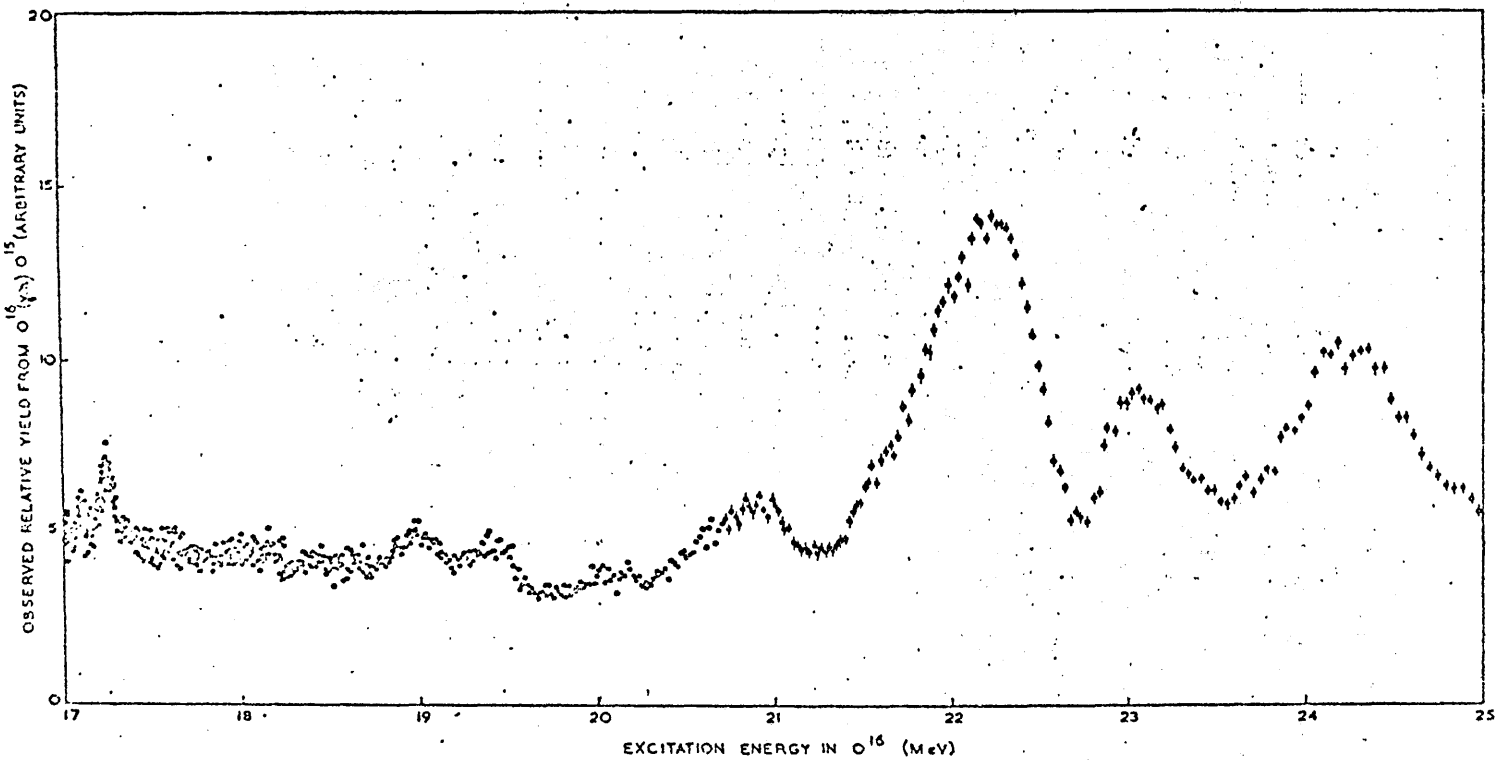

Fig. 1(b). The observed relative yield of photoneutrons from $O^{16}(\gamma, n)O^{15}$ when irradiated with 25 MeV bremsstrahlung. The resolution is 0.16 nsec · m^{-1}.

$O^{16}(\gamma,n)O^{15}$ SPECTRUM AT 90° FROM FIRK[59]

Fig. 45

Photonuclear Resonance Energies in O^{16} Table 10

Year	Authors	Resolution (keV)	Resolution Angle	Type	Resonance Energy (M.e.V.) 19.3	21.0	22.25	23.1	24.3	25.2
1962	Firk and Lokan[57]	200	90°	(γ,n)	19.1 19.6	20.7 21.0	22.2	23.0	24.3	25.0 25.4
1964	Firk[59]	100	90°	(γ,n)	19.0 19.4	20.9	22.1 22.3	23.1	24.1 24.3	-
1965	Verbinski and Courtney[63]	200	90°	(γ,n)	19.3	21.0	22.2	23.0	24.2	-
1967	Caldwell[101]	200	σ_T	(γ,n)	-	21.0	22.3	23.05	24.2	25.2
1962	Dodge and Barber[34]		90°	(e,e'p)	18.95 19.5	20.9	22.3	23.05	24.3	25.2
1964	Tanner et al[90]	100	90°	(p,γ)	19.05 19.6	21.0	22.3	23.05	24.3	25.2
1967	Earle and Tanner[92]	50	many	(p,γ)	19.0 19.5	21.0	22.2	22.9	24.3	-
1969	Baglin and Thompson[150]	100	many	(γ,p)	-	20.85	22.15	22.9	24.15	24.9
1972	Present Result	100	many σ_T	(γ,n)	19.05 19.45	21.0	22.25	23.10	24.35	weak
	" "	"	90°	"	19.075 19.50	21.025	22.275	23.10	24.15 24.45	25.15

In figure 42 the solid line is the result of a least squares fit to the data by a cubic, $A_o^D(k)$, in the LAB photon energy over the range shown (18 to 26 M.e.V.). The Partovi cross section was fitted to a cubic (P(k)) in a similar way and the total cross section for $O^{16}(\gamma,n)O^{15}$ was obtained from the O^{16} data ($A_o^{O16}(k)$) at each point 'k' by

$$\sigma_T^{O16}(k) = (P(k)/A_o^D(k))*((N_D/N_o)*NORM)*A_o^{O16}(k),$$

where N_D, N_o are the relative number of atoms of Deuterium and Oxygen used and NORM is the normalisation constant between oxygen and deuterium runs, obtained from the charge monitor. The 87^o differential cross section of $O^{16}(\gamma,n)O^{15}$ was obtained in a similar way.

5.4 Photoneutron Cross Sections for $O^{16}(\gamma,n)O^{15}$

The differential cross section at 87^o in the C.M. for the reaction $O^{16}(\gamma,n.)O^{15}$ is presented in figure 44, where ground state transitions have been assumed. By the choice of the bremsstrahlung end point, this condition is ensured above about 21.7 M.e.V. photon energy and some contamination from transitions to excited states of N^{15} is expected at lower energies. In this result, the small variation of C.M. angle with excitation energy has been neglected, as has the difference between excitation energy and photon energy. The shape of the differential cross section is in agreement with that found by other photoparticle measurements, for example the (p,γ) data[92] of Earle and Tanner (figure 4). Comparison with the good resolution $90^o(\gamma,n)$ data of Firk [59] (figure 45) shows good agreement with an improved signal-to-background ratio in the present result.

A survey of the excitation energies found by several different experiments for the prominent resonances is presented in table 10, where

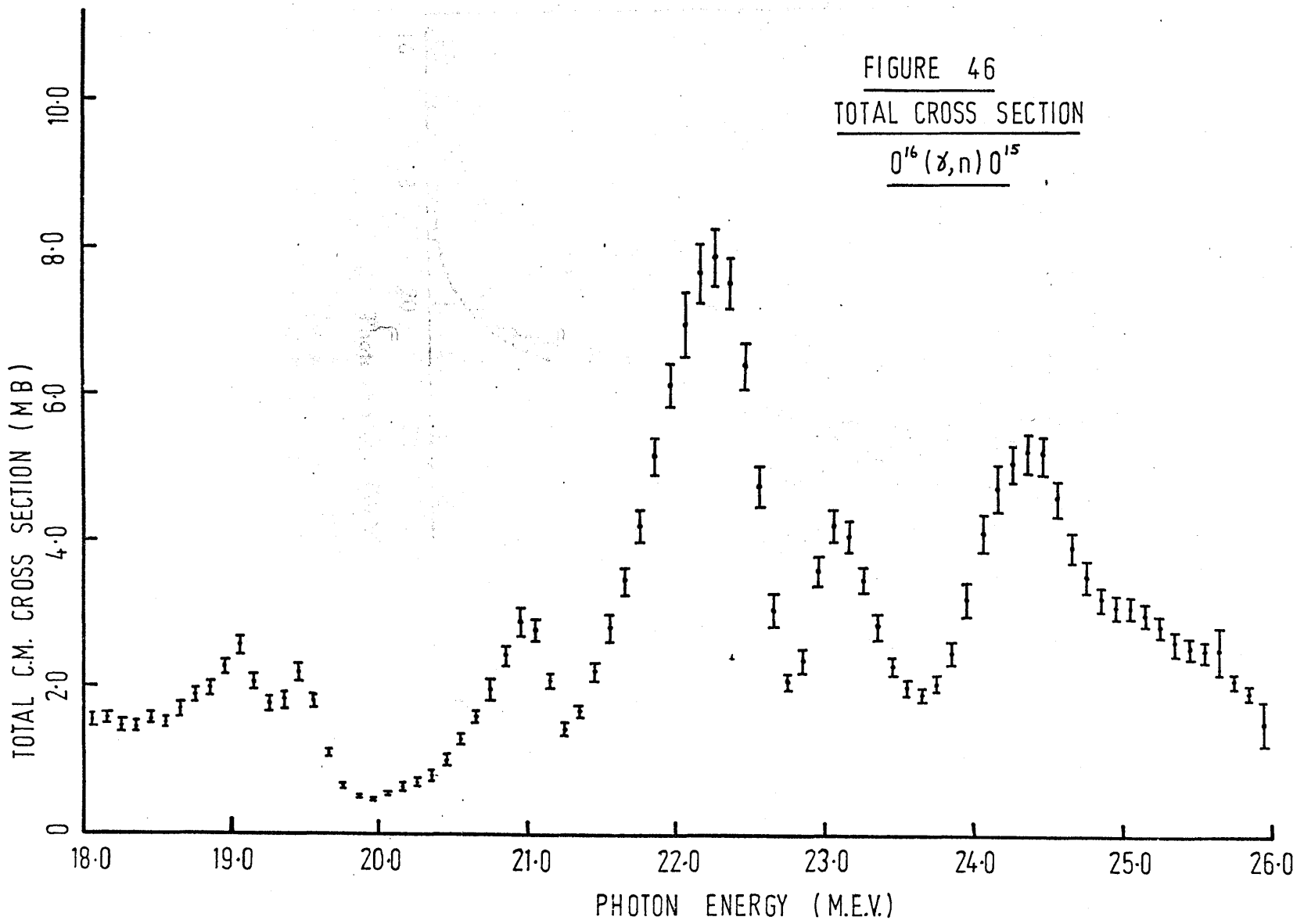
FIGURE 46
TOTAL CROSS SECTION
$O^{16}(\gamma,n)O^{15}$
TOTAL C.M. CROSS SECTION (MB)
0
2·0
4·0
6·0
8·0
10·0
18·0
19·0
20·0
21·0
22·0
23·0
24·0
25·0
26·0
PHOTON ENERGY (M.E.V.)

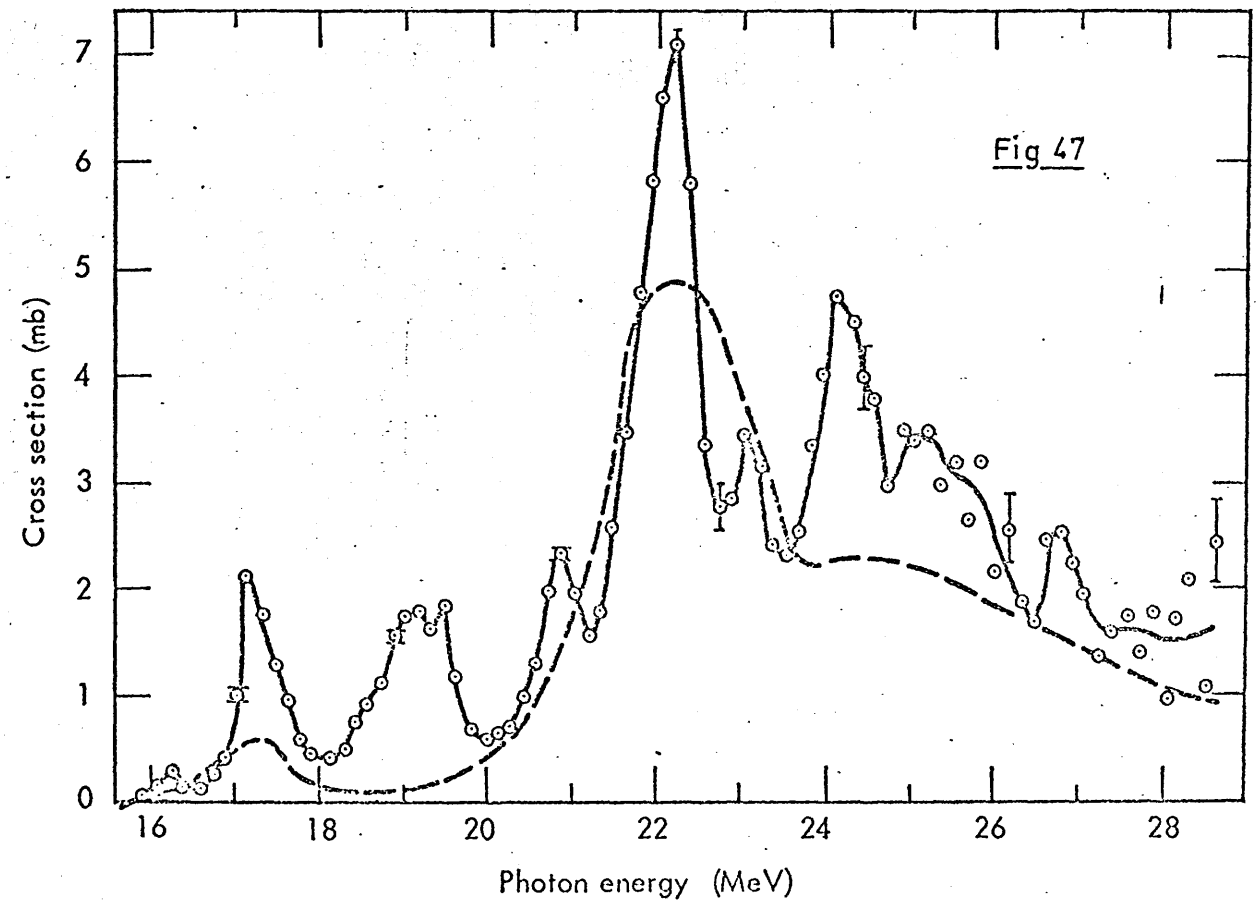

(REPRODUCED FROM CALDWELL[101])

Fig. 47 4π absolute cross section for the reaction $O^{16}(\gamma,n)O^{15}$ leading to ground-state transitions. Dashed curve from Buck and Hill.[10]

O^{16} (γ,n) O^{15} Cross Sections in the 22.25 M.e.V. O^{16} Peak. Table 11

Authors	Date	Method	Resolution (k.e.V.)	wrt D? (±10%)	Angle (CM.)	Differential (γ,n_0)	Differential (γ,n)	Total (γ,n_0)	Total (γ,n)	Remarks
Present	1972	T.O.F.	100	YES	87^0	.768±.04	-	.787±.38	-	
Khan et.al	1968	T.O.F.	100	YES	98^0	1.00±.05	-	(10.0±.5)	-	
Wu et al	1968	T.O.F.	100	YES	90^0	1.05±.05	-	(10.5±.5)	-	
Verbinski	1962	T.O.F.	200	NO	93^0	-	.69±.01	-	(6.9±.1)	34 M.e.V. Brem.
Bolen et al	1962	Yield	1000	NO	-	-	-	-	8.5±.35	
Caldwell et al	1965	Monochr. γ Yield	200	NO	-	-	-	7.0±.1	-	
Caldwell (Thesis)	1967	"	200	NO	-	-	-	7.05±.1	8.8±.1	
Cook et al	1966	Yield	?	NO	-	-	-	-	19.5±?	Rejected
Geller and Muirhead	1963	Yield	136	NO	-	-	-	-	12.8±1.5	Normalised to Bolen.

Note: The numbers in brackets are derived from the measured 90^0 cross-sections using the measured angular distributions from the present work.

it may be seen that agreement holds to within about 100 k.e.V. over most of the range and for both proton and neutron reactions. This holds too for the present work (table 10) and the energy calibration is confirmed.

The total cross section obtained from the present data is presented in figure 46 under the same ground state assumption (ensured above 21.7 M.e.V.). The shape of the total cross section is similar to the 87^{o} spectrum and comparison may be made with figure 47 which shows the ground state $(\gamma,n.)$ cross section measured by a monochromatic photon technique by Caldwell[101] and the results of the lplh calculation of Buck and Hill.[38] Caldwell's results agree well with the present data and the calculation reproduces the gross distribution of the cross section strength quite well, without predicting the observed finer structure.

Table 11 is a summary of the (γ,n) cross sections found in the 22.25 M.e.V. peak by various experiments whose characteristics are noted. To allow a full discussion of the cross section scale, the equivalent total cross section has been extracted from the previous '90^{o}' differential cross section values using the multiplicative factor obtained from the present angular distribution (=10.2).

The 90^{o} differential cross section values found by Wu et. al.[140] and Khan et. al.[141] agree but are quite different from that of Verbinski and Courtney.[63] The present result

$$\left(\frac{d\sigma}{d\Omega}\right)_{87^{\circ}\ 22{\cdot}3\ \mathrm{MeV}}(O^{16}(\gamma,n)O^{15},) = 0.768 \pm 0.040 \text{ mb.}$$

lies between these two values. The quoted error does not include a possible 10% systematic error in the assumed Partovi cross section for

$D^2(\gamma,n)p$ and this would allow agreement with only the lower of the two previous values.

In discussing the total cross section at 22.25 M.e.V. the results of Cook et. al.[144] will be disregarded since they are so different from all the other measurements that some systematic error is implied. The absolute cross section scale of Geller and Mairhead[142] was derived from the earlier measurement of Bolen and Whitehead[143] but their result is some 50% higher in the 22.25 peak and some doubt must be cast on the validity of their normalisation technique which was sensitive to the large differences in resolution between the two data sets.

With these omissions, the two total (γ,n) cross section values of Bolen and Whitehead[143] and Caldwell[146] are in good agreement despite the differences in technique, but the total (γ,n_o) cross section to the ground state is in dispute. The higher value (around 10 mb.) proposed by Khan et. al.[141] and Wu et. al.[140] is in fact above the agreed (γ,n) cross-section value while the present result for the ground state cross-section:

$$\sigma_{T,22.3M.e.V.}(O^{16}(\gamma,n_o)O^{15}) = 7.87 \pm 0.38 \text{ mb.}$$

agrees within the 10% error on the Partovi cross section with the lower value (~7.mb.) of Caldwell[101,145] and Verbinski and Courtney.[63]

There is additional evidence that the lower cross section scale is to be preferred, for Caldwell[101] used the available (γ,p_o) ground state data with his own measurements of the neutron total cross-section and the cross-section of proton decays via excited states to systhesise a 'total n+p absorption' cross-section which agreed extremely well with

the total photonuclear cross-section measurements of Wycoff et. al.[101,146] and Ben-David et. al.[101,147] (The absolute value of the similar Burgov[33] data shown earlier (figure 2) is in dispute with the majority of such measurements.[148]) Physically the 'n+p' cross-section must be less than the total absorption cross section, and in fact Caldwell found equality at 22.3 M.e.V. Substitution of the author's (γ,n_0) cross-section instead of that of Caldwell does not affect the agreement within the statistical errors but use of the higher (γ,n_0) cross-section values gives a synthesised cross-section which exceeds the physical limit (25 mb.) by 3 mb. or 12% – outside the statistical uncertainty.

The neutron detection efficiency of the apparatus used by Caldwell was essentially independent of neutron energy,[101] so that the C^{12} (γ,n_0) cross-section so measured should be consistent with that for $O^{16}(\gamma,n)$. Wu et. al. find agreement with Caldwell for $C^{12}(\gamma,n)$[140] despite the difference seen for O^{16}. The only real difference in these experiments on C^{12} and O^{16} at a given photon energy is the kinetic energy of the emitted photoneutron so that some error in the treatment of the correction factors described in chapter 4 seems likely in the results of Wu et. al. and Khan et. al. (They used an experimental technique similar to that of the author).

The cross-section scale found by the author is seen to be consistent with several other experiments including the total photonuclear absorption cross-section.[196,197]

(Table 12) Integrated cross sections for O^{16} photoreactions.

Reaction	Final state (MeV)	$\int_{Th}^{28.7} \sigma dE$ (MeV-mb)	Fractional $\int_{Th}^{28.7} \sigma dE$
(γ,p)	Ground state	34.42	0.287
	5.3 $(1/2^+, 5/2^+)$	4.94[a]	0.041
	6.33 $(3/2^-)$	22.30	0.185
	7.30 $(3/2^+)$	5.47	0.047
	9.1	2.03	0.017
	9.22	1.50	0.013
	9.9	2.36	0.020
	10.8	2.34[b]	0.020
(γ,n)	Ground state	26.67	0.223
	5.2 $(1/2^+, 5/2^+)$	3.49	0.029
	6.18 $(3/2^-)$	9.43	0.079
	6.79 $(3/2^+)$	4.50	0.038
(γ,α)	15.11 $(1^+, T = 1)$	0.23	0.002

[a]The 9.22 MeV cascade transition cross section has been subtracted from the 5.3 $(1/2^+, 5/2^+)$ values.

[b]Observed 10.8 MeV yields multiplied by $\frac{\Gamma_{tot}}{\Gamma_{\gamma_0}} = 3.0 \pm 0.5$ from Ref. 25.

Note: Reproduced from Caldwell[101].

O^{16} (γ,p) N^{15} cross-sections at 22.25 M.e.V. Table 13

Authors	Date	Method	Resolution or spacing	wrt D^2? (±10%)	$\left(\frac{d\sigma}{d\Omega}\right)_{90°}$ (mb.)	σ_T(mb.)	
						g.s.	+ rest
Morrison et al[93]	1965	(γ,p)	200 keV.	YES	1.0 ±.05	(10.0) (±.5)	11.5 ±.5
Baglin and Thompson[150]	1969	(γ,p_o)	100 keV.	NO	1.28 ±.06	12.8 ±.62	-
Tanner et al[90,92] (detailed balance)	1966 1963	(p,γ_o)	100 keV.	NO	1.2 ±.25	12.0 ±2.5	-

Note that the total cross-sections shown in brackets have been obtained from the 90° differential cross-sections using the numerical factor found from the relevant angular distribution data.[92,150]

5.5 Integrated Cross Sections.

The integrated cross-section for ground state photoneutron emission in O^{16} is found to be:

$$\int_{21.5}^{26.0} \sigma_T(\gamma,n_o)\, dE = 16.74 \pm .97 \text{ M.e.V. - mb.},$$

where the ground state transitions have been assumed to hold down to 21.5 M.e.V. This compares favourably with Caldwell's value of 15.2 ± 1.5 M.e.V. mb., for the same range.(101) We may therefore adopt Caldwell's results for the wider range from Threshold to 28.6 M.e.V. some of these integrated cross-sections are shown in table 12, where it may be seen that the "total photonuclear cross-section" in this range, obtained from the neutron and proton results, is only 118 M.e.V.-mb. or just about half the 240 M.e.V.-mb. dipole sum rule for O^{16}, confirming the well-known existence of substantial dipole strength above the giant resonance of the light nucleii.

5.6 Isospin Impurity in the O^{16} Dipole Resonance.

Few of the photoproton (or(p,γ)) spectrum measurements have been absolute and the (γ,p_o) cross section scale is in dispute. The (γ,p_o) cross sections at 22.3 M.e.V. of Baglin and Thompson(150) and Morrison(93) et. al. are compared with that derived from the (p,γ) data of Earle and Tanner(92) in table 13. Unfortunately the errors on the (p,γ) data are too large to allow discrimination between the conflicting (γ,p) results but the lower value is favoured by the same argument presented in the neutron case, since the (γ,p_o) data used by Caldwell to construct his 'total p+n absorption' cross-section used the lower (Morrison) scale.(101) It is convenient that both Morrison's data and that of the author were taken with respect to the deuterium cross-section so that the 10% possible error in assuming the Partovi

ISOSPIN IMPURITY IN THE O^{16} G.D.R. Fig. 48

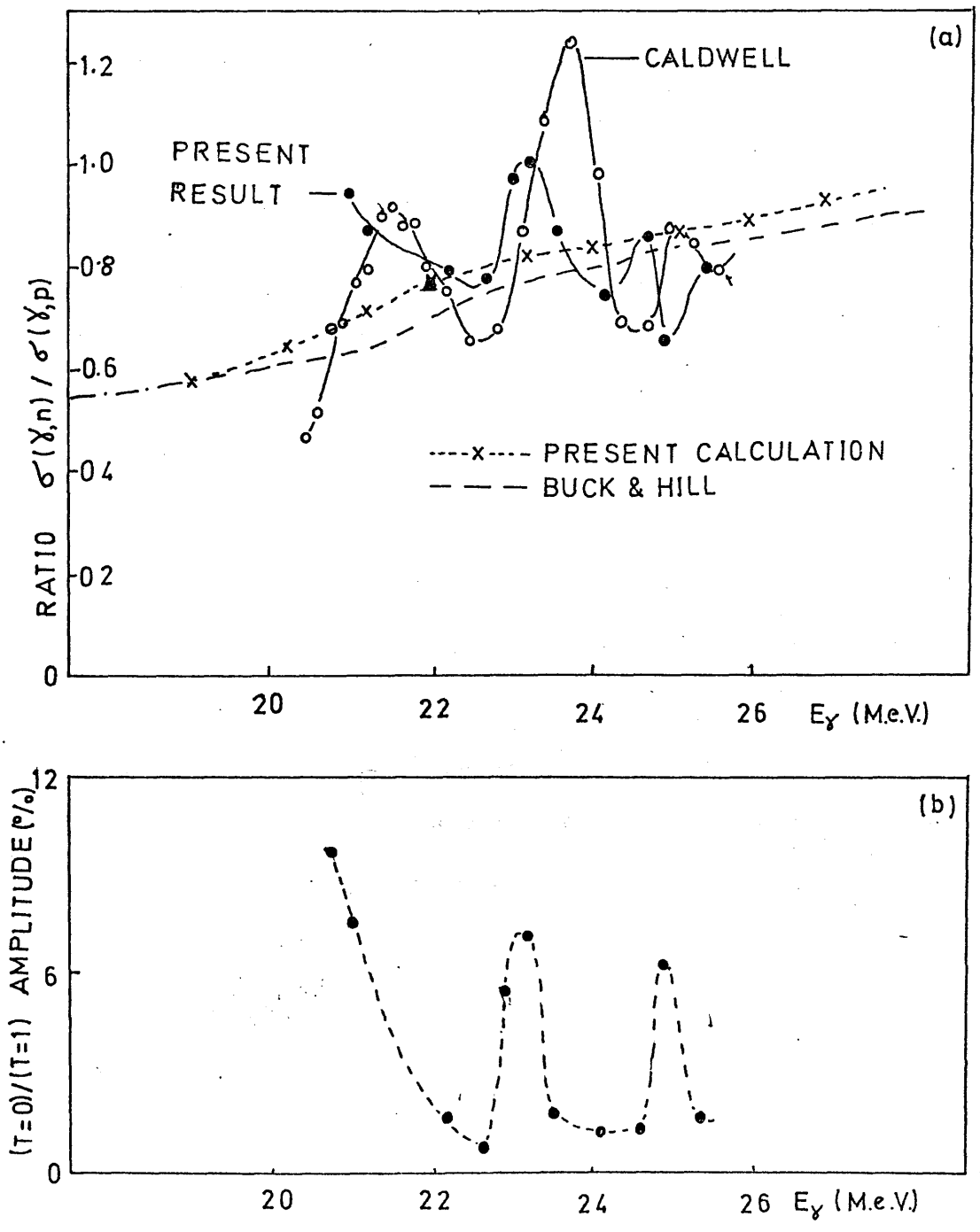

cross-section does not arise in the comparison of these cross-section curves. Morrison's data is not necessarily ground state beyond 24 M.e.V. however, and the resolution is somewhat inferior to that of the present data and that of the other proton work[92,150] so that the comparison has been made with the spectrum shape from this other data, normalised to the absolute scale of Morrison. This avoids the generation of spurious structure by comparison of two spectra of quite different energy resolution.

The $(\gamma,n)/(\gamma,p)$ cross-section ratio so obtained is compared with measurements by Caldwell and the predictions of Buck and Hill[38] in figure 48(a) where the general trend and magnitude of the experimental result is seen to follow that of the theory. The calculated ratio may be taken as the ratio of penetrability factors in the Barker-Mann[42] expression

$$\frac{\sigma(\gamma,p)}{\sigma(\gamma,n)} = \frac{P(p)}{P(n)} \cdot \left|\frac{1+a}{1-a}\right|^2$$

for it arises entirely from the effect of the Coulomb force for protons in the optical model potential used by Buck and Hill and all other perameters for neutrons and protons were identical.[38] This ratio was confirmed by a calculation of the transmission factors for protons and neutrons incident on mass 15 nuclei using a general form of the optical model potential whose perameters are given in figure 49(a). The programme (kindly supplied by Dr. J.D. Kellie of this laboratory) had already been successfully applied to calculation of average total cross-sections for nuclei with mass 30[128] and was further modified to calculate the phase shift of the reflected wave which is required later. Results of transmission factors for protons and neutrons with up to 3

OPTICAL MODEL CALCULATION PERAMETERS

Fig. 49(a)

$$V(r) = V_{Coulomb} - V_c f_1(r) - iW_c f_2(r) + V_s \lambda_\pi^2 \underline{\sigma}\cdot\underline{l}\,\frac{1}{r}\,\frac{df_1}{dr}$$

$$f_1(r) = (1 + \exp[(r - R_1)/a_1])^{-1}, \qquad R_1 = r_0 A^{1/3} + r_1 ,$$

$$f_2(r) = \exp\left[-(r - R_2)^2/a_2^2\right], \qquad R_2 = r_0 A^{1/3} + r_2 ,$$

$r_0 = 1.16$ fm., $\quad V_c = (47.25 - 0.25\,E_{n,p})$ M.e.V. ,

$W_c = 8.5$ M.e.V., $\quad V_s = 7.$ M.e.V., $\quad r_1 = 0.6$ fm. ,

$a_1 = 0.62$ fm., $\quad a_2 = 0.5$ fm., $\quad r_2 = 1.1$ fm. .

NEUTRON TRANSMISSION COEFFICIENTS IN O^{15}

Fig. 49(b)

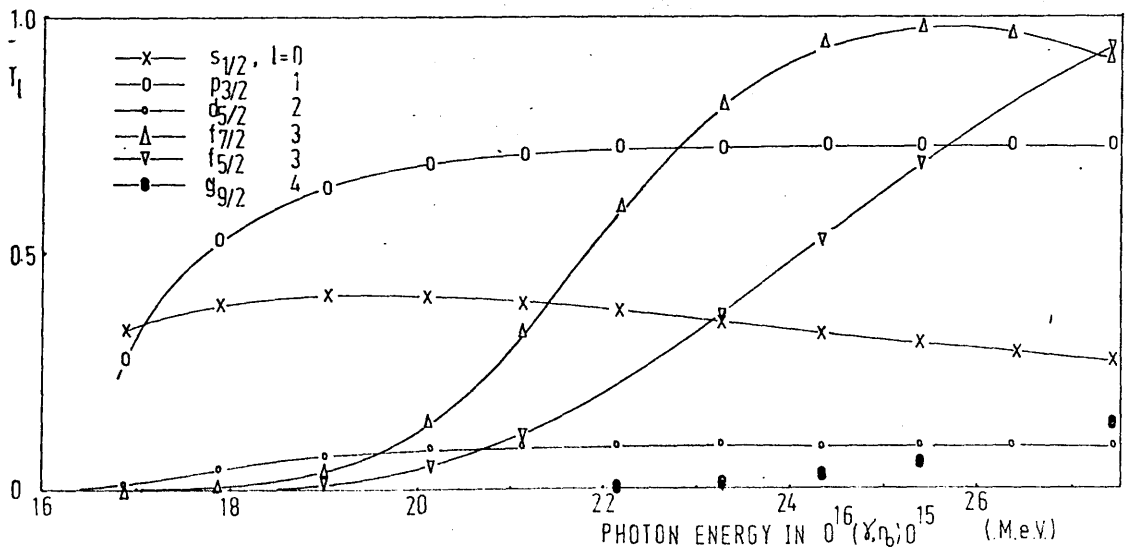

PROTON TRANSMISSION COEFFICIENTS IN N^{15}

Fig.49(c)

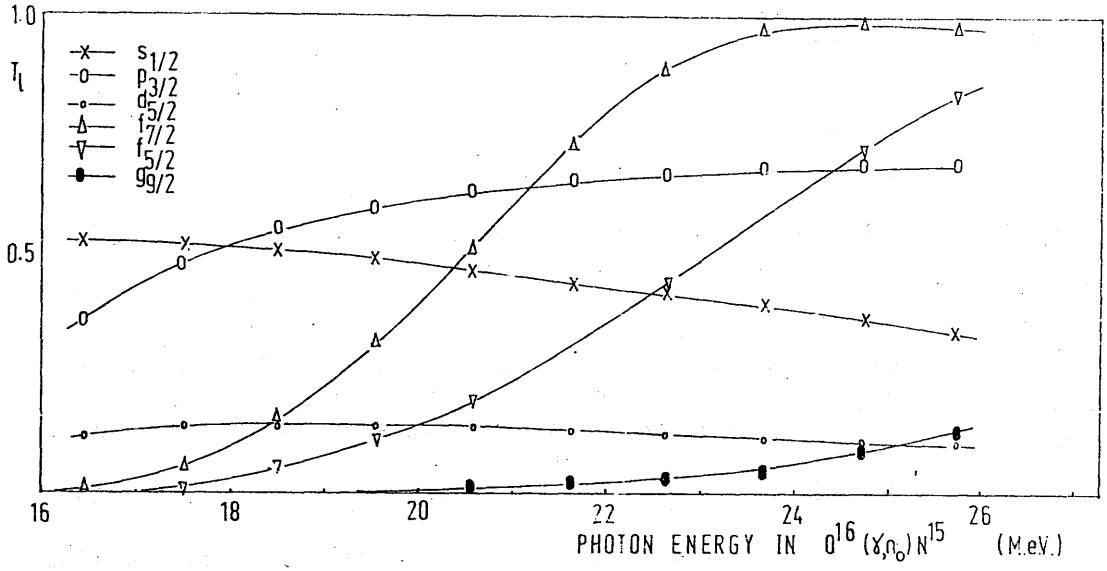

Fig. 49 (d)

PHASE DIFFERENCE BETWEEN s & d WAVES FOR O^{16} PHOTOPARTICLES

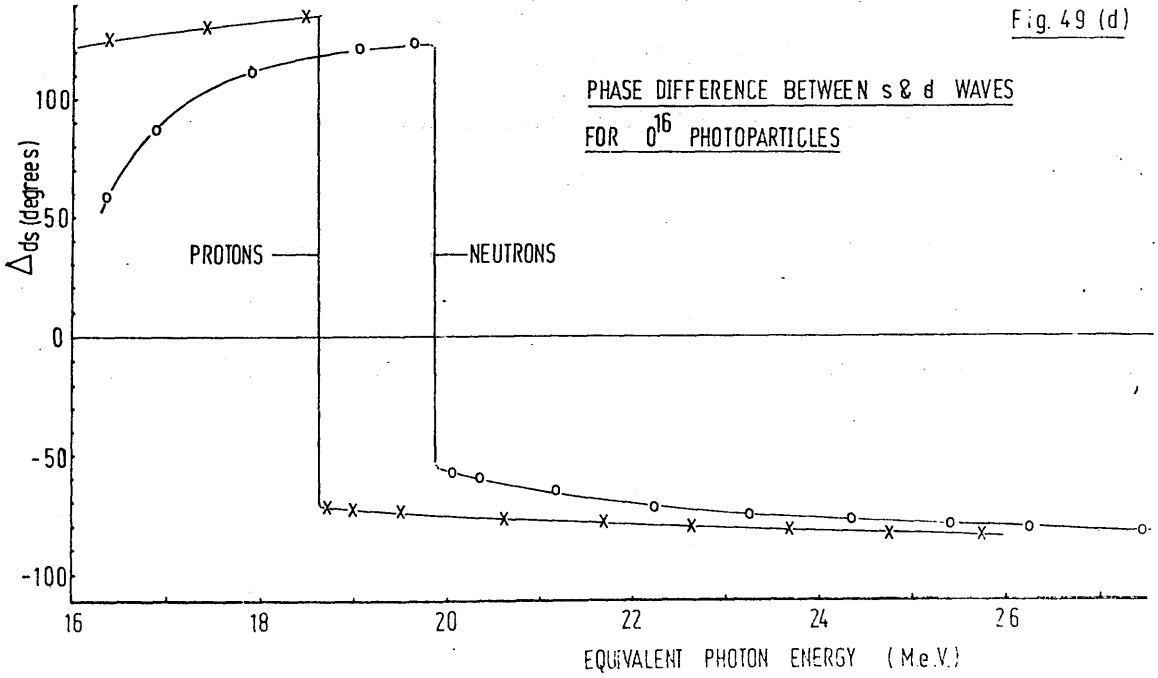

units of angular momentum are presented in figures 49 (b), 49 (c) at equivalent photon energies in ($0^{16}+\gamma$) and the phase difference between s and d waves is shown in figure 49 (d). The ratio of $d_{5/2}$ penetrability factors is shown in figure 48(a) and good agreement is obtained with the Buck and Hill result.

In an earlier comparison, Wu et. al.[140] assumed the penetrability factor ratio to be unity but the Buck and Hill values should be more reliable than this simple assumption for the similar ratios predicted for photonuclear decay to the excited mirror states of the residual nuclei were in excellent agreement with the measurements of Caldwell.[101] These should be reliable since the (γ,p*) and (γ,n*) reactions were detected simultaneously by observation of the de-excitation γ-rays with the same detector so that systematic errors were avoided.[101]

The amplitude 'a' of T=0 isospin impurity is given in figure 49(b) where it may be seen to be small with a maximum value a~ .07 between the two main resonances. The intensity of isospin impurity is below 0.1% in the main peaks at 22.3 and 24.3 M.e.V. and has a maximum value of 0.5% at 23 M.e.V. so that the giant resonance of O^{16} seems to be fairly pure T=1 on this basis.

The (γ,n)/(γ,p) cross-section ratio found by Caldwell is found to confirm the trend of the present results although the structure in this case may be somewhat exaggerated due to the comparison of spectra with quite different resolution.[101] The T=0 admixture is found to be of the same order as in the present result.

5.7 The Measured Angular Distribution of O^{16} Photoneutrons.

The Legendre coefficient ratios A_1/A_0 to A_4/A_0 for the angular

Fig. 50

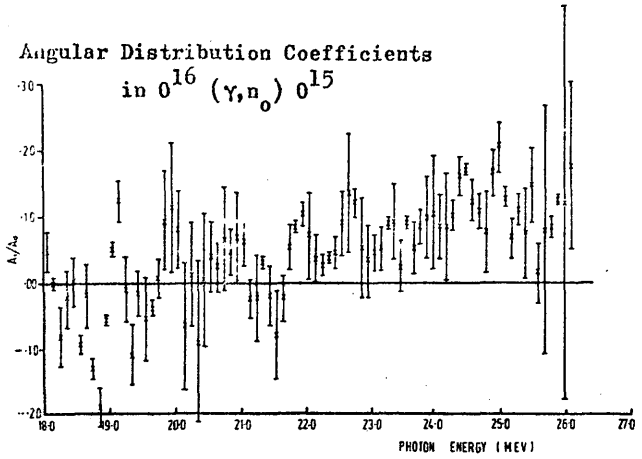
Angular Distribution Coefficients
in O^{16} (γ, n_o) O^{15}
PHOTON ENERGY (MEV)

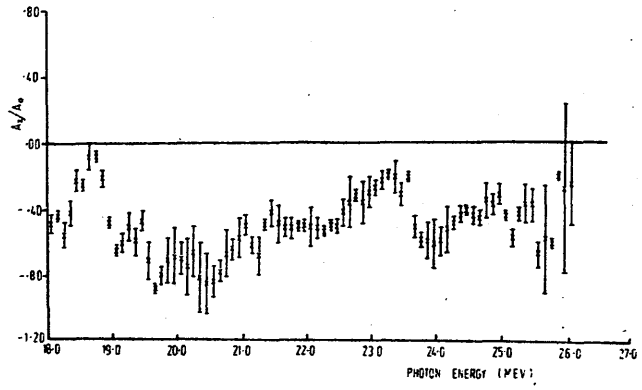
PHOTON ENERGY (MEV)

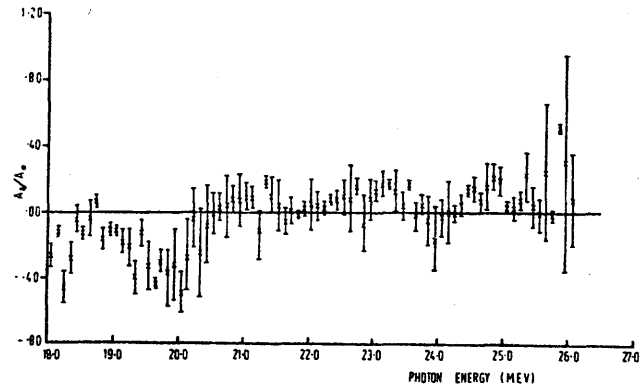
PHOTON ENERGY (MEV)

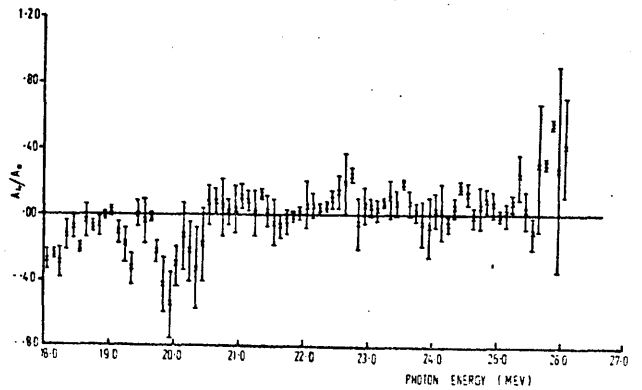
PHOTON ENERGY (MEV)

(γ,p) LEGENDRE COEFFICIENTS Fig 51

FROM BAGLIN[150]

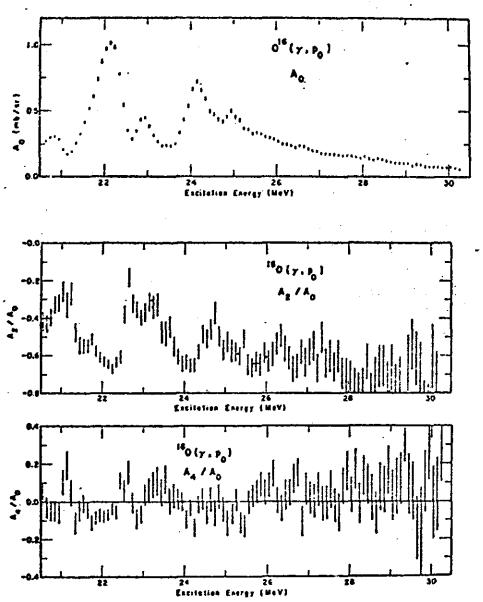

Fig. 5 Angular distribution for $^{16}O(\gamma, p_0)$. Legendre coefficients $a_2 = A_2/A_0$ and $a_4 = A_4/A_0$.

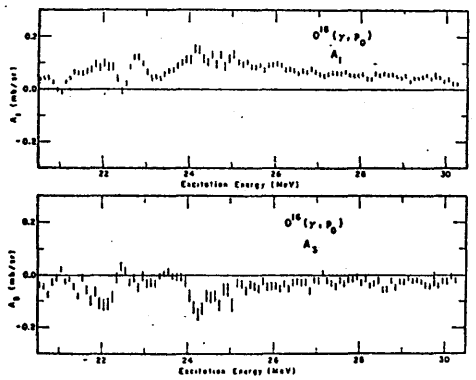

Fig. 6. Angular distribution for $^{16}O(\gamma, p_0)$. Legendre coefficients A_1 and A_3.

(γ, n_0) COEFFICIENTS FROM HEWIT et al

Fig. 52

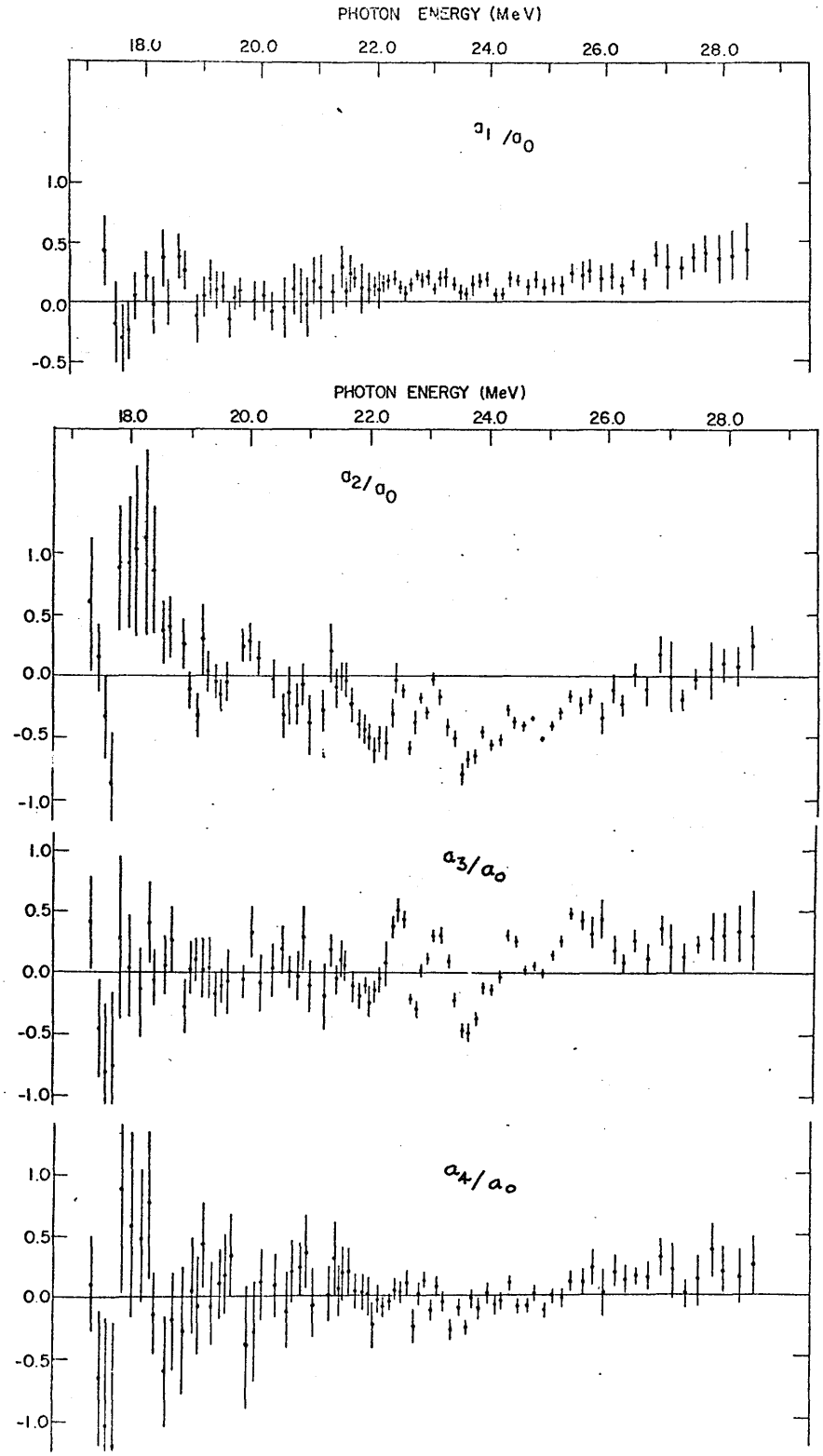

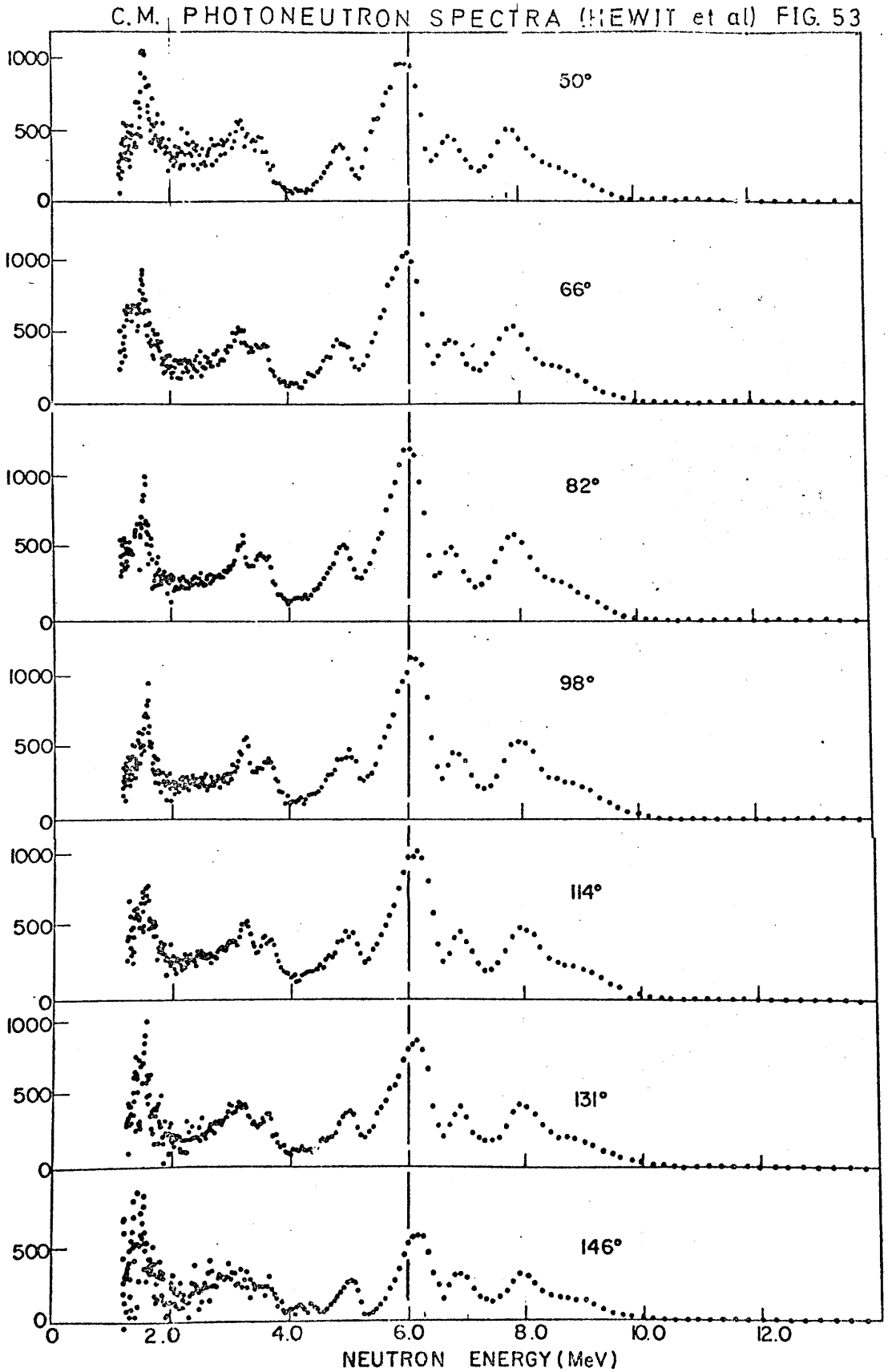
C.M. PHOTONEUTRON SPECTRA (HEWIT et al) FIG. 53
1000
500
0
50°
66°
82°
98°
114°
131°
146°
0
2.0
4.0
6.0
8.0
10.0
12.0
NEUTRON ENERGY (MeV)

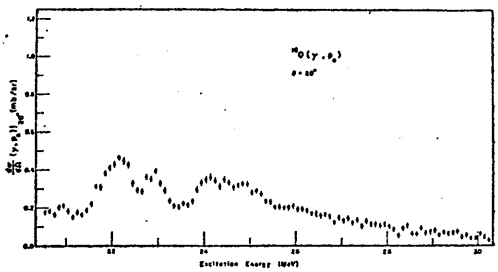

Fig. 2(a). $^{16}O(\gamma, p_0)$. Differential cross section at 20°.

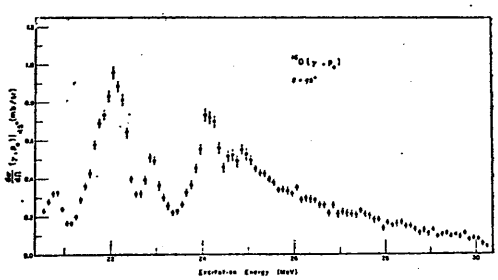

Fig. 2(b). $^{16}O(\gamma, p_0)$. Differential cross section at 45°.

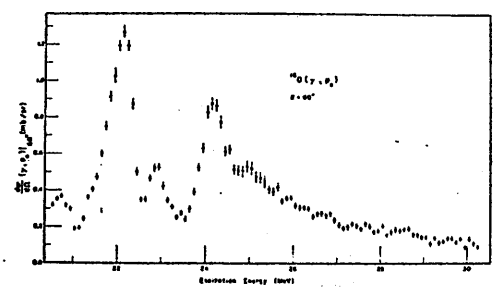

Fig. 2(c). $^{16}O(\gamma, p_0)$. Differential cross section at 60°.

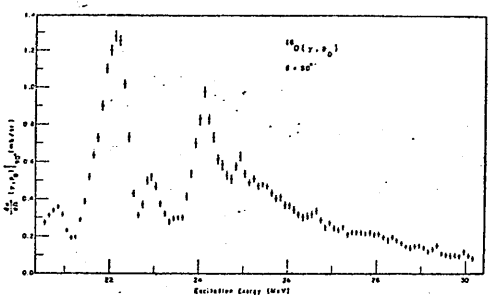

Fig. 2(d). $^{16}O(\gamma, p_0)$. Differential cross section at 90°.

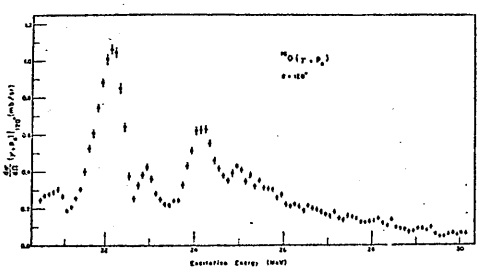

Fig. 2(e). $^{16}O(\gamma, p_0)$. Differential cross section at 120°.

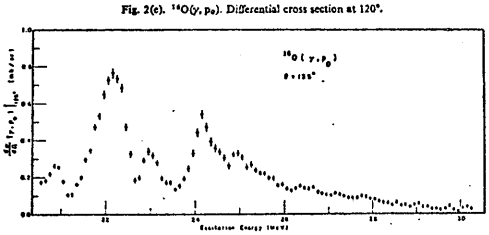

Fig. 2(f). $^{16}O(\gamma, p_0)$. Differential cross section at 135°.

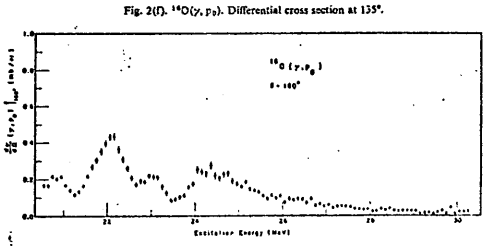

Fig. 2(g). $^{16}O(\gamma, p_0)$. Differential cross section at 160°.

Summary of agreement between different measurements

of angular distributions in $(0^{16} + \gamma)$ Energy range : 21.0 MeV-2.59 MeV

	No. times difference is inside error	A_1/A_0	A_2/A_0	A_3/A_0	A_4/A_0
I	(γ,p) : (p,γ) : Earle-Baglin	9/19	13/19	13/19	-
II	(γ,n) : (γ,p) : Syme -Baglin	8/40	25/48	21/48	24/48
III	(γ,n) : $(\gamma,n)^*$: Syme --Hewitt*	5/7	6/7	6/7	5/7

NOTES: I Earle-Baglin show substantial agreement ($\gtrsim$ 50% of time)

II (a) Syme-Earle $\fallingdotseq$ Syme-Baglin; within the errors

(b) Syme-Baglin are inside errors $\sim$ 50% of the time except for A_1. Some of the different A_3 values are very different (opposite sign) and this is not a comparison which necessarily should be exact.

III (a)* Uses re-normalised Hewitt results for $(\gamma,n)^*$

the surprising agreement is due to two things -

(i) The errors on the renormalised Hewitt coefficients are larger, due to the approximations in the method. Hence agreement is easier.

(ii) There is some better agreement, especially in A_2/A_0 and A_3/A_0 where the large oscillations in the coefficients are substantially reduced at some of the few points tested.

distribution of O^{16} photoneutrons are presented in figure 50. These may be compared with the corresponding (p,γ)[92] and (γ,p)[150] results (figures (4,51)) and with the similar (γ,n) measurements made by Hewitt et. al.[151] (figure 52).

The latter experiment used a T.O.F. technique with one flight path and successive deflection of the electron beam to produce several angles. Little agreement is found between the two (γ,n_0) measurements. The author believes this to be due to a systematic error in the energy calibration used by Hewitt et. al., for their published C.M. spectra (reproduced in figure 53) show an increase in energy of the peaks from forward to backward angles which does not appear in either the present work (figure 39) or the (γ,p_0) data (reproduced in figure 54). The misalignment is of order 300 k.e.V. between extreme spectra and can easily account for the oscillatory nature of all the coefficient ratios found by this group. It is equally unfortunate that although the experiment of Hewitt et. al. was performed relative to Deuterium,[151] the absolute cross-section scale was later renormalised to the earlier measurement of Khan et. al.[141] and no confirmation of this earlier result was obtained. These measurements are now being repeated[152] and the forthcoming data may provide a useful comparison with the present result.

The results of the present angular distribution experiment are seen to be similar in form to those from the (p,γ) and (γ,p) reactions, with the exception of the A_3/A_0 coefficient which has the opposite sign. Interpretation of this data requires a knowledge of the relationship between the observed coefficients and the matrix elements of the competing reaction channels.

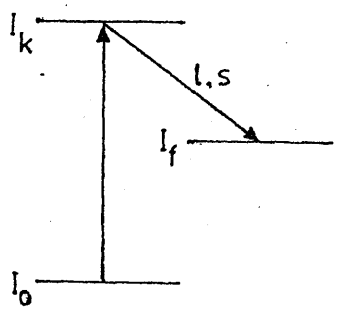

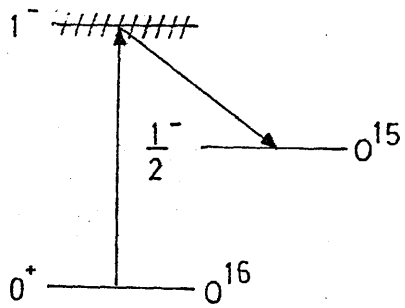

Representation	General Formula	O^{16} (γ,n) O^{15} case
		$s = \frac{1}{2}$ l = even (parity)
channel spin	$s + I_f = S$ $S + l = I_k$	S = 1 only l = 0,2
j-representation	$l + s = j$ $j + I_f = I_k$	$l = 0 : j = \frac{1}{2}$ $l = 2 : j = \frac{5}{2}, \frac{3}{2}$

Angular Distribution Expansion. $\left(\frac{d\sigma}{d\Omega}=\frac{\lambda^2}{8}\sum_{L=0}^{4}A_L\,P_L(\cos\theta)\right)$ Table 14

$$A_0 = 3B_p^2(0,M1) + 3B_p^2(M1) + 3B_s^2(E1) + 3B_d^2(E1) + 5B_p^2(E2) + 5B_f^2(E2)$$

$$A_1 = 2\left[-3.7\ \mathrm{Re}(B_s^*(E1)B_p(M1)) + 4.7\ \mathrm{Re}(B_s^*(E1)B_p(E2))\right.$$
$$-2.6\ \mathrm{Re}(B_d^*(E1)B_p(M1)) - 0.7\ \mathrm{Re}(B_d^*(E1)B_p(E2))$$
$$\left.+4.9\ \mathrm{Re}(B_d^*(E1)B_f(E2))\right]$$

$$A_2 = -3\ B_p^2(0,M1) - 1.5\ B_d^2(E1) + 1.5\ B_p^2(M1) + 2.5\ B_f^2(E2)$$
$$+2\left[2.1\ \mathrm{Re}\ (B_s^*(E1)B_d(E1)) - 5.8\ \mathrm{Re}\ (B_p^*(M1)B_p(E2))\right.$$
$$\left.-4.7\ \mathrm{Re}\ (B_p^*(M1)B_f(E2)) - 0.9\ \mathrm{Re}\ (B_p^*(E2)B_f(E2))\right]$$

$$A_3 = 2\left[3.9\ \mathrm{Re}\ (B_s^*(E1)B_f(E2)) + 4.0\ \mathrm{Re}\ (B_d^*(E1)B_p(E2))\right.$$
$$\left.-2.2\ \mathrm{Re}\ (B_d^*(E1)B_f(E2))\right]$$

$$A_4 = 14.\ \mathrm{Re}\ (B_p^*(E2)B_f(E2)) - 2.9\ B_f^2(E2)$$

Simplified Expression. (No M1) and with $B_1=a_1e^{i\delta_1}$ and $\Delta_{sd}=\delta_s-\delta_d$, etc.

$$A_0 = 3(a_s^2 + a_d^2) + 5(a_p^2 + a_f^2)$$

$$A_1 = 9.48\ a_s a_p\ \cos\Delta_{ps} - 1.34\ a_d a_p\ \cos\Delta_{pd} + 9.86\ a_d a_f\ \cos\Delta_{fd}$$

$$A_2 = 2.5\ a_p^2 - 1.5\ a_d^2 + 2.86\ a_f^2 + 3\sqrt{2}\ a_s a_d\ \cos\Delta_{ds} - 1.74\ a_p a_f\ \cos\Delta_{fp}$$

$$A_3 = 7.74\ a_s a_p\ \cos\Delta_{ps} + 8.04\ a_d a_p\ \cos\Delta_{pd} - 4.38\ a_d a_f\ \cos\Delta_{fd}$$

$$A_4 = 14.\ a_p a_f\ \cos\Delta_{fp} - 2.86\ a_f^2$$

Polarization Expansion. (No M1) $\left(\frac{d\vec{P}}{d\Omega}=\hat{k}\,\lambda^2 0.44\sum_{L=1}^{4}C_L\,P_L(\cos\theta)\right)$

$$C_1 = -0.79\ a_s a_p\ \sin\Delta_{ps} + 0.45\ a_d a_p\ \sin\Delta_{pd} + 0.82\ a_d a_f\ \sin\Delta_{fd}$$

$$C_2 = 0.47\ a_s a_d\ \sin\Delta_{ds} - 0.33\ a_p a_f\ \sin\Delta_{fp}$$

$$C_3 = 0.69\ a_s a_f\ \sin\Delta_{fs} - 0.72\ a_d a_p\ \sin\Delta_{pd}$$

$$C_4 = 1.06\ a_p a_f\ \sin\Delta_{fp}$$

5.8 The relationship between the Legendre coefficients and the reaction matrix.

The Legendre coefficients of the angular distribution may be expressed in terms of particular elements of the reaction matrix in either the j-representation[154-155] or the channel spin representation[130-153] for coupling the final angular momenta to obtain that of the intermediate state and hence the multipolarity of the transition (figure 55). The reaction amplitude associated with channel spin S is just a linear combination of the two corresponding amplitudes in the j-representation and similar formulae result. That from the channel spin representation[156] is quoted here in table 14(a), in the notation used by Baglin and Thompson,[150] for the Legendre coefficients A_0 to A_4 in the angular distribution of the reaction

$$\gamma + A \rightarrow (A-1) + \text{nucleon},$$

with E1, M1 and E2 excitations considered.

In this expression $B_l(S,gL)$ represents the matrix element of the process with channel spin 5 in which a nucleon of arbital angular momentum l is emitted following electric (g=E) or magnetic (g=M) multipole excitation of order L, and λ is the reduced wavelength of the incoming photon. Table 14(b) shows the same expression with the matrix elements expressed as the product of an amplitude and a phase factor: (153)

$$B_l(S,gL) = a_l e^{i\delta_l}$$

where the phase difference is defined as $\Delta_{l_1 l_2} = \delta_{l_1} - \delta_{l_2}$

The similar expansion of the angular distributions of differential polarization[155,153] is presented in table 14(c), and the combination of the nine equations may be sufficient to obtain the relative

amplitudes and phase relations once complete polarization distributions are published, but this is not possible at present.

5.9 Analysis of Angular Distribution Data in the Pure E1 Approximation.

Electric Dipole processes are known to dominate the giant resonance region so that a preliminary analysis may be made neglecting the higher multipoles. In this case the expression given for the angular distribution expansion simplifies to

$$A_2/A_o = \alpha = (-0.5 + \sqrt{2}.X.\cos\Delta)/(1+X^2) \qquad (5.9.1)$$

where $X = a_s/a_d$ is the ratio of the E1, s-wave amplitude to that of the E1, d-wave and $\Delta = \Delta sd$. The range of excursions of A_2/A_o in the present data from the pure d-wave value of -0.5 indicates a minimum value of $X \approx 0.2$ so that the intensity of s-wave admixture is $a_s^2/a_d^2 \approx 0.04$, in agreement with similar rough analyses of their proton data by Daglin and Thompson[150] and Earle and Tanner.[92]

The relative polarisation is defined by Baldin et. al.[155] with respect to the eigenvalue (j_n) of the intrinsic spin of the particle, by

$$f = (1/j_n)\frac{dP}{d\bar{\Omega}} \Big/ \frac{d\sigma}{d\bar{\Omega}} \qquad (5.9.2)$$

For pure E1 absorption, the expansion already given for the differential polarisation simplifies so that the relative polarisation is given by

$$\beta = j_n f = \hat{\underline{k}} * 1.06 * (-x\sin\Delta/(1.75+2x^2+(1/\sqrt{2})x\cos\Delta))\sin 2\theta$$

where $\hat{\underline{k}}$ is a unit vector normal to the scattering plane. The relative polarisation is a maximum at 45^o and has been measured at this angle by Cole[153,156] whose preliminary results are shown in figure 57. The resolution of this data is much improved from the early results of Bertozzi et. al.[39] (figure 4) but is not as good as that of the angular distribution measurements and the energy scales do not

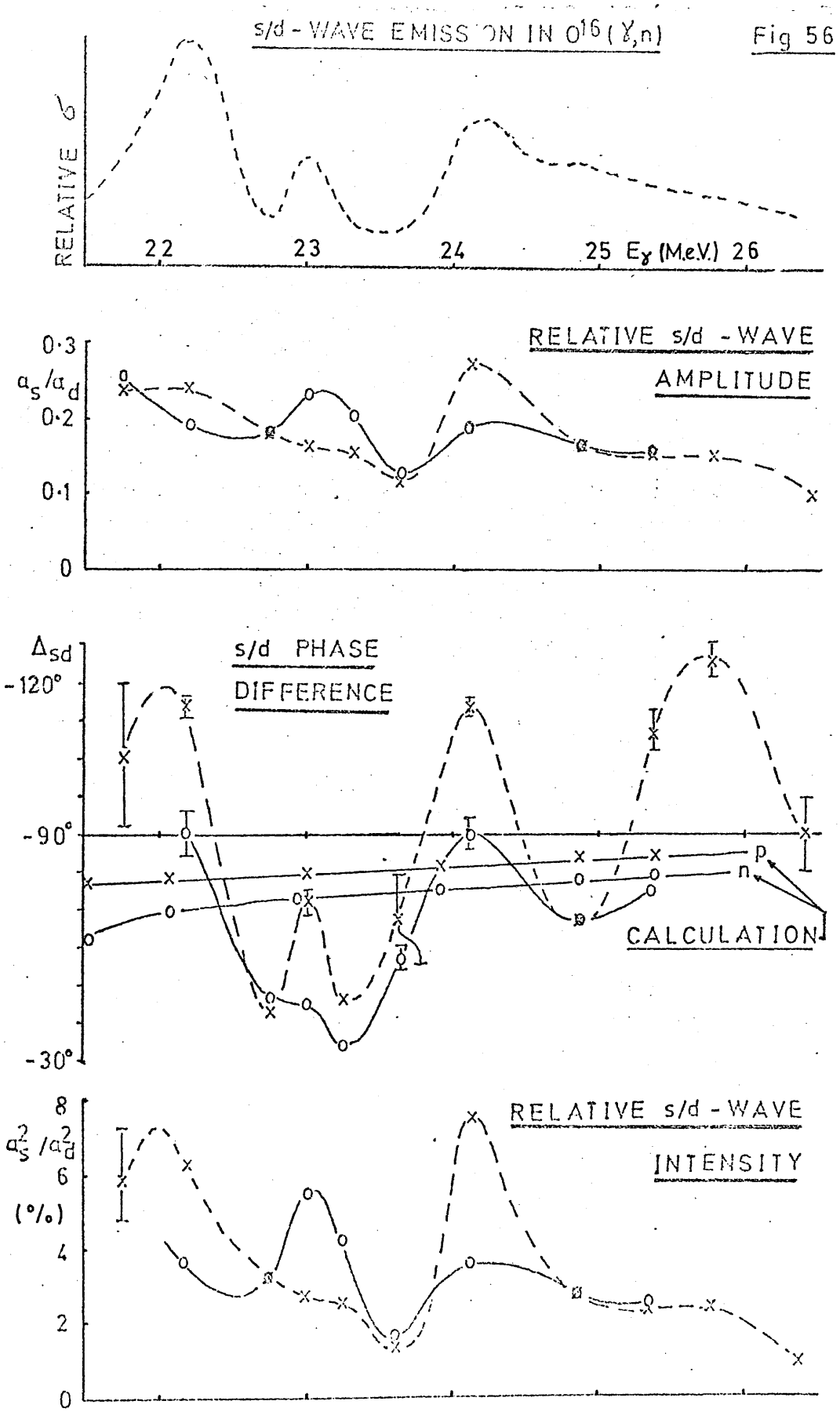
s/d - WAVE EMISSION IN $O^{16}(\gamma,n)$
Fig 56
RELATIVE σ
22
23
24
25 E_γ (M.eV.) 26
RELATIVE s/d - WAVE AMPLITUDE
a_s/a_d
0·3
0·2
0·1
0
Δ_{sd}
s/d PHASE DIFFERENCE
-120°
-90°
-30°
p
n
CALCULATION
RELATIVE s/d - WAVE INTENSITY
a_s^2/a_d^2
(%)
8
6
4
2
0

O^{16} (γ,n) Polarization Data (Cole) Fig. 57.

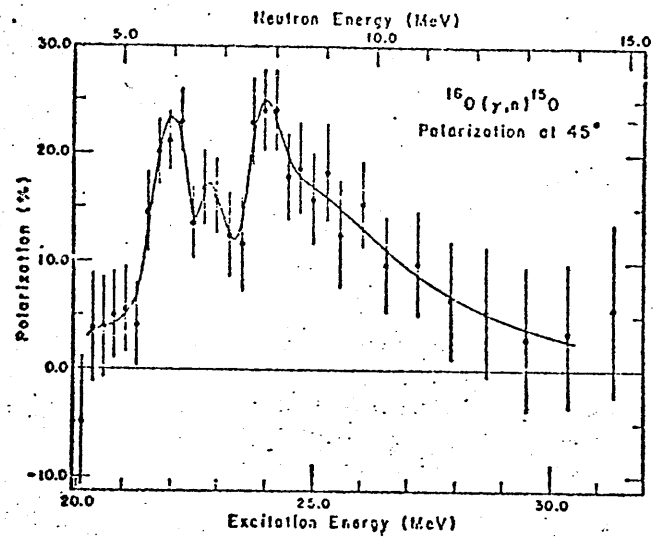

O^{16} (γ,n) Predictions of Fujji Fig. 58.

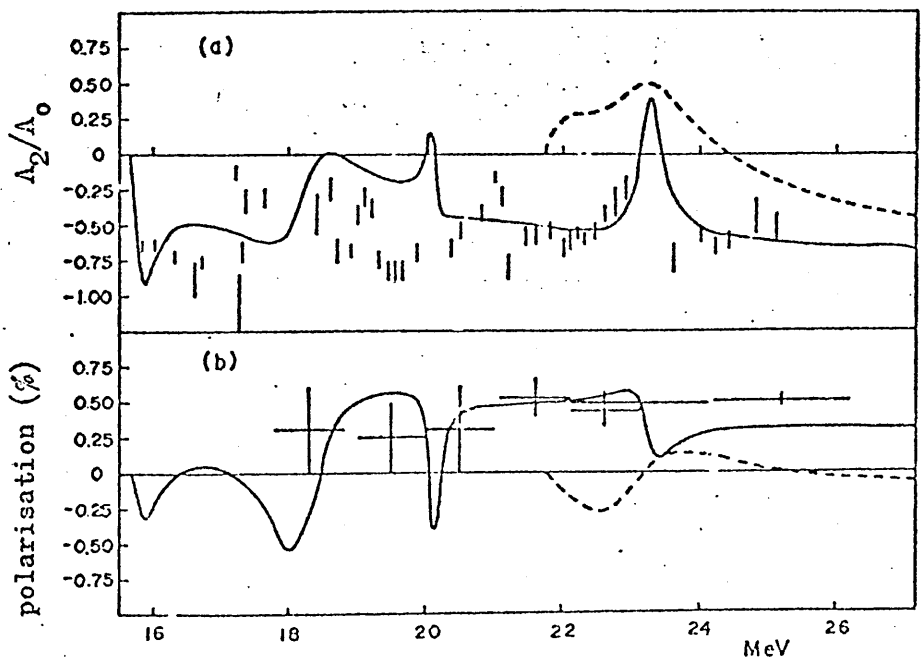

correspond exactly so that the comparison of data sets is more safely made in the peaks and valleys than in the regions of rapidly varying cross-section.

Equations (5.9.1) and (5.9.3) have been solved at several energies through the giant resonance, giving $x^2 = a_s^2/a_d^2$ as a function of α and β and therefore determining Δ with an ambiguity in sign. The polarisation data of Cole and the A_2/A_o ratio from the present result were used and the analysis was also carried out with the (γ,p_o) data of Baglin and Thompson, to examine possible differences in the phase relations of neutron and proton emission. This analysis is sensitive to the errors on both sets of data and is subject to some uncertainty due to the undoubted presence of some higher multipole radiation (and the assumption that the neutron polarisations may be used for protons) but it should provide a reasonable first assessment of the distribution of s-wave intensity.

From the results (figure 56) the intermediate structure of the O^{16} giant dipole resonance would appear to be reasonably well correlated with a varying interference between the partial s and d wave emission following El excitation, with a fairly regular oscillation of the phase difference with energy. This oscillation is similar in energy dependence for both protons and neutrons although the magnitude of the phase difference variation associated with proton emission seems greater and the average phase difference is nearer $-\pi/2$ in this case, in accordance with the optical model predictions of the gross (potential + coulomb) phase shifts shown in figures 49,56.

The intensity of s-wave admixture a_s^2/a_d^2 is $\lesssim 8\%$ and is seen to

follow the resonant structure with differences in the distribution of strength in the neutron and proton channels. This arises from the slight difference in the A_2/A_0 coefficient for neutrons and protons and its significance must be clouded by the equally probable slight difference in neutron and proton polarisations which is unknown at present.

From the calculation of Gillet[32] (table 1) the maximum non-d-wave impurities in the two dominant transitions ($1p^{-1}1d5/2$; "22 M.e.V."), ($1p^{-1}1d3/2$, "25 M.e.V.") are 20% and 8% respectively. The present results do not contradict these estimates, and the O^{16} dipole resonance is confirmed to be dominated by d-wave emission following E1 excitation.

5.10 Comparison of A_2/A_0 coefficient with 1plh calculations

The (p,γ) angular distribution and (γ,n_0) polarisation predictions of Buck and Hill[38] (figure 4) may be compared with the results of a similar (γ,n_0) continuum calculation by Fujji[44] (figure 58) and with the present data. Both calculations correctly predict a dominance of d-wave emission and therefore an isotropy $A_2/A_0 = -0.5$ in the giant resonance, with s-wave interference generating a slightly positive value at 20 M.e.V., contrary to experiment. (This region is not entirely ground-state in the present result). The main feature of the measured A_2/A_0 coefficient is the small negative value at ~23.3 M.e.V., seen also in the (p,γ) work (figure 4). This trend is in accord with the Fujji calculation where it appears to be exaggerated and a positive value is predicted. The calculations produce fairly similar polarisation spectra whose average value and lack of resonant structure are in dispute with the modern measurements of Cole[156] (figure 57).

It seems reasonable to summarise that the mixture of partial s and d waves is not predicted very well at present and some further consideration of this problem is justified by the previous analysis of the polarisation data and the present angular distributions. The lplh approximation does not seem to account for the observed variation in the A_2/A_0 ratio and higher (npnh) configurations may have to be included.

5.11 Examination of Information from the A_4/A_0 Coefficient

It may be seen from table 14 that the A_4 coefficient arises entirely from E2 terms so that non-zero values of this perameter provide definite location of E2 absorption. The present results therefore confirm significant E2 absorption in several specific energy regions through the giant resonance (figure 50) in contrast with the (p,γ) data[92] and the general conclusions reached by Baglin et. al. from their (γ,p_0) experiment.[150] However the A_4/A_0 coefficient from the (γ,p_0) data is reproduced in figure 51 and there is a close similarity between the structure observed therein and that seen in the present experiment, although the average value seen by Baglin is about zero. Since the present data was normalised to $A_4/A_0 = 0$ for $D^2(\gamma,n)p$ the average A_4/A_0 ratio should be fairly well defined.

Within the errors, $A_4/A_0 \approx 0$ in the ground state region of the present data except in a few specific energy regions. As no significantly negative values are found in this region, both f and p wave emission are present in the E2 absorption seen here, and the following limited observations can be made.

$$a_p \geq 0.207\, a_f \quad \text{and} \quad \cos \Delta_{pf} \geq 0$$

If $a_p = 0$ then $a_f = 0$ and $A_4 = 0$

Further analysis requires consideration of the combination of all coefficient values with polarisation data.

In the non ground-state region at about 20 M.e.V., large negative values of A_4/A_0 are found, probably due to E2 f-wave transitions to the 6.18 M.e.V. 3/2 excited state of O^{16}. The shape of the A_4/A_0 depression is consistent with the increase in the $f_{7/2}$ transmission coefficient at these energies and the cut-off imposed by the bremsstrahlung spectrum end-point at about (26.9 - 6.2) M.e.V. = 21.7 M.e.V. for transitions to this state. Caldwell[101] found that this transition took almost 30% of the strength in the ground state transition up to 28.6 M.e.V. (table 11).

5.12 The Odd Legendre Coefficients

A_1 and A_3 consist of cross terms representing interference between radiation of opposite parity. A_3 involves only E1/E2 interference while A_1 also includes E1/M1 terms. The ratios of the odd coefficients with respect to A_0 for the (γ,p_0) reaction have been calculated from the raw coefficients published by Baglin and Thompson[150] and are presented in figure 59 for comparison with the (p,γ) work[92] (figure 4) and the present (γ,n_0) result of figure 50.

The (γ,p_0) results show a gradually increasing positive A_1/A_0 ratio with regular variations around the average value. The (p,γ) data confirm the general trend but unfortunately do not cover the region of interest in sufficient detail to check all the variations although the significant change between 22.2 and 22.8 M.e.V. is confirmed. Thus the conclusion derived from the (p,γ) work of a relatively constant A_1/A_0

ODD COEFFICIENTS IN $O^{16}(\gamma, p_0)$ FIG. 59

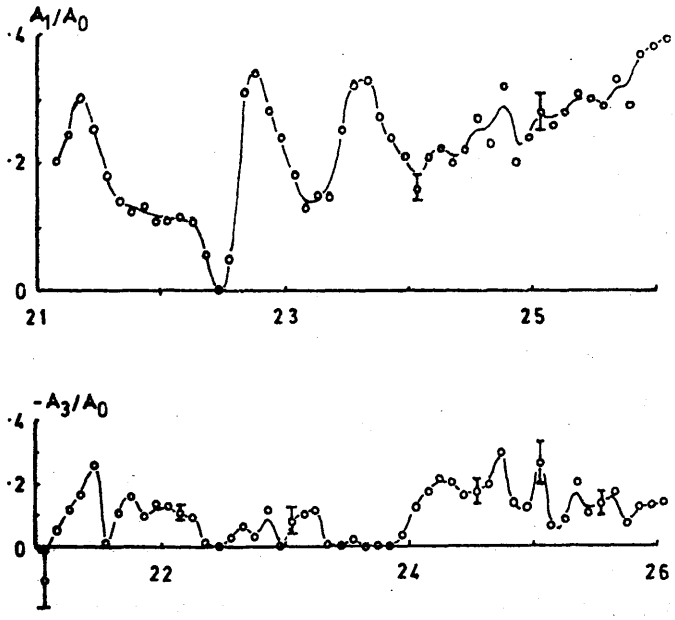

A_3/A_1 RATIOS FIG. 60

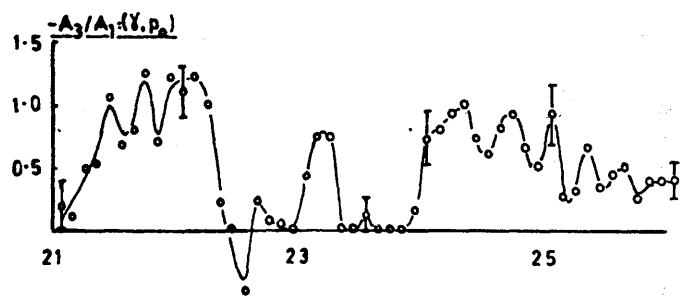

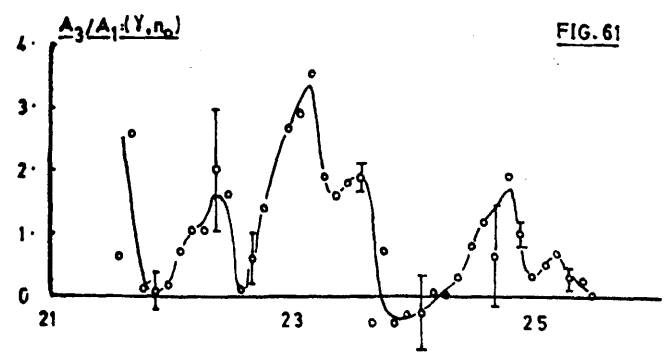

FIG. 61

(92) is seen to have been drawn from the uncertainties in that data. The general increase seen by both these experiments in the average A_1/A_0 value from 21 to 26 M.e.V. may indicate the presence of a broad E2 state expected just above the giant dipole resonance or a distribution of weak states in the region or both, while M1 effects are not excluded.

The present (γ,n_0) results show a similar trend, with a positive A_1/A_0 value increasing from about 0.05 to 1.5 in the 21 to 26 M.e.V. energy range and with superimposed fluctuations about the average value, which is about half that found for protons at all energies. This finite positive value immediately contradicts the prediction of a small negative assymetry made by the quadrupole effective charge hypothesis. Other mechanisms to explain this forward peaking will be discussed later. The neutron assymmetry ratio appears to be slightly more structured and the only obvious correlation with the proton data is the maximum at 22.7 M.e.V.

A similar comparison of the A_3/A_0 coefficient ratios shows the distribution of strength in A_3/A_0 to be similar in the $(p,\gamma)/(\gamma,p_0)$ and (γ,n_0) cases but the neutron ratio has a different sign (Note the negative plot of the (γ,p_0) results). The positive A_3/A_0 ratio observed in (γ,n) requires the presence of both partial waves in emission following E2 excitation (Table 13(b)). Because the average magnitudes of A_1/A_0 and A_3/A_0 were similar in their (p,γ) data, Earle and Tanner suggested E1/M1 interference (giving $A_3 = 0$) as less likely than E1/E2 and, neglecting the E1 s-wave component, showed that A_3/A_1 should be -6.0 or - 0.44 for interference entirely from E1x(E2,p) or

entirely from E1x(E2,f), respectively.[92] They obtained $A_3/A_1 = -0.8$ and concluded that E2 transitions were dominated by the f-wave emission component, despite their zero A_4/A_0 value.

The analysis of section 5.9 has shown that neglect of the E1, s-wave amplitude is not a very good approximation ($a_s = 0.25\ a_d$) but the same analysis has been performed (with this reservation in mind) for the (γ,p_o) data[150] and the present (γ,n_o) results and the corresponding A_3/A_1 ratios are compared in figures 60 and 61. The (γ,p_o) A_3/A_1 ratio (negative plot) confirms the earlier (p,γ) value but only in three well-defined energy regions, the result being about zero between these. This corresponds to essentially zero values of A_3, whose existence in the earlier work was not conclusive. A similar distribution of (A_3/A_1) with zeroes at about the same energies is found in the neutron case, but the sign is opposite and the magnitude is larger, especially in the area around 23 M.e.V. This confirms the earlier conclusion that both p and f waves are significant for E2 emission of neutrons.

Some orders of magnitude may be obtained in the energy regions where $A_3 = 0$, for if the s-wave amplitude of E1 emission is neglected, then

$$A_3 = 0 = a_p \cos\Delta_{pd} \approx 0.55\ a_f \cos\Delta_{fd} \qquad (5.12.1)$$

and neglecting the intensity terms of higher multipoles in A_o and M1 terms in A_1 it can be shown that:

$$A_1/A_o \approx 3(a_f/a_d) \cos\Delta_{fd} \approx 5.4(a_p/a_d) \cos\Delta_{pd} \qquad (5.12.2)$$

For protons this implies no E2 absorption at ~22.5 M.e.V., while at 23.6 M.e.V. $a_f/a_d \gtrsim 0.1$, $a_p/a_d \gtrsim 0.055$. A similar conclusion of no E2

FIGURE 62

E2 CROSS SECTIONS

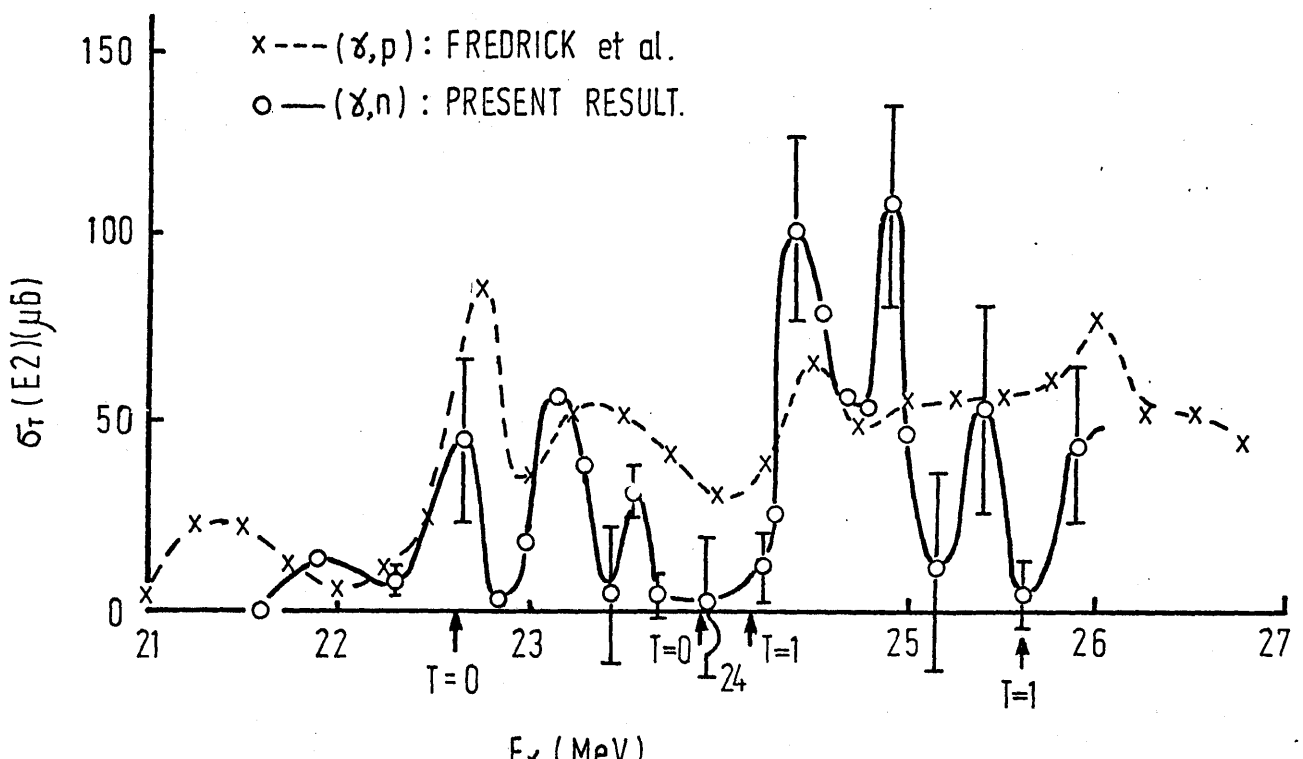

FIG. 2A

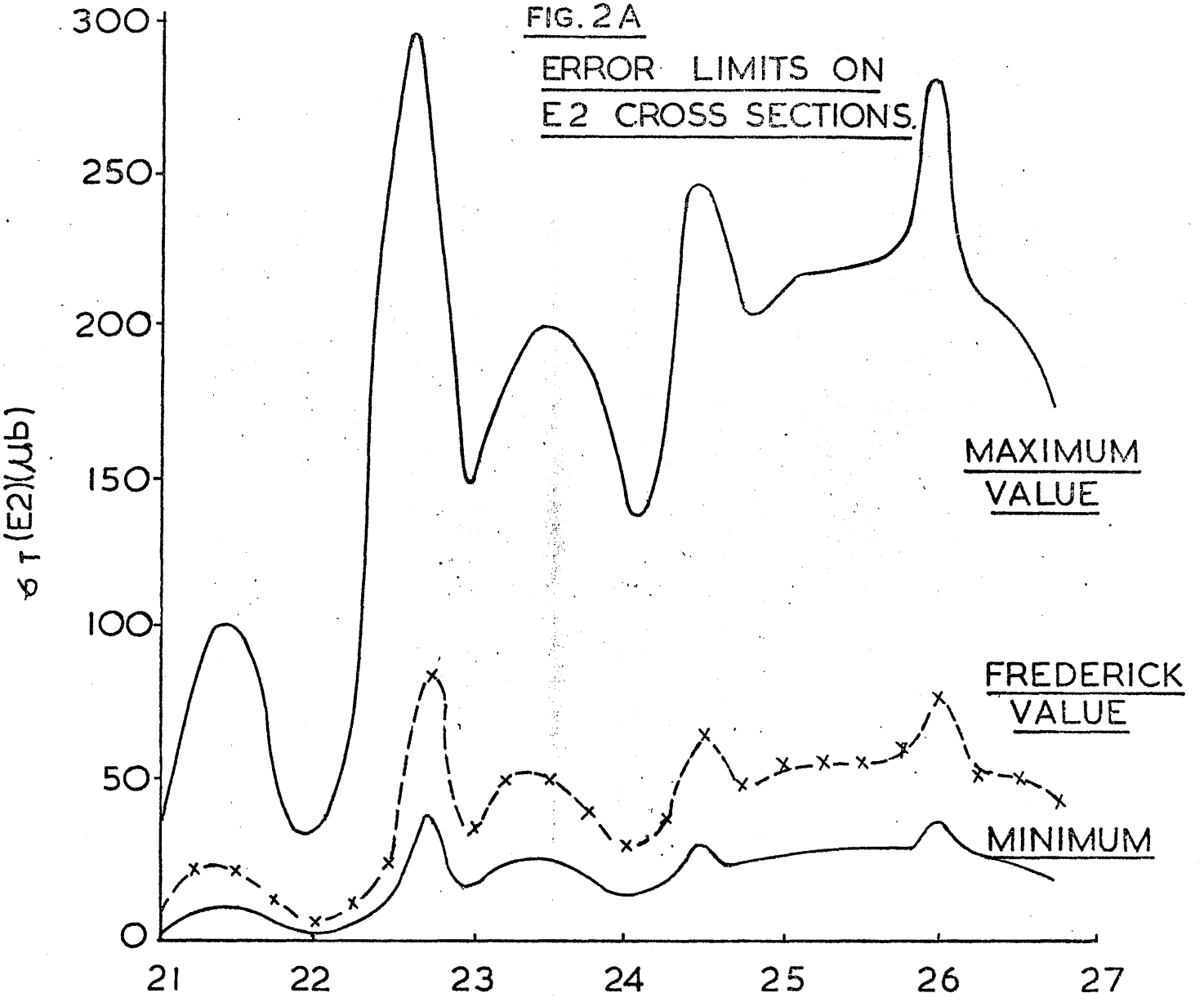
ERROR LIMITS ON
E2 CROSS SECTIONS.
MAXIMUM
VALUE
FREDERICK
VALUE
MINIMUM
σ τ (E2)(μb)
300
250
200
150
100
50
0
21
22
23
24
25
26
27

absorption at 25.6 M.e.V. in the neutron data is verified by $A_4/A_o = 0$ at that point, while other zero values of A_3 give $a_f/a_d \geq .03$, $a_p/a_d \geq .018$ for the E2 photoneutron transitions.

M1 transitions in the present energy range are expected to be weak, for Spicer and Eisenberg[35] predict no significant magnetic dipole strength except possibly at 19 M.e.V. and 28 M.e.V. in O^{16}. It is not possible to obtain information on the relative strength of magnetic transitions from the present data without extensive new polarization data.

5.13 The E2 ground-state cross-section.

Interference terms appear to be of the same magnitude for neutron or proton emission so that it would seem reasonable to obtain an order of magnitude of the E2 cross section for neutron emission using the formula of Fredrick,[155] which was calculated for 1plh E2 transitions involving protons under the simple 'off-resonance' assumption of zero phase differences:

$$\sigma(E2)/\sigma(E1) \approx (5.69A_1^2 + 6.65A_3^2 + 7.70A_1A_3)/(22.9A_o^2) \qquad (5.13.1)$$

Figure 62 shows the $E2(\gamma,n_o)$ cross section obtained from this equation, (assuming $\sigma(E1) \approx \sigma_T$(measured)) and also the similar result obtained from the (γ,p) results of Fredrick et. al.[26] Note that this (γ,p) data was taken with 33 M.e.V. bremsstrahlung and is likely to be contaminated by non-ground state events which may explain the less definite structure obtained, but the general distribution of strength is in good agreement.

The E2 (γ,n) cross section appears to exhibit two broad ($\Gamma \gtrsim$1M.e.V.) resonances at about 23 M.e.V. and 24.7 M.e.V., with a possible finer

structure. This is more consistent with the distribution of many weak 1p1h and 2p2h E2 states predicted by Eisenberg et. al.[35,36] than the single broad resonance considered by Scherchenko and Yudkin[161] and Earle and Tanner.[92] For example, the T=0, 1p1h, E2 states in this energy range were predicted by Eisenberg and Spicer[35] to be at 22.6 and 23.9 M.e.V. with 7.1% and 5.0% of the T=0 transition strength respectively and the T=1, 1p1h, E2 levels took 0.4% and 18.6% of the T=1 strength at 24.15 and 25.6 M.e.V. The positions of these levels are shown in figure 47 where the comparison with the measured energies is not exact but not outwith the uncertainties involved in the determination of the energy eigenvalues. The sudden increase in E2 strength in the higher part of the 24.1-24.4 M.e.V. resonance to about 2% of the total cross-section and the corresponding increase in the interference effects at this energy may explain an earlier disagreement on the multipolarity of the 24.3 M.e.V. 'level'.[25,49,34]

The value obtained for the integrated E2 (γ,n_0) cross section in the ground-state region is:

$$\int_{21.6\ \text{M.e.V.}}^{26.0\ \text{M.e.V.}} \sigma(\gamma,n_0)dE = 129\ \text{M.e.V.} - \mu\text{b.}$$

or 1.3% of the total cross section. The corresponding value obtained from the (γ,p) results of Fredrick et. al.[26] is 215 M.e.V. - μb. From the present data,

$$\int_{21.6\ \text{M.e.V.}}^{26.0\ \text{M.e.V.}} \frac{\sigma(\gamma,n_0)}{E^2}\ dE = 0.243\ \mu\text{b./M.e.V.}$$

so that about 5% of the Gell-Mann Telegdi[15] sum rule (=5.5μb/M.e.V.) is exhausted. The corresponding proton figures are 0.378μb/M.e.V. and 7%

of the sum rule.

Although only 12% of the sum rule is accounted for by ground state transitions to proton and neutron channels, the large assymmetries seen in the non-ground-state region of the present experiment show that the E2 contribution to transitions through excited states may be important.

5.14 Discussion

Calculations in the El, 1plh approximation predict the gross distribution of dipole strength in O^{16} fairly well and therefore might be expected to provide a reasonable estimate of the trend of the polarization and the A_2/A_0 coefficient in the angular distribution of photoneutrons since these are dominated by the El terms. It has been shown that the 1plh model fails in this respect and that the interference between the s and d wave emission is correlated with the well-known structure of intermediate width (~700 k.e.V.) in the O^{16} giant resonance, and it is known that this structure cannot arise from a El-1plh basis.(157) Also this structure does not arise mainly from interference between the dominant El mode and higher multipoles since it appears at all angles with the same distribution (in first order) and also in the total cross-section. This situation leads naturally to the consideration of the effect of more complicated particle-hole configurations (or their equivalent) in the mainly 1plh giant dipole resonance.

It would seem reasonable to ask if such configurations are significant in present treatments of the O^{16} wave functions. Purser et. al.(159) measured the intensity of 2p2h impurity in O^{16} by the pick-up reactions $O^{16}(d,t)O^{15}$ and $O^{16}(d,He^3)$ and confirmed the existence of pair excitations in the O^{16} ground-state wave function with

CALCULATIONS OF FINE STRUCTURE IN $O^{16}(\gamma,n)O^{15}$

Fig 63

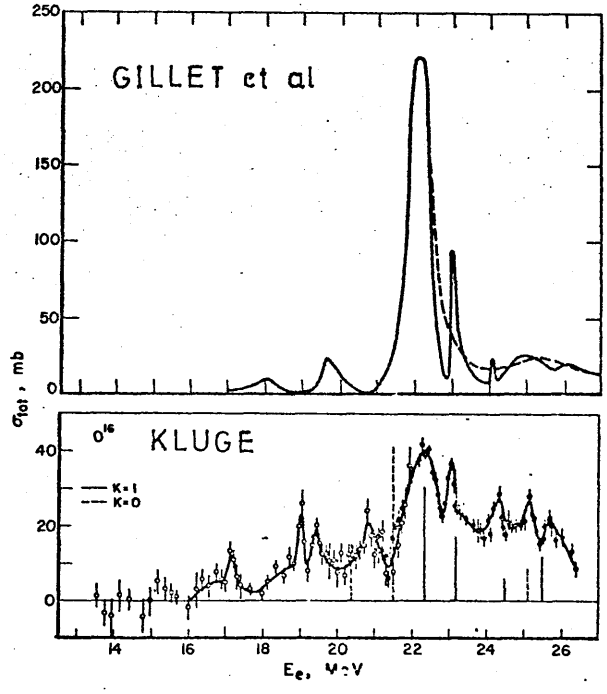

FIGURE 26. *The upper dashed curve is the result of the continuum calculation of reference 102.*

The solid curve is the result [111] of including the interference with the $2p-2h$ quasibound states listed in table 11 as well as the $4p-4h$ states at 21.05 MeV. The lower curve shows the experimental total absorption cross section [84] as well as the result of Kluge [105] who assumed the O^{16} ground state to have a slight positive deformation.

[– FROM HAYWARD (148)]

Fig 64

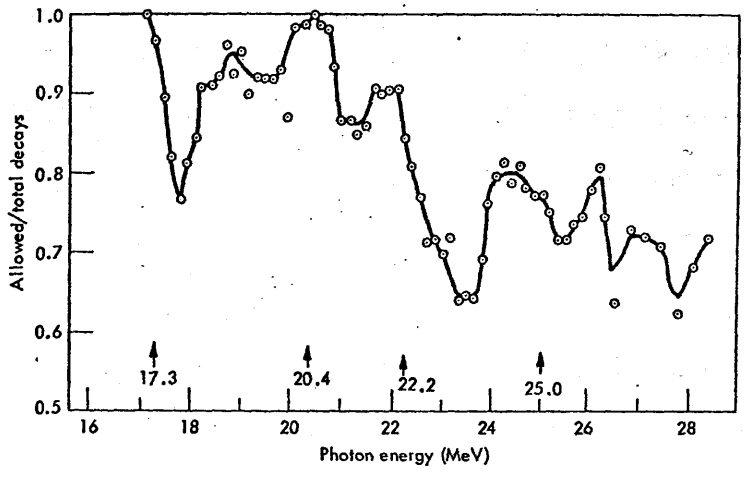

Fig. 37. Ratio of particle-hole theory "allowed" transition cross sections to total absorption cross section. Allowed transitions are the $1/2^-$ ground-state and $3/2^-$ third excited-state transitions in N^{15} and O^{15}.

[FROM CALDWELL[101]]

intensity comparable to the prediction of Brown and Green,[158,159] viz.

(5.14.1)

$$\psi_{16} = 0.874|0p,0h\rangle + 0.469|2p,2h\rangle + 0.120|4p,4h\rangle$$

This calculation[159] explained the existence of the low-lying positive parity states in O^{16} and the large E2 enhancements between them so that use of this wave function is equivalent to mixing the rotational band based on the 6 M.e.V.,0^+ state into the ground state, giving a slight positive deformation.[148] Kluge has treated photoabsorption in O^{16} in this way,[148,160] and the 1p1h dipole states were found to split according to the K=0 or K=1 transitions.

This effect of 2p2h excitations has been considered directly by Gillet et. al.[40] who showed there to be four 2p2h quasi-bound states in the O^{16} dipole resonance region and that the main 1p1h resonance was split by destructive interference with these 2p2h states. The results of the calculations of Kluge and Gillet et. al. are shown in figure 63 and good agreement is found with the total cross section shape for both methods.[148]

The calculation of Gillet was based largely on the peak in the $N^{14}(d,\gamma)$ reaction found in the valley of the dipole structure at 22.7 M.e.V. (Suffert et. al.[41]), for this reaction must proceed through a 2p2h excitation. The angular distribution of the emitted photon was found to be slightly forward-peaked in a way characteristic of E1 radiation with interference from other radiation of opposite parity (E2 or M1). As this reaction is isospin-inhibited for E1 radiation, some indication of both E2 absorption and isospin impurity are to be expected in this energy region. It is significant that both these features are evident in the data presented by the author. Both the E2

cross section and the T=0 admixture peak at about this energy (figures 62,49). Above 24.2 M.e.V., both quantities again rise and this may be related to the higher 2p2h states or the 3p3h states associated with resonances in this energy region for the reaction $C^{13}(He^3,\gamma)O^{16}$ ( )

Figure 64 shows the ratio of negative parity decays (E1,1p1h allowed) to total decays in the O^{16} giant resonance as measured by Caldwell.(101) The E1-1p1h mode is dominant, for 80% of the decays up to 28 M.e.V. are 'allowed', but the fraction of positive parity decay increases with energy, corresponding to the opening up of more decay channels. The large dip at 23.5 M.e.V. confirms the presence of up to 40% non-E1-1p1h decays in this region and other dips occur above 24 M.e.V. Also the isospin impurity measured by Caldwell tends to peak in these areas (figure 33) and the findings from the present data are confirmed. Since the isospin impurity and the E2 cross-sections are small, neither would seem to be the cause of the structure and the interference mechanism of Gillet appears attractive in explaining the structure and these small associated effects.

It seems important that the calculations of the dipole resonance involving higher particle-hole configurations or their equivalent be extended to include prediction of the polarization and angular distribution of photonucleons, even in a basically E1 approximation, for the experimental information is available to test for any improvement over the 1p1h approximation. Also polarization spectra at other angles will soon be available and the relative contributions of the positive parity transitions will then be accessible and the degree of agreement expected with the theoretical approximations may be somewhat better defined.

REFERENCES

LIST OF ABBREVIATIONS

Ann. Rev. Nuc. Sci.	Annual Review of Nuclear Science.
J. Phys. Rad.	Journal Physique et Radium.
N.I.M.	Nuclear Instruments and Methods.
N.P.	Nuclear Physics.
P.R.	Physical Review.
P.R.L.	Physical Review Letters.

References.

1.	Danos, M. and Fuller, E.G.	Ann. Rev. Nuc. Sci. 15, 29 (1965).
2.	Levinger, J.S.	'Nuclear Photodisintegration' Oxford Univ. Press, 1960.
3.	Fuller, E.G. and Hayward, E.	'Nuclear Reactions', Vol. 11, p113, North Holland., 1962.
4.	Hayward, E.	'Nuclear Structure and Electromagnetic Interactions'. Scottish Universities Summer School 1964.
5.	Eisenberg, J.M. and Greiner, W.	'Excitation Mechanisms of the Nucleus' North Holland, 1970.
6.	Siegert, A.J.F.	P.R. 52, 787, (1937)
8.	Trainor, L.E.H.	P.R. 85, 962, (1952)
9.	Radicatti, L.A.	P.R. 87, 521, (1952) Proc. Phys. Soc. A, 66, 139 (1953)
10.	Wilkinson, D.H.	Phil. Mag. Ser 8, 1,379, (1956)
11.	Thomas, Reiche and Kuhn.	Naturwissenschaften 13, 627 (1925) Z. Physik 33, 408, (1925)
12.	Heitler, W.	'The Quantum Theory of Radiation'. Clarendon Press, Oxford; (1954)
13.	Levinger, J.S. and Bethe, H.A.	P.R. 78, 115, (1950)
14.	Gell-Mann, M., Goldberger, M.C., and Thirring, W.E.	P.R. 95, 1612, (1954).
15.	Gell-Mann, M. and Telegdi, V.L.	P.R. 91, 169, (1953)
15'.	Wilkinson, D.H.	Phil. Mag. 44, 542, 1019, 1269, 1322, (1953)
16.	Baldwin, G.C. and Klaiber, G.S.	P.R. 71, (1947)
17.	Baldwin, G.C. and Klaiber, G.S.	P.R. 73, 1156, (1948).
18.	Goldhaber, M. and Teller, E.	P.R. 74, 1046, (1948).
19.	Migdal, A.	J. Phys. U.S.S.R., 8, 831, (1944).
20.	Toms, E.	U.S. Naval Res. Lab. B.I.B.24 (1965).

21.	Levinger, J.S.	P.R. 84, (1951).
22.	Steinwedel, H.and Jensen, J.H.D.	Z. Naturforch, 5a, 413, (1950).
23.	Danos, M. and Greiner, W.	P.R.L. 8, 113, (1964). P.R. 134, B,284, (1964). P.R. 138, B,876, (1965).
24.	Danos, M.	N.P. 5, 23, (1958).
25.	Okamoto, K.	P.R. 110, 143, (1958).
26.	Frederick, D.E., Stewart, J.J. and Morrison, R.C.	Preprint, 1969 Iowa State University.
27.	Wilkinson, D.H.	Ann. Rev. Nuc. Sci., 9, 1, (1959). Physicia, 22, 1039, (1956).
28.	Brink, D.	N.P. 4,215, (1957).
29.	Bohr, N.	Nature, 137, 344, (1936).
30.	Elliot, J.P, and Flowers, B.H.	Proc. Roy. Soc. (London) A242, 57 (1957).
31.	Brown, G.E. and Bosterli, M.	P.R.L. 3, 472, (1959).
32.	Gillet, V.	N.P. 54,321, (1964). and Thesis, Univ. of Paris.
33.	Burgov, N.A. et al.	Soviet Phys. J.E.T.P. 16, 50 (1963).
34.	Dodge, W.R., and Barber, W.C.	P.R. 127, 1740, (1962).
35.	Spicer, B.M. and Eisenberg, J.M.	N.P. 63,520 (1965).
36.	Eisenberg, J.M., Spicer, B.M. and Rose, M.E.	N.P. 71,273 (1963).
38.	Buck, B. and Hill, A.D.	N.P. A95,271, (1967).
39.	Bertozzi, W. et al.	Congr. Intern. Phys. Nucl. V, p1026, Paris (1964).
40.	Gillet, V., Melkanoff, M.A. and Raynal, J.	N.P. A97, 631, (1967)
41.	Suffert, M., Costa, C. and Magnac - Valette, D.	J. Phys. Rad., 24, 1029, (1963).
42.	Barker, F.C. and Mann, A.K.	Phil. Mag 2, 5, (1957).
44.	Fujii, S.	N.P. A312, 385, (1967).
47.	Kerst, D.W.	P.R. 60, 47, (1941).
48.	Barber, W.C. et al.	P.R. 120, 2681 (1961).

49.	Isabelle D.B., and Bishop, G.R.	N.P. 45(2), 209 (1963).
50.	Barber, W.C.	Ann. Rev. Nuc. Sci., 12, 1967.
51.	Bishop, G.R.	Nuclear Structure and Electromagnetic Interactions, Scottish Universities Summer School, 1964.
52.	de Forest, T., and Walecka, J.D.	Advances in Physics, 15, 1 (1966).
52.	Yanaguchi A. et al.	P.R.(C) 3, No.5, 1750, (1971).
54.	de Forest, T.	N.P. A312, 305, (1969).
55.	Sargent, C.P.	Proc. Acc. Conf. Cambridge, Mass., (1958).
56.	Bertozzi, W., Paolini, and Sargent, C.P.	P.R.(L), 110, 750, (1958).
57.	Firk, F.W.K. and Lokan, K.H.	P.R.L. 8, 321, (1962).
58.	Frik,F.W.K., Whittaker, Boway, Lokan and Rae	N.I.M. 23, 141, (1963).
59.	Firk, F.W.K.	N.P. 52, 437, (1964).
60.	Firk, F.W.K.	N.I.M. 28, 205, (1964).
61.	Bertozzi, W. et al.	N.I.M. 33, 199, (1965).
62.	Neiler, J.H. and Good, W. (ed. Marion, J.B. and Fowler, J.L.)	'Fast Neutron Physics' part I. Interscience, N.Y., (1960).
63.	Verbinski, V.V. and Courtney, J.C.	N.P. 73, 398, (1965).
66.	Koch, H.W. and Foote, R.S.	P.R. 91, 455A, (1953).
67.	Ziegler, B.	Z. Angew Phys. 10, 397, (1958). Z. Phys. 152, 506, (1958).
68.	Fuller, E.G. and Hayward, E.	P.R. 101, 692 (1956).
69.	Hirzel, O. and Waffler, H.	Helvitica Physica Acta, 20, 373 (1947).
70.	Penfold, A.S., and Leiss, J.E.	P.R. 114, 1332, (1959).
71.	Fuller, E.G., and Hayward, E.	P.R.L. 1, 1507, (1958), Int. Conf. Nuc. Str. Proceedings, Toronto Press, 1960.
72.	Ambler, E., Fuller, E.G., and Marshak, H.	P.R. 138, 117, (1965).

73.	Kelly, M.A., Berman, B.L., Bramblett, R.L., and Fultz, S.C.	P.R. 179, 1094, (1969).
74.	Huber, O., Leinhard, O., Scherrer, P., and Waffler, H.	Helv. Phys. Acta. 16, 431, (1943) 17, 139, (1964).
76.	Gorbunov, A.N. and Spiridonov, V.M.	J.E.T.P. 6, 16, (1958) 7, 596, 600, (1958).
77.	Milone, C. et al.	Nuovo Cimento 7, 729, (1958).
78.	Milone, C. and Rubbino, A.	Nuovo Cimento 13, 2607, (1959).
79.	Hatcher, C.R., Bramblett, R.L., Hansen, N.E., and Fultz, S.C.	N.I.M. 14, 337 (1961).
83.	Bertozzi, W. and Kowalski, S. (Eds.)	M.I.T. - 2098 - No 470, 1967.
85.	Mann, A.K. and Halpern, J.	P.R. 82, 882, (1951).
86.	Weinstock, E.W. and Halpern, J.	P.R. 94, 1651, (1954).
87.	Penner, S. and Leiss, J.E.	P.R. 144, 1101, (1959).
88.	Tanner, N.W., Thomas, G.C. and Meyerhof, W.E.	Nuovo Cimento 14, 257, (1959)
89.	Cohen, S.G., Fisher, P.S. and Warburton, E.K.	P.R. 121, 858, (1961).
90.	Tanner, N.W., Thomas, G.C., and Earle, E.O.	N.P. 52, 29, 45 (1964).
91.	Tanner, N.W.	N.P. 63, 383, (1965).
92.	Earle, E.D. and Tanner, N.W.	N.P. A95, 241 (1967)
93.	Morrison, R.C.	(Thesis, Univ. of Yale (1965))
	Morrison, R.C, Stewart, J.R., and O'Connell, J.S.	P.R.L. 15, No.8, 367 (1965)
100.	U.S. Dept. of Commerce	National Bureau of Standards Handbook 55. (1954)
101.	Caldwell, J.T.	Thesis, University of California, 1967. (U.C.R.L. - 50287).
102.	Hopkins, J.C., Martin, J.T., and Seagrave, J.D.	N.I.M. 56, 175, (1967)
103.	Price, B.T., Horton, C.C. and Spinney, K.T.	'Radiation Shielding' Pergammon Press, London, 1957.

104.	Reid, J.M.R.	Internal Report, Kelvin Laboratory, University of Glasgow, 1966.
105.	Bertozzi, W. et al	N.I.M. 33, 199, (1965).
106.	Wishart, L.P., Plattner, R. and Cranberg, L.	N.I.M. 57, 237, (1967).
108.	Gatti, E. and Svelto, V.	N.I.M. 30, 213, (1964).
109.	Sigfridsson, B.	N.I.M. 54, 13, (1967).
110.	Cocchi, M. and Rota, A.	N.I.M. 55, 365, (1967).
111.	McDonald, W.J. and Gedke, D.A.	N.I.M. 55, 1, (1967).
112.	Williams, C.	'Timing with photomultipliers', 'Ortec News', Ortec Ltd., Oak Ridge, Tenn.
113.	Gedke, D.A., and McDonald, W.J.	N.I.M. 58, 253, (1968).
114.	Kirkbride, J., Yates, E.C., and Crandall, D.G.	N.I.M. 52, 293 (1967).
115.	McKeown, J.	Thesis, University of Glasgow, 1971.
116.	Kellie, J.D.	Thesis, University of Glasgow, 1970.
120.	Bezic, N. et al	Institut Jozef Stephan Report R - 572, 1969.
121.	Koch, H.W., and Motz, J.W.	Reviews of Modern Physics, 31, 44, 1959.
122.	O'Dell, A.A. Jr., Sandiffer, C.W., Knowlen, R.B., and George, W.D.	N.I.M. 61, 340, (1968).
123.	Weissman, B.	Thesis, University of Yale, 1969 EAL Internal Report, No.81.
124.	Partovi, F.	Annals of Physics 27, 79 (1964).
125.	Berger, M.J. and Seltzer, S.M.	P.R.(C) 2, No.2, 621, (1970).
126.	Browning, Jr., W.E.	Nucleonics, Vol.9, No.3, 63, September, 1951.
127.	Mutchler, G.S.	Thesis, M.I.T. 1966.
128.	Kellie, J.D., Islam, M.N., Syme, D.B.C.B., and Crawford, G.I.	Accepted for publication in Journal of Physics (A) 1972.

129.	Foster, D.G., and Glasgow, D.W.	P.R.(C), 3, No. 2 (1971).
130.	Baldin, A.M., Gol'Danskii, V.I., and Rozenthal, I.L.	"Kinematics of Nuclear Reactions" Pergammon, London, 1961.
131.	Michalowicz, A.	"Kinematics of Nuclear Reactions" Iliffe Books Ltd., 1967, (Translated).
132.	Schwartz, R.B., Schrack, R.A., and Heaton, H.T.II.	N.B.S. Report to A.E.C. N.C.S.A.C. - 33.
133.	Bosco, B. and Fubini, S.	Nuovo Cimento 9, 350, 1958.
134.	Kuo, S.S.	'Numerical Methods and Computers'. Addison - Wesley, Mass. U.S.A.
135.	Heikkinen, D.	Decus 7-22, 1966 Digital Equipment Co. Ltd., (Distributors).
136.	Powell, M.J.D.	Computer Journal 7, 155 (1964).
140.	Wu, C.P., Firk, F.W.K., and Phillips, T.W.	P.R.L. 20, No.21, 1182 (1968).
141.	Khan, T.A., Hewitt, J.S., and McNeill, K.G.	Canadian J. Phys. 47, 1038 (1969).
142.	Geller, K.N., and Muirhead, E.G.	P.R.L. 11, No.8, 371, (1963).
143.	Bolen, L.N., and Whitehead, W.D.	P.R.L. 9, No.11, 458 (1962).
144.	Cook, B.C., Baglin, J.E., Bradford, J.N., and Griffin, J.E.	P.R. 143, 712 (1966).
145.	Caldwell, J.T., Bramblett, R.L., Berman, Harvey and Fultz.	P.R.L. 15, 976, (1965).
146.	Wycoff, J.M., Ziegler, B., Koch, H.W., and Uhlig, R.	P.R. 137, B576 (1965).
148.	Hayward, E.	'Photonuclear Reactions' N.B.S. Monograph 118, August 1970.
150.	Baglin, J.E.E., and Thompson, M.N.	N.P. A138, 73 (1969).
151.	Jury, J.W., Hewitt, J.S., and McNeil, K.G.	Canadian Journal of Physics 48, No.14, 1635 (1970).

152.	Drake, T.E.D.	Private Communication, December (1971).
153.	Firk, F.W.K.	'Low Energy Photonuclear Reactions' Ann. Rev. Nuc. Sci., 1970.
154.	Devons, S. and Goldfarb, L.J.B.	Encyclopedia of Physics XLII S. Flugg (Ed.) (1957), Springer - Verlag, Berlin, 458.
155.	Fredrick, D.E.	N.P. A101, 250 (1967).
156.	Cole, G.W. Jr.	Thesis 1970, University of Yale, Conn. U.S.A.
157.	Sarius, A.M., and Marangoni, M.	N.P. A132, 433, (1969).
158.	Purser, K.H., Alford, W.P. et al.	N.P. A132, 75, (1969).
159.	Brown, G.E., and Green, A.M.	N.P. 75, 401, (1965).
160.	Kluge, G.	Zeits f. Physik 197, 288 (1966), and Ref. 148.
161.	Scherchenco, V.G., and Yudin, N.	Atomic Energy Review 3, 3 (1965).

APP.1. Detection Efficiency of Organic Scintillators for Fast Neutrons.

Introduction: The Scintillation Counter.

Ionising radiations are known to produce fluorescence emission in suitable materials (Ref.1). Detection of this emission by any light - sensitive device allows the combination to function as a Scintillation Counter. Birks (Ref.1) gives a complete history of the development of the device from the visual scintillation counting practised with zinc sulphide screens in the 1930 era (Ref.2), to the fast, efficient range of instruments now in common use. Significant in the development of fast efficient neutron detectors were the combination of photomultiplier and zinc sulphide screen (Ref.3) and the detection of fast neutrons by scintillations due to recoil protons in crystalline Anthracene (Ref.4). The demonstration of similar properties in organic liquids (Ref.5) and plastics (Ref.6) allowed the development of large volume scintillation detectors with very fast (2-3 n.s.) decay times. Such organic scintillators have been found convenient detectors in neutron time of flight spectrometers by many authors. (Ref.7).

Fast Neutron Detection by Organic Scintillators and the Development of Efficiency Calculations.

The uncharged neutrons interact primarily with the nuclei of an absorber material and may be detected by the ionisation caused by secondary particles in these nuclear reactions. Fast neutrons ($E_N \geq 0.5$ Mev.) are best detected by (n,p) elastic scattering because the cross section for this process is an order of magnitude greater than the alternative process of absorption by light nuclei and the fraction of the incident neutron energy transferred to the elastic recoil is greatest

for scattering on hydrogen (Ref.1). Organic scintillators provide a conveniently high hydrogen content. Consideration of the (n,p) kinematics shows that:

$$EP = EN*COS^2(ALAB)$$

Where the quantities are respectively the proton and neutron energies, and the laboratory angle of scatter (= half the C.M. angle). Since the scattering is found to be isotropic in the C.M. for energies less than 10 Mev. (Ref. 10) the recoil proton energy is uniformly distributed from zero to EN.

Early uses of organic scintillators for neutron detection (Ref.8) concentrated on their use as proton recoil spectrometers, using the edge of this 'white' spectrum to identify the energy of the corresponding neutron group, and the number of pulses divided by the 'efficiency' to find the incident flux of neutrons. The basis of such techniques was a compromise in scintillator size. Small detectors were inefficient in stopping neutrons and liable to distortion of the recoil proton spectrum by proton losses, while large detectors promoted multiple neutron interactions in the scintillator. Since the scintillation response is non - linear in energy for heavily ionising particles (Ref.1), spectrum distortion also occurred and further, the detection efficiency was no longer simply related to the simple formula used, which assumed only single hydrogen collisions to be possible.

Corrections for the non - linear proton response (Refs. 1,9,10) were made and useful results were obtained for simple neutron spectroscopy, (Ref. 11) but efficiencies were low, (typically 2%) and many workers required larger detectors. Therefore, calculations of

RECOIL PROTON SPECTRA FROM HARDY (Ref. 12)

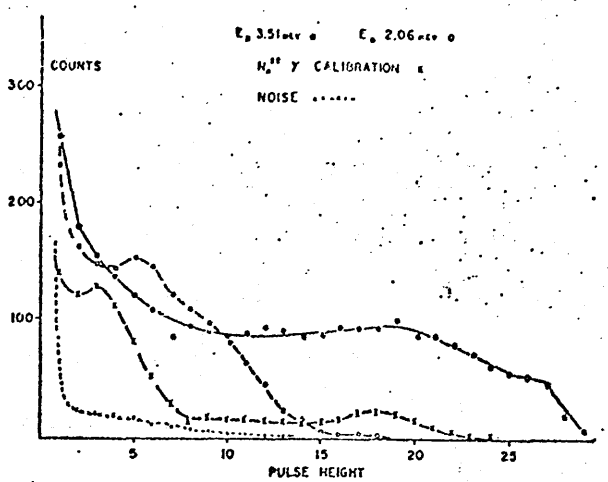

(A)

FIG. 3. Response to neutrons.

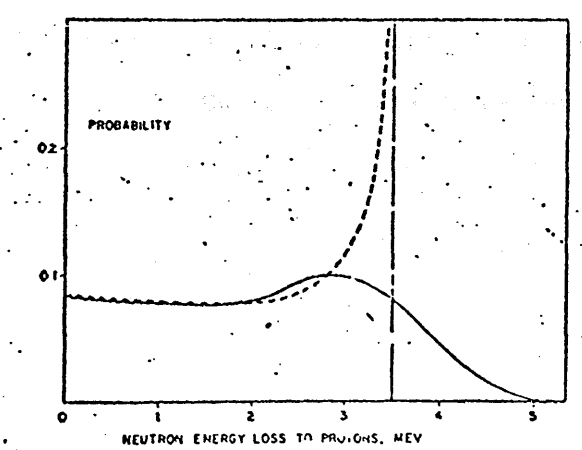

(B)

FIG. 4. Calculated proton recoil spectra.

detector efficiency of a more involved kind were undertaken by Hardy (Ref.12), who included carbon scattering and double hydrogen scattering as reactions contributing to the detection probability. These corrections led to improved agreement with the measured efficiency of a 2" thick sample of Ne 213 liquid scintillator, despite considerable discrepancy in the distribution of measured and calculated recoil scintillation spectra. In these results, (Fig.1) the effects of instrumental resolution and multiple scattering are evident in the complicated distribution of pulse heights. Hardy was unable to produce these effects by calculation and suggested the cause as further multiple scattering. Despite this, measurements on scintillators of similar size, (Refs.13,14) showed the Hardy model to predict the magnitude and energy dependence of the efficiency curve to within 10%. Good results were therefore expected from a complete treatment of all the possible combinations of reactions in the scintillator, but this required extensive computation.

One of the first such calculations was performed by Batchelor et. al. (Ref.15) in 1961. A 'Monte Carlo' computer programme was used to find the complete trajectory of each neutron in a sample of the liquid scintillator Ne 213, 2" thick×2" diameter. Measurement of the light response functions of recoil ions in the scintillator allowed the total amount of light produced by a neutron to be calculated, even for very complicated combinations of reactions. The detection efficiency at any neutron energy was then equal to the number of 'total light' pulses greater than the low energy bias point, divided by the number of incident neutrons. Comparison against a long counter gave an efficiency

curve and light pulse spectra showing fair agreement with experiment.

More exact calculations for a similar detector were made by Verbinski et. al. in 1968 (Ref.16). They measured proton responses to much lower and higher energies than Batchelor, using incident neutrons. Primary values of LP(E), the light response at each energy, were used to perform Monte Carlo calculations, including resolution smearing, and recoil proton scintillation spectra were produced to compare with the originals.. Corrections were obtained and the process repeated, to give values of LP(E) accurate to 2% from 0.1 Mev. to 40 Mev. This enabled tables of differential efficiency at many bias levels to be produced with accuracy sufficient to provide a 'response matrix' for the unfolding of neutron energy spectra from pulse height distributions (Ref.17).

Calculations of Efficiency Functions for Large Organic Scintillation Detectors.

Introduction:

The 'State of the Art' in efficiency calculations has been outlined in the previous section. Since previous publications were for smaller detectors the author undertook similar calculations for scintillators suitable for the Kelvin Laboratory time of flight system. Typical detectors are the liquids Ne 213 and Ne 211 and plastic Ne 102A in the form of 5" diameter by 5" or 2" thick cylinders with neutrons incident on the flat face.

Basic information on the Monte Carlo method and the convenient treatment of the associated reactions has been drawn largely from Refs.16, 17 and 18. A summary of the programme organisation and techniques peculiar to the author's calculation is given in section (A). Large amounts of data in the form of mean free paths and probabilities of competing reactions

must be consulted by the programme. The sources of this data and its tabulation are described in section (B). To calculate the light output from each interaction, data on the scintillation response to heavily - ionising particles was required. Much of the available data was found to be inconsistent, so that the responses for the 3 scintillators mentioned were measured by the author. These measurements, the results and the published data are discussed in section (C) with emphasis on the Ne 102 scintillators actually used in the author's experiment. Results of the Monte Carlo calculations are presented in section (D), and compared with experimental and calculated results of other authors.

(A) The Monte Carlo Method and Organisation of the Computer Programme.

The Monte Carlo method of making decisions between competing possibilities is to allocate each an interval on (0,1) proportional to its known probability of occurrence (normalised to a total probability of 1). A choice of number RANDOM in (0,1) will then select a particular interval and a corresponding possibility. The correct selection ratio for the possibilities is obtained by repeating the choice a large number of times.

This definition is applied directly in deciding which nuclear reaction will occur in any collision of a neutron in scintillator material. The cross section data is used to precompute probabilities for each of the possible reactions and angles of scatter and then particular selections are made as above.

The number of competing possibilities is often infinite, but the previous definition of the Monte Carlo method is extended to cover this in the obvious way: the intervals become smaller, tending to zero, and the

If NH and NC are the numerical densities of Hydrogen and Carbon atoms in the scintillator and SH and SC the corresponding total cross sections at energy E, we define a stopping parameter (U) as

$$U = NC*SC+NH*SC \tag{1}$$

The number of interactions of the n particles in dL is as usual:

$$dn = n*U*dL \tag{2}$$

so that:

$$n = n_0*\exp(-UL) \tag{3}$$

The relative probability of a Hydrogen collision is, from (1) and (2)

$$PH = NH*NC/(NH*NC+SH*SC) \tag{4}$$

The probability of a collision between L and dL is, from (2) and (3)

$$p(L)dL = \exp(-UL)*(UdL) \tag{5}$$

so that the probability of collision by distance d is

$$P(d) = \int_0^d p(L)dL = 1-\exp(-Ud) \tag{6}$$

The mean free path, λ, is defined as the average distance to collision in an infinite medium.

$$\lambda = \int_0^\infty L*p(L)dL = 1/U$$

Values of P(d), chosen from uniformly distributed numbers (R) on the range (0,1) of P(d), will provide a value of each 'd' from relation (6), ie., setting

$$R = P(d) = 1-\exp(-d/\lambda)$$

defines d as:

$$d = -\lambda*\ln(1-R) = -\lambda*\ln(R) \tag{7}$$

since R is uniformly distributed on (0,1). Thus distances are chosen with a bias of the probability distribution function P(d) for collision distance.

probability of occurrence of each interval becomes a continuous 'probability density function' (Ref.18). This function we define as $p(x)dx$ = the probability of finding x between x and (x+dx), with dx tending to zero. If the probability of finding any x is normalised to 1 in the range of x ($a \leq x \leq b$), ie., if $\int_a^b p(\varepsilon)\, d\,(\varepsilon) = 1$, then the function P(x), defined as,

$$P(x) = \int_a^x p(\varepsilon)\, d\,(\varepsilon)$$

is termed the 'probability distribution function' and may be taken to mean the probability of the inequality $\varepsilon \leq x$. If we set

$$R = P(x) = \int_a^x p(\varepsilon)\, d\,(\varepsilon)$$

then x is defined uniquely as a function of R, in such a way that if R is uniformly distributed on the interval ($0 \leq R \leq 1$), x falls in the interval (x,x+dx) with frequency p(x)dx, so that values of the variable x are chosen from R in the normalised ratio of their probability of occurrence.

In favourable cases, a simple algorithm exists between the random number (R) and the associated parameter (x). An example is presented in figure 2 where an explicit expression for the distance travelled to a particular collision is found in terms of the mean free path and a random number. (The probability of hydrogen collision is also calculated in Fig.2 for later reference). If 'x' cannot be expressed as an analytic function of 'R', we are forced to treat x as a non - continuous variable, storing values of P(x) for discrete intervals through the range of x and strobing these by random number to find a particular x as previously described.

The calculation is conveniently organised as a main programme

FIG. 3

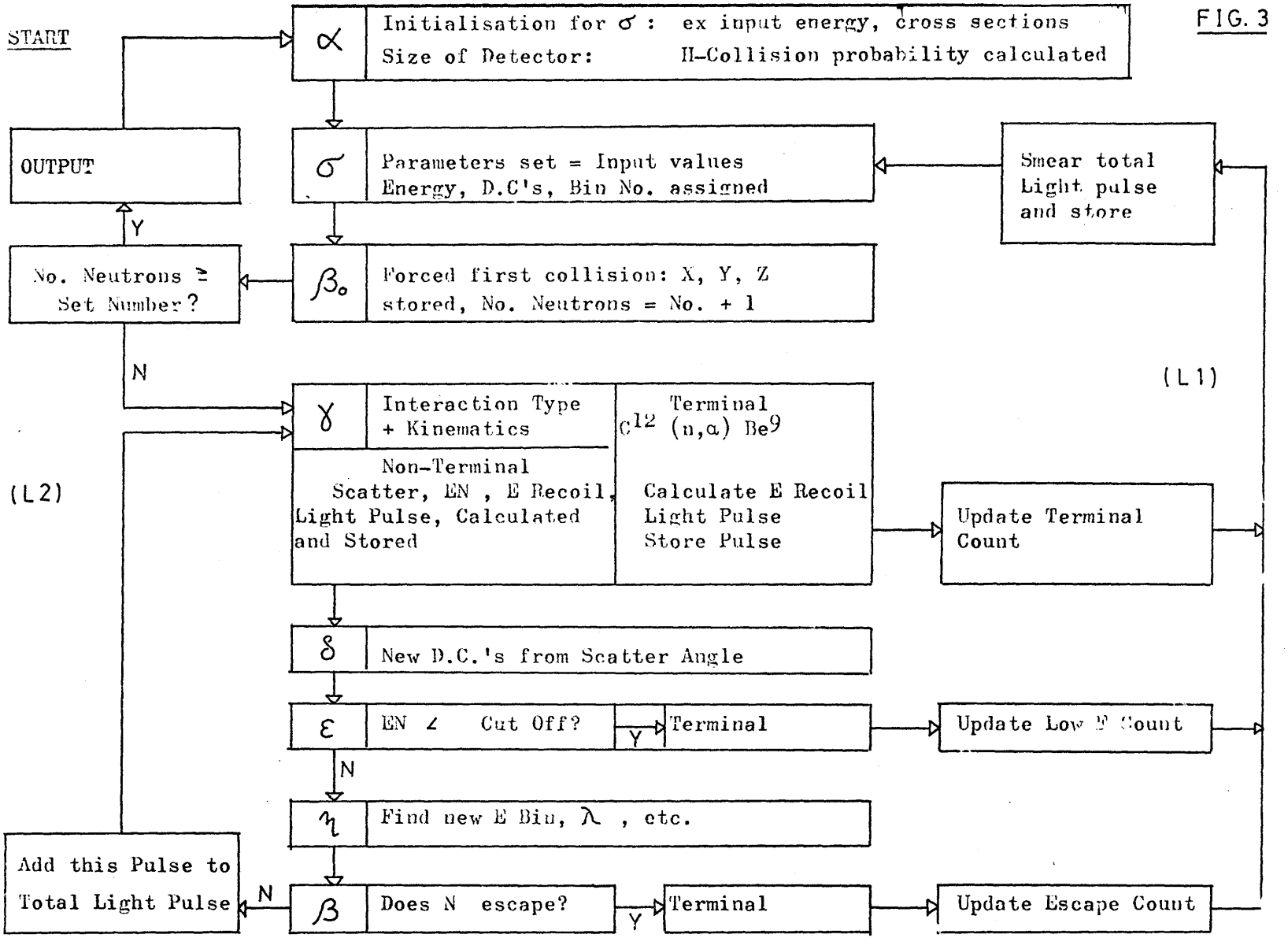
START
α
Initialisation for σ : ex input energy, cross sections
Size of Detector: H-Collision probability calculated
OUTPUT
σ
Parameters set = Input values
Energy, D.C's, Bin No. assigned
Smear total Light pulse and store
Y
No. Neutrons ≥ Set Number?
β₀
Forced first collision: X, Y, Z stored, No. Neutrons = No. + 1
N
(L1)
(L2)
γ
Interaction Type + Kinematics
Terminal
C12 (n,α) Be9
Non-Terminal
Scatter, EN , E Recoil, Light Pulse, Calculated and Stored
Calculate E Recoil
Light Pulse
Store Pulse
Update Terminal Count
δ
New D.C.'s from Scatter Angle
ε
EN ∠ Cut Off?
Y
Terminal
Update Low E Count
N
η
Find new E Bin, λ , etc.
Add this Pulse to Total Light Pulse
N
β
Does N escape?
Y
Terminal
Update Escape Count

which provides neutron input conditions and 'bookkeeping' facilities and a set of subroutines which treat particular kinematic or geometrical computations as they are needed in plotting each neutron 'history'. Fig. 3 is a flow diagram indicating the order of treatment of the different physical processes involved, the different possible terminations of a neutron history and they way the output information is stored. After accepting input conditions the programme works in the loop (L1), which supervises completion of the correct number of neutron histories and updates the spectrum of 'total light' pulses. Inside (L1) each neutron is guided through its reaction - geometry lifetime by loop (L2) until it reaches one of the terminal categories.

Scattered neutrons can have any energy up to that before interaction and the parameters affecting the 'future' of the neutron (the mean free path and probabilities of different interactions) are functions of the strongly energy - dependent hydrogen and carbon cross sections. These parameters are therefore stored in 35 bins which cover neutron energies from thermal to 20.M.e.V. and follow the fluctuating trend of the carbon total cross section. The stopping power of the scintillator as a function of energy would then be of the form of Fig.4, and significant changes in efficiency would be expected at the edges of bins. In order to avoid this effect, the author has compiled lists of hydrogen and carbon total cross sections for many neutron energies from 0.3 M.e.V. to 20.0 M.e.V. from Refs. 19 and 20. These are stored in the programme, which calculates the input values of the mean free path and the probability of Hydrogen interaction, accurate to the knowledge of the cross - sections (described in Section B). Subsequent assignments of

FIG.4

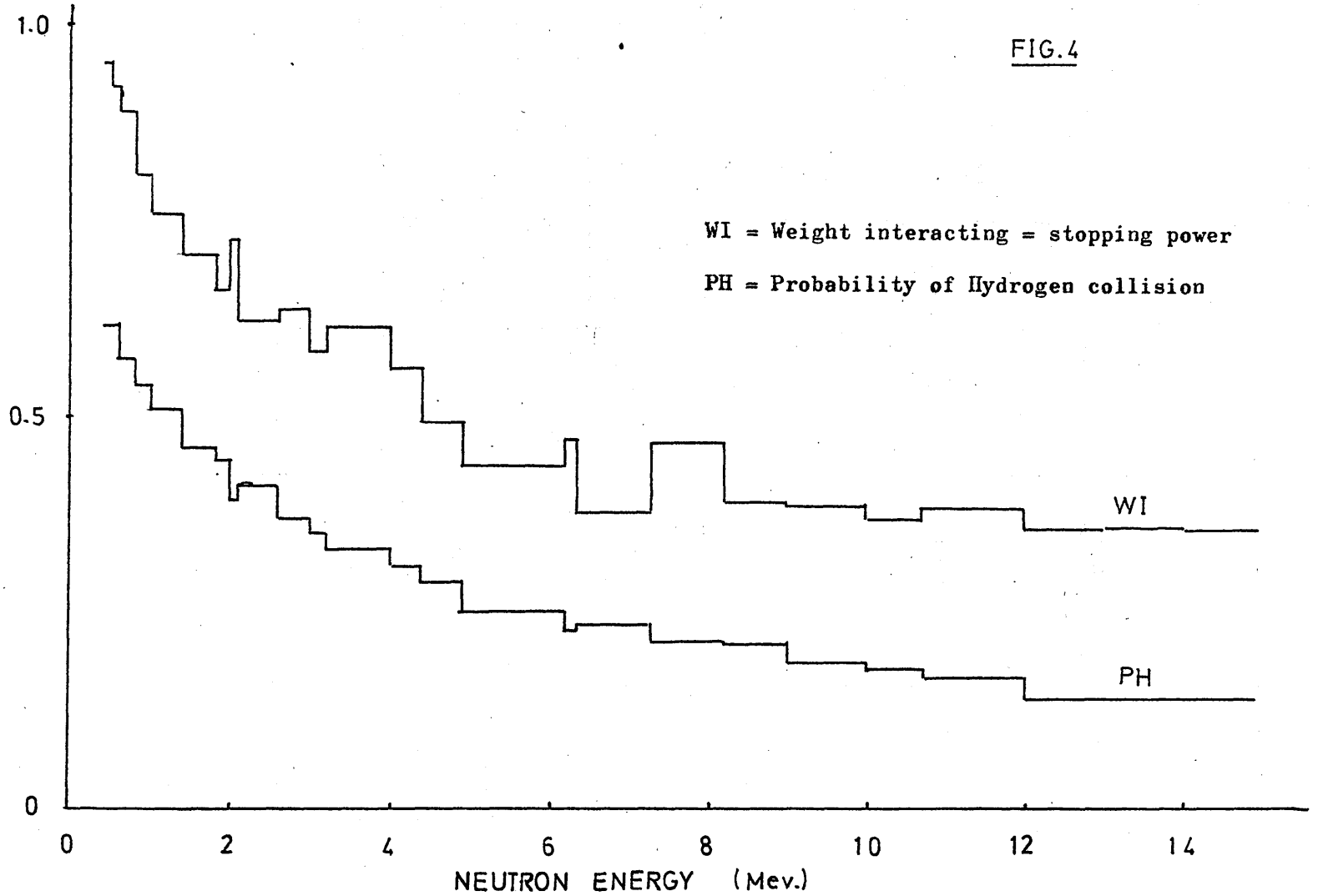
1.0
0.5
0
0
2
4
6
8
10
12
14
NEUTRON ENERGY (Mev.)
WI = Weight interacting = stopping power
PH = Probability of Hydrogen collision
WI
PH

Neutron Reactions in Scintillator Material. Table 1.

ATOM and numerical density (Nel02) ($cm.^{-1}$ $Barn^{-1}$)	Neutron Reaction Possible	Q-Value (Mev.)	Lowest Energy Treated (Mev.)	Reaction Treatment and Approximations
H	(n,p) elastic	-	-	isotropic in C.M. kinematics
0.052	capture	-	-	neglected.
C	elastic scattering	-	-	known angular distribution and kinematics
0.048	inelastic scattering	-4.43	6.2	Isotropic, light from γ only.
	$C^{12}(n,\alpha)$ Be9	-5.70	7.3	known angular distribution and kinematics. All to G.S.
	$C^{12}(n,3\alpha)n'$	-7.22	9.0	Isotropic and kinematics. Equal energies
	$C^{12}(n,p)B^{11}$	-12.58	-	neglected (small for E < 16Mev.)
	$C^{12}(n,X)Y$	-13.73		neglected, small
O,N (<10^{-6})				neglected

parameters are subject to this edge effect, but these are less important in determining the efficiency. Also, the main light - producing collisions are (n,p) scatters so that the light production power is mainly determined by the product of the stopping power and the probability of Hydrogen interaction defined in Fig.2. This product has smaller fluctuations than the actual stopping power (Fig.4) so the final spectra are produced with good accuracy.

By standard techniques (Ref.18) neutrons are caused to have their first collision in the scintillator. (The number transmitted is accounted for by assigning a weight proportional to the stopping power of each input group). In order to determine the collision type, the probability of Hydrogen collision (PH) is strobed by a random number (R). If R is less than PH, (n,p) scattering is treated. If R is greater than PH a Carbon Collision occurs, and the type is determined by another random strobe of the stored probabilities for the 4 possible Carbon reactions shown in Table (1). The accumulation of this data is described in Section (B). (n,p) scattering is treated as isotropic in the C.M. frame. This was inferred to cause about 2% error as an approximation at slightly higher energies by Verbinski (Ref.17) using the 14.1 M.e.V. data then available (Ref.19). However, more recent data (Ref.20) in the 13 - 20 M.e.V. range has shown the angular distribution to be essentially isotropic.

The treatment of Carbon collisions is standard for elastic, (n,α) and (n,3α) reactions, the angle of scatter which determines the recoil and scattered neutron (if any) energies, being obtained by random number strobing of the compiled angular distribution data. Extrapolation is avoided and only 20 scattering angles are possible. This could

distort the light spectra and alter the escape probability of the neutrons, but the large size of the scintillators and the corresponding predominance of multiple scattering smear any 'quantisation' effects. For elastic scattering, the energies of the scattered neutron and recoil carbon ion are obtained from the angle of scatter by simple kinematics as presented in Ref.18. The $C^{12}(n,\alpha)Be^{9}$ reaction was treated from the angle of (alpha emission) by the relativistic formulation of Ref.34 for the kinematics of two - body disintegration. No angular distributions were available to determine the neutron angle of scatter in the $C^{12}(n,3\alpha)n'$ reaction so that isotropy was assummed. The treatment was then as for the (n,α) reaction, with the '(3α)' treated as one particle in the two - body break up. (For calculation of light responses, the 3 alpha particles were considered to share the kinetic energy equally). Branching to excited states in the alpha reactions was neglected because of the lack of data on branching ratios.

Inelastic neutron scattering was treated by the following assumptions: (1) Only the 4.43 Mev. gamma ray is excited, (2) the angular distributions are isotropic for neutrons and gammas, (3) light is produced by detection of the gamma ray only (ie., the Carbon recoil is neglected) and (4) the gamma ray is detected by the Compton Effect only, giving a uniform recoil electron spectrum up to the Compton Edge. Under these conditions, a value for the 'mean free path' for stopping the 4.43 Mev. gamma rays in scintillator material allowed the escape or detection decision to be made by the usual routine. The probability of inelastic scattering (above threshold) is always a significant fraction ($\doteq\frac{1}{5}$th) of the total cross section (Ref.21,22) but the detection probability of the gamma ray is

small ($=\frac{1}{8}$th) so that the contribution made to light production (and particle detection) is about 2.5% of the total and an approximate treatment is justified.

The data on nuclear masses required in the above calculations was obtained from Refs. (31,32) and the value used of the relationship between a.m.u. and M.e.V. units was the most recent available Ref. (33). Table (1) gives a summary of the reactions treated or neglected. Conspicuous is the neglect of neutron capture in hydrogen, made because of the low probability of the process for the energies considered (Ref. 35). Neutrons are followed down to an arbitrary bias energy (usually about 1 k.e.V.) to avoid lengthy tracking of particles which cannot contribute significantly to the light yield.

The light output in each collision is calculated from the energy of the recoil particle in the kinematic subroutine. The amplitude of this pulse reaching the photocathode is adjusted by the known attenuation of the scintillator for its own radiation, and the distance to the photocathode (without reflections). A further adjustment is derived from the light collection efficiency, as a function of the radius from the scintillator-photomultiplier axis. This function was measured by the author along with the variation of gain over the scintillator face, using collimated gamma rays from Na^{22} and Am^{241} sources. This was necessary because the scintillator diameter was larger than that of the photocathode and a fall in light collection efficiency was expected near the edges. The results are presented in Fig. 5A and 5B.

Gain Variation over Scintillator Face.

Fig.5A.

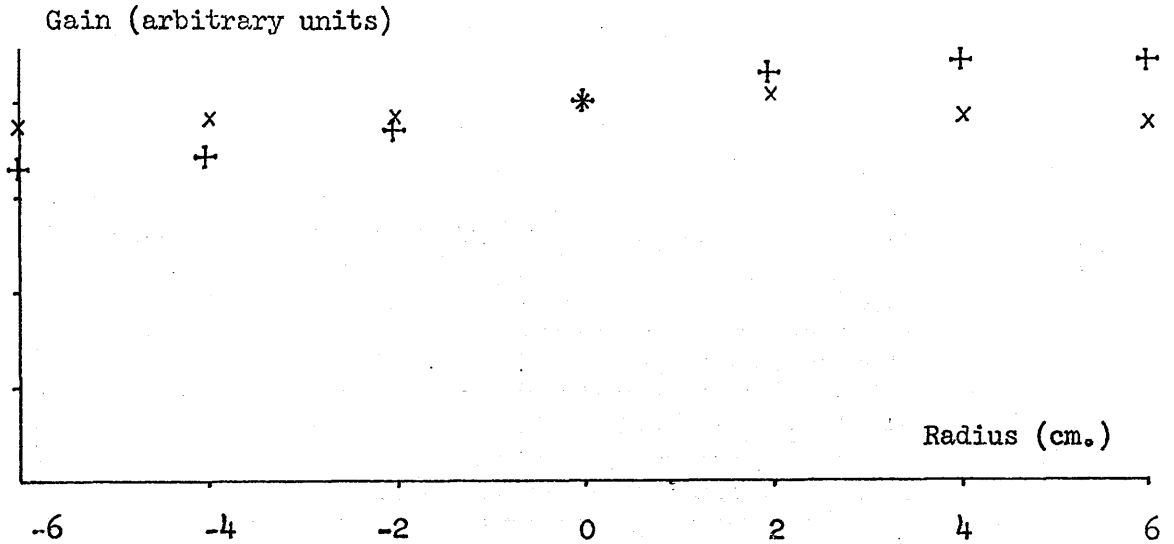

Light Collection across Scintillator Face.

Fig.5B.

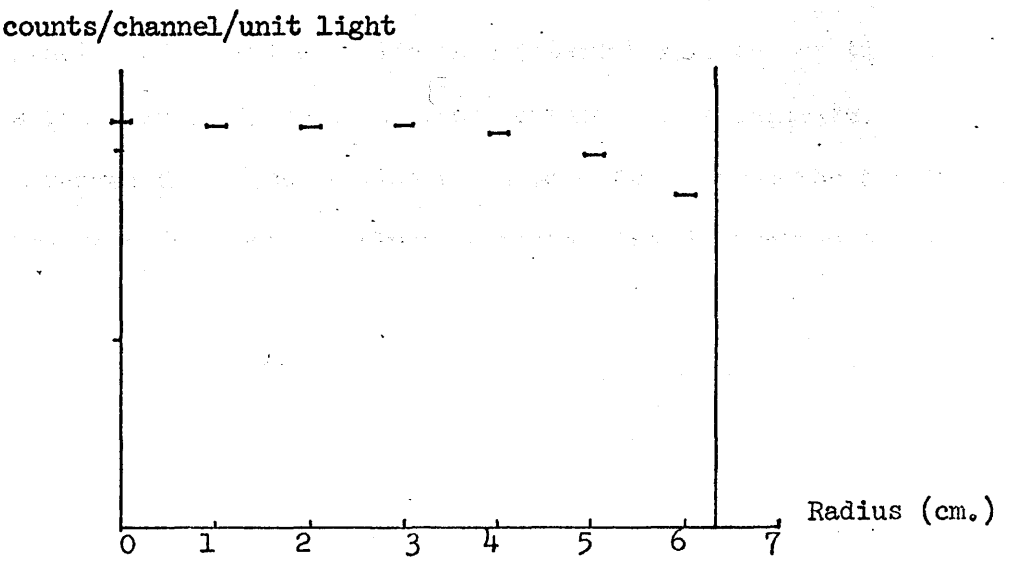

Due to the non - linear relationship between proton energy and scintillation response, a neutron of energy (EN) twice that energy equivalent to the light bias (B) produces light up to 3 times the bias level (Fig.7B). If such a neutron has 2 interactions, then the distribution of first pulses, on a uniform basis, is approximately:

EN/B	Fraction of light above Bias (B)	Fraction of Light below Bias (B)	
		Fraction $>\frac{1}{2}$B	Fraction $<\frac{1}{2}$B
3	2/3	1/6 = A	1/6 = B

and that for second pulses (whose first pulse was not B) is:

First Pulse Type	EN'/B average	Fraction of Light > B	Fraction of Light < B	
			Fraction $>\frac{1}{2}$B	Fraction $<\frac{1}{2}$B
A	9/4	5/9 = A'	2/9 = B'	2/9 = C'
B	11/4	7/11 = A"	2/11 = B"	2/11 = C"

The fast discriminator may make errors if each pulse is < B but the total is > B. The probability of this is:

$$P \doteq AB' - \tfrac{1}{2}(AC' - BB'') = 7\%,$$ here, and

the characteristic of the scintillation decay is = 2ns. so that reactions occurring inside this interval will be considered to add in a fast discriminator, and those outside to be separate. Nature has arranged the cross section trend ($\sigma \propto 1/v$) so that the time to traverse the mean free path is almost constant for all neutron energies at 2ns. Therefore about .37 of the double interactions appear separate and the 'wrong' decision is made on $2\frac{1}{2}\%$ of the initial neutrons by a fast discriminator. This effect decreases almost as the square of the incident neutron energy and is therefore negligible for higher EN.

The gain variation is small and averages to zero over the scintillator surface, and since the details of the variation would vary between photomultipliers and with the settings of electrode voltages for each, the effect was not treated. But the light collection efficiency averaged over the scintillator volume produced a 5% decrease in the number of pulses registered, enough to warrant a more exact treatment, in which the light collection efficiency function value at each interaction point was random number strobed to determine the light collection decisions.

The summed light pulse does not take the time variation of the component pulses into account, but, if the light produced is collected over a time which is long compared to the pulse decay time, this difficulty to overcome, as in the case where a slow discriminator, which makes a pulse height decision on the total charge, is used. Where only a fast 'trigger' discriminator is used, the discreteness of the pulse components may affect the detection efficiency slightly at energies where light pulses of the order of the light bias level are common. An order of magnitude calculation of this effect for the worst energy range is made in Figure 5C and the effect upon the detection decision (= efficiency) is shown to be small for neutrons of energy greater than twice the bias energy.

The detector efficiency above any light bias level is defined as the

fraction of the 'total light' pulses greater than the bias times the stopping power for each particular neutron group. The programme output included a list of detection efficiencies for all bias levels, so that smearing of the bias point could be introduced to duplicate the slow cut - off characteristic of the fast discriminators used. This cut-off function was measured by accumulating Co^{60} gamma ray linear pulses gated by the fast discriminator set in the flat part of the Compton recoil spectrum.

By duplicating all the physical processes as closely as possible as described above, good agreement with the real case can be expected. Results are presented in Section (D).

(B) Cross Section Data for Monte Carlo Calculations.

The data required and the energy bin assignments for data storage have been discussed in Section (A). Values of the mean free path (λ) and the probability of Hydrogen interaction (PH) were precomputed from the total cross sections for Hydrogen and Carbon interactions (Refs.21,22,23,) averaged over each bin, using the numerical densities of the atoms provided by the manufacturer* The Hydrogen total cross section average was accurate to 3% and the Carbon one to about 8%. With this data stored as a function of energy the probability of obtaining a collision, then its type, could be determined. (The treatment of particular reactions is listed in Table (1)).

Decisions on the reaction type in Carbon collisions required probability data to be obtained from the corresponding partial cross sections. Those for elastic scattering have been well studied and were obtained from Ref.(22) and by summing components in the measured angular distributions (Ref.19,20). Since only a small number (between 1 and 7) of discrete energies had been measured in each bin the error assigned to the averaged

* Nuclear Enterprises Ltd., Edinburgh, Scotland.

value varied but was typically =10%. Below 4.43 Mev., only elastic scattering is possible so that the elastic should equal the total cross section. This was found to be the case within the 10% error quoted. At some higher energies (9-12 Mev. and 16 + Mev.) no measurements were available and the cross section was found by extrapolation from the 8 Mev. and 14 Mev. data. The values so obtained were checked by subtracting the known non - elastic cross section (Ref.22) from the total. The accuracy of this cross section is about 15% from 7 Mev. to 15 Mev. The results agreed to within this error.

Data on the cross sections for inelastic scattering, $C^{12}(n,n'\gamma)C^{12}$ was obtained from Refs. 21 and 22., where again no measurements had been made in the 9 - 14 Mev. and 15 - 20 Mev. regions and extrapolation was used. The associated errors were small (10%) up to about 9 Mev., but increased to about 20% in the unknown regions. Similar extrapolation was required for the $C^{12}(n,\alpha)Be^{9}$, cross sections, where the published measurements (Refs.22,26, 27,28,29,30) were made at 8 Mev. and 14 Mev. only, and similar error estimates resulted.

Fairly complete data in the energy range required was available for the $C^{12}(n,3\alpha)n'$ reaction (Ref.24) and was extrapolated to threshold using the theory of Sachs (Ref.25) which gave good fit to the measurement of Ref.24. Errors were of the order of 20%.

The $C^{12}(n,p)B^{12}$ cross section is less than 10m.b. below 16 Mev. (Ref.22) and the reaction was neglected, as were the contributions from the other $C^{12}(n,X)Y$ reactions, whose thresholds are all greater than 13.7Mev.

To check the above values, the sum of the non - elastic reactions considered was found and compared with that of Ref.22 for each energy bin.

The mean error was about 15%, the same as the accuracy of the test. From the above compilation, each partial cross section was divided by the total cross section to provide a list of reaction probabilities for each energy bin. Adding these in turn to the first, (the total sum = 1) gave integral probability values $P(n),(n=1,4)$, to be strobed by random number R so that, if $R<P(1)$, then Reaction 1 (= elastic scattering) was chosen; if $R\geq P(1)$ and $R<P(2)$; Reaction 2 (= inelastic scattering) was chosen and so on.

Having decided the reaction type, the kinematic treatment required a choice of scattering angle to be made from the known angular distributions.

Fairly complete data on the elastic scattering angular distributions was obtained from Refs.(19,20). From this, twelve energy bins were selected to have fairly constant angular distributions, and the average differential cross section found for each of twenty bins of equal solid angle over the range zero to π in each energy bin. A probability distribution function of angle was then formed and stored for each energy bin and angles were chosen by the method already described. The same data was used to provide the elastic partial cross sections for the 'reaction - type' energy bins described earlier.

The angular distribution of alpha particles from the $C^{12}(n,\alpha)Be^{9}$ reaction was measured by Kital and Peck (Ref.27) with 14 Mev. neutrons, but covering only angles forward of about 120^{o}. By comparing their cross section with that measured into 4π by other workers at the same energy, (Refs.26,28,29,30) the average differential cross section in the unmeasured region was found to be the same as that measured at 90^{o} and

120^{o}, so that this value was assumed constant for all backward angles. The isotropic treatment of the $C^{12}(n,3\alpha)n'$ reaction has already been described.

The approximations involved in the non - elastic treatments are necessary because of lack of data, but since the probability of obtaining such a reaction is of the order of 5% compared to Hydrogen and Carbon elastic scattering, the errors introduced into the efficiency values are relatively small (20% of 5%). The fact that the significantly large light pulses come from proton recoils improves the accuracy of the detector efficiencies still further.

(C) The Light Response Functions of Organic Scintillators.

Introduction:-

Fluorescence is produced in organic scintillators due to the excitation or ionisation of π electron molecular binding systems in the material (Ref.1). These two processes lead to the well known fast and slow components of the fluorescence radiation. A fast electron depositing all of its energy in such a scintillator will convert some fraction S (=4%) of this energy to scintillation emission of fluorescence photons by the above process, the rest being absorbed non - radiatively. Particles producing heavier densities of ionisation and excitation show a decreased absolute scintillation efficiency (S) due to simple space - charge effects (ie., 'ionisation quenching' (Ref.1)). Hence the scintillation response (L) to electrons, protons and alpha particles of 5 Mev. energy, is in the approximate ratio 10:5:1. Since dE/dr is a function of energy and particle type, in general, L is a non - linear function of these perameters.

Ionisation quenching affects the fast component (excitation part) of the scintillation only so that the total scintillation pulse is a function of this quenching and therefore of the type of incident particle. This property allows the use of pulse shape discrimination (P.S.D.) to differentiate between types of particle.

For lightly ionising relativistic particles,

$$dL/dr = S.\ dE/dr \qquad (1)$$

The terms are the specific fluorescence (dL/dr) the absolute scintillation efficiency (S) and the specific energy loss (dE/dr), where r is the range in the scintillator in cm. air equivalent or mg. $cm.^{-2}$ This equation has been verified by many authors, as listed in Ref.1. The various components of ionisation quenching are described in Ref.1, as is the semi-empirical relation due to Birks

$$dL/dr = (S.dE/dr)/(1+kB.dE/dr) \qquad (2)$$

which allows for the quenching effect of the specific density of ionised and excited molecules along the particle track. (B and k are constants). Obviously (2) reduces to (1) for small dE/dr, ie., fast electrons. For large dE/dr, (2) becomes

$$dL/dr = S/kB = \text{constant} \qquad (3)$$

Equations (2) and (3) have been verified by many authors listed in Ref.1. In particular, Prescott and Rupal found kB = $9.1(\pm 0.6)$mg.$cm.^{-2}$ for Ne 102A using electrons, protons and alpha particles (Ref.36). Evans and Bellamy obtained kB = $10.0(\pm 1.0)$mg.$cm.^{-2}$ using protons and electrons for the same scintillator (Ref.37).

For Monte Carlo calculations, the response of the different ionising particles may be obtained by measurement or by equation (3),

FIG. 6.

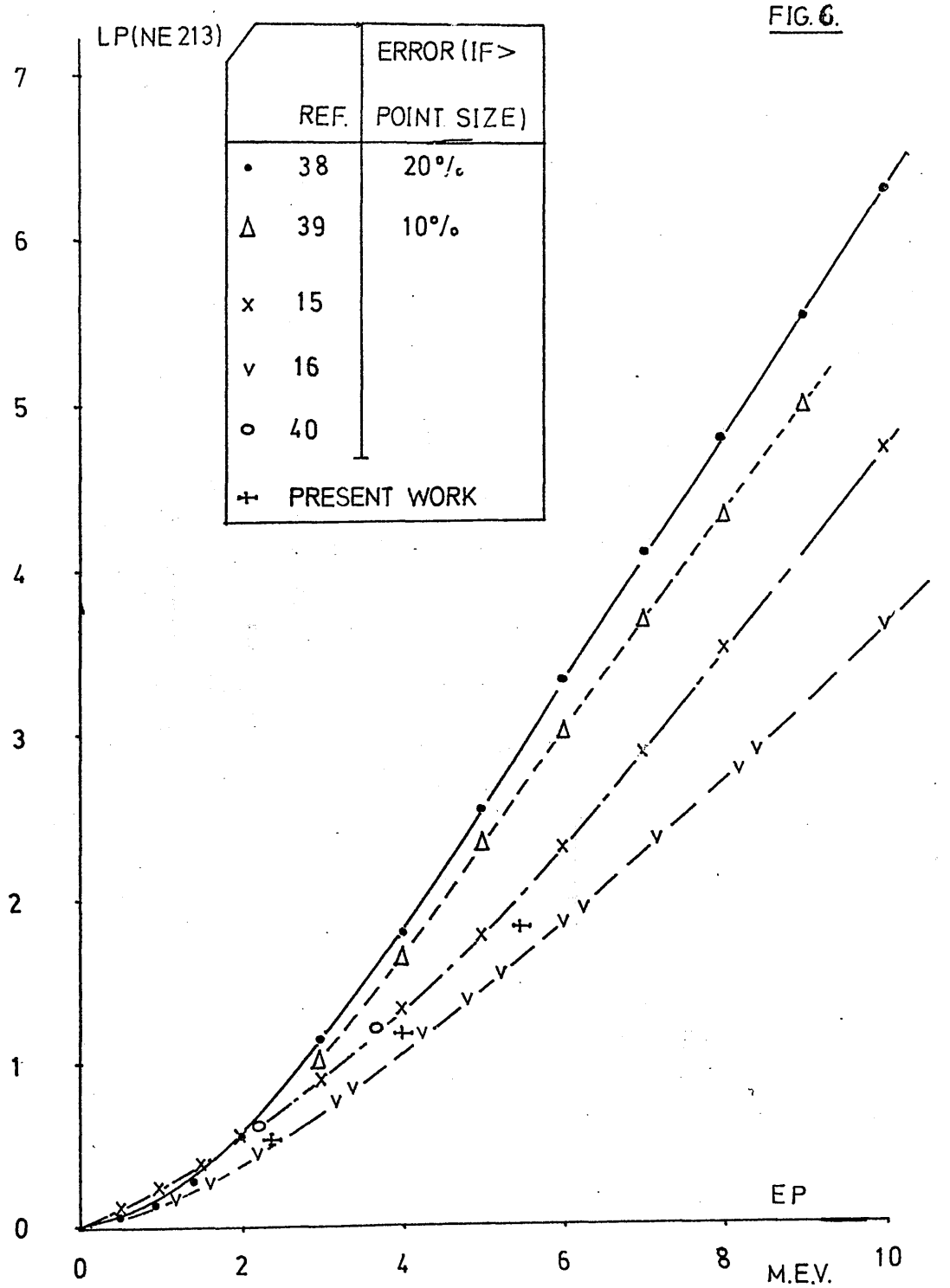
LP(NE 213)
ERROR (IF > POINT SIZE)
REF.
38 20%
39 10%
15
16
40
PRESENT WORK
7
6
5
4
3
2
1
0
0
2
4
6
8
10
EP
M.E.V.

FIG.7A

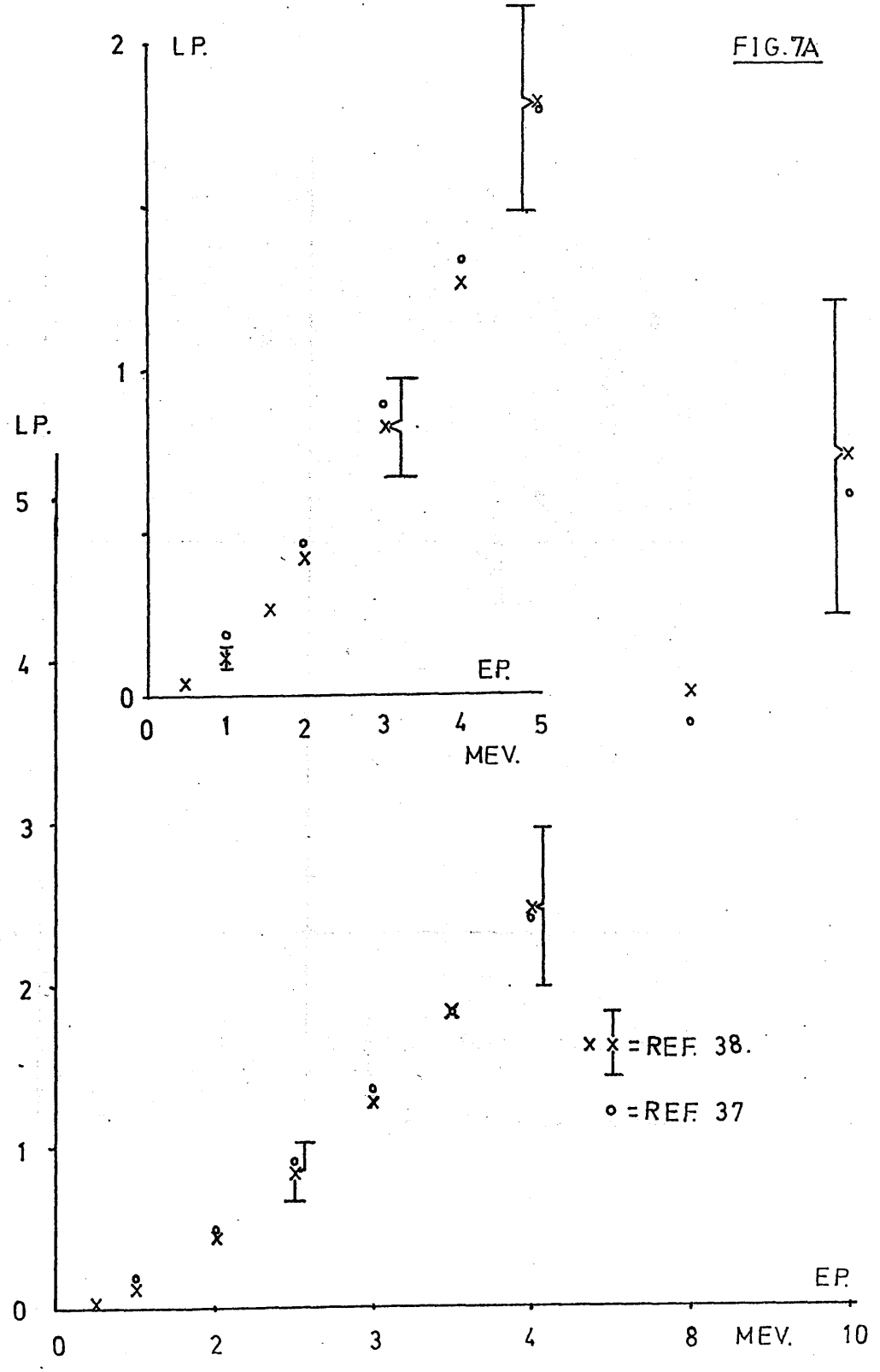

FIG. 7B

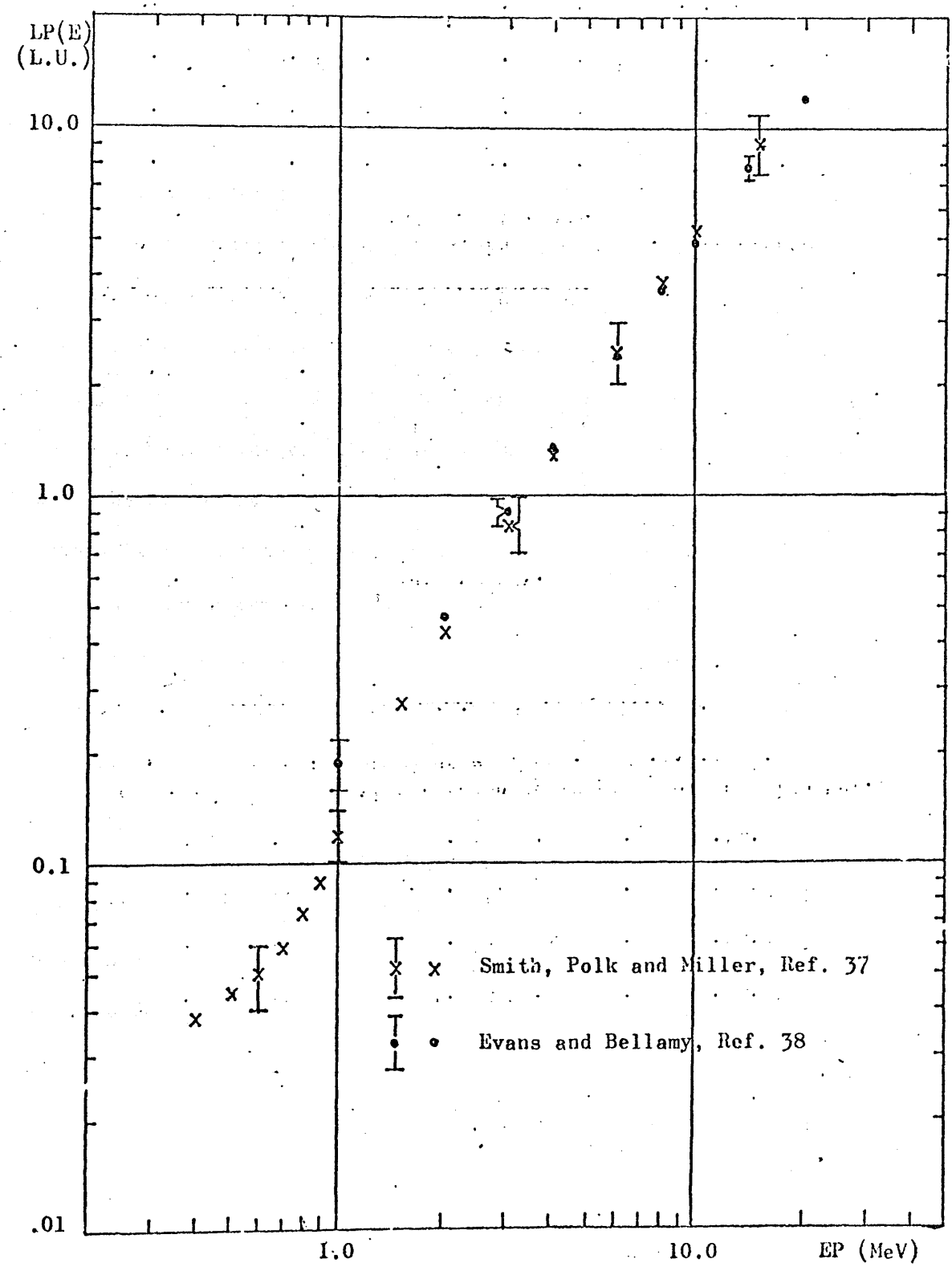
LP(E)
(L.U.)
10.0
1.0
0.1
.01
1.0
10.0
EP (MeV)
Smith, Polk and Miller, Ref. 37
Evans and Bellamy, Ref. 38

using one measured response to drive kB. This method was used by Batchelor et. al. (Ref.15) as previously described.

Data Available on Scintillation Responses to Protons.

The recoil proton scintillations dominate the light output of organic scintillators when bombarded with fast neutrons, so than an accurate knowledge of the non - linear scintillation response to protons is required to predict the efficiency of such a detector. The published responses for Ne 213 liquid scintillator are presented in Figs.6,7(Refs.15,16,17,38,39). There are large disagreements between the different results. The response of Ne 211 is identical to Ne 213 over the energy range of interest. (Ref.16). For Ne 102A plastic scintillator, the two published measurements agree to within the 20% error at high energies but show discrepancies of the order of 50% below 1.5 Mev. (Figs.7A,B.). The author undertook measurements of these responses to resolve the conflict in the available data.

Measurement of the Scintillation Response to Protons in Organic Scintillators.

The scintillation response to protons may be measured by direct proton bombardment, as in Ref.37, or by using proton recoils from neutron bombardment, as in Ref.38. The second method avoids surface effects for low energy protons (Ref.1), but does require the usual measurement of the maximum proton energy (= input neutron energy) as the edge of the recoil plateau, unless coincidence techniques are used (Ref.38). Neutron bombardment was convenient to the author because the recoil spectra obtained would be just those which a calculation must match to determine the detector efficiency properly.

ELECTRONIC ARRANGEMENT

FIG.3

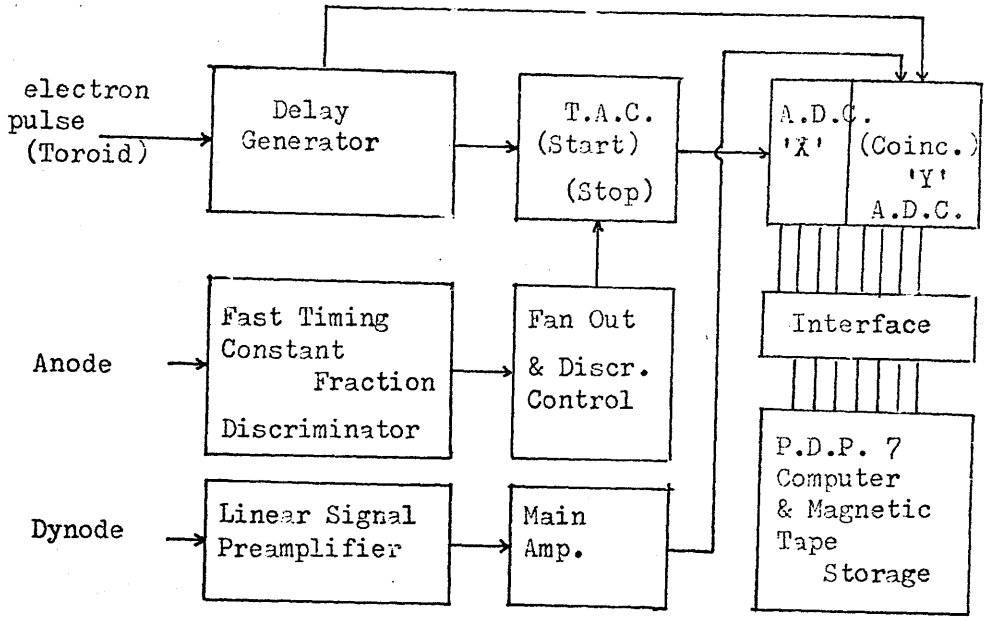

D_2O PHOTONEUTRON T.O.F. SPECTRA.

FIG.9

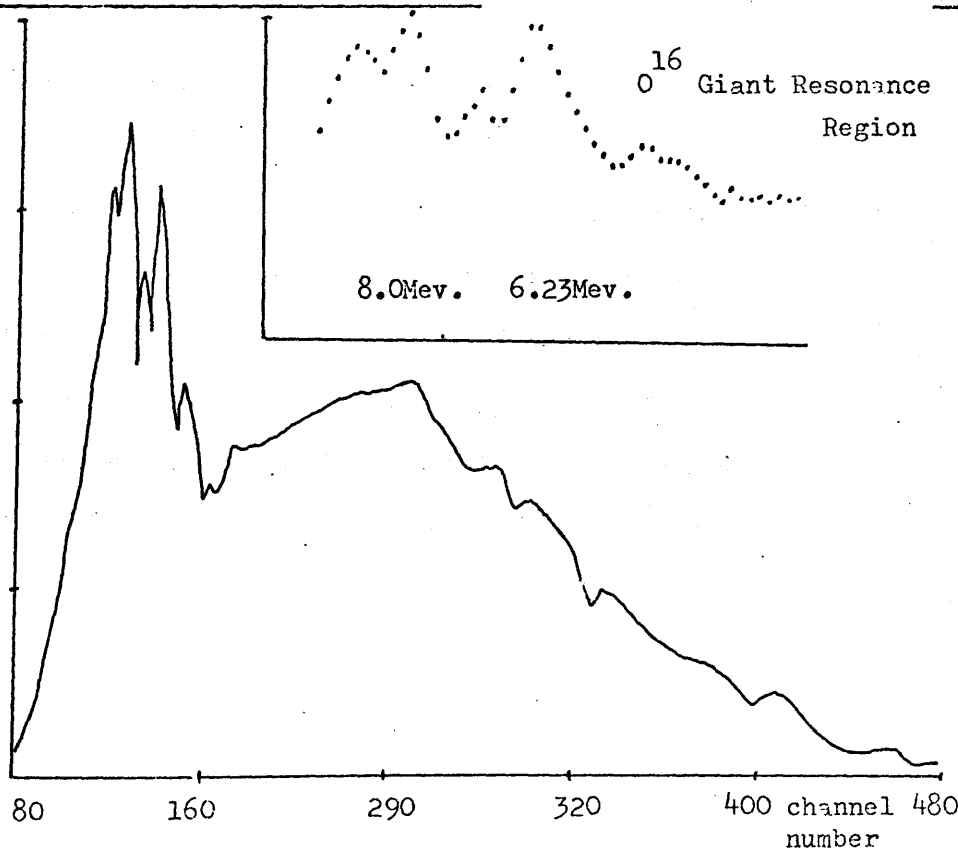

For this reason, the measurements were made using the large scintillators which the author wished to calibrate. Smaller scintillators could have been used and possible multiple interaction effects diminished, but this would have required much more accelerator time to achieve the same statistics, and the large scintillator measurements would still have been required. Neutrons of known energy were obtained by time of flight measurement in the multi - angle spectrometer constructed by the author. The Scintillators used were samples of the liquids Ne 211 and Ne 213 in cylindrical form 5" diameter by 2" thick and Ne 102A plastic scintillator 5" diameter by 5" thick. Each was mounted directly on an XP1040 photomultiplier fitted with a commercial integral assembly of base divider chain, linear preamplifier and constant fraction timing trigger.* Fig.8 shows the electronic arrangement used, which included fast timing and linear channels and a coincidence gating requirement, enabling the time of flight of each neutron to be stored in coincidence with the proton recoil pulse height it produced.

Data was taken simultaneously for the three scintillators on 3 different flight paths, all at 20m., and was sorted into a PDP 7 computer by the A.D.C. interface system designed by the author. The computer programme (Ref.41) allowed simultaneous acquisition of data from three bidimensional devices, using parts of memory as buffer stores for each input, and dumping the contents onto magnetic tape when the buffers were full. By this means, 250 linear channels by 512 time of flight channels were available for storage of each

* Ortec Inc., Oak Ridge, Tenn., U.S.A.

Table 2. GAMMA RAY CALIBRATION LINES AND ELECTRON ENERGIES

Source	Gamma Ray Energy	Photo – Peak	Compton Edge Value (Mev.)	Observable Compton Edge (Mev.)
Am^{241}	60 kev.*	Yes		
Na^{22}	1.274Mev.		1.060Mev.	1.102Mev.(±.01)
	0.511Mev.		0.3407Mev.	0.354Mev.(±.004)
Cs^{127}	0.6612Mev.		0.4747Mev.	0.494Mev.(±.004)
Th^{228}	2.615Mev.		2.379Mev.	2.476Mev.(±.03)

* Because of the non – linear response to electrons of 125 kev. energy, this 60 kev. appears as = 57 kev. (Ref.1,p.186).

Table 3. RESOLUTION PER 4n.s. CHANNEL AT 20m.

Neutron Energy (Mev.)	Energy Resolution	
	%	Absolute (kev.)
1	0.7	7
4	1.3	55
9	2.	185
16	3.	440

Table 4. CONSISTENCY IN THE TWO GAIN RUNS.

Neutron Energy Mev.	High Energy LP. (Low Gain)	Low Energy LP. (High Gain)	Difference
4.00	1.425(±.02)	1.388(±.05)	+.037(±.05)
3.52	1.195(±.03)	1.215(±.03)	–.020(±.04)
3.00	0.910(±.015)	0.920(±.01)	–.010(±.02)
2.51	0.685(±.015)	0.675(±.007)	+.010(±.02)

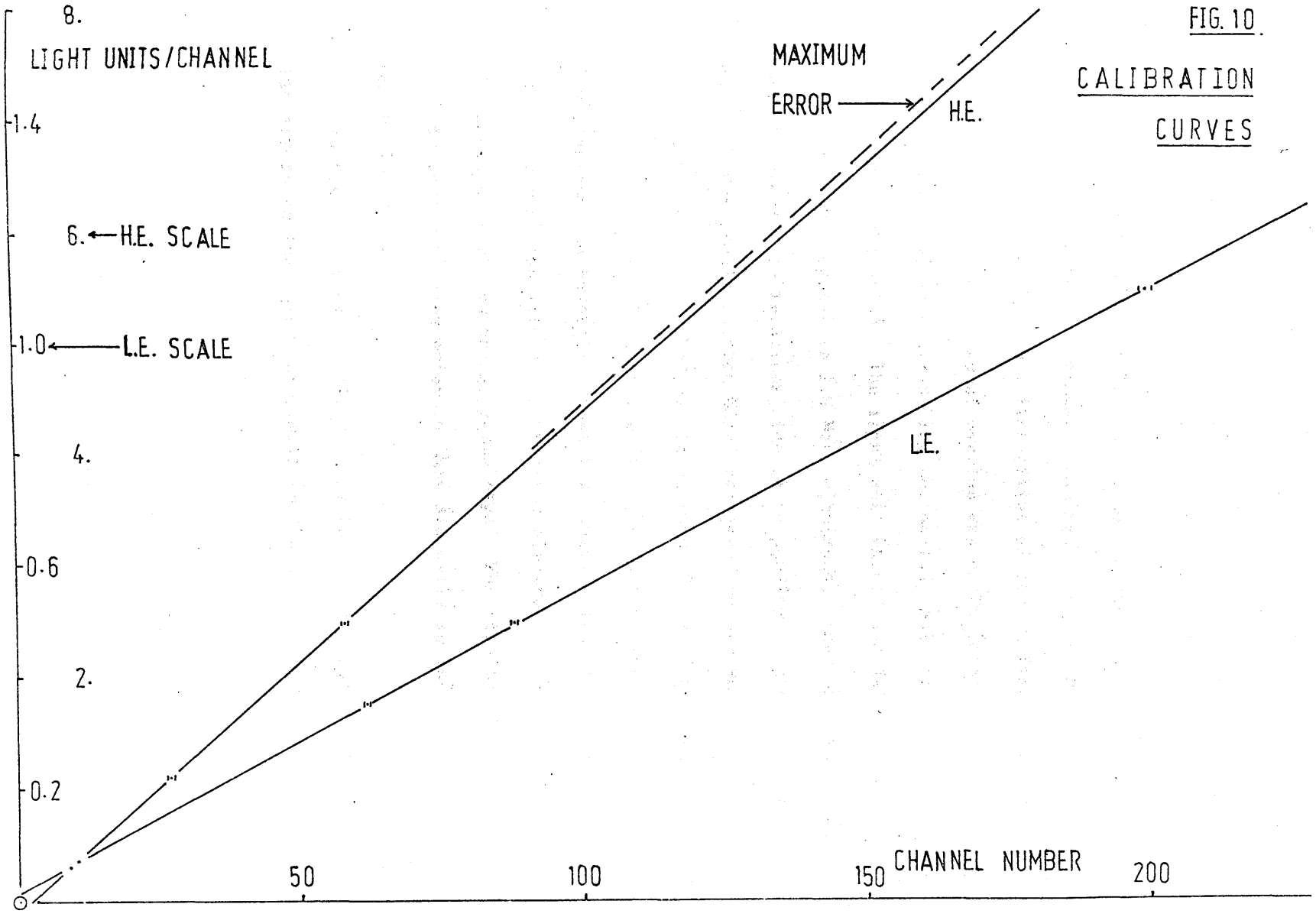

FIG. 10.

CALIBRATION CURVES

input spectrum.

Consideration of the previously published measurements showed an increase in scintillator response of about 200 as the neutron energy was increased from 0.5 to 16.0 Mev., so that two runs with different gains in the linear channel were required to cover the range without distortion (caused by non - linearities of the analysers in the first few channels). The region of overlap was conveniently set to include a range of pulse heights straddling the halfway point in the total range, (about one light unit). The light unit (L.u.) was defined as the scintillation response to 1.0 Mev. electrons. The gamma ray energies used to provide calibrations, the corresponding Compton Edge energies and the 'Observable Compton Edge' energies are presented in Table 2. In 1964 Flynn et. al. (Ref.42) found this 'Observed Compton Edge', taken as the half height of the fall off in the observed Compton distribution, to be $4(\pm 1)\%$ greater in pulse height than the expected one, by comparison with K - conversion electrons of known energy and the photopeaks of low energy gamma rays. The results of Evans and Bellamy were published prior to this discovery so that their results may be low by 4%.

In Fig.10 the calibration graphs for the two gain runs are shown. The errors on the points are small (= the size of the point) and both the relations are linear, so that the calibration is accurate to $\leq 2\%$ (including the 1% error in the 4% multiplicative constant). The highest calibration point is 2.476 L.u., equivalent to about 5.5 Mev. neutron energy. Errors in extrapolation to higher light levels are small, due to the good linearity of the system, and an estimate of this

effect is included in the experimental errors assigned to such points.

Great care was taken in the normalisation of the two gain runs, and complete spectra for neutron energies between 2.5 Mev. and 4.0 Mev. were taken in both gain settings. In order for the two spectra to be properly aligned, consistent values of LP(E) had to be obtained from both gain runs, over all the overlap region. These results are presented in Table 4 and show the two calibrations to give identical results to within the experimental error.

During data acquisition, possible overload or 'after pulsing' effects, caused by the large flux of Compton scattered gamma rays from the (γ,n) target, were avoided by choosing the electronic delays so that this prompt 'Gamma Flash' was on scale (about channel 30) on the time to amplitude converter(T.A.C.). In this condition, the system could not measure any more events until another start pulse was provided by the accelerator, so that spurious counts were avoided. The gamma pulse was stored for a very short time in practice, to provide a convenient time calibration point, then it was biased out by a low level discriminator on the analyser to avoid storing a large number of uninteresting pulses. (The T.A.C. was still inhibited in this mode). A compromise between neutron count rate and losses due to gamma inhibits was achieved by optimising the thickness of lead absorber at the target end of the flight path. This attenuated the (low energy) gamma rays about 5 times more than the neutrons. To minimise further the number of gamma rays per neutron, flight paths at angles backward of 90° to the electron beam were used, since the Compton scattered gamma rays are highly forward peaked. The number of high

energy neutrons per unit gamma flash was further maximised by the choice of light elements to make the photoneutron target. Heavy water (D_2O) was found to be convenient because the Deuterium gave a good flux of high energy neutrons and the clear structure in the Oxygen giant resonance provided an absolute energy calibration. A typical time of flight spectrum is shown in Fig.9.

To cover the time from zero to greater than that of a 0.5 Mev. neutron at 20m. required 2.5 u.s., so that 5 n.s. per channel was obtained from the 500 channels available. The total time resolution due to the electron beam width and electronic effects was less than 4 n.s., so that the channel width gives a good indication of the total resolution of the system. Some typical neutron energy resolution values are presented in Table 3. The time per channel calibration was made by standard techniques using an oscillator of known frequency and the zero of time was calculated from the gamma flash channel and the flight path length. The calibrations reproduced the energies of the 6.23 Mev. and 8.0 Mev. $O^{16}(\gamma,n)O^{15}$ peaks to within the expected accuracy (1 time channel).

A typical count rate for neutrons or gamma flash pulses was 1000 per minute, which allowed the accumulation of about 2 million counts in each gain run of 3 days. The background count rate was all due to random gamma rays and was always less than 3% of the real rate so that it was neglected. Gains were checked periodically and no significant drifts were observed.

Data Reduction.

The large matrix of data to be handled posed special problems, most of which had previously been solved by Mr. J. Kellie of this

CALCULATED
SPECTRA OF 1·0 MeV NEUTRONS
IN Ne 102

FIG 11

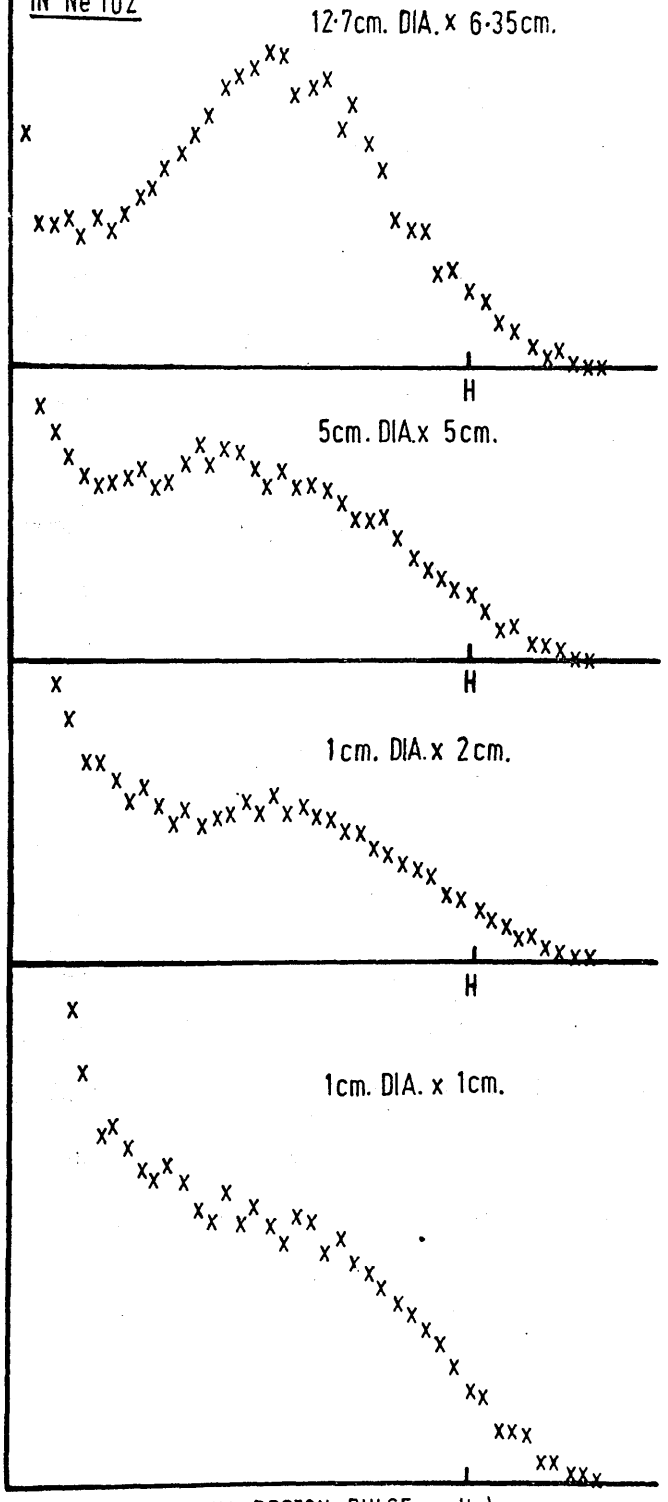

(MAXIMUM PROTON PULSE = H)

laboratory, who kindly provided the programmes (Ref.41). Data stored sequentially was converted to a matrix array on magnetic tape, which could be consulted by a programme allowing display and hard copy output of linear spectra in coincidence with selected time of flight channels, that is, spectra produced by neutrons of known energy. This is the information required, but the lack of statistics at high energies, where there were relatively few neutrons and the linear spectra covered many channels, demanded summing over several channels of pulse height. Between 70 and 100 final channels were normally chosen.

Other authors have assumed the equality between the incident neutron energy (= the maximum proton recoil energy) and the half height of the fall off on the recoil proton plateau curve (Refs.15,16), but preliminary Monte Carlo calculations made by the author, based on the proton response curve of Evans and Bellamy (Ref.37), showed this assumption to be invalid for neutrons below 4M.e.V. energy in thick scintillators. The large multiple scattering probability and the non - linear light response combine to produce a bigger fraction of large pulses and the resultant recoil proton spectra are extremely non - uniform. This is shown in the measured responses of Hardy (Fig.1) and also in Fig.11, where calculated proton recoil spectra are presented for 1Mev. neutrons incident on various sizes of Ne 102A plastic scintillator. There is obviously no relationship between the 'half slope' and the (constant) position of the cut-off in the spectrum of individual Hydrogen recoil pulses. Further preliminary calculation determined the actual relationship between the maximum energy of recoil proton and a significant feature of the final recoil spectrum

PROTON RESPONSE EVALUATION BELOW 1.5 M.e.V. Fig. 12

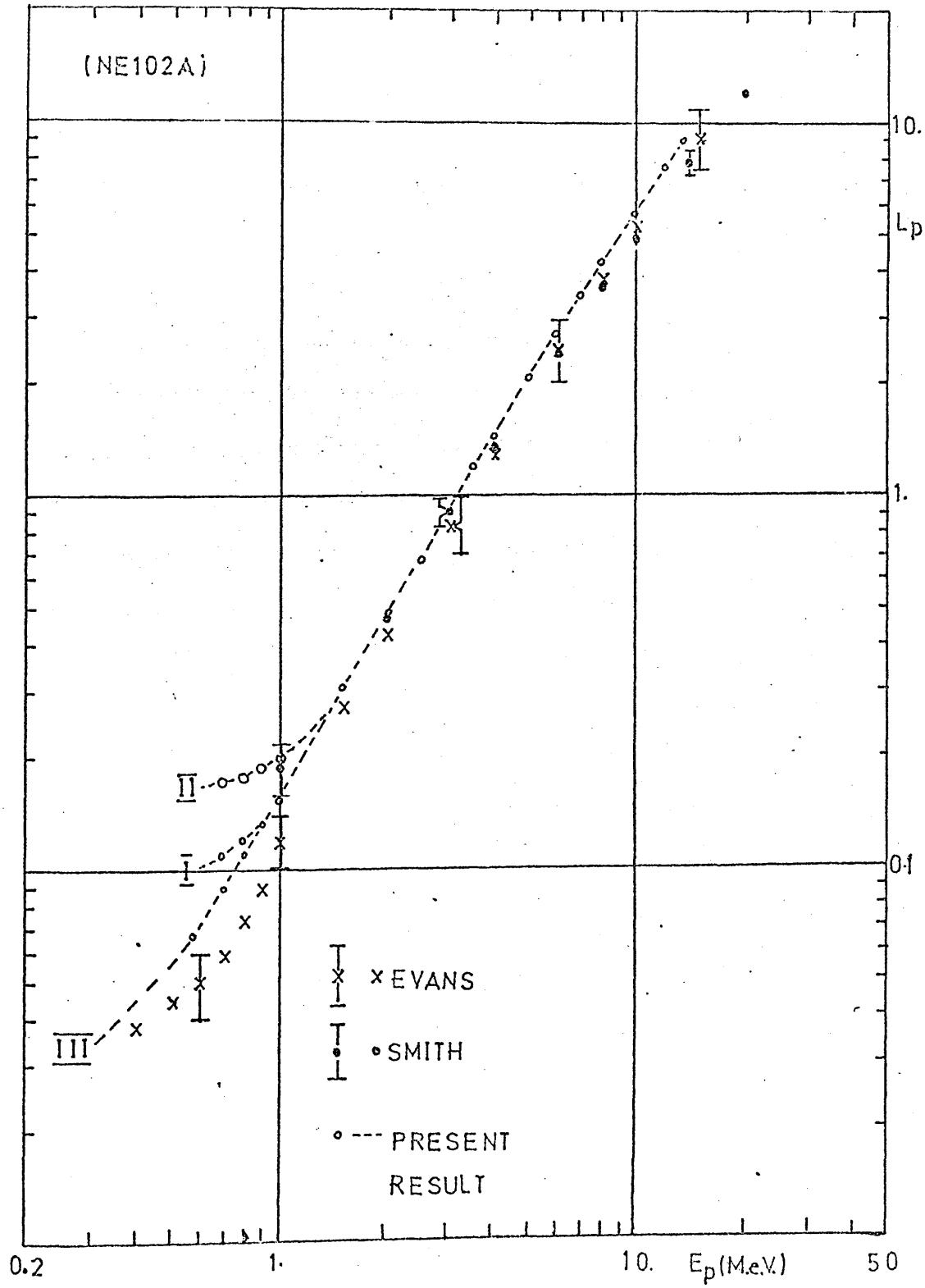

for each neutron energy. The fraction of the recoil plateau peak producing the correct channel was found to decrease from the expected 0.5 at high energies (8Mev.) to 0.25 at 0.7Mev. This is consistent with the increase in distortion by multiple scattering for neutrons of lower energy which have relatively more interactions in the scintillator.

Using the above criteria, the linear channel corresponding to each neutron energy was found and converted to the scintillation response using Fig.9. The resulting response curve, (Fig.12 curve I) was used as input to a second Monte Carlo calculation, the cut - off relationship was found and the original data re-examined on this basis. A response curve was again made and found to reproduce the original above 1.5Mev. although the results at lower energies were not so consistent (Fig.12 curve II). This inconsistency was found to be due to a change in the trend of the light response function at energies lower than those measured. Such a response was indicated by the results of Smith et. al. (Fig.7). The effect of a decrease of the slope of the logarithmic curve is to make lower energy protons give slightly larger pulses, so that the effect of many small interactions is to 'lift' the value of the total light pulse, and the half slope becomes greater than the one expected on the trend of the higher energy response alone.

An approximating function to this trend was produced as in Fig.12, with a 'gradient' determined by the results of Smith et. al. (Fig.7) and the condition that the response pass through the origin, or the energy axis, so that LP must vary more quickly than linearly with E.

FIGURE 14

PROTON SCINTILLATION RESPONSE OF NE102A

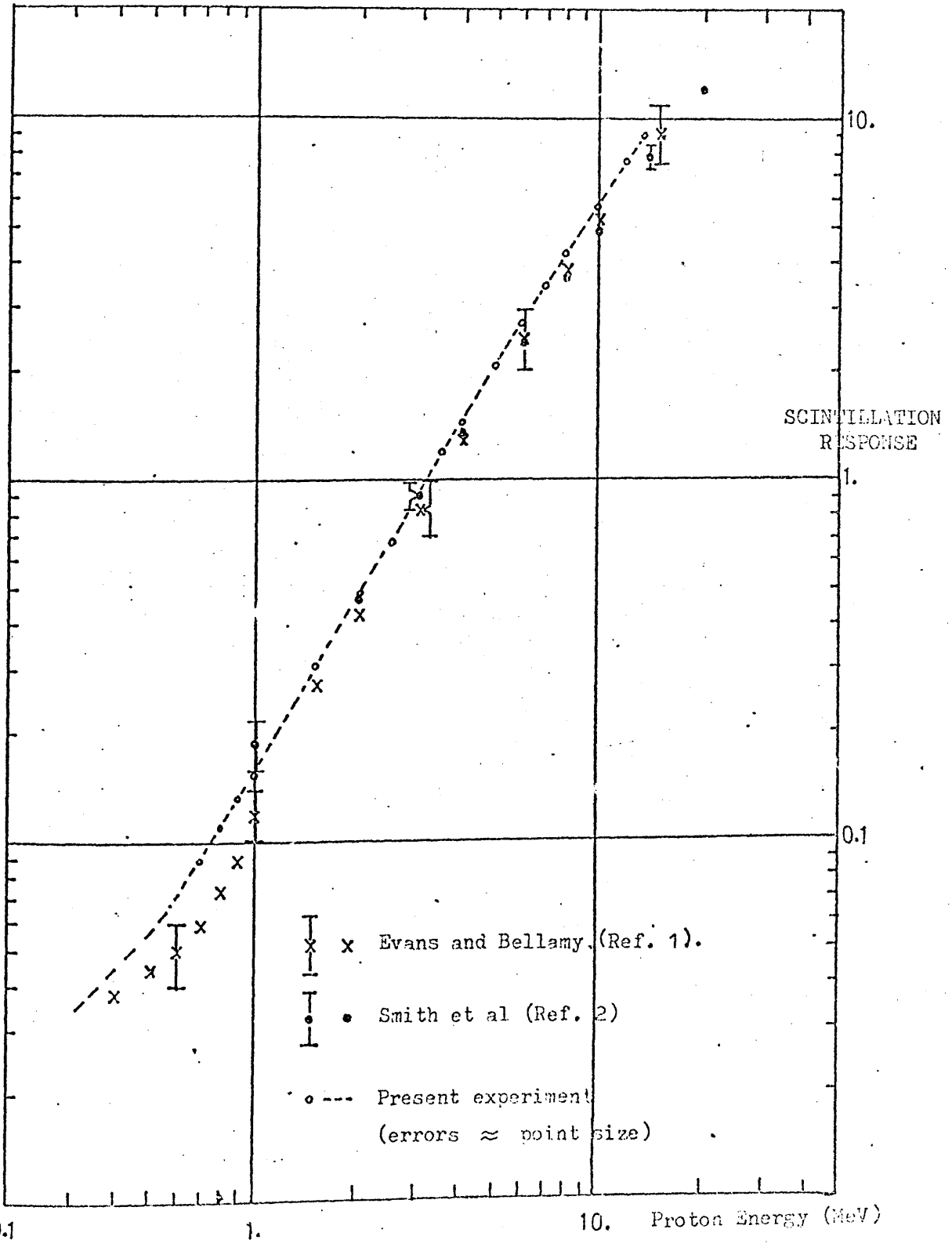

SCINTILLATION RESPONSE OF NE102A TO PROTONS. Fig. 15

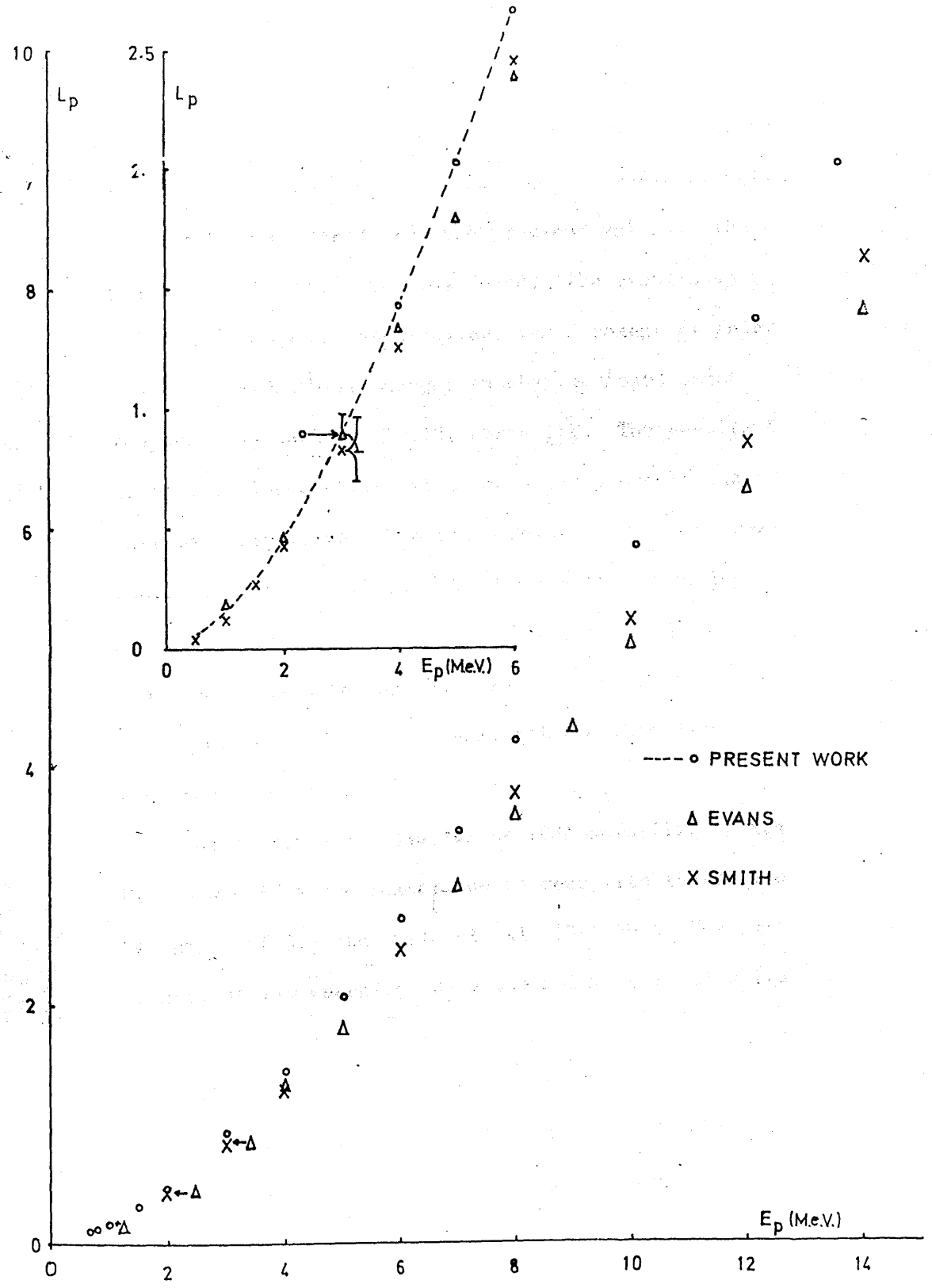

Altering the position of intersection of the low energy trend with the high, varied the magnitude of the multiple scattering effect in the sensitive area (0.7 to 1.0Mev.) and therefore the calculated relation between the peak in the light spectrum and the Hydrogen cut - off. Values of LP were then obtained from the measured data with the new criteria and compared with the previous values. The process was repeated until consistency was found. The results were highly sensitive to the position of intersection, for a change of intersection point from 0.5 to 0.55Mev. brought on obvious improvement. The final response is shown in Fig.12, curve III. The results in the 0.7Mev. to 1.0Mev. region are felt to be accurate since the consistency test was extremely sensitive. The trend below 0.6Mev. is presented as an indication only, although it is probably a good approximation to a more continuous real response. The results above 1.5Mev. were not measureably affected by the changes in response at very low energy. These were always self - consistent and this data is presented with confirmed accuracy.

The author's results for Ne 102A scintillator are presented in Fig.14 and 15 where comparison is made with the data of Evans and Bellamy (Ref.37) and Smith et. al. (Ref.38). The agreement is seen to be good at low energies where the author's results lie between the other two measurements, and to be just within the errors at energies above 6Mev. where the author's curve lies above the others by about 10%. Errors on the author's results are shown unless they are smaller than the points, and it can be seen that measurements have been made with a useful increase in accuracy over the whole range.

Responses to p, C and α ions in NE102A Fig. 16

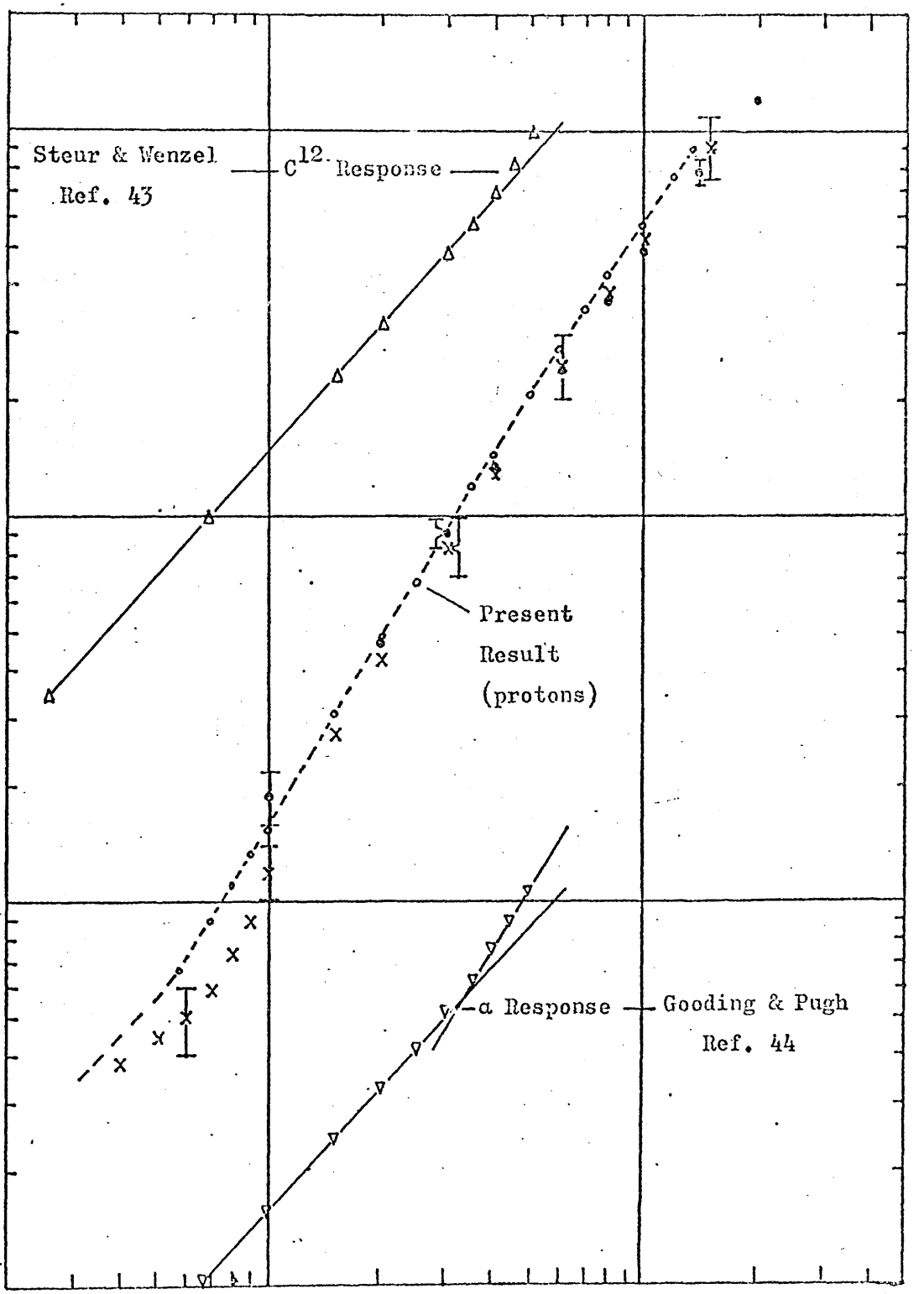

Fig. 17

MEASURED AND CALCULATED SCINTILLATION SPECTRA
5" DIA x 5" THICK Ne 102 A SAMPLE

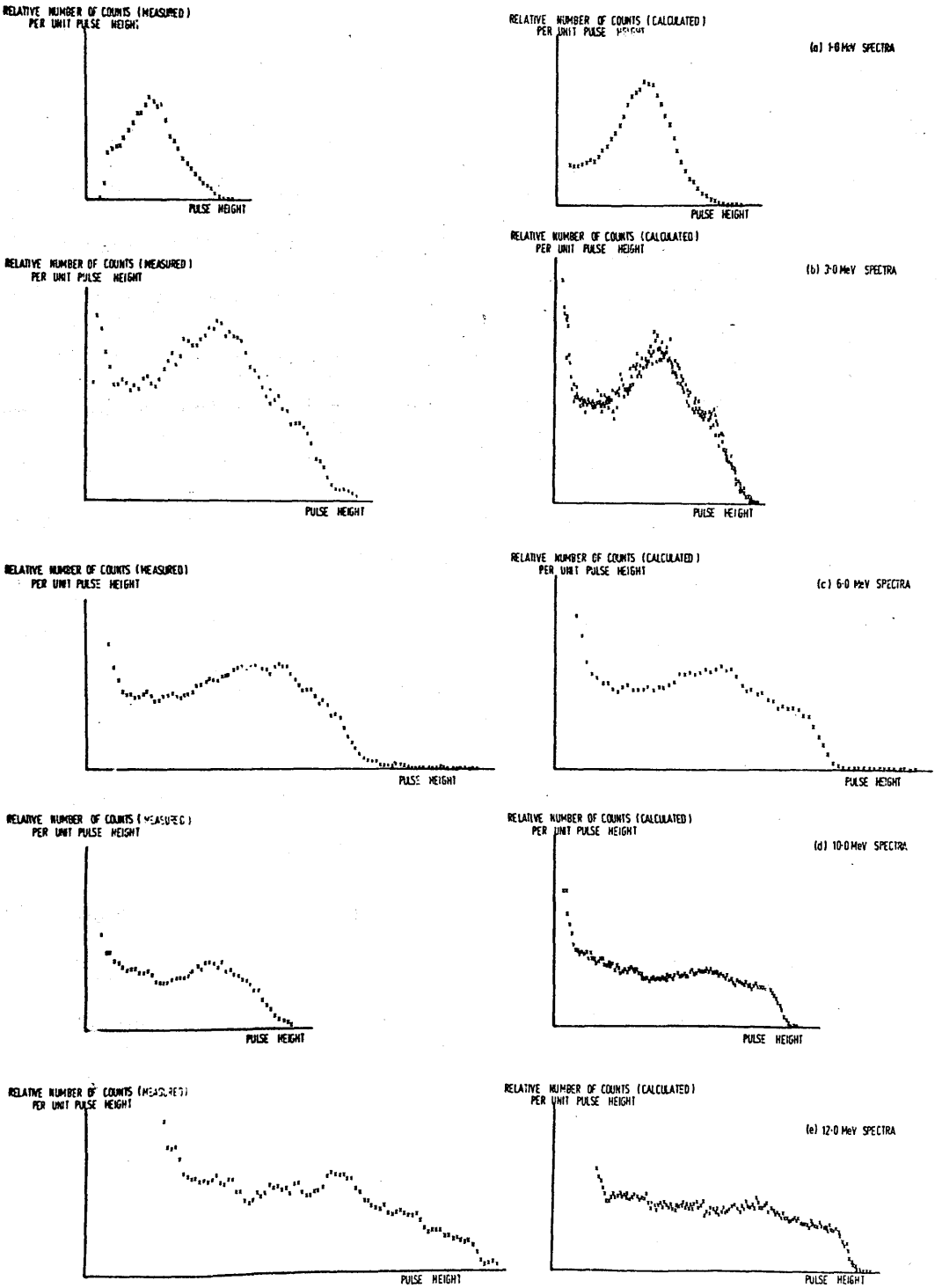

Results for Ne 102A have been presented in detail because this scintillator was actually used in the author's photoneutron experiment. The data on Ne 211 and Ne 213 is still under analysis at this time, but a previous trial run on Ne 211 had given results similar to those found by Verbinski (Ref.16) for both these scintillators. This information is presented in Fig.6.

The Scintillation Response of Carbon and Alpha Recoils.

The responses to Carbon recoils in Ne 102A and Ne 213 were accurately measured by Steur and Wenzel (Ref.43), and these results were used directly by the author. Interestingly, the value of response in Ne 213 is $2\frac{1}{2}$ times lower than that predicted by Batchelor (Ref.15) using equation (2) although Ne 102 shows the expected value. Alpha responses in Ne 102 were obtained from the measurements of Gooding and Pugh (Ref.44) and in Ne 213 from the presentation by Verbinski (Ref.16).

In Fig.16 are shown these responses to protons, carbon ions and alpha particles for Ne 102 scintillator, and the fit to each used for mathematical convenience in the Monte Carlo calculations. Errors in the approximations should be small (=1%).

(D) Comparison of the Measured and Calculated Light Spectra and the Detector Efficiency Results.

Typical measured and calculated light spectra from neutrons of energies between 0.7 and 13.5Mev. are presented in Figs.17(a)-17(e). These may be compared with the measurements and predictions of Hardy (Fig.1) to see how agreement with experiment has been improved. This excellent agreement lends authority to the values of detector efficiency calculated through these spectra.

FIGURE 18

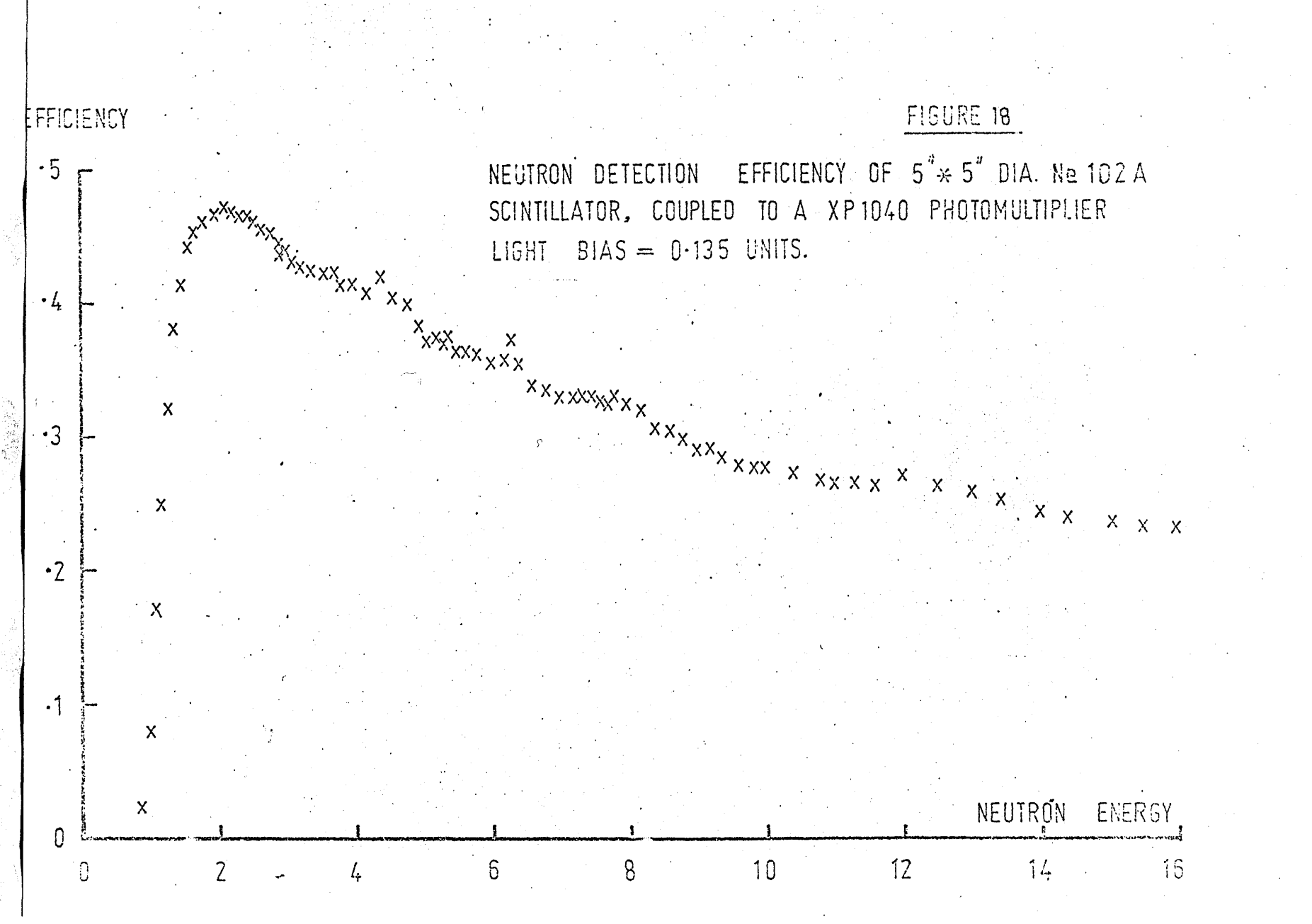
EFFICIENCY
·5
·4
·3
·2
·1
0
NEUTRON DETECTION EFFICIENCY OF 5" * 5" DIA. Ne 102 A SCINTILLATOR, COUPLED TO A XP 1040 PHOTOMULTIPLIER LIGHT BIAS = 0·135 UNITS.
NEUTRON ENERGY
0
2
4
6
8
10
12
14
16

Fig. 19

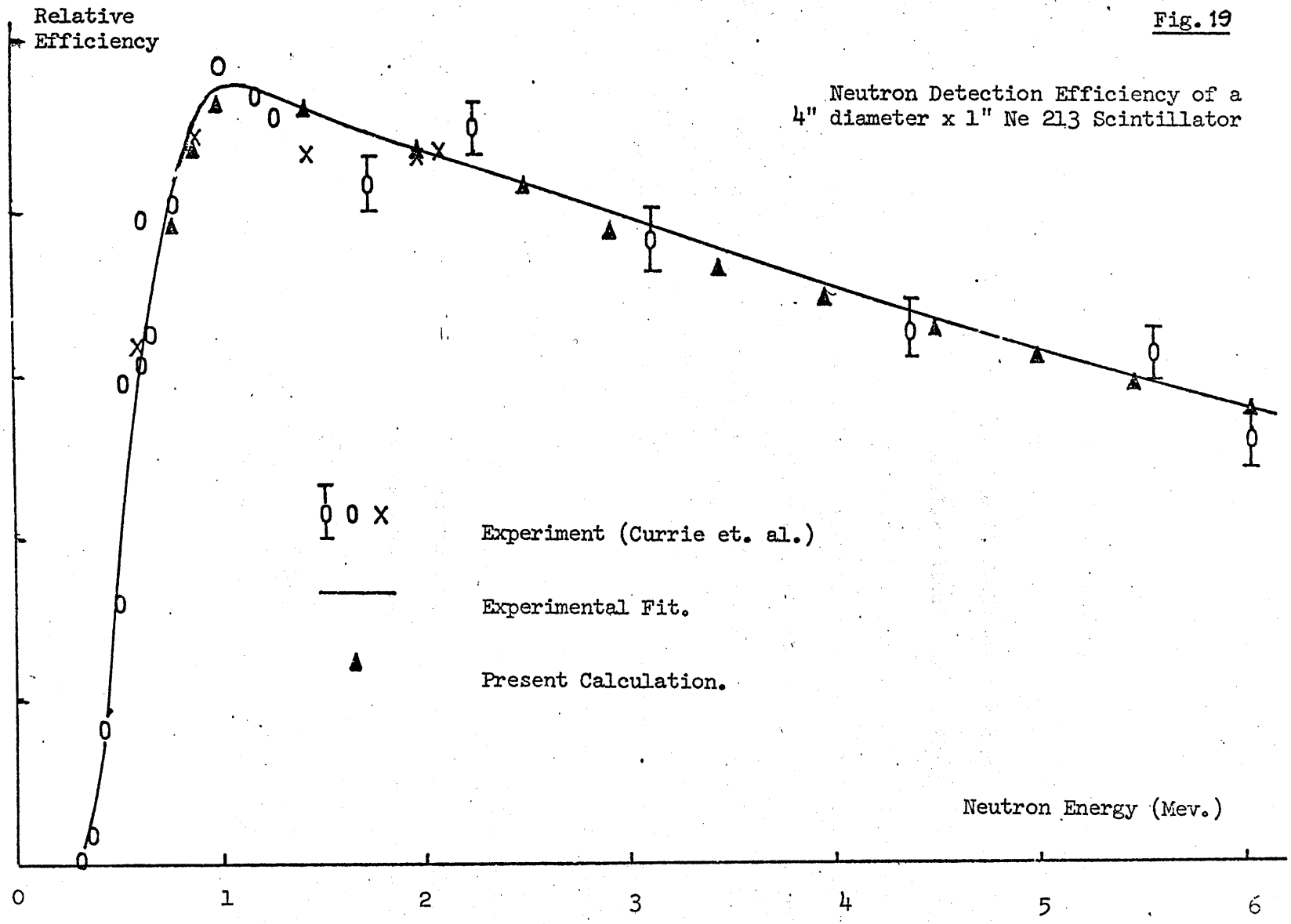
Relative Efficiency
Neutron Detection Efficiency of a 4" diameter x 1" Ne 213 Scintillator
Experiment (Currie et. al.)
Experimental Fit.
Present Calculation.
Neutron Energy (Mev.)
0
1
2
3
4
5
6

Fig.18 shows the efficiency curve calculated for the 5" dia. x 5" Ne 102A plastic scintillators at various bias levels. The slow discriminator cut - off effect is also shown. To the author's knowledge, no measurements of efficiency have been made for such a scintillator, but experimental results for the 4" dia. x 1" thick Ne 213 scintillators were available (Ref.45) and these were used to check the results for an exactly similar calculation on these detectors. The comparison is made in Fig.19 where the relative efficiency measured (Ref.45) has been normalised to the author's value at 2Mev. Calculation and experiment agree, to well within the experimental errors, and this is taken as justification of the calculation technique common to all scintillator types and dimensions. Note that these measurements were made with a slow (total charge) discriminator. No suitable efficiency measurements at energies above 6Mev. are available for comparison to the author's knowledge.

Estimates of the accuracy of the efficiency values can be made by consideration of the possible errors in the important parameters, although to estimate their effect on the final result is not always straightforward. The Hydrogen and Carbon cross sections are accurate to 1% and to between 2% and 5% respectively in the energy range. The error so produced in the mean free path is typically about 2% but the stopping power (the main component of the efficiency) is not in error by this amount, because:

$$W = 1-\exp(-t/\lambda)$$

so that:

$$dW = (d\lambda/\lambda)*(t/\lambda)*\exp(-t/\lambda)$$

substitution of typical values shows dW/W to be less than 0.5% in the

worst case, and therefore negligible. The same 2% error in λ dominates the uncertainty in PH, the probability of Hydrogen reaction. Most large light pulses come from Hydrogen collisions so that this quantity is important in simple efficiency models, but the large probability of a second interaction, in the present scintillator, allows many neutrons to be detected despite having first Carbon collisions, so that the efficiency is less sensitive to PH errors. A value of $\pm$ 1.5% was typical.

Errors in the scintillation responses measured by the author and the approximating functions used in the programmes to duplicate these are less than 2% and these have little effect upon the detection efficiency of most neutrons whose average pulse height is much above the bias level. The large multiple interaction probability and the possibility of large light pulses from the α and (n,n') reactions decrease the 7% error in the light production, caused by the 15% uncertainties in C^{12} reaction branching ratios, to about $3\frac{1}{2}$%, since detection requires only one pulse component to be greater than the light bias. Further errors due to the approximate treatments of some of the non - elastic Carbon reactions are estimated to affect the efficiency by less than 1%, so that, below 6Mev. where non - elastic events are insignificant, the total error is less than 2%. At higher energies the uncertainty increases to 4%.

The size of systematic errors introduced at very low neutron energies by use of a fast discriminator only have been estimated in Fig.5C. This difficulty is normally overcome by only using the efficiency curve for energies above these, and this was suitable to the

purposes of the author, who required calibrated neutron detectors above about $1\frac{1}{2}$Mev. energy for measurements of Giant Dipole Resonance photoneutron cross sections. The present calculations are seen to provide the required calibrations with good accuracy.

References Chapt.(APP 1)

1. Birks, J.B. 'The Theory and Practice of Scintillation Counting'. (Pergammon Press) (1964).

2. Rutherford, E., Chadwick, J. and Ellis, C.D. 'Radiations from Radioactive Substances' (Cambridge University Press) (1930)

3. Curran, S.C. and Baker W.R. Rev. Sci. Instr., 19, 116(1948)

4. Bell, P.R. Phys. Rev., 73,1405(1948)

5. Ageno, M., Chiozzotto, M and Querzoli, R. Acad. naz Lincei, 6,626(1949)

6. Schorr, M.G., and Torney, F.L., Phys. Rev., 80,474(1950)

7. (a) Firk, F.W.K. and Lokan K.H. Phys. Rev. Letters. 8,No.8.p321(1962).

   (b) Bertozzi, W., Demos, P.T., Kowalski, S., Paolini, F.R., Sargent, C.P. and Turchinetz, W. N.I.M. 33,199(1965)

   (c) Verbinski, V.V. and Courtney, J.C. Nuclear Physics 73,398(1965)

   (d) Oliver, C.J., Collinge, B. and Kaye, G. N.I.M. 50,109(1967)

   (e) Wishart, L.P., Plattner, R. and Cranberg, L. N.I.M. 67,237(1967)

8.

9. Poole, M.J.,

Proc. Phys. Soc. A65,453(1952)

10. Prescott, J.R. and Rupal, A.S.,

Canad. J. Phys. 39,221(1961)

11. Brock, H.W. and Anderson, C.E.,

Rev. Sci. Instr. 32,1063(1960)

12. Hardy, J.E.

Rev. Sci. Instr. 29,705(1958)

13. Grassler, H. and Tesch, K.

N.I.M. 10,353(1961)

14. Cranberg, L. and Levin, J.S.

Phys. Rev. 103,343(1956)

15. Batchelor, R., Gilboy, W.B., Parker, J.B. and Towle, J.H.

N.I.M. 13,70(1961)

16. Verbinski, V.V., Burrus, W.R., Love, T.A., Zobel, W. and Hill, N.W. and Textor, R.

N.I.M. 65,8(1968)

17. Burrus, W.R. and Verbinski, V.V.

N.I.M. 67,181(1969)

18. Cashwell, E.D., Everet, C.J. and Rechard, O.W.

'A practical Manual on the Monte Carlo Method for Random Walk Problems'.

Los Alamos Report LA-2120(1957)

19. Goldberg, M.D., May, V.M. and Stehn, J.R.

'Angular Distribution in neutron induced reactions, Z=1 to 22'

Brookhaven National Laboratory Report BNL-400, 2nd edition, volume 1(1962)

20. Garber, D.I., Stromberg, L.G., Goldberg, M.D., Cullen, D.E. and May, V.M.

BNL-400,3rd edition, volume 1(1970)

21. Hughes, D.J. and Schwartz, R.B.

Brookhaven National Laboratory Report BNL 325 (2nd edition) (1958)

Hughes, D.J., Magurno, B.A., and Brussel, M.K.

BNL 325 (2nd edition) Supplement No.1

22. Stehn, R.S., Goldberg, M.D., Magurno, B.A. and Weiner-Chasman, R.

B.N.L. 325, 2nd edition, Supplement No.2 1964.

23. Cierjacks, S., Forti, P., Kopsch, D., Kropp, L., Nebe, J. and Unseld, H.

'High Resolution Total Neutron Cross Sections between 0.5-30Mev.'

Institut Fur Angewandte Kernphysik, Karlsrue, 1968

24. Frye, Rosen and Stewart.

P.R. 99,1375(1955)

25. Sachs, M.

P.R. 103 p671 1956

26. Graves and Davis.

P.R. 97,242(1955)

27. Kital and Peck, J.R.

P.R. 130,1500(1963)

28. Chatterjee and Sen.

N.P. 51,583(1963)

29. Gardner and Wu.

N.P. 60,49(1964)

30. Barton

N.P. 36,247(1962)

31. Mattauch, J.H.E., Thiele, W. and Wapstra, A.H.
N.P. 67, 1 (1965)

32.

33. Taylor, Parker and Langenberg

Rev. Mod. Phys. 41,375(1969)

34. Baldin, A.M., Goldanski, V.I. and Rozenthal, I.L.

'Kinematics of Nuclear Reactions'

Pergammon Press, 1961.

35. Segre, E.

'Experimental Nuclear Physics' VI

J. Wiley & Sons, Inc., 1953.

36. Prescott, J.R. and Rupal, A.S.

Canad. J. Phys. 39,221(1961)

37. Evans, H.C. and Bellamy, E.H.

Proc. Phys. Soc. 74,483(1959)

38. Smith, D.L. Polk, R.G. and Miller, T.G.

N.I.M. 64,157(1968)

39. Rotheberg et. al.

P.R. 132.2664(1963)

40. Bertini, A., Vitale, A. and Placci, A.

N.I.M. 91,649(1971)

41. Kellie, J.D. and Crawford, G.I.

N.I.M. 72,329(1969)

42. Flynn, K.F., Glendenin, L.E., Steinberg, E.P. and Wright, P.M.

N.I.M. 27,13(1964)

43. Stever, M.F. and Wenzel, B.E.

N.I.M. 33,131(1965)

44. Gooding, T.J. and Pugh, H.G.

N.I.M. 7,189(1960)

45. Currie, W.M., Martin, J. and Stewart, D.T.

Harwell Report A.E.R.E. - R5618

APPENDIX 3

Summary of the main errors inherent in the calculation of the E2 cross-section from (γ,p) angular distribution coefficients using the formula of Frederick.

(1) The effective charge of E2 transitions in light nucleii is about $\frac{1}{2}$ for both protons and neutrons as opposed to the theoretical (lplh) value of 29/32 used for protons in the derivation of the formula. The cross-sections are therefore liable to be over estimated by a factor of ~ 4.

(2) Several simplifying assumptions are made about the two E1 components, viz. $\cos(\rho\, 3/_2 1 - \rho\, \frac{1}{2}\, 1) \doteq 1$; $\rho\, 3/_2{}^2 1 = 0.999$; $\rho\, \frac{1}{2}{}^2 1 = .001$ and $A_2/A_0 \doteq -0.55$. Experimentally observed variations in A_2/A_0 may cause ~ 25% errors if neglected, anf the associated average values of $\rho\, 3/_2{}^2 1$ and $\rho\, \frac{1}{2}{}^2 1$ are experimentally 0.96 and 0.04 respectively. This decreases the calculated E2 cross-section by $\sim$ X2 for typical A_1, A_3 values in the proton distributions. The cross-sections shown may therefore be too large by this amount.

(3) The model applies to protons, that the neutron results are similar is unexpected on a lplh basis.